

Silver Nanostructures on Oxide Surfaces: Growth, Characterizations and Applications

By

Puspendu Guha

(PHYS07201204004)

Institute of Physics, Bhubaneswar

A thesis submitted to the

Board of Studies in Physical Sciences

In partial fulfillment of requirements

for the Degree of

DOCTOR OF PHILOSOPHY

of

HOMI BHABHA NATIONAL INSTITUTE

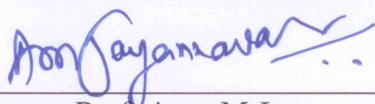


August, 2018

Homi Bhabha National Institute

Recommendations of the Viva Voce Committee

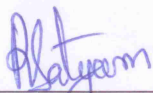
As members of the Viva Voce Committee, we certify that we have read the dissertation prepared by **Mr. Puspendu Guha** entitled "**Silver Nanostructures on Oxide Surfaces: Growth, Characterizations and Applications**" and recommend that it may be accepted as fulfilling the dissertation requirement for the Degree of Doctor of Philosophy.



Chairman - Prof. Arun M Jayannavar

08-08-2018

Date:



Guide / Convener - Prof. Parlapalli V Satyam

Date: 08 August 2018

Co-guide - <Name> (if any)

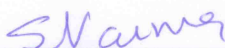
Date:



Examiner – Prof. N Ravishankar

8/8/18

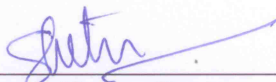
Date:



Member 1- Prof. Shikha Varma

8/8/18

Date:



Member 2- Prof. Suresh Kumar Patra

Date: 08/08/2018

Final approval and acceptance of this dissertation is contingent upon the candidate's submission of the final copies of the dissertation to HBNI.

I hereby certify that I have read this dissertation prepared under my direction and recommend that it may be accepted as fulfilling the dissertation requirement.

Date: 08 August 2018

Place: Bhubaneswar

<Signature>

Co-guide (if applicable)



<Signature>

Guide

डॉ. पी.वी. सत्यम / Dr. P.V. Satyam
प्रोफेसर / Professor
भौतिकी संस्थान / Institute of Physics
भुवनेश्वर / Bhubaneswar

STATEMENT BY AUTHOR

This dissertation has been submitted in partial fulfillment of requirements for an advanced degree at Homi Bhabha National Institute (HBNI) and is deposited in the Library to be made available to borrowers under rules of the HBNI.

Brief quotations from this dissertation are allowable without special permission, provided that accurate acknowledgement of source is made. Requests for permission for extended quotation from or reproduction of this manuscript in whole or in part may be granted by the Competent Authority of HBNI when in his or her judgment the proposed use of the material is in the interests of scholarship. In all other instances, however, permission must be obtained from the author.

Puspendu Guha

Puspendu Guha

DECLARATION

I, Puspendu Guha, hereby declare that the investigation presented in the thesis has been carried out by me. The work is original and has not been submitted earlier as a whole or in part for a degree / diploma at this or any other Institution / University.

Puspendu Guha

Puspendu Guha

List of Publications arising from the thesis

Journal

1. Ag Nanoparticles Decorated Molybdenum Oxide Structures: Growth, Characterization, DFT Studies and Their Application to Enhanced Field Emission, **P Guha**, A Ghosh, R Thapa, E M Kumar, S Kirishwaran, R Singh and P V Satyam, *Nanotechnology*, **2017**, 28, 415602.
2. In-situ Synchrotron X-ray Diffraction Study of Coherently Embedded Silver Nanostructures Growth in Silicon, **P Guha**, R R Juluri, A Bhukta, A Ghosh, S Maiti, A Bhattacharyya, V Srihari and P V Satyam, *CrystEngComm*, **2017**, 19, 6811–6820.

Chapters in books and lectures notes

Conferences

1. Ion Beam Induced Endotaxial Silver Nanostructures in Silicon, **P Guha**, R R Juluri and P V Satyam, *Nucl. Instr. Meth. Phys. Res. B*, **2017**, 409, 209–215.
2. Energetically Favored Site Specific Ag NPs Decorated Molybdenum Oxide Heterostructures: Microscopy Observations and Field Emission Study, **P Guha**, A Ghosh and P V Satyam.
(Poster presented @ An International Conference on Electron Microscopy “Electron Microscope Society of India - 2016 (EMSI2016)” jointly organized by Electron Microscope Society of India (EMSI) and Indian Institute of Technology (Banaras Hindu University), Varanasi, (IIT, BHU) during 2nd - 4th June, 2016 at IIT, BHU, Varanasi)
3. Electron Microscopy Study of Silver Nanoparticles on Oxide Surfaces, **P Guha**, A Ghosh, R R Juluri and P V Satyam.
(Poster presented @ An International Conference on Electron Microscopy “Electron Microscope Society of India - 2017 (EMSI2017)” jointly organized by Electron Microscope Society of India (EMSI), Indira Gandhi Centre for Atomic Research, Kalpakkam (IGCAR, Kalpakkam) and Indian Institute of Technology, Madras (IITM) during 17th - 19th July, 2017 at Mahabalipuram, Tamil Nadu)
4. *P*-type β -MoO₂ Nanostructures on *n*-Si by Hydrogenation Process: Synthesis and Application towards Self-Biased UV-Visible Photodetection, **P Guha**, A Ghosh, A Sarkar, S Mandal, S K Ray, D K Goswami and P V Satyam.
(Oral presented @ An International Conference on Electron Microscopy “Electron Microscope Society of India - 2018 (EMSI2018)” organized by Electron Microscope Society of India (EMSI), in collaboration with IOPB, NISER, CSIR-IMMT, IIT BBS, ILS, CSIR-CGCRI during 18th - 20th July, 2018 at Bhubaneswar, Odisha)

Others

Puspendu Guha
Puspendu Guha

DEDICATED TO ALL MY FAMILY MEMBERS

ACKNOWLEDGMENTS

I am pondering to write this section for expressing my sincere gratification, who has aided me in my thesis works. Please forgive me if I forget to mention someone unconsciously or unwittingly.

First and foremost, I would like to convey my earnest gratitude to Prof. P V Satyam as my supervisor for providing me an opportunity to work in his group. I am incredibly grateful for his guidance, encouragement and supervision during my research period. I do feel myself as lucky person being a PhD scholar in his research group. He has given me full freedom to carry out research works in my own interest, which I have enjoyed a lot and I must extend my great depth of gratitude and indebtedness to him for that. I would like to thank him for giving me a very well setup and healthy organized laboratory. I must thank him for getting an opportunity to carry out synchrotron based high temperature XRD experiments at Indian Beam line 18B, Photon Factory, KEK, Japan.

I am really grateful to Saha Institute of Nuclear Physics (SINP), India especially to Dr. M K Mukhopadhyay, Dr. S Maiti and Mr. A Bhattacharyya for facilitating and accomplishing the experiments at Photon Factory, Japan.

I am gratified to Dr. B K Jena (IMMT, BBSR) and his group especially Mr. B Mohanty for allowing me and helping me to carry out measurements in their laboratory whenever I wanted and it's my great pleasure to work with them.

In the course of my PhD candidature, I have got opportunity to collaborate with Dr. R Thapa from SRM University (Kattankulathur, Chennai) and his group and I feel privileged to have worked with his group. I am honestly obliged to Prof. S K Ray and Dr. D K Goswami and their group for facilitating all photodetection measurements (including all associated experiments). I do hope that many opportunities will come in the future to collaborate with them.

I would like to acknowledge Prof. T Som (IOP, BBSR) and his group specially Mr. R Singh for carrying out several measurements e.g., UV-vis, electron field emission, KPFM for many times. I want to give thanks to Dr. D Topwal (IOP, BBSR) and his student Mr. P Nandi for

XRD and PL measurements for several times whenever I needed. My good wishes to Mr. R Singh and Mr. P Nandi for their research works.

Sincere thanks go to Prof. A Jayannavar, Prof. S Varma and Prof. S K Patra as my thesis committee members for their beneficial suggestions and colossal advices throughout my research tenure at IOP. I want to thank Dr. S Sahoo for fundamental discussions with him about molybdenum oxide work. My earnest appreciation to all the Directors at IOP BBSR for their support and kindness over these years.

It has given me immense pleasure to spend more than 4 years in electron microscopy group at IOP. I wish to acknowledge all the members in our group for their respective help and support. They have provided with a friendly, concerted and an excellent research atmosphere. I genuinely convey my cordial gratefulness to all my lab fellow workers Dr. R R Juluri, Dr. A Ghosh, Dr. A Bhukta and Mrs. P Maiti. My innermost acknowledgement to Dr. Juluri and Dr. A Ghosh. I have learned many technical skills from them. Their incredible levels of skill, expertise, knowledge and experience have enriched me to a great extent. A very special appreciation goes out to my senior Dr. Arnab Ghosh, without whom I couldn't able to complete my thesis works in time. Thank you very much Arnab da for his enormous and continuous cooperation in every regards right from ideas, experiments to paper writings. I have spent a very great time with him and I will relish all the moments. I wish my lab junior Paramita the best of luck for her research endeavors.

I am really thankful to our group postdoctoral fellows Dr. T Arun, Dr. B Rakshit, Dr. H Rath and Dr. A Mitra for their assistances in all aspects. I would like to thank Mr. S R Mohanty and Dr. B K Dash as our proficient scientific assistants for providing each and every requirement. A very special thank goes to Mr. S R Mohanty for his continuous, quick and reliable assistance in both academic and non-academic contests whenever I required.

Thanks to my friends, batch mates, seniors, juniors for making enjoyable and memorable experience during my whole stay here. We have shared joys and struggling in tough times.

I acknowledge the excellent library and computer facilities provided by the IOP and all the members of IOP for their direct or indirect help in many cases.

Last but not the least, I am deeply indebted to all my family members for their love and support, which they have given me throughout my life. Without their constant sacrifice and

guidance, this accomplishment would have never been completed. They always believed in me and kept me going through tougher times. Thanks to all of you.

CONTENTS

Synopsis	1
List of Figures	9
List of Tables	15
Chapter 1: Introduction	16
Chapter 2: Experimental Techniques	26
2.1 Introduction	26
2.2 Fabrication and growth of thin films and nanostructures	27
2.2.1 Physical vapor deposition (PVD) technique: thermal evaporation in high vacuum (HV) chamber	27
2.2.2 Chemical vapor deposition (CVD) technique	29
2.2.2.1 Vapor-solid (VS) growth mechanism	31
2.2.3 Ion beams for synthesis and modification	32
2.2.3.1 Energy losses: nuclear and electronic	33
2.3 Characterization techniques	33
2.3.1 Transmission electron microscopy (TEM)	34
2.3.1.1 Instrumentation	35
2.3.1.2 Diffraction and imaging	38
2.3.1.3 Beam (electrons)-specimen interaction	40
2.3.1.4 Sample preparation (mechanical process)	41
2.3.2 Focused ion beam – scanning electron microscope (FIB – SEM) cross beam system	43
2.3.2.1 Scanning electron microscopy (SEM)	44
2.3.2.2 Focused ion beam (FIB)	48
2.3.3 X-ray diffraction (XRD)	49
2.3.3.1 Instruments: Photon Factory	50
2.3.4 X-ray photoelectron spectroscopy (XPS)	51
2.3.5 Raman spectroscopy	53
2.3.6 UV-Vis-NIR	54
2.3.7 Kelvin probe force microscopy (KPFM)	55
2.4 Applications	55
2.4.1 Field emission (FE)	56
2.4.2 Photodetector (I-V) characteristics	58
2.4.3 Surface enhanced Raman spectroscopy/scattering (SERS)	58
2.5 References	60
Chapter 3: In-situ Synchrotron X-ray Diffraction Study of Coherently Embedded Silver Nanostructures Growth in Silicon	63
3.1 Introduction	63

3.2 Experimental	65
3.3 Results and discussion	66
3.3.1 Effects of temperature and crystallite size on thermal expansion coefficient (TEC)	71
3.4 Conclusion	74
3.5 References	75
Chapter 4: Ion Beam Induced Endotaxial Silver Nanostructures in Silicon	77
4.1 Introduction	77
4.2 Experimental	78
4.3 Results and discussion	79
4.3.1 Un-irradiated system	79
4.3.2 High energy (MeV) irradiated system	80
4.3.3 Low energy (keV) irradiated system	81
4.4 Conclusion	90
4.5 References	90
Chapter 5: Ag Nanoparticles Decorated Molybdenum Oxide Structures: Growth, Characterization, DFT Studies and Their Application to Enhanced Field Emission	92
5.1 Introduction	92
5.2 Experimental	95
5.2.1 Growth	95
5.2.2 Characterization	96
5.2.3 Computational details	97
5.3 Results and discussion	97
5.3.1 Structural characterization	97
5.3.2 Growth mechanism: theoretical model	101
5.3.3 XPS	105
5.3.4 Raman	107
5.3.5 Field emission and KPFM results	109
5.4 Conclusion	116
5.5 References	116
Chapter 6: Role of Ambience on the Growth of Site Specific Ag Nanoparticles Decorated MoO₃ Structures: Applications to Surface Enhancement Raman Scattering	120
6.1 Introduction	120
6.2 Experimental	121
6.3 Results and discussion	122
6.3.1 Ambient dependency: structural characterization	122
6.3.2 SERS substrates: detection of crystal violet (CV) molecules	124
6.4 Conclusion	125
6.5 References	126

Chapter 7: <i>P-type</i> β-MoO₂ Nanostructures on <i>n</i>-Si by Hydrogenation Process: Synthesis and Application towards Self-Biased UV-Visible Photodetection	128
7.1 Introduction	128
7.2 Experimental	130
7.3 Results and discussion	132
7.3.1. Structural characterization	132
7.3.1. Growth mechanism	133
7.3.3 Spectroscopic studies	135
7.3.4 UV-Vis absorbance	136
7.3.5 Photodetector device characterization	137
7.3.6 Energy band diagram	140
7.4 Conclusion	144
7.5 References	145
Chapter 8: Summary and Conclusions	148

Synopsis

Nanoscale structures/materials are extensively studied for their interesting physical, chemical and mechanical properties at the nano/subatomic scale as well as their technological applications [1-4]. The thesis work is focused on novel methods of incorporating metal nanostructures on the surfaces and at the interfaces of oxide materials. The oxide nanostructures found to have many applications and in combination with metal nanostructures (in particular with Ag nanostructures), the physical and chemical properties gets modified, resulting in enhanced performances [5–8]. For many decades, metal-semiconductor junctions have been studied due to their large importance in electronic industry [5–8]. With the size of the electronic devices being pushed towards nanometer scale, nano-metal and semiconductor interfaces play a vital role in present and future technology. When metal NPs are proximal to semiconductor, the electrons from metal can directly be transferred into conduction band of the semiconductor, providing enhanced capabilities in many applications [5–8]. However, high quality metal-semiconductor structures are very difficult to achieve due to their chemical and structural dissimilarities [9]. The present thesis work emphasizes the growth of nanostructures that can be either *on (epi)* the oxide layers or *in (endo)* the oxide/substrate nanoscale systems. When a material/overlayer grows on a crystalline substrate, where the overlayer is in registry with the substrate, then the growth is known as epitaxial growth. On the other hand, when material/precipitate grows into a bulk matrix, where the precipitate will be coherently surrounded by the matrix, then the process is known as endotaxy. *This thesis work is focused on the novel growth of metal (silver) - semiconductors (GeO_x or MoO_3) combinations, understanding the growth process through computer simulation works and their potential enhanced applications, such as, field emission, photo detection, surface enhanced Raman scattering, etc.*

Nobel metal (Au, Ag, Pt, Ni) nanoparticles (NPs) are of great scientific significance in diverse technological applications, such as, optical, electrical, biological applications due to their plasmonic properties and large surface to volume ratio [10–13]. Among metal NPs, silver (Ag) shows highest electrical conductivity and is the best applicant for electrical

characterization [14, 15]; silver is also the leading candidate for catalysts [16], sensors [17] detecting organic dye-molecules, bio-molecules via surface enhanced Raman spectroscopy (SERS) technique [18, 19]. In recent times, embedded silver nanostructures are used as SERS substrate to detect sub-micro molar dye-molecule, such as, crystal violet (CV) [20, 21]. Molybdenum oxides, wide band gap (2.6-3.2 eV) semiconductors, are found to be one the most fascinating transition metal oxide (TMO) for their unique structural, electrical, optical, mechanical properties and multi-directional applications [22–24]. Molybdenum oxide has been extensively used in diversified applications such as photochromic devices, electrochromic devices, gas sensing, photocatalysis, resistive switching, lithium ion batteries, catalysis, field emission, photovoltaic, transistors, inorganic light emitting diode, capacitors, panel displays, smart windows [25–27] etc. Even though MoO_3 is being employed as potential applicant in several fields, its poor electrical and ionic conductivity have become roadblocks for its manifold uses [28, 29], which need to be enhanced for achieving greater applications. Several possibilities to enhance the conductivity properties, such as, incorporating oxygen vacancies into lattice [28], conjugating with metal nanoparticles (NPs) with MoO_3 structures [8, 30], metal doping [31] and etc. are being actively studied. Achieving a good growth technique/process for coupling of MoO_3 with metal is not very easy in a *single step* process. The combination of plasmonic metal and semiconductor nanomaterials have been explored comprehensively in the past decades as these heterostructure materials can offer even better performances in diverse territories compared to individuals [5–8].

This thesis work is based on the silver nanostructures incorporation in two oxide materials: germanium oxide (GeO_x) and molybdenum tri-oxide (MoO_3). The thesis also deals with the applications of these materials following the modification with Ag nanostructures. First part of this thesis work is devoted on silver nanoparticles embedded inside oxide layer GeO_x on a silicon substrate [32, 33]. Though the earlier work on the endotaxial Ag nanostructure growth was reported [20, 21], the tasks of carrying out *real time* and *in-situ* measurements were necessary to shed a light on endotaxial growth. The present thesis work, presents a simple but elegant ways of studying the grow process and the real time structural and thermal properties of the embedded nanostructures by carrying our real time X-ray diffraction measurements at a synchrotron beam line. Here, we present a *novel* method by making a simple chemical vapor deposition system using a high temperature setup mounted on 6-circle goniometer at photon factory in KEK, Japan. Besides the use of pre-deposition of a thin Ag layer using a physical vapor system, the report also presents the effect of low (tens

of keV) and high energy (\approx MeV) Ag ion irradiations. In the first case, we are reporting the *real time* and *in-situ* growth of crystalline coherently embedded silver nanostructures in modified single crystalline silicon substrate by performing growth through chemical vapor obtained from evaporation of Ag from a silver wire. In the second case, defects have been created in GeO_x layer and crystalline silicon matrix to enhance the reaction rate by increasing the silver diffusion towards substrate. It is also shown that by using low energy ion implantation at high fluences, and followed by annealing process could indeed achieve endotaxial growth. Next part of this thesis contains silver nanoparticles above another oxide material (MoO_3). Here, we report an interesting new technique to synthesize site specific Ag-decorated MoO_3 nanostructures [34]. Interestingly, the Ag nanoparticles grow only on certain MoO_3 surfaces (i.e. (100) and (001)), but not on (010). Density functional theory (DFT) calculations have been executed to explain the preferred growth of the Ag nanoparticles on MoO_3 surfaces. We have also examined the role of different ambiances on the growth of Ag nanoparticles decorated MoO_3 structures. Ag-decorated MoO_3 nanostructures have been utilized for electron field emission device, detecting sub-micro molar dye molecules [34, 35]. However, the intrinsic MoO_3 exhibits low electrical and thermal conductivity and weak photoresponse. In order to improve the conductance, H_2 annealing is best process to enhance the conductivity [28]. We have prepared MoO_2 structures from MoO_3 structures via H_2 process to utilize as-grown MoO_2 in UV photodetection device application, which is presented in the last section of this thesis [36].

This thesis is constituted of eight chapters. The first chapter encompasses a brief introduction and motivation to the need of growing silver (Ag) nanoparticles (NPs) either inside or on the two oxide materials (GeO_x or MoO_3) and their properties with possible applications. The experimental methods used in the thesis are presented in Chapter 2. The 3rd and 4th chapters include the works referring to Ag NPs inside GeO_x and the subsequent chapters carry the works concerning Ag NPs above MoO_3 surfaces.

Experimental methods and their basic operating principles, which are employed for the synthesis, characterizations and applications of the materials, have been discussed in chapter 2. Thermal evaporation techniques like physical vapor deposition (PVD) and chemical vapor deposition (CVD) technique are used to grow the nanostructures. Besides the evaporation methods, the ion implantation (irradiation) technique (both low energy and high energy) have been exploited to synthesis silver nanostructures. Field emission gun based scanning electron microscope (SEM), transmission electron microscopy (TEM) capable with high resolution mode coupled with selected area electron diffraction (SAED), X-ray

diffraction (XRD) including high temperature stage, Raman, X-ray photoelectron spectroscopy (XPS), UV-Vis reflectance/absorption spectroscopy, Kelvin probe force microscopy (KPFM), field emission (FE), current voltage (I-V) measurements and surface enhanced Raman spectroscopy (SERS) have been utilized to study the growth, characterizations and applications of the materials related to this thesis work.

Coherently embedded structures in a single crystalline matrix are known as endotaxial structures. Chapter 3 reports the *real time* and *in-situ* growth of endotaxial silver nanostructures (Ag NSs) in modified silicon (Si) matrix by performing growth through chemical vapor obtained from evaporation of Ag from a silver wire under ambient conditions during synchrotron based high-temperature XRD measurements. A ≈ 17 nm thick GeO_x film was grown on native oxide covered silicon substrates ($\text{GeO}_x/\text{SiO}_x/\text{Si}$) using a physical vapor deposition (PVD) method, that were used as substrates for Ag NSs growth. For growing Ag NSs, silver wires were kept on the specimen hot stage (chemical vapor deposition) along with the above mentioned substrates. All the *in-situ* growth and *real time* XRD were done under atmosphere conditions. Besides reporting on the direct evidence for crystalline growth of endotaxial Ag NSs, this work also presents the determination of thermal expansion coefficient of Ag NSs during the growth. Ex-situ growths were carried out separately and after several days, XRD and electron microscopy measurements were done (at room temperature) to determine the lattice constant of embedded Ag structures. The lattice constant of Ag nanostructures obtained from ex-situ growth specimens were used to compare with the *real time, in-situ* - high temperature XRD measurements. As the temperature is raised from room temperature to 850 °C while performing in-situ growth, the evolutions of various diffraction peaks, reflecting from growth facets of Ag NSs were monitored. With the increase of temperature, the FWHM of Ag(200) were decreasing and the position of the peaks were getting shifted towards lower θ . Shift of Bragg angles in lower value represents the increment in the effective lattice constant values. This also means the variation in thermal expansion coefficients (TECs) corresponding to Ag nanostructures. We show that the TECs go inversely with the growth temperature. Crystallite size doesn't contribute to the sizable change in the lattice parameter as well as TEC. The TEC values were determined and found to vary from $\approx 1.9 \times 10^{-5}$ /°C to 1.82×10^{-5} /°C with the increase of annealing temperature from 750 °C to 850 °C for our case. The activation energy (E_0) for the growth of silver NSs estimated to be 0.171 ± 0.004 eV for this particular case [32].

In chapter 4, growth of silver (Ag) endotaxial structures in silicon using the aspects of both ion implantation and irradiation are covered. In one case, endotaxial nanostructures of Ag at the Si interface are formed with 30 keV Ag ions on $\text{GeO}_x/\text{SiO}_x/\text{Si}$ system. In another case, 30 keV Ag ions are used to create defects in GeO_x , SiO_x and in silicon substrate. Further deposition of a thin layer of Ag on irradiated $\text{GeO}_x/\text{SiO}_x/\text{Si}$ system yielded endotaxial Ag nanostructures relatively at lower temperature (700 °C) compared to the system without any irradiation effects by enhancing the Ag diffusion to form endotaxial nanostructures. However, high energy (1.8 MeV) Ag ions do not have any impact for endotaxial Ag NSs formation at less than 800 °C. We have shown that it is essential to have crystalline silicon substrate to form Ag endotaxial nanostructures [33].

The detailed growth of MoO_3 and Ag- MoO_3 heterostructures (HSs) with theoretical modeling and their applications in electron field emission (FE) devices are presented in chapter 5. Here, we have successfully grown α - MoO_3 structures and energetically suitable site specific Ag nanoparticle (NP) decorated α - MoO_3 structures in *single step* process on varied substrates, having almost similar morphologies and oxygen vacancies. XRD and TEM data revealed the orthorhombic phase of MoO_3 (α - MoO_3) with $[001] > [100] \gg [010]$ growth rate order, oriented mostly along the $[0\ 2k\ 0]$ direction. Interestingly, Ag NPs are not present on all the surface of the MoO_3 structures; Ag NPs decoration density is more on the $\text{MoO}_3(001)$ surface than on the $\text{MoO}_3(100)$ surface; interestingly, the presence of Ag NPs on the $\text{MoO}_3(010)$ surface is not observed at all. We have demonstrated the probable growth mechanism for site specific Ag decoration on MoO_3 surfaces by calculating the surface energies of Ag(111)/ $\text{MoO}_3(100)$, Ag(111)/ $\text{MoO}_3(010)$ and Ag(111)/ $\text{MoO}_3(001)$ structures employing density functional theory (DFT). From the DFT studies, the binding energy is found to be higher for (100) and (001) surfaces (≈ -0.98 eV), compared to the (010) surface (≈ -0.15 eV) and thus it is likely that Ag NP formation is not favorable on the $\text{MoO}_3(010)$ surface. To the best of our knowledge, there are no reports where $\text{MoO}_3(010)$ has been experimentally found to be a weakly interacting and stable surface compared to its other surfaces. Ag- MoO_3 sample has showed enhanced field emission properties with an approximately 2.1 times lower turn-on voltage of $1.67\text{ V }\mu\text{m}^{-1}$ and one order higher field enhancement factor (β) of 8.6×10^4 compared to the MoO_3 sample without Ag incorporation. The reason behind this better FE performance has been assigned to the ≈ 0.47 eV reduction in work function (Φ) of the Ag- MoO_3 sample ($\approx 5.70 \pm 0.05$ eV) compared to the MoO_3 sample ($\approx 6.17 \pm 0.05$ eV), as experimentally probed by the KPFM technique. The reduction in the Φ value of the Ag- MoO_3 sample can be understood by the electrons transfer induced lifting of

the Fermi energy of MoO₃ towards vacuum, which we discussed in details. The presence of oxygen vacancies together with Ag NPs lead to the highest β and lowest turn-on field among the reported values under the MoO₃ emitter category [34].

In chapter 6, works are involved on the different routes for the formation of site specific Ag NP decorated MoO₃ structures and also for the role of ambience during the growth of Ag-MoO₃ heterostructures (HSs). 4 nm thick silver film has been deposited on as-grown MoO₃ structures and then annealed the system under different ambient conditions viz air, argon (Ar), low vacuum (LV) and high vacuum (HV) and their resultant outcomes have been discussed in this chapter. Site specific growth was found only in Ar ambience for both the cases, implying that vapor pressure and also oxygen partial pressure are very crucial for this growth. These Ag-MoO₃ HSs have been used as free standing SERS substrates to detect sub-micro molar Crystal Violet (1 μ M CV solution) molecule with an analytical enhancement factor (AEF) of $\approx 10^4$ [35].

Growth of MoO₂ structures from previously grown MoO₃ structures/*n-type* Si via hydrogenation process at 450 °C and its application towards ultra-violet (UV) photodetector are presented in chapter 7. TEM, XRD, XPS and Raman confirm the monoclinic phase of MoO₂. We haven't observed any peak related to α -MoO₃ or any sub-oxidized phase of molybdenum oxide and thus parent structure (i.e., α -MoO₃) has been converted into MoO₂ phase perfectly. To explore the optoelectronic properties of *p-type* MoO₂ NSs, we have fabricated *p-type* MoO₂/*n-type* Si heterojunction (as-grown) photodetector device with Au as top and Al as bottom contacts. The device exhibits peak photoresponsivity of 0.155 A/W with maximum detectivity $1.28 \times 10^{11} \text{ cm-Hz}^{1/2}\text{-W}^{-1}$ and 44% external quantum efficiency (EQE) around $\approx 436 \text{ nm}$, following its highest photoresponse ($I_{\text{ph}}/I_{\text{d}} \approx 6.4 \times 10^2$) and fast response speed (raising time $\sim 29 \text{ ms}$ and decay time $\sim 38 \text{ ms}$) at -1.5 V . Importantly, this device also shows good self powered high speed (raising time $\sim 47 \text{ ms}$ and decay time $\sim 70 \text{ ms}$) photodetection performance with peak responsivity and detectivity of $\approx 45 \text{ mA/W}$ and $\approx 4 \times 10^{10} \text{ cm-Hz}^{1/2}\text{-W}^{-1}$, respectively. This broad-band UV-visible light detection feature can be attributed to the coordinated effects of MoO₂ band-edge absorption, interfacial defects and self absorption in Si. The photodetection behavior of the fabricated device has been understood by proposed energy band diagram with the help of experimentally derived work function of as-grown MoO₂ nanostructured film [36].

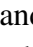
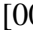


Summary and conclusions including future plans of entire thesis work are presented in chapter 8.

References

- [1] C N R Rao, P J Thomas and G U Kulkarni, *Nanocrystals: Synthesis, Properties and Applications* (Springer, 2007, ISBN: 978-3-540-68751-1).
- [2] P Alvisato, *Science* **1996**, 271, 933.
- [3] Z G Yan and C H Yan, *J. Mater. Chem.* **2008**, 18, 5046.
- [4] X S Fang, Y Bando, U K Gautam, C H Ye and D Golberg, *J. Mater. Chem.* **2008**, 18, 509.
- [5] A Ghosh A, P Guha, A K Samantara, B K Jena, R Bar, S K Ray and P V Satyam, *ACS Appl. Mater. Interfaces* **2015**, 7, 9486.
- [6] A Ghosh, P Guha, S Mukherjee, R Bar, S K Ray and P V Satyam, *Appl. Phys. Lett.* **2016**, 109, 123105.
- [7] A Ghosh, P Guha, R Thapa, S Selvaraj, M Kumar, B Rakshit, T Dash, R Bar, S K Ray and P V Satyam, *Nanotechnology* **2016**, 27, 125701.
- [8] W Dong, H Huang, Y Zhu, X Li, X Wang, C Li, B Chen, G Wang and Z Shi, *Nanotechnology* **2012**, 23 425602.
- [9] T Zheleva, K. Jagannadham and J Narayan, *J. Appl. Phys.* **1994**, 75, 860.
- [10] Y C Yeh, B Creran and V M Rotello, *Nanoscale* **2012**, 4, 1871.
- [11] C J Murphy, T K Sau, A M Gole, C J Orendorff, J Gao, L Gou, S E Hunyadi and T Li, *J. Phys. Chem. B* **2005**, 109, 13857.
- [12] N V Long, N D Chien, T Hayakawa, H Hirata, G Lakshminarayana and M Nogami, *Nanotechnology* **2010**, 21, 035605.
- [13] Y Chen, D L Peng, D Lin and X Luo, *Nanotechnology* **2007**, 18, 505703.
- [14] A H Alshehri, M Jakubowska, A Młóżniak, M Horaczek, D Rudka, C Free and J D Carey, *ACS Appl. Mater. Interfaces* **2012**, 4, 7007.
- [15] D Chen, X Qiao, X Qiu and J Chen, *J. Mater. Sci.* **2009**, 44, 1076.
- [16] T Bell, *Science* **2003**, 299, 1688.
- [17] S O Obare, R E Hollowell and C J Murphy, *Langmuir* **2002**, 18, 10407.
- [18] K G Stamplecoskie, J C Scaiano, V S Tiwari and H. Anis, *J. Phys. Chem. C* **2011**, 115, 1403.
- [19] B Sharma, R R Frontiera, A I Henry, E Ringe and R P V Duyne, *Mater. Today* **2012**, 15, 16.

- [20] R R Juluri, A Rath, A Ghosh, A Bhukta, R Sathyavathi, D Narayana Rao, K Muller, M Schowalter, K Frank, T Grieb, F Krause, A Rosenauer and P V Satyam, *Sci. Rep.* **2014**, *4*, 4633.
- [21] R R Juluri, A Ghosh, A Bhukta, R Sathyavathi and P V Satyam, *Thin Solid Films* **2015**, *586*, 88.
- [22] B Hu, L Mai, W Chen and F Yang, *ACS Nano* **2009**, *3*, 478.
- [23] D O Scanlon, G W Watson, D J Payne, G R Atkinson, R G Egdell and D S L Law, *J. Phys. Chem. C* **2010**, *114*, 4636.
- [24] T Ressler, R E Jentoft, J Wienold, M M Gunter and O Timpe, *J. Phys. Chem. B* **2000**, *104*, 6360.
- [25] L Mai, F Yang, Y Zhao, X Xu, L Xu, B Hu, Y Luo and H Liu, *Mater. Today* **2011**, *14*, 346.
- [26] S Balendhran, J Deng, J Z Ou, S Walia, J Scott, J Tang, K L Wang, M R Field, S Russo, S Zhuikov, M S Strano, N Medhekar, S Sriram, M Bhaskaran and K Kalantar-zadeh, *Adv. Mater.* **2013**, *25*, 109.
- [27] R Linag, H Cao and Q Qian, *Chem. Commun.* **2011**, *47*, 10305
- [28] D Xiang, C Han, J Zhang and W Chen, *Sci. Rep.* **2014**, *4*, 4891.
- [29] X Hu, W Zhang, X Liu, Y Mei and Y Huang, *Chem. Soc. Rev.* **2015**, *44*, 2376.
- [30] Y Wang, X Zhang, Z Luo, X Huang, C Tan, H Li, B Zheng, B Li, Y Huang, J Yang, Y Zong, Y Ying and H Zhang, *Nanoscale* **2014**, *6*, 12340
- [31] Y Xu, X Cao and Y Zhang, *Can. J. Chem.* **2014**, *92*, 16.
- [32] P Guha, R R Juluri, A Bhukta, A Ghosh, S Maiti, A Bhattacharyya, V Srihari and P V Satyam, *CrystEngComm* **2017**, *19*, 6811.
- [33] P Guha, R R Juluri and P V Satyam, *Nucl. Instr. Meth. Phys. Res. B* **2017**, *409*, 209.
- [34] P Guha, A Ghosh, R Thapa, E M Kumar, S Kirishwaran, R Singh and P V Satyam, *Nanotechnology* **2017**, *28*, 415602.
- [35] P Guha, A Ghosh and P V Satyam, **2018** (under preparation).
- [36] P Guha, A Ghosh, A Sarkar, S Mondal, S K Ray, D K Goswami and P V Satyam, *Nanotechnology* **2018** (under review).

List of Figures

1.1	Illustration of orthorhombic crystal structure of MoO_3 ($\alpha\text{-MoO}_3$) viewed from (a) [100], (b) [010] and (c) [001] directions;  \rightarrow Mo atom and  \rightarrow O atom.	19
1.2	Illustration of monoclinic crystal structure of MoO_2 ($\beta\text{-MoO}_2$);  \rightarrow Mo atom and  \rightarrow O atom.	19
2.1	Schematic diagram of thermal evaporation process.	28
2.2	High vacuum coating unit (M/s Vacuum Techniques Pvt. Ltd), Institute of Physics, Bhubaneswar.	29
2.3	Schematic illustration of the single zone horizontal quartz tube furnace, that is used as chemical vapor deposition (CVD) setup for the growth related to this thesis.	30
2.4	Schematic representations on vapor solid (VS) growth mechanism for MoO_3 growth.	31
2.5	Schematic diagram of various ion-solid interaction processes.	32
2.6	A schematic diagram of (a) filament and illumination part, (b) diffraction pattern formation and image formation [20].	36
2.7	Parallel-beam operation in the TEM: the basic principle illustrated (left) and the practical situation in most TEMs (right) [20].	36
2.8	200 keV JEOL JEM-2010 TEM, Institute of Physics, Bhubaneswar.	37
2.9	A schematic diagram showing the geometry of diffraction pattern formation [20].	39
2.10	Schematic presentation of various signals generated when a high-energy beam of electrons interacts with a thin specimen.	40
2.11	Schematic diagram of a typical planar TEM specimen preparation procedure.	42
2.12	Schematic diagram of a typical cross-sectional TEM specimen preparation procedure.	42
2.13	FIB-SEM cross-beam system (M/S. Carl Zeiss, Neon 40), Institute of Physics, Bhubaneswar.	44
2.14	Schematic representation of various signals generated due to the electron-specimen interaction in SEM.	46
2.15	Schematic representation of X-ray diffraction occurring in a crystal with inter-planar spacing d .	49
2.16	(a) Experimental setup to perform XRD measurements (Indian beam line 18-B, Photon Factory, Japan). High temperature setup mounted on goniometer and	

loaded with sample: (b) without the graphite dome and (c) covered with graphite dome [27].	50
2.17 Schematic illustration of core energy level during photoelectron emission process.	52
2.18 Energy level diagram, showing three types of possible scatterings, i.e., Rayleigh, Stokes and Anti-Stokes scattering states involved in Raman signal.	54
2.19 (a) 1D Potential energy barrier for an electron near a metal surface, (b) schematic representation of electron field emission (EFE) process, showing the emission of electron from an emitter.	57
2.20 Model of LSPRs at the spherical nanoparticle surface.	60
3.1 (a) Schematic representation for in-situ annealing and cooling of 17 nm $\text{GeO}_x/\text{SiO}_x/\text{Si}(100)$ sample with two silver wires kept close to the sample. (b) Schematic diagram of the experimental procedure followed during annealing.	66
3.2 (a) Low magnification and (b) high resolution cross-sectional TEM images of 17 nm $\text{GeO}_x/\text{SiO}_x/\text{Si}(100)$.	67
3.3 (a) Temperature evolution of Ag(200) peak during heating; (b) plot of full width half maxima (FWHM) of Ag(200) peak versus temperature; (c) variation in crystallite size of Ag with temperature.	67
3.4 Time evolution of the Ag(200) peak at (a) 750 °C, (c) 800 °C and (e) 850 °C; corresponding crystallite size of Ag with respect to stabilization time at (b) 750 °C, (d) 800 °C and (f) 850 °C.	68
3.5 Area under Ag(200) peak with respect to stabilization time at (a) 750 °C, (c) 800 °C and (e) 850 °C; corresponding FWHM of Ag(200) peak with respect to stabilization time at (b) 750 °C, (d) 800 °C and (f) 850 °C.	69
3.6 (a) and (b) High magnification SEM image and cross-sectional TEM image of the sample after <i>in-situ</i> annealing, confirming the formation of endotaxial silver nanostructures.	70
3.7 (a) Ag(200) peak intensity of 2 nm Ag/ $\text{GeO}_x/\text{SiO}_x/\text{Si}(100)$ annealed at three different temperatures 750 °C, 800 °C, 850 °C (<i>ex-situ case</i>). (b) Corresponding crystallite size dependent $d_{(200)}$ of silver. (c) Plot of $d(200)$ versus T all together (<i>in-situ</i> and <i>ex-situ cases</i>).	72
3.8 Typical SEM images of endotaxial Ag nanostructures formed at (a) 750 °C and (c) 800 °C and corresponding size distribution of endotaxial Ag nanostructures formed at (a) 750 °C and (c) 800 °C.	73
3.9 (a) Plot of $\Delta d/d$ versus ΔT (<i>in-situ case</i>); (b) corresponding temperature dependent TEC. (c) Plot of $\ln(\text{FWHM})$ versus $1/T$ (<i>in-situ case</i>).	74
4.1 Cross-sectional TEM micrographs of 2 nm Ag/15 nm $\text{GeO}_x/\text{SiO}_x/\text{Si}(100)$ (no irradiation) annealed at (a) 600 °C, (b) 650 °C and (c) 700 °C.	79
4.2 Planar TEM and corresponding cross-sectional TEM micrographs of 2 nm Ag on 15 nm $\text{GeO}_x/\text{SiO}_x/\text{Si}(100)$ -Ir 1×10^{15} ions/cm ² annealed at (a) and (b) 600 °C, (c) and (d) 650 °C and (e) and (f) 700 °C. The results are similar as shown in Figure 4.1 (un-irradiated systems).	81
4.3 (a) Cross-sectional TEM image of 15 nm $\text{GeO}_x/\text{SiO}_x/\text{Si}(100)$ sample. (b) Cross-sectional TEM image of 15 nm $\text{GeO}_x/\text{SiO}_x/\text{Si}(100)$ - 5×10^{15} ions/cm ² (as-	

- implanted) sample; (c) high resolution TEM image from the yellow region in (b), showing the amorphous silicon due to ion implantation and (d) corresponding high resolution TEM image from red region in (b). **82**
- 4.4** (a) and (b) SEM and cross-sectional TEM images of 2 nm Ag on 15 nm $\text{GeO}_x/\text{SiO}_x/\text{Si}(100)$ - 5×10^{15} ions/cm² annealed at 500 °C; (c) and (d) high resolution TEM images taken from the yellow and red regions in (b), respectively. **83**
- 4.5** (a) and (b) SEM and cross-sectional images of 2 nm Ag on 15 nm $\text{GeO}_x/\text{SiO}_x/\text{Si}(100)$ - 5×10^{15} ions/cm² annealed at 600 °C; (c) and (d) corresponding high resolution cross-sectional TEM images of silver-silicon interface and GeO_x layer with silver nanoclusters, respectively. **84**
- 4.6** (a) and (b) SEM and cross-sectional images of 2 nm Ag on 15 nm $\text{GeO}_x/\text{SiO}_x/\text{Si}(100)$ - 5×10^{15} ions/cm² annealed at 700 °C; (c) and (d) corresponding high resolution cross-sectional TEM images of silver-silicon interface and GeO_x layer with silver nanoclusters, respectively. **85**
- 4.7** (a) and (b) SEM and cross-sectional TEM images of 2 nm Ag on 15 nm $\text{GeO}_x/\text{SiO}_x/\text{Si}(100)$ - 5×10^{15} ions/cm² annealed at 800 °C; (c) corresponding high magnification TEM image; (d) high resolution TEM image of the GeO_x layer along with silver nanoclusters, showing crystalline Ag nanoclusters and amorphous GeO_x . **86**
- 4.8** Cross-sectional TEM images of 50 nm $\text{GeO}_x/\text{SiO}_x/\text{Si}(100)$ - 5×10^{15} ions/cm² (as-implanted) sample. **87**
- 4.9** (a) Cross-sectional TEM image of 70 nm $\text{GeO}_x/\text{SiO}_x/\text{Si}(100)$ - 5×10^{15} ions/cm² (as-implanted) sample; (b) corresponding SAED pattern taken from yellow dotted marked region in (a); (c) corresponding high resolution TEM image from red dotted rectangular area in (a). **87**
- 4.10** Planar TEM images of 2 nm Ag on 70 nm $\text{GeO}_x/\text{SiO}_x/\text{Si}(100)$ - 5×10^{15} ions/cm² annealed at (a) 700 °C and (c) 750 °C; corresponding cross-sectional TEM images are presented in (b) and (d) respectively. **88**
- 4.11** (a) Cross-sectional TEM image of 15 nm $\text{GeO}_x/\text{SiO}_x/\text{Si}(100)$ - 2×10^{16} ions/cm² (as-implanted) sample. (b) and (c) SEM and cross-sectional TEM images of 15 nm $\text{GeO}_x/\text{SiO}_x/\text{Si}(100)$ - 2×10^{16} ions/cm² annealed at 800 °C. **88**
- 5.1** Schematic illustration of the single zone side entry horizontal quartz tube furnace for MoO_3 and Ag- MoO_3 growth. **95**
- 5.2** (a) Low magnification SEM micrograph of as-grown products grown on silicon substrate; inset shows corresponding high magnification SEM image. (b) XRD spectrum of the corresponding sample. (c) TEM micrograph of MoO_3 structure; inset shows selected area electron diffraction (SAED) pattern from dotted yellow region, taken along [010] zone axis, suggests single crystalline nature of as-synthesized product. (d) High resolution TEM (HRTEM) image obtained from marked region (red) of (c), representing preferential growth along [001], which is consistent with SAED pattern. **98**

- 5.3** (a) Low and (b) high magnification SEM micrographs of the as-grown structures grown on 4 nm Ag/SiO_x/Si substrate. (c) SEM image of a single structure. **99**
- 5.4** Size distributions of (a) Ag NPs on MoO₃ structures and (b) bulk Ag NPs on Si. **99**
- 5.5** (a) XRD spectrum obtained from as-synthesized Ag-MoO₃ heterostructures (HSs). (b) TEM micrograph of Ag-MoO₃ HS. (c) SAED pattern taken from the dotted marked (yellow) region in (b) along [010] zone axis, suggests single crystalline nature of as-synthesized product. (d) High resolution TEM (HRTEM) image of Ag-MoO₃ structure from the solid marked (red) region in (b), represents preferential growth of MoO₃ along [001], which is consistent with SAED pattern; inset shows the FFT pattern with the plane (111) of silver obtained from the red region in (d). **100**
- 5.6** (a) High magnification and (b) corresponding high resolution SEM micrographs of the as-grown sample grown on 1.5 nm Ag/SiO_x/Si substrate. **101**
- 5.7** The optimized heterostructures for (a) Ag(111)/MoO₃(001), (b) Ag(111)/MoO₃(100) and (c) Ag(111)/MoO₃(010). Blue and red brace represents the free and fixed layers in the heterostructures respectively. ●, ●, ● represent the silver, molybdenum and oxygen atoms respectively. The 3D charge density difference plot of (d) Ag(111)/MoO₃(001) and (e) Ag(111)/MoO₃(100). Blue (negative isosurface) and yellow (positive isosurface) show charge depletion and accumulation zones respectively. **102**
- 5.8** Temperature dependent growth study: substrate temperature (a) 500 °C and (b) 400 °C. **103**
- 5.9** Schematic presentations on the possible growth model for site specific silver nanoparticles decorated MoO₃ structure (focusing on very few Ag-MoO₃ heterostructure (HS)). **104**
- 5.10** (a) Mo 3d and (b) O 1s XPS spectra from MoO₃ sample; (c) Mo 3d, (d) O 1s and (e) Ag 3d XPS spectra from Ag-MoO₃ sample. **105**
- 5.11** Raman spectra of (a) as-grown MoO₃ sample and (b) as-grown Ag decorated MoO₃ heterostructures. **107**
- 5.12** (a) XRD and (b) Raman spectra of Ag-MoO₃ sample grown at 400 °C; (c) Ag 3d XPS spectrum of the corresponding sample. **108**
- 5.13** (a) Field electron emission current density as a function of applied field (J–E) for the as-grown MoO₃ sample (black) and Ag-MoO₃ heterostructures sample (red); (b) Corresponding Fowler–Nordheim (F–N) plots. Work function mapping images of the as-grown (c) MoO₃ and (d) Ag-MoO₃ heterostructures samples using Kelvin probe force microscopy (KPFM). Scale bars in the images correspond to 2 μm for both cases. **109**
- 5.14** (a) Schematic illustration of energy levels of silver and MoO₃ separately. (b) Schematic representation of energy levels when Ag NP is on the surface of MoO₃, showing the uniform Fermi energy level due to the transfer of electron from Ag NP to MoO₃. (The mentioned work function values $\Phi_{\text{MoO}_3} = 6.17$ eV and $\Phi_{\text{Ag-MoO}_3} = 5.70$ eV are obtained from our samples using KPFM technique). **111**

- 5.15** UV-Vis reflectance data from (a) MoO₃ and (b) Ag-MoO₃ samples; insets of (a) and (b) are the corresponding $(\alpha h\nu)^2$ vs. $h\nu$ plots. **112**
- 5.16** The optimized structures of (a) Ag(111)/MoO₃(100), (b) MoO₃(100) in presence of oxygen vacancy. The black sphere represents oxygen vacancy site in the structures. **113**
- 5.17** Electrostatic potential along the z-axis considering vacuum as the reference energy for (a) Ag(111)/MoO₃(100) (b) MoO₃(100) (c) O vacancy in Ag(111)/MoO₃(100) and (d) O vacancy in MoO₃(100). Energy of the Fermi and vacuum level is represented by E_f and E_v , respectively. Φ defines the work function of the defined surface. **113**
- 5.18** SEM micrographs of as-grown MoO₃ structures grown on (a) GaAs, (b) ITO and (c) Ge substrates and Ag-MoO₃ HSs on (d) GaAs, (e) ITO and (f) Ge substrates. **115**
- 6.1** (a) Low magnification and (b) high magnification SEM images of ≈ 4 nm Ag deposited on α -MoO₃ structures/Si, showing the MoO₃ structures fully covered with silver nanoparticles. **122**
- 6.2** ≈ 4 nm Ag/MoO₃ Ss/Si annealed at 450 °C for 20 min in different ambient conditions: (a) 45 sccm argon flow, (b) air, (c) low vacuum (LV; $\approx 10^{-3}$ mbar) and (d) high vacuum (HV; $\approx 10^{-6}$ mbar). **123**
- 6.3** (a) SERS spectrum of 5 μ M concentration CV on 4 nm Ag/MoO₃ structures/Si annealed at 450 °C under argon atmosphere with 514.5 nm excitation. UV-vis specular reflectance spectra obtained from (b) 4 nm Ag/MoO₃ structures/Si @ 450 °C (argon atmosphere) and (c) Ag nanoparticles/Si samples. **124**
- 6.4** (a) SERS spectrum of 5 μ M concentration of CV on as-grown Ag-MoO₃ HSs/Si (in a single step process) with 514.5 nm excitation. (b) SERS spectrum of lowest concentrated CV (1 μ M) on the Ag-MoO₃ HSs/Si sample with 514.5 nm. (c) Reproducible SERS spectra of CV for 5 μ M concentration dropcasted on the as-grown Ag-MoO₃ HSs/Si. **125**
- 7.1** Schematic illustration of the single zone horizontal quartz tube furnace that is used for hydrogenation process to grow MoO₂ from MoO₃. **131**
- 7.2** (a) Low and (b) high magnification SEM micrographs of as-grown MoO₂ nanostructures grown on Si substrate; inset of (a) shows high magnification SEM image of the parent α -MoO₃ structures on Si substrate; inset of 1(b) presents single MoO₂ structure. (c) XRD spectrum of the corresponding sample, showing β -MoO₂ phase. (d) Low magnification TEM micrograph of as-prepared MoO₂ structure. (e) SAED pattern and (f) high resolution TEM image from the corresponding structure. **133**
- 7.3** A schematic diagram of hydrogenation process to demonstrate the conversion of MoO₃ structures (SS) to MoO₂ nanostructures. **134**
- 7.4** (a) Mo 3d and (b) O 1s XPS spectra from as-grown MoO₂ sample. (c) Raman spectrum of as-grown MoO₂ sample. (d) UV-vis absorption spectrum from MoO₂ nanostructures in methanol; inset shows corresponding plot of $(\alpha h\nu)^2$ as a function of photon energy ($h\nu$). **136**

- 7.5** (a) Schematic illustration of p-type MoO₂/n-type Si heterojunction photodetector device structure under illumination. (b) I–V characteristics of the as-prepared device under dark condition; inset shows numerical fitting of forward bias I–V characteristics of the device under dark condition using diode equations. **138**
- 7.6** (a) I–V characteristics of as-fabricated device measured in the dark, under 325 nm UV-illumination (240 mW/cm²) and white light (100 mW/cm²). (b) I–V characteristics of controlled device (i.e., Au/n-type Si/Al) (c) Time responses of the device at two different applied biases under white light. (d-f) Figure of merits, i.e., spectral responsivity, detectivity and EQE spectra of the corresponding device respectively. **139**
- 7.7** (a) Work function mapping image of the as-grown MoO₂ sample using Kelvin probe force microscopy (KPFM) technique; scale bars in the image corresponds to 500 nm. (b) Valence band XPS spectra of the parent α -MoO₃ and as-grown β -MoO₂ on Si substrates acquired at the pass energy of 50 eV. (c) Energy band diagram of isolated MoO₂ nanostructured film and Si substrate. Where, Φ is work function, ψ is electron affinity, E_g is band gap, E_F is Fermi level, E_C is the bottom of conduction band and E_V is the top of valence band for corresponding materials. (d) Energy band diagram of p-type MoO₂/n-type Si heterojunction device at reverse bias condition under illumination. **141**

List of Tables

3.1. Real particle size (from SEM images), crystallite size (from Scherrer formula) and d(200) of silver structures at different temperatures for all the cases (<i>in-situ</i> and <i>ex-situ</i> cases).	72
4.1. Microscopy observations from the low energy irradiated samples.	89
5.1. Dimensions and areal densities of the as-grown samples.	98
5.2. XPS analyses of the as-grown samples in detail.	106
5.3. Work function analysis of pure and oxygen vacant structures MoO ₃ (001), MoO ₃ (100), MoO ₃ (010), Ag(111)/MoO ₃ (001), Ag(111)/MoO ₃ (100) and Ag(111)/MoO ₃ (010) along with the energy values of E _f , E _v and Φ.	114
7.1. Comparison of molybdenum oxide and related oxide materials based various photodetectors	143

Chapter 1

Introduction

In recent times, nanoscience and nanotechnology are the most extensively exploited terms in modern science, growing very rapidly and impacting strongly on multidisciplinary fields due to its diversified field of applications. Nanoscience is the fundamental study to understand the physical/chemical phenomena at atomic or molecular scale of a material and nanotechnology is the design, characterization and applications of that material at the nanometric scale. Material properties at nanoscale are different from those at its bulk form as nanomaterial has large surface area over volume with respect to that at its larger scale [1–7]. Nanometric scale is universally defined as 1-100 nm (i.e., characteristic length < 100 nm at least in one direction). It is also expected that the quantum effects begin to dominate on the properties of nano sized material, which changes the electronic, optical, magnetic and chemical properties of the material at nano level [1–7]. Nanoparticles constitute a major class of nanomaterials. The diameters of nanoparticles can vary anywhere between one and a few hundreds of nanometers. For any nano sized material, its shape, size, surface composition, surrounding dielectric environment, inter particle distance and interactions are the major ingredient for tuning the physical/chemical properties [1–12]. Metal nanoparticles are a widely studied system in the literature. Noble metal (Au, Ag, Pt) nanoparticles (NPs) are of great scientific significance in diverse technological applications, such as, optical, electrical and biological applications due to their plasmonic properties and large surface to volume ratio [13–16]. The electronic absorption spectra of metal nanoparticles are dominated by the surface plasmon band which arises due to the collective coherent excitation of the free electrons within the conduction band. Among metal NPs, silver (Ag) shows highest electrical conductivity ($\sigma_{\text{Ag}} = 6.30 \times 10^7$ S/m at ≈ 20 °C) and is the best applicant for electrical

characterization [17, 18]; Ag is also the leading candidate for detecting organic dye-molecules, biomolecules via surface enhanced Raman spectroscopy (SERS) technique [19, 20]. Embedded Ag nanostructures are known to be efficient for detecting the dye-molecules via SERS technique [21, 22].

Inorganic semiconductors represent the foundations for all conventional, commercialized device applications, due to long-term stability under mechanical, electrical, and environmental stress, their largely tunable stable physical, chemical and mechanical properties along with easy large scale synthesis viability [5, 7, 23]. One-dimensional (1D) inorganic semiconductor nanostructures (NSs) having different morphologies have great importance in basic science as well as in technological development for their potential applications [1–12, 24, 25]. In recent days, molybdenum oxide material has attracted in modern nanoscience and nanotechnology for its versatile properties that have been employed in diversified applications [26, 27]. Moreover, material properties can be enhanced/improved by various meanings such as metal doping, creating oxygen vacancies, conjugating metal in a single step process or post metal coupling. When a metal nanoparticle (NP) is on semiconductor surface, electrons can be easily transferred from the metal NP to the semiconductor surface, resulting in a uniform Fermi energy level in the metal-semiconductor heterostructure (HS) system. The transferred electrons are subsequently assembled at the interface of metal and semiconductor. Then, the work function of the HS will be reduced by lifting the Fermi energy level of semiconductor towards vacuum [28–30]. While conjugating metal nanoparticles with semiconducting materials, it may so happen that the metal nanoparticles above semiconducting nanostructures are following the symmetry of that material during growth [31, 32].

When a material/overlayer grows on a crystalline substrate, where the overlayer is in registry with the substrate, then the growth is known as epitaxial growth. Epitaxy can be two types: homo-epitaxy and hetero-epitaxy. In homo-epitaxy, depositing film and substrate will be same material; in contrast, hetero-epitaxy, the material of depositing film and substrate will be different. The surface and interface energies and strain (in plane and out of plane) in the system determine the thermodynamically favored growth modes. Usually, in-situ reflection high energy electron diffraction and scanning tunneling microscopy measurements carried out during epitaxial growth carried under ultra-high vacuum conditions in a molecular beam epitaxy systems. Three types of growth modes are possible: Frank-van der Merwe (FM) or layer by layer, Stranski Krastanov or layer plus island and Volmer-Weber or island growth

[33, 34]. These different kinds of growth can be occurred depending on the surface free energies of the overlayer, the substrate and their lattice misfit.

On the other hand, when material/precipitate grows into a bulk matrix, where the precipitate will be coherently surrounded by the matrix, the process is termed as endotaxy [ref]. In general, epitaxial or endotaxial structures can be synthesized by using molecular beam epitaxy (MBE) [35] or atomic layer deposition (ALD) [36] techniques under ultra high vacuum (UHV) conditions ($\approx 10^{-10}$ mbar). Recently, growth of endotaxial silver nanostructures (NSs) ambient conditions has been reported under atmospheric condition [21, 22, 37]. To understand the kinetics of growth, real time in-situ observations of these silver endotaxial structures has been studied using a simple hot stage for both the generation of Ag vapors and providing temperature for silicon substrates during high temperature X-ray diffraction experiments. These kind of embedded or endotaxial silver nanostructures maybe used in the applications in the areas of plasmonic for enhancing light absorption, dye-molecules detection via SERS technique and other optoelectronic applications. Nanoparticle size/shape plays a crucial role on their properties studies of the particle size and shape evolution could be useful in providing an insight into the manipulation and control of their properties. Therefore, apart from the direct evidence of endotaxial Ag nanostructure growth, determination of the thermal expansion coefficient of Ag nanostructures in a matrix and its relation with crystallite size has also been presented. This thesis work deals with the incorporation of metal silver nanostructures on the surfaces and at the interfaces of oxide materials either on oxide layer molybdenum oxide (MoO_3) or in the $\text{GeO}_x/\text{SiO}_x/\text{Si}$ system.

Molybdenum oxides, wide band gap (2.6-3.2 eV) semiconductors are found to be one the most fascinating transition metal oxide (TMO), as for their unique structural, electrical, optical, mechanical properties and multi-directional applications. Depending on oxygen concentrations and oxidation states (+6, +5, +4, +3, +2) of Mo, molybdenum oxide shows several phase structures like MoO_3 , Mo_9O_{26} , Mo_8O_{23} , Mo_5O_{14} , Mo_4O_{11} , MoO_2 etc and exhibits different electrical and optical properties. Normally, molybdenum trioxide (MoO_3) appears in three different forms: thermodynamically most stable orthorhombic MoO_3 (α - MoO_3), meta-stable monoclinic MoO_3 (β - MoO_3), and meta-stable hexagonal MoO_3 (h- MoO_3). However, h- MoO_3 shows an irreversible phase transition to transform α - MoO_3 at 436 °C. α - MoO_3 , having a unique two-dimensional layered structure, falls under the Pbnm space group with unit cell parameters $a = 3.96 \text{ \AA}$, $b = 13.85 \text{ \AA}$ and $c = 3.71 \text{ \AA}$ (JCPDS: 35-0906). Crystal structures of α - MoO_3 projected from [100], [010] and [001] direction are shown in Figure 1.1. α - MoO_3 is composed of bi-layers of distorted MoO_6 octahedra along [010],

Orthorhombic crystal structure : $a = 3.96 \text{ \AA}$; $b = 13.85 \text{ \AA}$; $c = 3.71 \text{ \AA}$

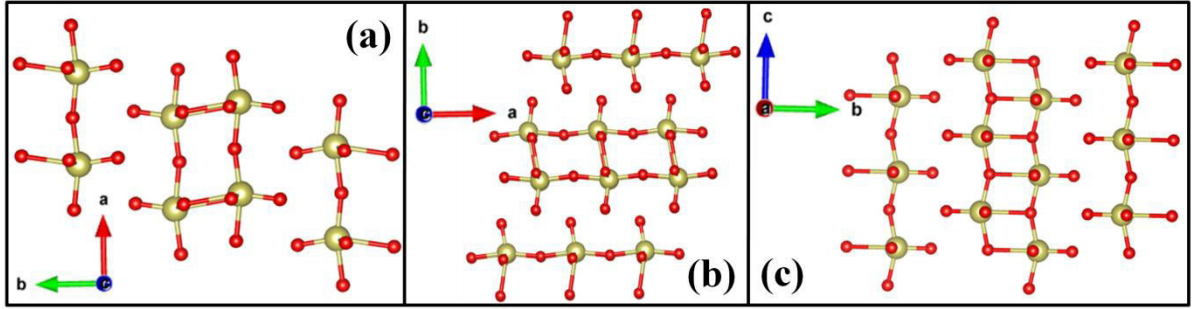


Figure 1.1: Illustration of orthorhombic crystal structure of MoO_3 ($\alpha\text{-MoO}_3$) viewed from (a) $[100]$, (b) $[010]$ and (c) $[001]$ directions; $\bullet \rightarrow \text{Mo atom}$ and $\bullet \rightarrow \text{O atom}$.

connected to the weak van der Waals forces. Within the double layers, MoO_6 are bounded by covalent and ionic bonds. In XZ plane, the MoO_6 octahedra forms corner sharing along $[100]$ and edge-sharing zig-zag along $[001]$. Oxygen atoms in MoO_3 crystal are categorized into three; (1) terminal oxygen atom bonded to only one Mo atom ($\approx 1.67 \text{ \AA}$), (2) symmetric bridging oxygen bonded to two Mo atoms ($\approx 1.95 \text{ \AA}$, equidistant) and weakly bonded to another Mo atom ($\approx 2.33 \text{ \AA}$), (3) asymmetric bridging oxygen atoms bonded to two Mo atoms ($\approx 1.74 \text{ \AA}$ and $\approx 2.25 \text{ \AA}$). Among the three principle surfaces (100), (010) and (001) of $\alpha\text{-MoO}_3$, the most stable surface is $\text{MoO}_3(010)$. The crystal structure of $\beta\text{-MoO}_3$ is similar to ReO_3 . MoO_6 octahedra share corners in three dimensions, forming a monoclinic MoO_3 . However, $\beta\text{-MoO}_3$ can be converted to $\alpha\text{-MoO}_3$ via thermal treatment above 350°C . The h-MoO_3 crystal is constructed utilizing similar zigzag chains of MoO_6 octahedra, which are also found in $\alpha\text{-MoO}_3$. Monoclinic MoO_2 ($\beta\text{-MoO}_2$) shows a deformed rutile structure with tetragonal orientation and falls under $\text{P2}_1/\text{c}$ space group having unit cell parameters $a = 5.620 \text{ \AA}$, $b = 4.860 \text{ \AA}$, $c = 5.630 \text{ \AA}$ and $\beta = 120.94^\circ$ (JCPDS card, #78-1070). MoO_6 octahedra

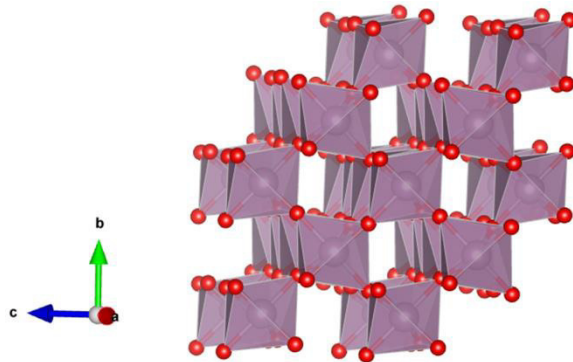


Figure 1.2: Illustration of monoclinic crystal structure of MoO_2 ($\beta\text{-MoO}_2$); $\bullet \rightarrow \text{Mo atom}$ and $\bullet \rightarrow \text{O atom}$.

chains share opposite edges along the crystallographic c-axis. Every Mo atom is coordinated by six oxygen atoms, whereas every oxygen atom is surrounded by three Mo atoms situated at the corners of an equilateral triangle. Along the rutile c axis two distinct metal to metal bond length of 2.51 Å and 3.02 Å arises due to the alternation of Mo-Mo distance (Figure 1.2) [26, 38–41].

MoO₃ nanostructures (NSs) with different morphologies such as nanowires, nanotubes, nanorods, nanobelts, nanoflakes, nanoribbons, whiskers, fibers, nanoplatelets, hollow nanospheres, nanoparticles, nanosheets, nanostructures have been prepared via various physical and chemical methods. Until now, diversified routes or techniques for synthesizing MoO₃ NSs successfully have been addressed such as thermal evaporation, chemical vapor deposition, pulsed laser deposition, hydrothermal, flame synthesis, sputtering, electrochemical technique, infrared irradiation, sol-gel, microwave method, sonochemical approach etc. Molybdenum oxide has been extensively probed in various advanced applications and showed promising performances in photochromic devices, electrochromic devices, gas sensing, photocatalysis, resistive switching, lithium ion batteries, catalysis, field emission, photovoltaic, transistors, inorganic light emitting diode, capacitors, panel displays, and smart windows [39–66].

Even though MoO₃ is being studied as potential material in several applications, main drawback with this material is its insulating nature. Pure MoO₃ shows poor electrical and ionic conductivity [67, 68]. So, to improve its properties, several ways have been attempted e.g., creating oxygen vacancies into MoO₃ lattice, conjugating with metal nanoparticles (NPs) with MoO₃ structures, metal doping etc [52, 69–72]. But a very few reports are available on metal-MoO₃ heterostructures. Here a novel method is reported on the incorporation of silver nanoparticles on molybdenum oxide surfaces in a *single step growth process*. It is also reported that electrical conductivity of MoO_x ($2 \leq x \leq 3$) increases with decreasing value of x; MoO₂ shows metallic behavior, high melting point, high chemical and thermal stabilities [27, 73]. D Xiang et. al., showed no photoresponse of MoO₃ for the visible spectrum. But after reduction in stoichiometric in MoO₃, the photodetector possessed wide visible spectrum response [67]. In this context, we believe that MoO₂ nanostructures can offer superior photoresponse characteristics; so far no report has been made related to this material.

This thesis is presented in following manner. In chapter 2, all the experimental techniques/methods and their basic working principles (that are employed for the preparation of samples and their characterizations and multifaceted applications) have been outlined in brief. Inclusion of silver nanoparticles on the surfaces and at the interfaces of two oxide

materials are the prime objects of this present thesis work: silver nanostructures either can be materialized *on (epi)* the oxide layer or *in (endo)* the oxide/substrate. 3rd and 4th chapters deal with the silver nanoparticles coherently embedded inside oxide layer GeO_x on a silicon substrate. In third chapter, *real time in-situ* growth of coherently embedded silver nanostructures in modified silicon Si matrix (i.e., $\text{GeO}_x/\text{SiO}_x/\text{Si}$) during synchrotron based high-temperature XRD measurements under ambient condition is addressed. Chapter 4 details the effect of energetic (both low and high energies) silver ion irradiations on $\text{GeO}_x/\text{SiO}_x/\text{Si}$ system to understand the growth of coherently embedded silver nanostructures. The silver nanoparticles on MoO_x structures have been dealt in chapter 5, 6 and 7. *Single step* growth of site specific silver nanoparticles decorated molybdenum oxide structures along with ambient aspects on the growth and their applications towards electron field emission, detection of sub-micro molar dye-molecules are reviewed in chapters 5 and 6. Chapter 7 covers a simple and reproducible growth of monoclinic *p-type* MoO_2 nanostructures (NSs) from previously grown $\alpha\text{-MoO}_3$ structures/*n-type* silicon substrate via hydrogenation process at 450 °C and explores their potential in UV-visible photodetection application using the as-grown *p-type* MoO_2 /*n-type* Si heterojunction itself. The summary of the works presented in the thesis including future scopes/plans are furnished in chapter 8 [39, 74–77].

References

- [1] C N R Rao, P J Thomas and G U Kulkarni, *Nanocrystals: Synthesis, Properties and Applications* (Springer, 2007, ISBN: 978-3-540-68751-1).
- [2] P Moriarty, *Rep. Prog. Phys.* **2001**, 64, 297.
- [3] P Alvisatos, *Science* **1996**, 271, 933.
- [4] C Burda, X Chen, R Narayanan and M A El-Sayed, *Chem. Rev.* **2005**, 105, 1025.
- [5] S Zhuiykov, *Nanostructured Semiconductor Oxides for the Next Generation of Electronics and Functional Devices: Properties and Applications* (Elsevier, 2013, ISBN: 978- 1-78242-220-4).
- [6] Y Xia, P Yang, Y Sun, Y Wu, B Mayers, B Gates, Y Yin, F Kim and H Yan, *Adv. Mater.* **2003**, 15, 353.
- [7] R K Joshi and J J Schneider, *Chem. Soc. Rev.* **2012**, 41, 5285.
- [8] J P Borel, *Surf. Sci.* **1981**, 106, 1.

- [9] Y D Glinka, S H Lin, L P Hwang, Y T Chen and N H Tolk, *Phys. Rev. B* **2001**, *64*, 085421.
- [10] S Chen, R S Ingram, M J Hostetler, J J Pietron, R W Murray, T G Schaa, J T Khoury, M M Alvarez and R L Whetten, *Science* **1998**, *280*, 2098.
- [11] N L Swanson and B D Billard, *Nanotechnology* **2003**, *14*, 353.
- [12] H Xu, E J Bjerneld, M Kall and L Borjesson, *Phys. Rev. Lett.* **1999**, *83*, 4357.
- [13] Y C Yeh, B Creran and V M Rotello, *Nanoscale* **2012**, *4*, 1871.
- [14] C J Murphy, T K Sau, A M Gole, C J Orendorff, J Gao, L Gou, S E Hunyadi and T Li, *J. Phys. Chem. B* **2005**, *109*, 13857.
- [15] N V Long, N D Chien, T Hayakawa, H Hirata, G Lakshminarayana and M Nogami, *Nanotechnology* **2010**, *21*, 035605.
- [16] D L Fedlheim and C A Foss, *Metal Nanoparticles: Synthesis, Characterization, and Applications* (CRC Press, 2001, ISBN: 978-0-58540-439-4).
- [17] A H Alshehri, M Jakubowska, A Młozniak, M Horaczek, D Rudka, C Free and J D Carey, *ACS Appl. Mater. Interfaces* **2012**, *4*, 7007.
- [18] D Chen, X Qiao, X Qiu and J Chen, *J. Mater. Sci.* **2009**, *44*, 1076.
- [19] K G Stampelcoskie, J C Scaiano, V S Tiwari and H Anis, *J. Phys. Chem. C* **2011**, *115*, 1403.
- [20] B Sharma, R R Frontiera, A I Henry, E Ringe and R P V Duyne, *Mater. Today* **2012**, *15*, 16.
- [21] R R Juluri, A Rath, A Ghosh, A Bhukta, R Sathyavathi, D Narayana Rao, K Muller, M Schowalter, K Frank, T Grieb, F Krause, A Rosenauer and P V Satyam, *Sci. Rep.* **2014**, *4*, 4633.
- [22] R R Juluri, A Ghosh, A Bhukta, R Sathyavathi and P V Satyam, *Thin Solid Films* **2015**, *586*, 88.
- [23] K J Yu, Z Yan, M Han and J A Rogers, *npj Flexible Electronics* **2017**, *4*, 1.
- [24] D K Ferry, *Semiconductors Bonds and bands* (IOP Publishing Ltd. 2013, ISBN: 978-0-750-31044-4).
- [25] M Balkanski and R F Wallis, *Semiconductor Physics and Applications* (Oxford University Press, 2000, 978-0-19851-740-5).
- [26] I A de Castro, R S Datta, J Z Ou, A Castellanos-Gomez, S Sriram, T Daeneke and K Kalantar-zadeh, *Adv. Mater.* **2017**, *29*, 1701619.
- [27] L Mai, F Yang, Y Zhao, X Xu, L Xu, B Hu, Y Luo and H Liu, *Mater. Today* **2011**, *14*, 346.

- [28] A Ghosh, P Guha, A K Samantara, B K Jena, R Bar, S K Ray and P V Satyam, *ACS Appl. Mater. Interfaces* **2015**, 7, 9486.
- [29] L Zhang, J C Yu, H Y Yip, Q Li, K W Kwong, A W Xu and P K Wong, *Langmuir* **2003**, 19, 10372.
- [30] A Ghosh, P Guha, S Mukherjee, R Bar, S K Ray and P V Satyam, *Appl. Phys. Lett.* **2016**, 109, 123105.
- [31] F R Fan, Y Ding, D Y Liu, Z Q Tian and Z L Wang, *J. Am. Chem. Soc.* **2009**, 131, 12036.
- [32] X Huang, Z Zeng, S Bao, M Wang, X Qi, Z Fan and H Zhang, *Nature Commun.* **2013**, 4, 1444.
- [33] I N Stranski and L Krastanow, *Ber. Akad. Wiss. Wien* **1938**, 146, 797.
- [34] I V Markov, *Crystal Growth for Beginners Fundamentals of Nucleation, Crystal Growth and Epitaxy* (World Scientific, 1995, ISBN: 981-238-245-3).
- [35] A Y Cho and J R Arthur, *Prog. in Solid State Chem.* **1975**, 10, 157.
- [36] M Leskel and M Ritala, *Thin Solid Films* **2002**, 409, 138.
- [37] R R Juluri, A Rath, A Ghosh and P V Satyam, *J. Phys. Chem. C* **2013**, 117, 13247.
- [38] T Ressler, R E Jentoft, J Wienold, M M Gunter and O Timpe, *J. Phys. Chem. B* **2000**, 104, 6360.
- [39] P Guha, A Ghosh, R Thapa, E M Kumar, S Kirishwaran, R Singh and P V Satyam, *Nanotechnology* **2017**, 28, 415602.
- [40] D Mariotti, H Lindstrom, A C Bose and K Ostrikov, *Nanotechnology* **2008**, 19, 495302.
- [41] L Zheng, Y Xu, D Jin and Y Xie, *Chem. Mater.* **2009**, 21, 5681.
- [42] M Chen, U V Waghmare, C M Frienda and E A Kaxiras, *J. Chem. Phys.* **1998**, 109, 6854.
- [43] A Michalak, K Hermann and M Witko, *Surf. Sci.* **1996**, 366, 323.
- [44] J N Yao, K Hashimoto and A Fujishima, *Nature* **1992**, 355, 624.
- [45] C Bechinger, S Ferrere, A Zaban, J Sprague and B A Gregg, *Nature* **1996**, 383, 608.
- [46] E Comini, L Yubao, Y Brando and G Sberveglieri, *Chem. Phys. Lett.* **2005**, 407, 368.
- [47] Y Chen, C Lu, L Xu, Y Ma, W Hou and J J Zhu, *CrystEngComm* **2010**, 12, 3740.
- [48] L Cheng, M Shao, X Wang and H Hu, *Chem. Eur. J.* **2009**, 15, 2310.
- [49] D Lee, D J Seong, I Jo, F Xiang, R Dong, S Oh and H Hwang, *Appl. Phys. Lett.* **2007**, 90, 122104.

- [50] L Q Mai, B Hu, W Chen, Y Y Qi, C S Lao, R S Yang, Y Dai and Z L Wang, *Adv. Mater.* **2007**, *19*, 3712.
- [51] J Zhou, S Z Deng, N S Xu, J Chen and J C She, *Appl. Phys. Lett.* **2003**, *83*, 2653.
- [52] B Yan, Z Zheng, J Zhang, H Gong, Z Shen, W Huang and T Yu, *J. Phys. Chem. C* **2009**, *113*, 20259.
- [53] Y B Li, Y Bando, D Golberg and K Kurashima, *Appl. Phys. Lett.* **2002**, *81*, 5048.
- [54] S Balendhran, J Deng, J Z Ou, S Walia, J Scott, J Tang, K L Wang, M R Field, S Russo, S Zhuiykov, M S Strano, N Medhekar, S Sriram, M Bhaskaran and K Kalantar-zadeh, *Adv. Mater.* **2013**, *25*, 109.
- [55] P S Wang, I W Wu, W H Tseng, M H Chen and C I Wu, *Appl. Phys. Lett.* **2011**, *98*, 173302.
- [56] R Linag, H Cao and Q Qian, *Chem. Commun.* **2011**, *47*, 10305.
- [57] S Hu and X Wang, *J. Am. Chem. Soc.* **2008**, *130*, 8126.
- [58] L Cai, P M Rao and X Zheng, *Nano Lett.* **2011**, *11*, 872.
- [59] S Wang, Y Zhang, X Ma, W Wang, X Li, Z Zhang and Y Qian, *Solid State Commun.* **2005**, *136*, 283.
- [60] C V Krishnan, J Chen, C Burger and B Chu, *J. Phys. Chem. B* **2006**, *110*, 20182.
- [61] K Kalantar-zadeh, J Tang, M Wang, K L Wang, A Shailos, K Galatsis, R Kojima, V Strong, A Lech, W Wlodarski and R B Kaner, *Nanoscale* **2010**, *3*, 429.
- [62] X W Lou and H C Zeng, *J. Am. Chem. Soc.* **2003**, *125*, 2697.
- [63] W Li, F Cheng, Z Tao and J Chen, *J. Phys. Chem. B* **2006**, *110*, 119.
- [64] I Navas, R Vinodkumar, K J Lethy, A P Detty, V Ganesan, V Sathe and V P M Pillai, *J. Phys. D: Appl. Phys.* **2009**, *42*, 175305.
- [65] D D Yao, J Z Ou, K Latham, S Zhuiykov, A P O'Mullane, K Kalantar-zadeh, *Cryst. Growth Des.* **2012**, *12*, 1865.
- [66] Y Li and Y Bando, *Chem. Phys. Lett.* **2002**, *364*, 484.
- [67] D Xiang, C Han, J Zhang and W Chen, *Sci. Rep.* **2014**, *4*, 4891.
- [68] X Hu, W Zhang, X Liu, Y Mei and Y Huang, *Chem. Soc. Rev.* **2015**, *44*, 2376.
- [69] W Dong, H Huang, Y Zhu, X Li, X Wang, C Li, B Chen, G Wang and Z Shi, *Nanotechnology* **2012**, *23*, 425602.
- [70] H Sinaim, A Phuruangrat, S Thongtem and T Thongtem, *Mater. Chem. Phys.* **2012**, *132*, 358.
- [71] Y Wang, X Zhang, Z Luo, X Huang, C Tan, H Li, B Zheng, B Li, Y Huang, J Yang, Y Zong, Y Ying and H Zhang, *Nanoscale* **2014**, *6*, 12340.

- [72] Xu Y, Cao X and Zhang Y 2014 *Can. J. Chem.* **92** 16.
- [73] B Hu, L Mai, W Chen and F Yang, *ACS Nano*. **2009**, *3*, 478.
- [74] P Guha, R R Juluri, A Bhukta, A Ghosh, S Maiti, S Bhattacharyya, V Srihari and P V Satyam, *CrystEngComm* **2017**, *19*, 6811.
- [75] P Guha, R R Juluri and P V Satyam, *Nucl. Instr. Meth. Phys. Res. B* **2017**, *409*, 209.
- [76] P Guha, A Ghosh and P V Satyam, **2017** (under preparation).
- [77] P Guha, A Ghosh, A Sarkar, S Mondal, S K Ray, D K Goswami and P V Satyam, **2017** (to be submitted).

Chapter 2

Experimental Techniques

2.1 Introduction

This chapter describes the experimental techniques with their basic operational principles utilized extensively for the growth, characterization and applications of the materials related to the thesis work. The chapter begins with a brief description on the growth techniques, such as, physical vapor deposition (PVD), chemical vapor deposition (CVD), ion implantation (both low energy and high energy). The endotaxial silver (Ag) nanostructures (NSs) have been grown by CVD technique and ion implantation technique, whereas silver-molybdenum oxide (Ag-MoO₃) heterostructures (HSs) have been grown by single step CVD technique. MoO₂ has been grown from MoO₃ structures via annealing under hydrogen atmosphere. The characterization techniques namely field emission gun based scanning electron microscope (FEG-SEM), transmission electron microscopy (TEM) capable with high resolution mode and selected area electron diffraction (SAED), X-ray diffraction (XRD) at room and high temperatures (real time mode), Raman spectroscopy, X-ray photoelectron spectroscopy (XPS), ultra-violet-visible (UV-Vis) reflectance/absorption spectroscopy and Kelvin probe force microscopy (KPFM) will be highlighted, which have been extensively used to characterize the as-prepared samples. The specimen systems synthesized/grown as a part of this thesis work, have showed potential applications in diversified fields such as UV-vis optoelectronic device, field emission (FE) and surface enhanced Raman spectroscopy (SERS), which will be discussed in this chapter.

2.2 Fabrication and growth of thin films and nano-structures

Modern technology requires thin films for different applications, e.g., optoelectronic devices, photonic devices, magnetic devices, solar cells etc. [1, 2]. A thin film deposition on a substrate/surface means a layer of material deposition by any technique onto a substrate or onto previously deposited layers, where there will be a control over the thickness of the deposited material (a few tens of nanometers to micron) [2]. Usually, this thin film can also be termed as nanoscale film. On the other hand, nanoscience and nanotechnology have gathered great deal of interest not only due to their fundamental importance in basic scientific research but also due to their potential technological applications [3, 4]. All materials at nanoscale exhibit unique physical, chemical and mechanical properties, which are significantly different from their bulk [5]. At current stage, there are various methods that are being pursued for growing nanostructures. In general, growth techniques can broadly be divided into two categories, depending on the physical (evaporative methods) or chemical process (gas and liquid-phase chemical processes with chemical reactions). Some of the other techniques which involve glow discharge and reactive sputtering can be regarded as physical-chemical methods. In this thesis, both physical viz. coating methods at high vacuum condition and chemical viz. CVD technique will be discussed briefly.

2.2.1 Physical vapor deposition (PVD) technique: thermal evaporation in high vacuum (HV) chamber

In a of physical vapor deposition (PVD) method, the common sources for producing the vapors are thermal evaporation, e-beam evaporation, plasma spray deposition, and sputtering [1]. In this thesis, only thermal evaporation technique has been used to grow thin films of different materials and hence will be discussed. Thermal evaporation means is the vaporization of a source material by providing heat to a certain temperature (close to melting point of that material) in vacuum, such that the vapor pressure becomes appreciable and source atoms/molecules come out from the surface [6]. Evaporation involves following basic steps, which is schematically represented in Figure 2.1: (i) evaporation of hot source material by heating, (ii) transportation of vapor from source to the substrate (target) and (iii) deposition of thin film on substrate by condensation of the vapor. Source material can be

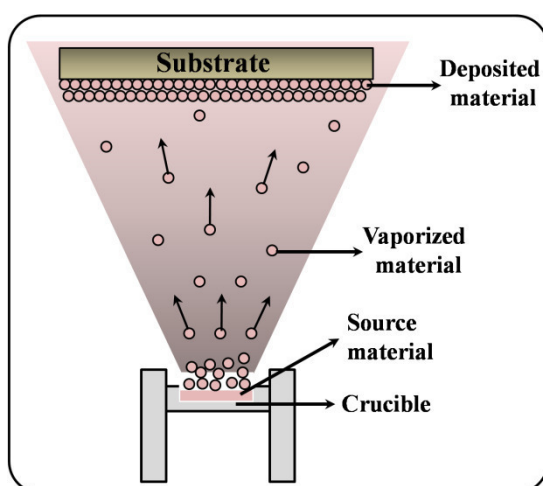


Figure 2.1: Schematic diagram of thermal evaporation process.

heated in different ways, for example, resistive heating. Normally, source material is kept on a tungsten/molybdenum boat (having high melting temperature such that boat will not react with source material), then resistively heated, so that the source material (being in thermal contact with the boat) melts and evaporates. Resistive evaporation is accomplished by passing a large current through a resistive wire/boat containing source material. For successful thin film growth, the mean free path of source atoms must be greater than the distance between the source and target object. Under high vacuum (HV) condition ($\approx 10^{-6}$ mbar), since the mean free path is very large, source vapors can easily travel towards the substrate without collision with residual gases inside the chamber [7]. Figure 2.2 shows PVD system (M/s Vacuum Techniques Pvt. Ltd) installed @ IOP, BBSR, that has been employed to grow all the thin film depositions that are described throughout thesis work. The coating unit consists of a cylindrical, stainless steel vacuum chamber, approximately ≈ 55 cm height and ≈ 40 cm in diameter, where three different materials can be co-deposited simultaneously. A heater is attached to the substrate plate, which can go up to 600°C from room temperature. Substrate temperature is measured by a thermocouple, placed close to substrate plate.

High vacuum is obtained by using a rotary oil pump, a dry pump and one turbo molecular pump (TMP). Pirani and penning gauges are used to monitor the vacuum condition. Thickness of deposited film is observed by thickness monitor having a quartz crystal microbalance by measuring variations in the resonant frequencies [8]. The resonance frequency of oscillations is dependent on the mass of the film deposited onto it. Quartz thickness monitor can measure thickness of about a single atomic layer with relatively high accuracy. A chiller is attached to this system to maintain thickness monitor at a lower temperature ($@ 20^\circ\text{C}$) during deposition process. Vacuum/pumping systems, power unit,

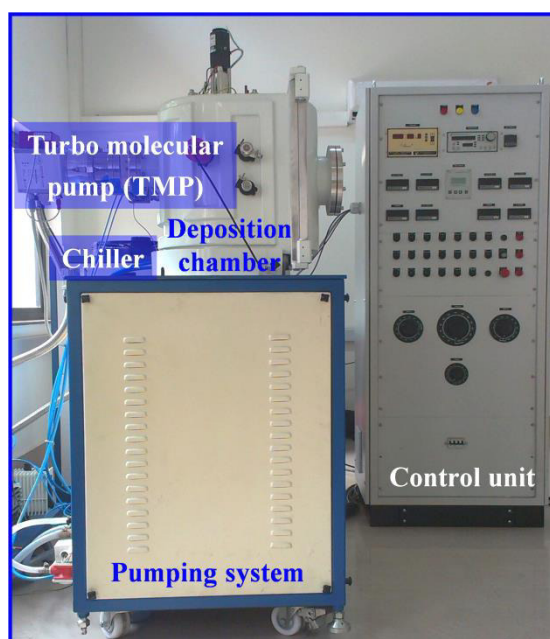


Figure 2.2: High vacuum coating unit (M/s Vacuum Techniques Pvt. Ltd), Institute of Physics, Bhubaneswar.

deposition rate etc. are controlled by a separate controller box (control unit). To obtain effective thickness values of deposited film, quartz thickness monitor is calibrated routinely with Rutherford backscattering spectrometry (RBS) analysis and cross-sectional TEM observations.

In this thesis work, amorphous germanium oxide (GeO_x) with 15 nm, 50 nm and 70 nm thick thin films (Ge as source material; as Ge gets easily oxidized) and 1 nm, 2 nm and 4 nm Ag thin films (Ag wire as a source material) have been deposited using molybdenum boat. For all the cases, source to substrate distance and source to thickness monitor distance were kept at 13.0 cm and 10.0 cm respectively with HV condition ($\approx 1.2 \times 10^{-6}$ mbar). The deposition rate was maintained at ≈ 1 Å/sec to get uniform high quality smooth thin films. Applied current and voltage values were 110 A and 1.0 V (for Ge) and 100 A and 0.9 V (for Ag) respectively [9–11].

2.2.2 Chemical vapor deposition (CVD) technique

Chemical vapor deposition (CVD) is an extensively utilized material synthesis technique, by which a thin solid film or nanostructures will be formed on a substrate by chemical reaction among vapor phase precursors [12]. This method is often used to grow a

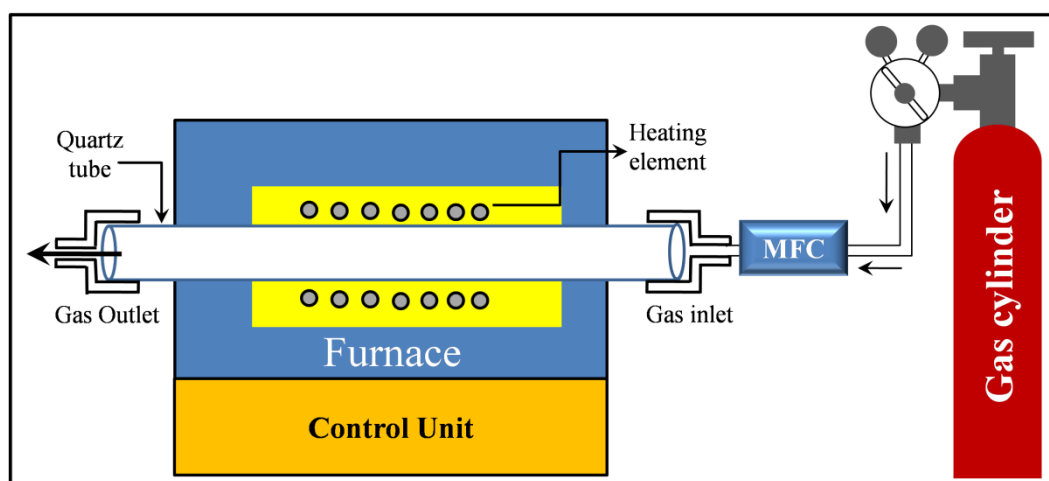


Figure 2.3: Schematic illustration of the single zone horizontal quartz tube furnace, that is used as chemical vapor deposition (CVD) setup for the growth related to this thesis.

very wide range of materials with different morphologies; moreover, this process is advantageous compared to other techniques to form compound materials [13]. The chemical reactions among precursors happen in gas phase and reach to the substrate. The reactions can be stimulated by heat (thermal CVD), higher frequency radiations like plasma (plasma enhanced CVD) or UV (photo assisted CVD). For the present thesis work, source materials will be heated to high temperatures in a horizontal tube furnace; the hot vapor will be transported by carrier gas and then subsequently deposited on substrate. Figure 2.3 shows a schematic diagram of the experimental apparatus used in the studies presented here. Silicon carbide rods are used as heating elements, which can raise the temperature of reaction chamber up to 1400 °C. The furnace consists of a ≈ 100 cm long horizontal quartz tube (inner diameter ≈ 4.5 cm, outer diameter ≈ 5.0 cm), where one side is connected to gas cylinder (inlet) controlled by a Sevenstar D07-19B mass flow controller (MFC) and the other side had a gas outlet. Normally, source powder or mixture is placed in a ceramic boat and positioned in the middle of the furnace, which is at the highest temperature. The substrates for collecting the vapor produced can be placed anywhere inside the tube depending on the experimental conditions and growth parameters. Both ends of the tube are covered by stainless steel flanges and sealed with rubber O-rings. This quartz tube furnace can also be evacuated in low vacuum order ($\approx 10^{-2}$ mbar). Flanges are water cooled during the growth so that either ends of the tube are maintained at relatively lower temperature to protect O-rings. In this thesis, we have grown MoO_3 structures and Ag-MoO_3 heterostructures (HSs) have been grown via vapor-solid (VS) mechanism using this CVD facility; so in the following section, we will mainly focus on VS mechanism.

2.2.2.1 Vapor-solid (VS) growth mechanism

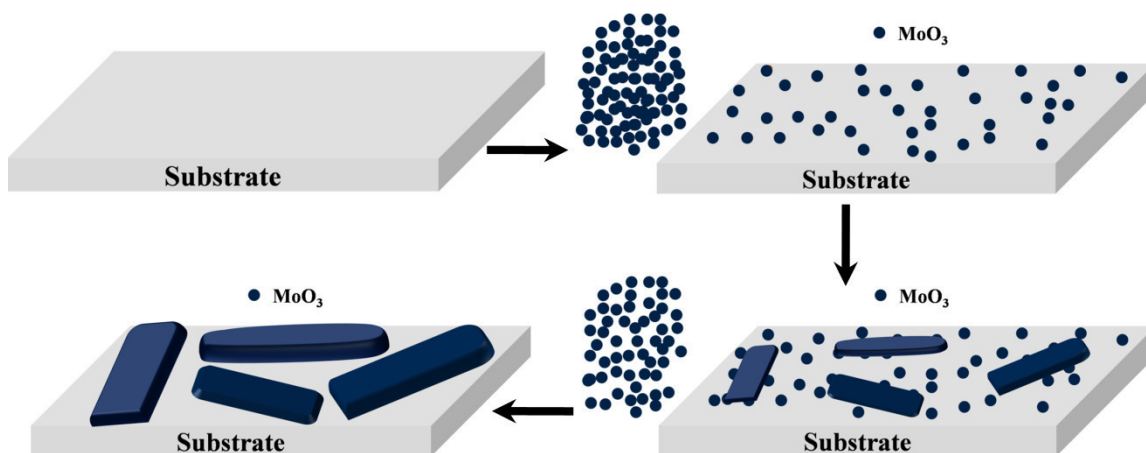


Figure 2.4: Schematic representations on vapor solid (VS) growth mechanism for MoO_3 growth.

The most popularly known vapor-liquid-solid (VLS) growth process is very common for catalyst-assisted nanostructures (out of plane in major cases) growth. In this present thesis work, no catalyst is used for growing MoO_3 structures. In general, terms, a nanostructure growth without the help of metal catalyst is known to be vapor-solid (VS) process [10]. Considering the MoO_3 structure growth, MoO_3 vapor is first produced from MoO_3 source powder by evaporation method and subsequently carried by carrier gas (as Argon) and condensed directly onto the substrate surface without an intermediate stage of a liquid catalytic droplet, initiation of MoO_3 structures (crystallization) and finally MoO_3 structures are formed (Figure 2.4) [10]. Different surfaces of a crystal show anisotropic properties and hence the atoms on the surfaces nucleate and form oriented structures, as a result of energy minimization process. At higher temperatures and longer dimensions, the overall size of MoO_3 nanostructures increases. In VS growth process, usually coverage is quite thin and nucleation occurs preferentially at substrate regions where there are imperfections (e.g. dislocations threading to the surface) [14]. Furthermore, surface defects, such as, impurities or etch pits on the substrate act as nucleation centers [15]. The dimensions of the nanostructures usually depend on the growth conditions and properties of the buffer or nucleation layer. Even if metal catalyst particles are employed in VS growth process, the catalyst particles only act as nucleation sites for the growth and they remain at the bottom during growth [16]; no supersaturation occurs during the growth, unlike in the VLS dominated growth.

2.2.3 Ion beams for synthesis and modification

Energetic ion beams have been used to modify materials either by incorporating various types of defects or by forming entirely new materials under non-equilibrium conditions. Usually, ion implantation refers to the implanted ions and their modification or synthesis and ion irradiation refers to the modifications or defects that occur due to impart of energy [17]. Modern semiconductor device fabrication industry has also embraced with ion implantation technique for its numerous technological advantages [18]. Ion implantation-induced nanoparticle formation inside host matrix, foreign material doping onto host matrix (to fabricate n-type or p-type material) etc. are enormously exploited in the past few years. Figure 2.5 depicts a schematic illustration of possible interactions of ions with the host matrix. The interaction between the energetic ions and the electrons of material is primarily columbic interaction during ion beam irradiation process. Irradiation may cause change in the chemical composition of target material, depending on implantation dose, which leads to the accumulation of foreign atoms within a solid and alter the host matrix composition/structure in the implanted zone. Spatial distribution of ions inside the matrix will usually be governed by the energy of impinging ion, mass and atomic numbers of the ions and host matrix. When an atom of host target gets displaced from its original position due to ion irradiation, then it may contribute to the collision cascade within the matrix. This can create vacancies, interstitial atoms and other type of lattice disorder in the area around the ion track. Target material can also be sputtered out if

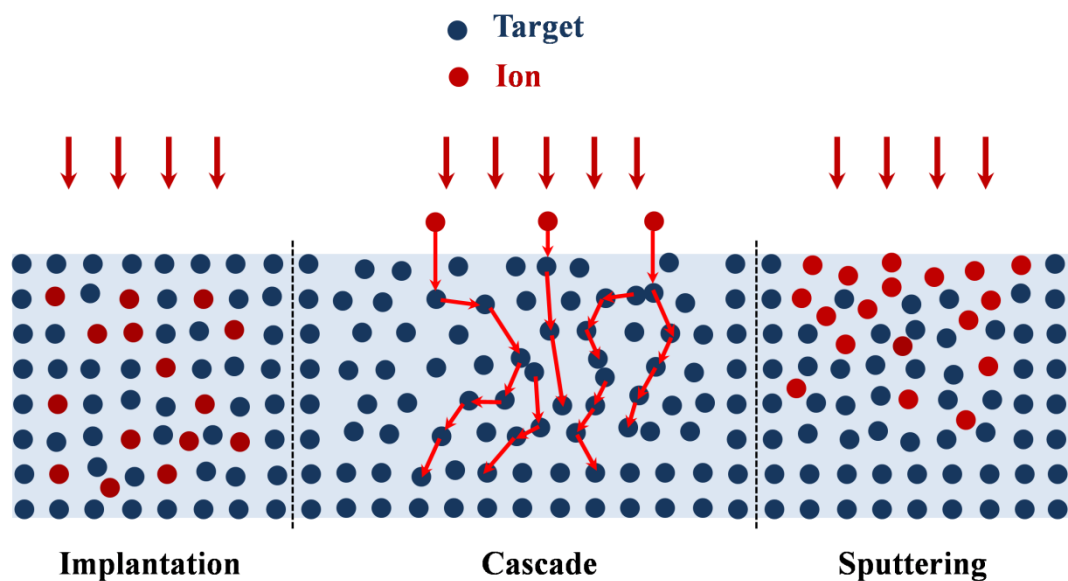


Figure 2.5: Schematic diagram of various ion-solid interaction processes.

sufficient momentum/kinetic energy is transferred from ion beam to the surface atoms of the target; lower the beam energy, more the sputtering of solid target. Sputtering phenomena will dominate during low energetic ion bombardment, whereas high energy (MeV) ion beam gives rise to lattice modifications. Here, lower energy refers to a few keV and higher energy refers to MeV ion beams.

2.2.3.1 Energy losses: nuclear and electronic

There are two basic energy loss processes when energetic ion strikes the surface of a material. If an ion beam is passing through solid material, it loses its energy due to the collisions with electrons (electronic stopping) and target nuclei (nuclear stopping). The first one is known as electronic energy loss ($S_e = (dE/dx)_e$) whereas the second one is called as nuclear energy loss ($S_n = (dE/dx)_n$). dE/dx is the stopping power defined as the transfer of energy per unit path length. In electronic energy loss, the energetic ions lose their energy through the excitation and ionization while colliding with atomic electrons inelastically. This process is dominating at higher energy of about few MeV/amu. In nuclear energy loss, ions lose their energy via elastic collisions with the atomic cores, which determines the energy transfer to and subsequent ejection of atoms from surface, leading to a phenomenon known as sputtering. S_n dominates at lower energies and hence more sputtering at these energies. At lower energy, electronic stopping power is small, increases with increasing energy until a maximum will be reached where the peak position is dependent on incident ion and target atoms. Again stopping power decreases at higher energies [19]. For implantation, the projected range (R_p), the maximum distance from a surface plays an important role. For example, the R_p of 1.8 MeV and 30 keV Ag ions in our $GeO_x/SiO_x/Si$ system is ≈ 780 nm and ≈ 23 nm, respectively [9].

In this thesis, we have irradiated specimens with low energy 30 keV Ag ions using low-energy ion implanter facility at Institute of Physics, Bhubaneswar (IOPB), India and also high energy 1.8 MeV Ag ions at room temperature using the 3.0 MV pelletron accelerator facility at IOPB [9].

2.3 Characterization techniques

In this section, we will discuss about all the characterization techniques broadly employed for thesis work. Field emission gun based scanning electron microscope

(FEGSEM), transmission electron microscopy (TEM) capable with high resolution mode coupled with selected area electron diffraction (SAED) techniques have been utilized to study surface morphology, shape, and size, local compositional analysis of the as-grown samples. X-ray diffraction (XRD) measurements including high temperature stage have been used to check the crystallinity of samples and also to perform real time, in-situ growth. We have also carried out Raman spectroscopy, X-ray photoelectron spectroscopy (XPS), UV-Vis reflectance/absorption spectroscopy, Kelvin probe force microscopy (KPFM) measurements at appropriate stages of this whole study.

2.3.1 Transmission electron microscopy (TEM)

Transmission electron microscopy (TEM) is a very important technique in the field of materials science and is routinely used for studying the crystal structure and microstructure of materials [20–22]. Microscopy can be carried out with various probes, such as visible light, X-rays, electrons besides various scanning probe methods as atomic force microscopy, scanning tunneling microscopy etc. Historically, TEMs were developed as the light microscope is limited by wavelength dependent diffraction limit. In 1932, Knoll and Ruska established the idea of electron lenses and illustrated by taking electron images in the instrument built by them [23]. This was the most important achievement, for which Ruska received the Nobel Prize in 1986. There are various types of TEM machines, in which both the particle and wave nature of electrons are utilized. In a TEM, a huge number of signals are generated due to the interaction of a highly energetic beam of electrons with the specimen, which can be utilized to get more information about that specimen (from a very small area). During transmission, the electrons interact with the specimen, giving rise to signals containing information about the internal structure and chemistry of the material. DPs and lattice images are two forms of data obtained in TEM. In TEM, DPs are the basis of all image formation as well as all crystallographic investigations and defect studies; DPs are interpreted in terms of Bragg reflection from planes of atoms of sample. In any TEM image, contrast basically comes from the scattering of the incident electron beam from the specimen. Lattice images are understood as interference patterns formed between the direct beam and diffracted beam, which are made use to form high resolution TEM (HRTEM) imaging. Usually the lattice spacing is obtained from the fringe width of HRTEM micrograph [20].

2.3.1.1 Instrumentation

A typical microscope either optical or electron consists of three parts: 1) illumination system, 2) objective lens/stage and 3) imaging system. In a TEM, the illumination system consists of an electron gun and the condenser lens assembly and is used to generate and to guide energetic electrons towards the specimen. The illumination system can be operated into two prime modes: parallel beam and convergent beam. The first mode is used primarily for conventional TEM imaging and selected area electron diffraction (SAED). The core part of any TEM is the objective lens (OL) and the specimen holder/stage system. The imaging system comprises of a few lenses to magnify the image or the DP formed by the OL and to focus these patterns on the viewing screen or onto the detector (like charged coupled device (CCD)).

Illumination section consists of electron source, acceleration column and condenser lenses. One of the most important parts in TEM is an electron source that illuminates the specimen and determines the image quality partially. There are two types of electron sources: thermionic emission (tungsten filaments or lanthanum hexaboride (LaB₆) crystals) and field emission (fine tungsten needles). An electrostatic lens in the form of Wehnelt cup is used after the filament to converge the maximum number of emitted electrons (Figure 2.6(a)). A high voltage is generated in a separated power supply unit using Cockcroft-Walton technique and is coupled to the acceleration column followed by condenser lens system assembly. After generation of electrons from the gun, they are accelerated towards the anode and enter into the acceleration column. As the velocity of the electrons close to the speed of light, the wavelength of the electrons having energy V (with relativistic correction)

$$\lambda = h/[2m_0eV(1 + eV/2m_0c^2)]^{0.5} \quad (2.1)$$

where, all the notations denote standard parameters. The function of the condenser lens system is to provide a parallel or convergent beam of electrons at sample surface (Figure 2.7). Gun crossover appears as the object for the first lens in the illumination system, having different condenser lenses. After this stage, specimen is used insert either from the side (our case) or from the top. Just below the sample (2-5 mm), objective lens (OL) is situated. The objective lens (OL) is the most crucial part of the TEM. OL is very important component of a TEM, as its quality determines the quality of all the information about the specimen that we observe. In diffraction mode, one has to adjust the imaging system lenses such that the back focal plane of the objective lens behaves as the object plane for the intermediate lens.

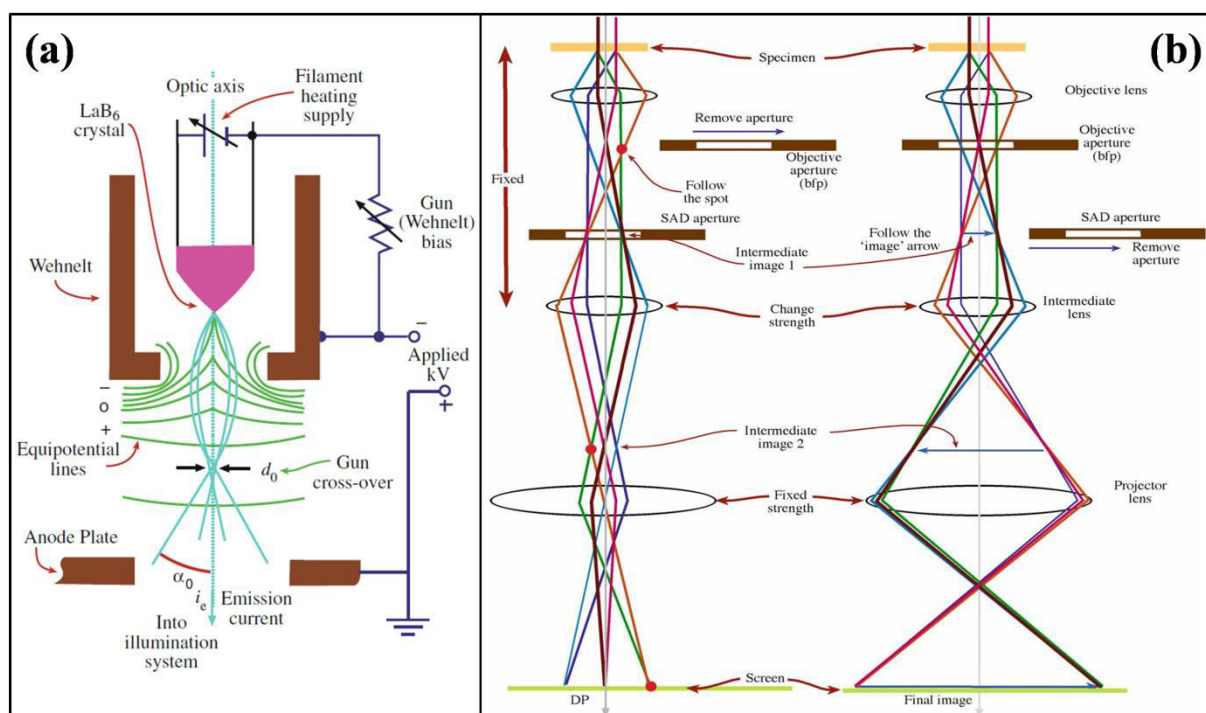


Figure 2.6: A schematic diagram of (a) filament and illumination part, (b) diffraction pattern formation and image formation [20].

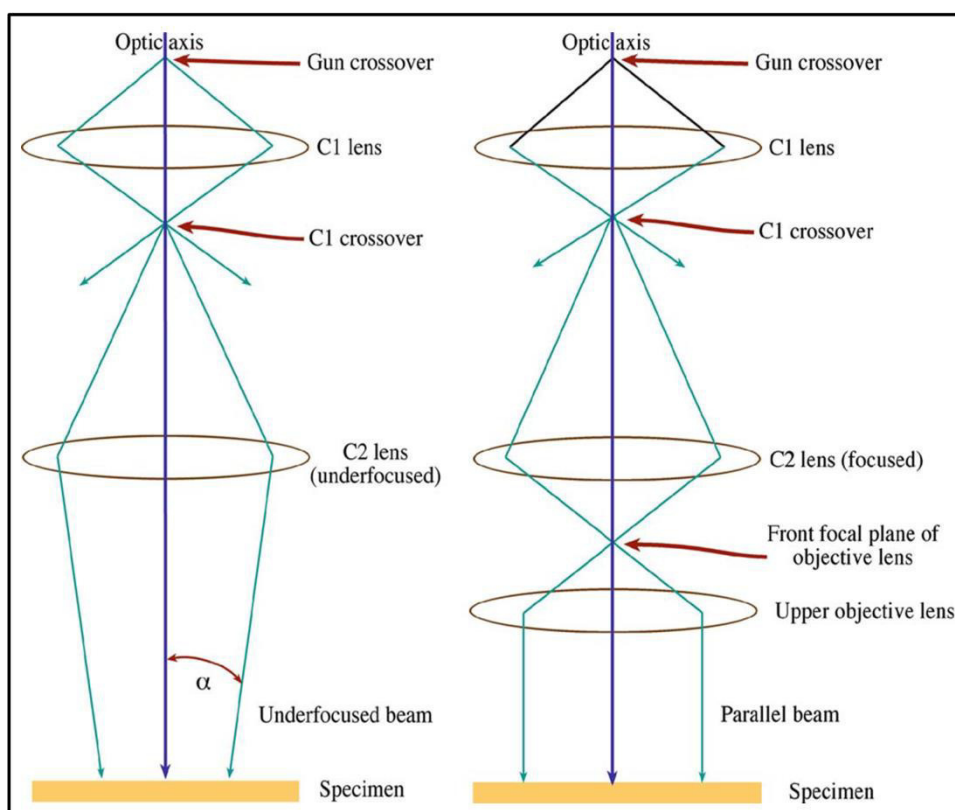


Figure 2.7: Parallel-beam operation in the TEM: the basic principle illustrated (left) and the practical situation in most TEMs (right) [20].

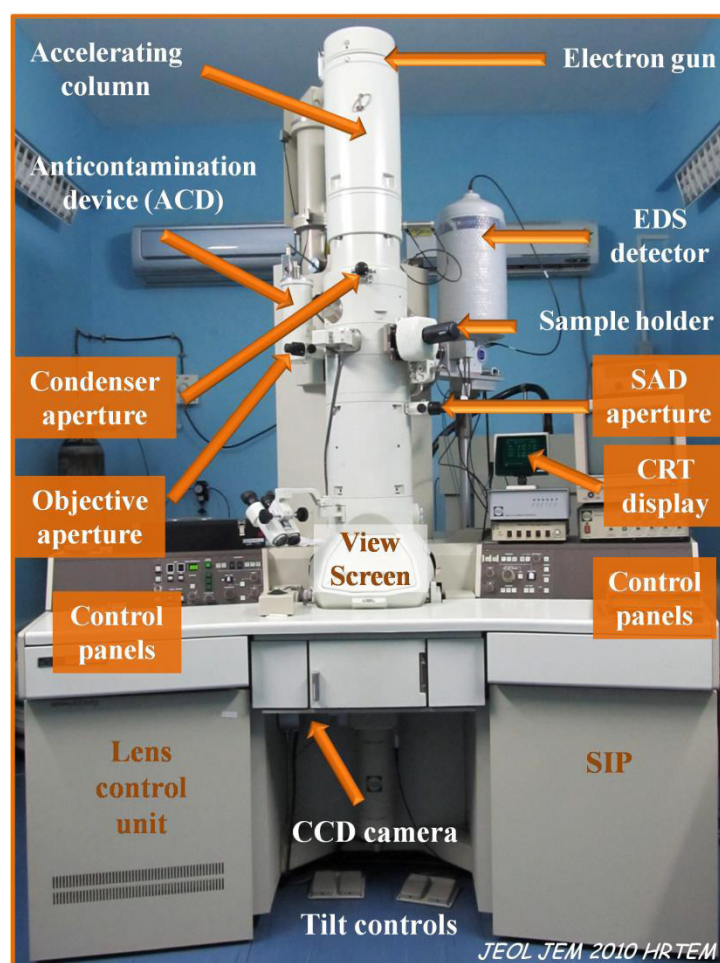


Figure 2.8: 200 keV JEOL JEM-2010 TEM, Institute of Physics, Bhubaneswar.

Then the DP is projected onto the viewing screen/CCD (Figure 2.6(b)). The imaging system consists of several magnifying lenses (termed as intermediate lenses), which magnify the image or SAD formed by the objective lens. Finally these will be projected onto the viewing screen/CCD detector. The combination of intermediate and projector lenses do the image magnification. Projector lens system projects the image onto electron detector (CCD/TV Camera), which is coupled to a computer to grab such images. Here, the quality of the image is taken care by the objective lens which eventually decides the resolution of the microscope. SAED aperture will select a specific area of the sample, which is in the image plane conjugate with the sample [20].

Electrons being charged particles, TEM column is always kept at high vacuum ($\sim 10^{-8}$ mbar) in order to get a collimated beam of electrons. In this thesis, all the TEM measurements have been carried out using JEOL JEM-2010 machine (Figure 2.8) with LaB_6 thermionic emission type gun operating at 200 keV (corresponding $\lambda \approx 0.0025$ nm). The pole piece of OL is an ultra high resolution pole piece (UHR-URP22) with a spherical aberration

coefficient (C_s) of 0.5 mm, which allows us to obtain point-to-point resolution of ≈ 0.19 nm. The images were recorded in a charge-coupled device (CCD) based detector with 40 ms time resolution and with 4008×2672 pixels (Model 832, Gatan Inc.).

2.3.1.2 Diffraction and imaging

TEM image contrast is coming due to the scattering of the incident electron beam by the specimen. When the electron wave is transmitting through a specimen, its amplitude and phase will be changed which will contribute to contrast of an image. Amplitude contrast has two forms: mass-thickness contrast and diffraction contrast. Amplitude contrast culminates from variations in mass or thickness or a combination of the two. From greater atomic number (Z) and/or higher thick specimen, electrons will be scattered more strongly, and therefore that area will appear as darker in bright field (BF) images (select direct beam to produce image) and brighter in dark field (DF) images (select diffracted/scattered beam to produce image). Diffraction contrast is simply a special form of amplitude contrast, where the scattering happens at special (Bragg) angles. Coherent elastic scattering produces diffraction contrast in TEM. In diffraction contrast, contrast depends up on the crystallinity of the specimen. However, for thin specimen at high resolution, this description fails because the wave nature of the electrons is then needs to be invoked. If the specimen is thin enough and crystalline, then elastic scattering is usually coherent and these scattered/transmitted electrons contribute to the image formation. After the exit of electrons (elastically transmitted coherent electron beams), the diffraction spots and image are used to form at back-focal plane and image plane of OL respectively. The diffraction pattern can be understood by taking the fast Fourier transform (FFT) of the wave function of electron at the back focal plane of OL. The lattice image will form due to interference between the direct and diffracted beams depending on the phase difference between these two. So the highly diffracted beams are used to cut down by the objective aperture. The resolution and the details of image formation are governed by the contrast transfer function (CTF). The CTF depends on microscope parameters such as λ , spherical aberration coefficient (C_s), chromatic aberration coefficient (C_c), defocus, width of defocus, stabilities in high voltage, OL current etc. To obtain the structural information about the sample from the images, the trajectory of the electron wave through the specimen needs to be calculated. In order to understand the geometry of electron diffraction, we can ignore the lens system, which merely magnifies the DP.

Normally we interpret the DPs in terms of Bragg reflection due to the planes of atoms in specimen and one can introduce diffraction vector \vec{g} associated with each Bragg reflection and link each g with a crystal plane (hkl). The reciprocal lattice provides a very simple way of understanding the diffraction, when combined with the Ewald-sphere construction. Bragg's law or the Laue equations are satisfied exactly, when the sphere exactly cuts through a point. The Ewald sphere has a radius of $1/\lambda$. Most importantly, since λ is small in TEM, the radius of the Ewald sphere is large and hence the Ewald sphere is quite flat. This results the formation of many spots in the DP. A schematic diagram showing the geometry of diffraction pattern formation and may consider the much simpler ray diagram shown in Figure 2.9. When a beam of electrons falls on a crystalline specimen, some of them will transmit through the specimen without any interaction (direct beam) and impinge on the CCD. Other electrons are diffracted through an angle 2θ by the crystal planes of spacing d and impinge on CCD detector at a distance R from the direct beam. According to Bragg's law, the diffracted beam follows the relation $2d\sin\theta = \lambda$, which can be simplified for the small angles as $\lambda/d = 2\theta$. From the trigonometric relation using small angle approximation, one can write $R/L = 2\theta$. Combining these two,

$$d = \lambda L/R \quad (2.2)$$

where, R is the distance between the direct and diffracted beams as measured on the screen. As the λ and L (camera length) are constant for the instrument, the quantity λL is called camera constant. So, d can be determined easily. Note that, L is not a physical distance between the specimen and screen, but is a notional distance which can be changed while operating [20].

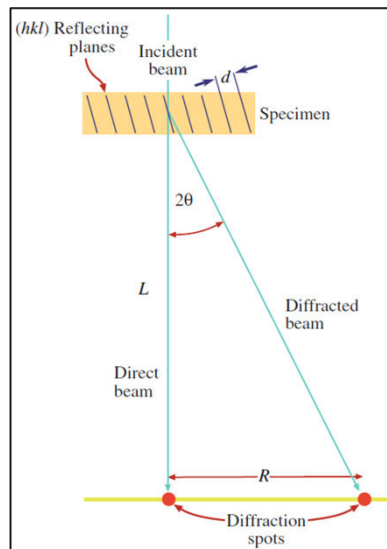


Figure 2.9: A schematic diagram showing the geometry of diffraction pattern formation [20].

2.3.1.3 Beam (electrons)-specimen interaction

Electron, being a low-mass, negatively charged particle, can easily be deflected while travelling close to other electrons or the positively charged nucleus of an atom. These Coulomb (electrostatic) interactions cause electron scattering, which can be broadly divided in two groups: elastic (no loss of energy) and inelastic (some measurable loss of energy) scattering. The all possible interactions of electrons with solid have schematically shown in Figure 2.10. One can also split the scattered electrons into coherent and incoherent. Elastic scattering is usually coherent (if the specimen is thin and crystalline) and usually occurs at relatively low angles ($1-10^\circ$). At higher angles ($> 10^\circ$) elastic scattering becomes more incoherent. After entering into the specimen, most of the electrons are scattered elastically by the nuclei of the atoms in the specimen. Some electrons are also scattered inelastically by the electrons in the specimen. Compared to X-ray or neutron diffraction, the interaction of electrons with the specimen is quite large and they go through multiple scatterings. The prime origin of contrast in TEM images are the elastically scattered electrons. When the specimen is thick, the interaction between the electrons and the specimen can be described by an incoherent particle model. However, considering thin specimen, the wave character of the electrons will dominate and the particle model can be discarded. The electrons, while transmitting through the specimen near the nuclei, are accelerated towards the nuclei and will

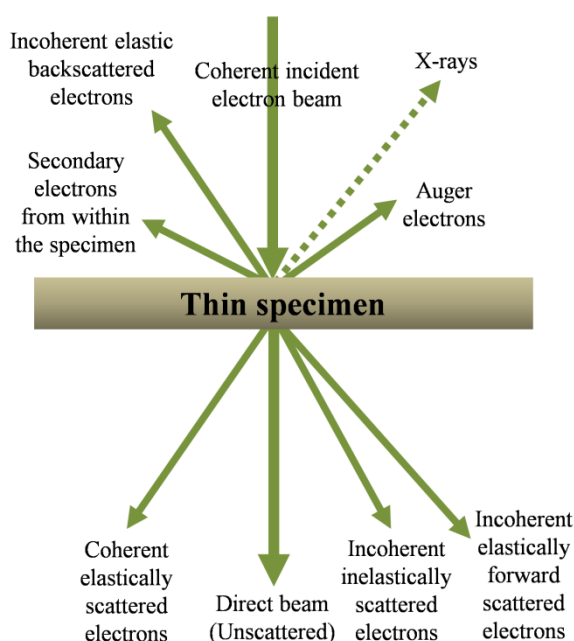


Figure 2.10: Schematic presentation of various signals generated when a high-energy beam of electrons interacts with a thin specimen.

experience a small change of phase of them. This minimal change in phase also contains structural information. For high resolution images, only the elastically scattered electrons are of importance. Inelastic scattering transfers energy to the specimen and generates a lot of useful signals, from which one can produce different images or gain spectroscopic knowledge regarding the chemistry and electronic structure of the specimen. Electron energy loss spectrum (EELS) of the inelastically scattered electrons provides the information about chemical composition of the sample at a very spatial high resolution. These inelastic scattered electrons also contribute to the formation of Kikuchi lines in the electron diffraction pattern that is needed for attaining the crystallographic alignment of the crystals in specimen [20].

2.3.1.4 Sample preparation (mechanical process)

Sample preparation is the most important aspect of all of TEM works. Since the electrons have to transmit through the specimen, the specimen has to be thin enough for the electron transparency. Generally, for 200 keV electron beam, sample thickness should be ≤ 100 nm (even thinner (<10 nm) for HRTEM) to transmit energetic electrons. There are two types of samples to be prepared depending on the interest of study. Cross-sectional TEM (XTEM) sample is required to study the interface and/or bulk solid while planar TEM specimen preparation is required for in-plane study. Figure 2.11 and Figure 2.12 display the schematic illustrations of conventional methods (mechanical process) to prepare both planar and cross-sectional TEM samples respectively.

Planar specimen preparation:

For Planar TEM sample preparation, we cut the sample into 3 mm disc using ultrasonic disc cutter and thin down to ≈ 80 -100 μm from rare side (substrate side) by using lapping and polishing system (South Bay Technology (SBT) Model 910). Here, the mechanical thinning is performed by grit paper with larger size initially, and then finer grit size and finally polished with finer polishing paper. The specimen is then loaded on dimple grinder stage (Gatan, Model 656). The aim of this process is to thin the center of the disk while minimizing damage to the surface of the sample and typically dimpling is carried out up to ≈ 20 μm thick using diamond paste and then polished by using alumina suspension. Final electron transparency is achieved by ≈ 3 keV Ar ion (Ar^+) milling at grazing incidence (5° - 7°) in the Gatan made precision ion polishing system (PIPS, Model 691) (Figure 2.11).

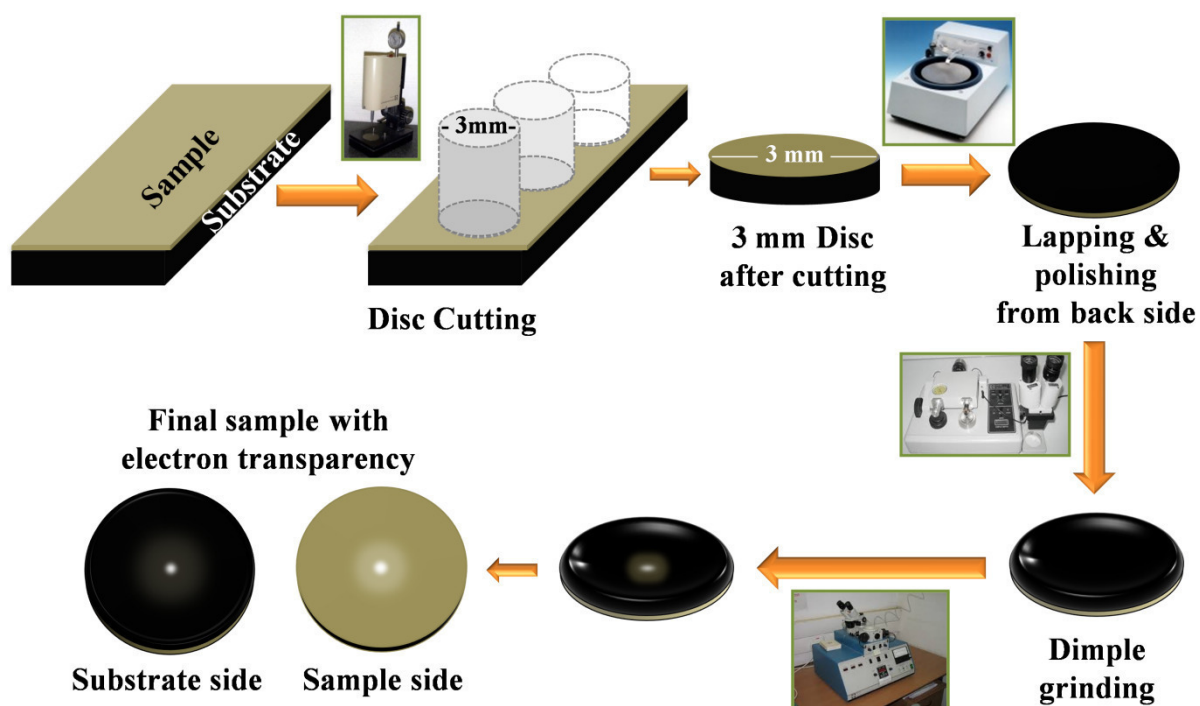


Figure 2.11: Schematic diagram of a typical planar TEM specimen preparation procedure.

Cross-sectional specimen preparation:

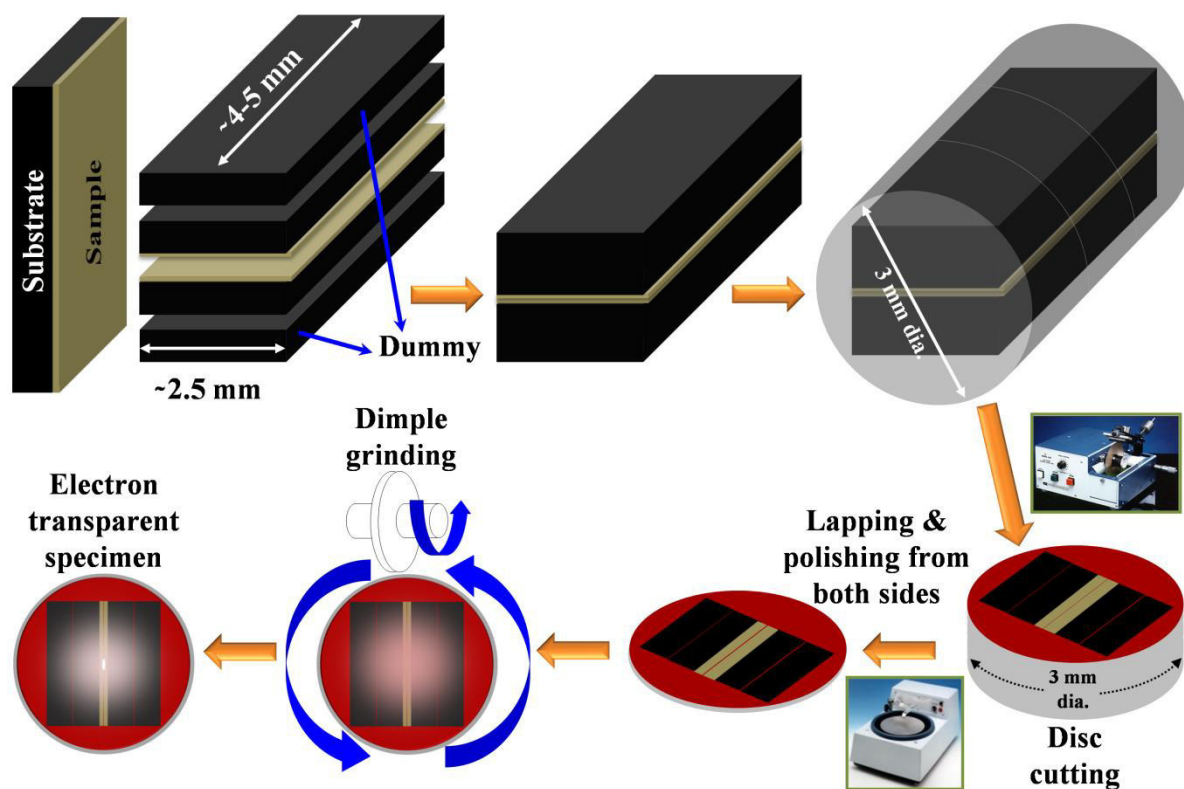


Figure 2.12: Schematic diagram of a typical cross-sectional TEM specimen preparation procedure.

For cross-sectional TEM sample preparation, we cut two rectangular pieces of dimensions ($\approx 2.5 \text{ mm} \times 5 \text{ mm}$) from the main sample using SBT made abrasive slurry saw (Model 850). Then the pieces were glued face to face using Gatan G1 epoxy. Following this, the above assembly is glued with two dummy pieces having similar sizes. After that the whole assembly is packed into a stainless steel tube having inner and outer diameter $\approx 2.9 \text{ mm}$ and $\approx 3.1 \text{ mm}$ respectively using the same epoxy glue. Next, we cut $\leq 500 \text{ }\mu\text{m}$ thick slices from the tube using SBT made Low speed diamond wheel saw (Model 650). Mechanical thinning and polishing are performed from both sides (using LPS) as like planar sample preparation case, and similarly one side is dimpled using DG. Finally, electron transparency is achieved by $\approx 3 \text{ keV}$ Argon ion milling using PIPS in similar way mentioned above (Figure 2.12).

2.3.2 Focused ion beam – scanning electron microscope (FIB – SEM) cross beam system

The scanning electron microscope (SEM) is used for observation of specimen surface. When a specimen is irradiated with a fine electron beam, secondary electrons (SEs) are emitted from the specimen surface and the topography of the surface will be visualized as an image constructed by the secondary electrons. A scanning electron microscope (SEM) was pioneered in the late 1940s by Charles Oatley and co-workers at Cambridge University. SEM provides the information about the surface topography and composition of specimen. The combination of field emission based scanning electron microscopy (FESEM) and focused ion beam (FIB) is the leading technique in modern nanoscience and nanotechnology. The focused ion beam (FIB) technique was developed almost 40 years back. This FIB technology facilitates coarse milling, fine milling, fine polishing, ion beam induced metal/insulator deposition with high precision and hence this technique is intensely utilized in device fabrication/modification, masking, process control and most importantly specimen preparation for TEM. In this thesis work, we have carried out SEM analysis vividly in a cross-beam scanning electron microscope (Carl Zeiss, Neon 40) with Gemini column and Canion 31 focused ion beam (FIB, Orsay Physics), equipped with gas injection system (GIS, Orsay Physics), SE detector, in-lens detector, STEM detector, back scattered electron detector and X-ray energy-dispersive spectrometry (EDS) detector (INCA, Oxford) (Figure 2.13). These two columns are situated at 54° angle; to see same spot with SEM and FIB, tilt

angle will be 54° with 5 mm working distance ((WD) \rightarrow defined as the distance between sample and pole piece). To provide full eucentric tilt at all operating conditions a 6-axis motorized eucentric specimen stage is used. This favors the real time processing done by FIB and observation through non-destructive non-contaminating SEM even if at high resolution. The sample can be tilted between 0° and 54° to face the ion beam or the electron beam perpendicularly. When tilt angle is 0° , which means electron beam is falling on specimen at normal incidence whereas ion beam is irradiating at 54° . Both SEM and FIB imaging techniques are dependent on the secondary electrons collected by the detectors. The FIB column operates at an accelerating voltage (Ga^+ ions), ranging from 2 to 30 kV with a minimal Gaussian beam diameter around 7 nm. The beam current can be varied from 1 pA to 50 nA. FIB system can be used for imaging, milling and deposition Pt/W using GIS. One Kleindiek micromanipulator is attached inside the specimen chamber for TEM lamella preparation. The system is fitted with a computer controlled gas injection system (GIS) in which five different gases for metal and insulator deposition or enhanced and selective etching could be possible. A turbo molecular pump ensures a dynamic pumping and the base pressure in the chamber is $\leq 10^{-6}$ mbar. The working principles of SEM and FIB are separately discussed below.

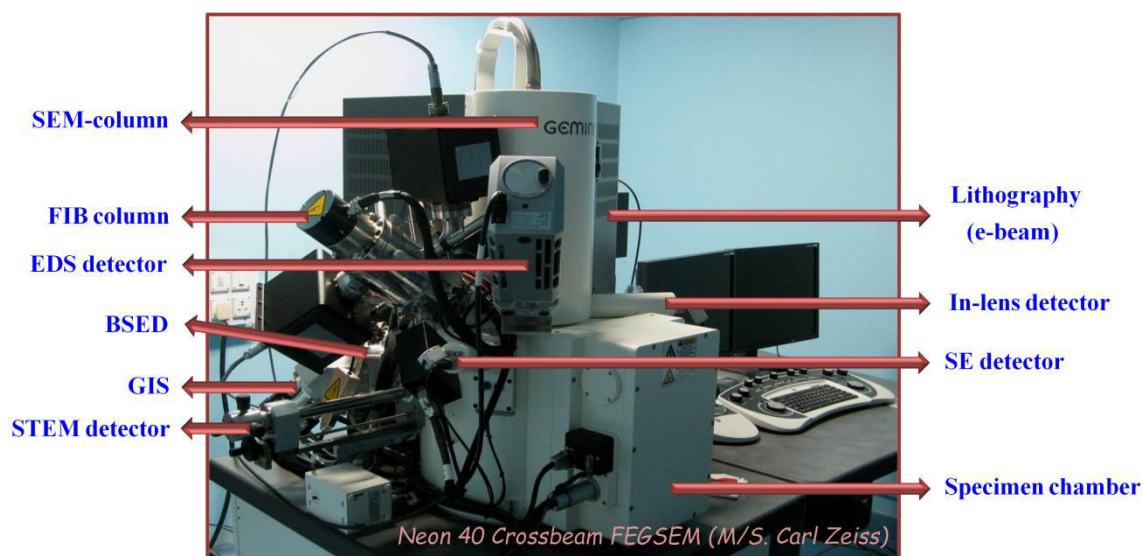


Figure 2.13: FIB-SEM cross-beam system (M/S. Carl Zeiss, Neon 40), Institute of Physics, Bhubaneswar.

2.3.2.1 Scanning electron microscopy (SEM)

The main constituents of a typical SEM are electron column, scanning system/

electron optics, detectors, vacuum pumps/system and electronics control. There will be a electron beam source which is accelerated down the column; then a series of condenser and objective lenses which will act to control the diameter of the beam as well as to focus the beam on the specimen; a series of apertures, through which the beam will pass and beam will be controlled; then specimen stage; beam-specimen interaction, which will generate different types of signals that can be detected by the detectors to provide the information about the sample. This SEM system has field emission based electron gun. The main characteristic of the GEMINI optics is the use of a beam booster and an objective lens which acts as a combined electrostatic/electromagnetic lens. The electrons generated at the gun tip are accelerated to the set acceleration voltage as they are accelerated towards the anode. However, the beam booster, which is installed directly after anode, is always at a potential of an extra 8 kV when the set acceleration voltage is ≤ 20 kV. When low voltages are used, this arrangement will ensure that the energy of the electrons in the beam path will always be 8 kV higher than the set acceleration voltage and will reduce the influence of magnetic stray fields on the electron beam. Before the electron beam exits the objective lens, the electrostatic lens reduces the potential by an opposite applied 8 kV. The electrostatic lens acts as a collector for the electrons generated at the sample surface. The sample electrons are accelerated and focused back up the beam path, where the detector is positioned. In SEM, magnification of an image is defined by area on the sample surface over which the electron beam is irradiated and the size of the CRT screen on which the image is displayed [24].

Image formation:

In the SEM, the image formation of an object depends on the collection of signals generated due to electron beam - specimen interactions, and are classified into two types: elastic interactions and inelastic interactions. When accelerated electrons are introduced into a solid, they are scattered both elastically (by electrostatic interaction with atomic nuclei) and inelastically (by interaction with atomic electrons). Due to the electron - specimen inelastic interaction, the specimen electrons are excited individually or collectively on which the amount of energy loss completely depends along with the binding energy of the electron to the atom, resulting the generation of secondary electrons (SEs). In addition to those signals, a number of other signals including the emission of characteristic X-rays, Auger electrons and cathodoluminescence are produced upon an electron beam impingement on the specimen (Figure 2.14). Impingement of primary beam of electrons on specimen causes the emission of

secondary electrons (SEs) [due to inelastic interaction] and backscattered electrons (BSEs) [due to the elastic interactions]. These SEs and BSEs are mainly used for imaging; SEs have lower energy compared to BSEs, they can be separated easily by applying an electric field. The range (R) for electrons having incident energy E is given by Reimer formula:

$$\rho R \approx aE^r \quad (2.3)$$

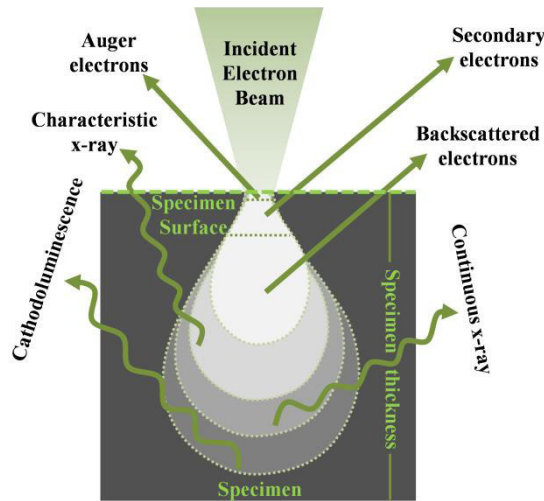


Figure 2.14: Schematic representation of various signals generated due to the electron-specimen interaction in SEM.

where, ρ is the density of the specimen. As the densities of solids tend to increase with atomic number, hence the distance R consequentially decreases with Z . On the other hand, the range R decreases substantially with decreasing the incident electron energy. Since the SEs are generated within very small depth (may be < 2 nm) below specimen surface, hence the SE image is a property of the surface structure (topography) of the specimen; the corresponding image is called as topographical image. Most commonly, an Everhart-Thornley detector (E-T detector), named after the scientists who first applied this design to the SEM, is used to detect the electron signals in the scanning electron microscope (SEM). The E-T detector consists of a Faraday cage covering a scintillator, an optical guide and a photomultiplier tube (PMT). The Faraday cage is placed outside the detector and either a negative or a positive bias voltage can be applied to it. The secondary electrons are first attracted toward a wire-mesh electrode biased positively by a few hundred volts. Most of the electrons pass through the grid and are accelerated further toward a positively biased scintillator by several thousand volts. The positive bias voltage causes the trajectory of electrons emitted from the sample over a large solid angle to be directed towards the detector. In the detector the electrons are accelerated to the scintillator where they induce light emission. The light is guided to the photomultiplier tube (photocathode) amplifying the signal and converting it into an electric

current which can be read out on a screen. In some high resolution SEMs, the objective lens has a small focal length (a few millimeters) and the specimen is kept at a very low working distance (WD). Secondary electrons, generated close to the optic axis, are attracted toward a positively biased detector. Basically, secondary electrons, which are coming out almost perpendicularly with respect to specimen surface, are detected by in-lens detector and hence there will be no directional or shadowing effects [24].

A backscattered electron (BSE) is a primary electron that has been ejected from a solid by elastic scattering through an angle $> 90^\circ$ and yield a useful signal for imaging the sample. BSEs are basically primary electrons which have been reflected back from a specimen via elastic collision events in one of two ways: (1) under the strong Coulomb field of an atomic nucleus (i.e. Rutherford scattering) and (2) incident beam of electrons can undergo multiple low-angle deflections/scattering which together comprise a deflection of $> 90^\circ$. In first case, cross-section for high-angle elastic scattering is proportional to Z^2 . One can expect a strong atomic number (Z) contrast image/information by using BSEs signal (image known as Z-contrast image). If specimen contains the elements of different atomic number Z, then the BSE image will give different intensities and contrasts. Higher Z area will appear as brighter than smaller Z area unlike to SE image (SE emission is almost Z independent). Since BSEs are coming from the deep (unlike to SEs), BSE signal contains little topographic contrast but does show material (atomic number, Z) contrast. BSEs can be detected by a scintillator/PMT detector if the bias on the first grid is made negative to reject all the secondary electrons [24].

X-ray energy-dispersive spectrometry (EDS)

X-ray energy-dispersive spectrometry (EDS) is an analytical technique used for the elemental or chemical compositional characterization of a sample. The EDS was developed in the late 1960s and by the mid-1970s was an option on many TEMs and even more widespread on the SEM. The X-ray spectrum produced within specimen, consists of element-specific characteristic peaks with well defined energies superimposed on a non-characteristic background. When an incident electron is scattered inelastically it knocks out a core electron and then an electron from a higher orbital fills the empty state (hole) in lower (core) orbital. The energy difference between these two orbitals is released in the form of photons (their energy used to be in the X-ray regime when a core level electron is knocked out), whose energy is characterized for the transition in the respective target atom by Mosley's law. The

EDS detector (Si(Li)) is the only X-ray spectrometer currently used to detect X-ray. When X-ray emitted from specimen falls on the detector crystal, its energy is absorbed by electrons in the valence band of the semiconductor and goes to the conduction band, leaving behind holes in the valence band. With an application of reverse bias voltage to the diode, electrical charge starts flowing through the junction (and around an external circuit) and the charge is purely correlated to the energy of the incident X-ray produced during the interactions. Then the field effect transistor (FET) circuit attached to the backside of the detector converts charge signal to a voltage signal. An EDS spectrum displays peaks across the energy range that contains all the characteristic peaks for which the most X-rays are received. The higher intensity peak in a spectrum corresponding to an element corroborates its more presence in the sample [20, 24].

2.3.2.2 Focused ion beam (FIB)

A focused ion beam (FIB), means a well-controlled beam of gallium ions (Ga^+), is used to cut thin slices, often for TEM measurements of metal or semiconductor. The ion column design is quite similar to electron column. Basic components of a FIB system are ion source, ion optics column (for acceleration), beam deflector and specimen stage. The ion beam (Ga^+) is produced from a liquid metal ion source (LMIS) by applying of a strong electric field. Ga is used because it has quite low melting point (30 °C, i.e., liquid around room temperature) and low steam pressure (applicable in HV). A liquid metal ion source (LMIS) is a field emission ion source, which generates highly focused ion beam from neutral atoms or molecules, by field induced ion production at the tip of needle like emitter. Here, a metal is heated to the liquid state and delivered at the end of a capillary or a needle. Then a Taylor cone is formed by applying a strong electric field at the tip of a tungsten needle. As the cone's tip gets sharper, the electric field becomes larger and ions are generated by field application. A typical extraction voltage 7 kV is applied to the tungsten needle. The emission current under normal operating conditions is $\leq 2.0 \mu\text{A}$. The ion beam energy can vary from 2 keV to max 30 keV. A set of apertures (motor controlled) define the probe size and provides a range of ion currents (1 pA – 50 nA). Cylindrical octupole lenses perform multiple functions such as beam deflection, alignment, and stigmation correction. Beam blankers are used to deflect the beam away from the centre of the column. A vacuum of about 10^{-10} mbar is maintained inside the ion gun column [25].

2.3.3 X-ray diffraction (XRD)

X-ray diffraction technique is a very essential tool in material research to examine the crystal structure and to study surfaces and interfaces etc. of materials. X-rays are extensively employed in the field of material science to obtain atomic scale information from a macroscopic area. When an X-ray interacts with materials, scattering or absorption of X-ray may occur. Since, X-ray interacts weakly with the material, one can neglect multiple reflections. X-ray can penetrate deep into a material and the penetration depth depends on its energy and also on that particular material. Instrumentation of an XRD system broadly consists of an X-ray source, goniometer for mounting the sample and the detector in the reflection geometry. In XRD, X-rays are focused on a material and the scattered rays are observed from various angles at large distance. In an elastic scattering process, which is the case for XRD, an incident X-ray falls on a sample and is then reflected with the same angle as incident angle and is collected by a detector that is interfaced to a computer to display the spectrum of intensity vs. angle of incidence. When the sample stage moves in the θ the detector is moved to a value of 2θ to collect the data (this is called θ – 2θ geometry) [26].

Bragg's Law:

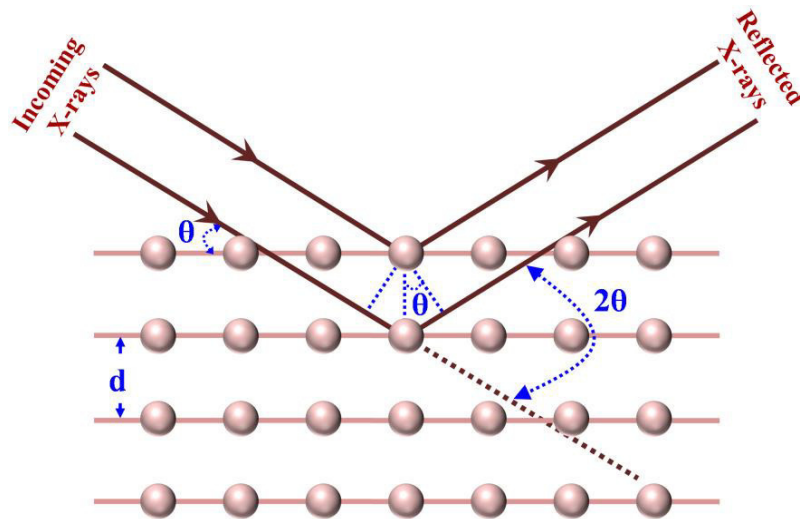


Figure 2.15: Schematic representation of X-ray diffraction occurring in a crystal with interplanar spacing d .

The Bragg's law is given by,

$$2d\sin\theta = n\lambda \quad (2.4)$$

Here d is the inter-planar spacing of the diffracting planes, θ is the incident angle, n is an integer and λ is the wavelength of the incident X-ray beam (Figure 2.15).

In this thesis work, XRD technique has been broadly utilized; 3rd chapter of this thesis extensively deals with XRD results. We have used synchrotron X-rays at Photon Factory, Japan (Indian beam line). The energy tunability of X-rays allows to work with an appropriate wavelength for specific experiments.

2.3.3.1 Instruments: Photon Factory

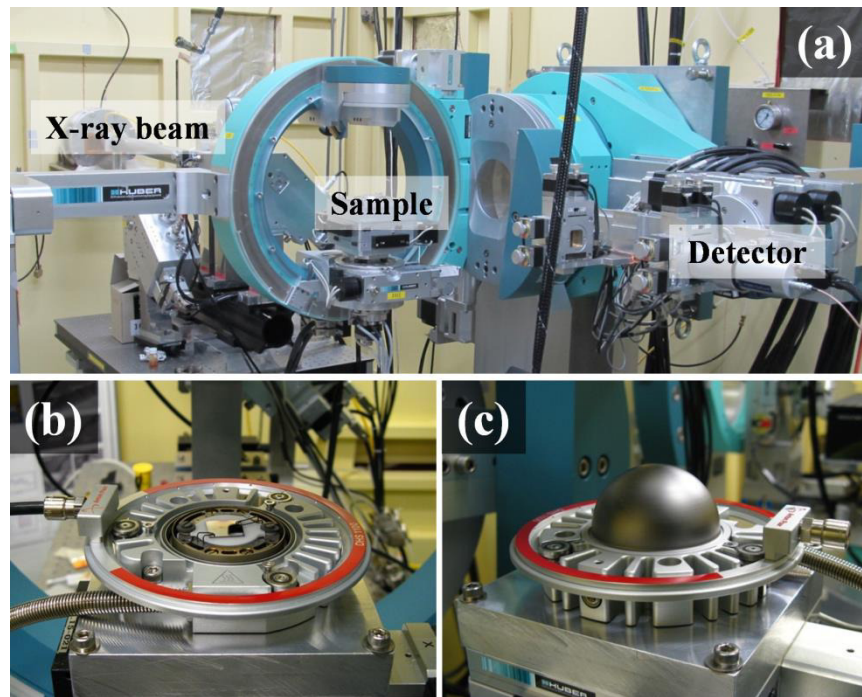


Figure 2.16: (a) Experimental setup to perform XRD measurements (Indian beam line 18-B, Photon Factory, Japan). High temperature setup mounted on goniometer and loaded with sample: (b) without the graphite dome and (c) covered with graphite dome [27].

The Photon Factory is an accelerator-based light source facility and operates two storage rings, the 2.5 GeV PF ring and the 6.5 GeV PF Advanced Ring (PF-AR). The X-rays provided by the light source are directed towards beam line 18-B to perform the experiments at multipurpose monochromatic hard X-ray station by using bending method. The X-ray beam is directed to the desired sample using a double crystal monochromator (consisting of channel cut Ge single crystal), which selects the desired wavelength. Sample is mounted on 6 axis goniometer which has an angular resolution of 10^{-3} mrad. This goniometer allows us to move the sample in X, Y and Z axis and also can be rotated in Euler angles θ , φ , χ . Sample

will be mounted on this goniometer which is aligned eccentrically. Incident X-rays fall on the sample and diffracted beam is collected by scintillation counter (model X2000, Cyberstar). This detector is connected with a computer through a serial link RS232. The diffracted signals are collected by this detector and pre-amplified and send it to the amplifier for the further signal processing and counting process and interfacing computer. Real time in-situ experiments were performed using a heating holder (Model DHS 1100, M/s. Anton Paar GmbH). Control of the temperature is controlled through TCU 200 controlling unit. The heating holder has a sample holder made of aluminium nitride above the heater to hold the sample of maximum diameter up to 25 mm and thickness up to 2 mm. This sample stage has virtues like fast and stable heating up to 1100 °C, excellent temperature homogeneity across the heating plate, accurate measurement of the sample temperature and chemically resistant ceramic heating plate with minimum tilt and expansion during the heating. Near the sample holder, there is a Pt-10% Rh-Pt thermocouple to measure the temperature. In order to maintain vacuum or avoid oxygen contamination on the sample, a dome, made of graphite, (highly transparent) which has a transparency of 65% for Cu K α radiation is usually used to cover the sample. The sample is fixed to the heater by the Inconel clamps. The graphite dome is kept on temperature setup after loading the sample. RS232 cable of the temperature controller is connected to the windows system, meant for the beam control. From this computer the temperature controller can be accessed using iTools software. This high temperature setup can operate from room temperature to 1100 °C for air, N₂, vacuum or inert gas atmosphere and 1000 C with He gas. In our experiment, a ramping rate of ≈ 7 °C/minute was used to arrive high temperatures with an X-ray wavelength of 0.8587 Å [11].

In this thesis work, we have also performed XRD measurements at room temperature using Bruker DAVINCI D8 ADVANCE diffractometer equipped with Cu K α radiation ($\lambda = 0.15406$ nm) for other samples [10, 28].

2.3.4 X-ray photoelectron spectroscopy (XPS)

Photoemission spectroscopy (PS) tool is based on the photoelectric effect [29], where electrons are emitted from the sample via interaction with electromagnetic radiation. In 1905, photoelectric effect was explained by Albert Einstein through a hypothesis that light energy is carried in discrete quantized energy packets [30]. In X-ray photoelectron spectroscopy (XPS) technique, X-ray is probed on material for the emission of photogenerated electrons. XPS is a

surface sensitive technique by which the surface chemistry of a material in its as-synthesized state, or after some post treatment is analyzed. The unique ability of XPS to identify the chemical states of atoms, as a function of depth, makes it an invaluable tool for understanding the elemental composition and chemical interactions. Compared to ultraviolet photoelectron spectroscopy (UPS) where the energy of the impinging radiation is order of few tens of eV, the energy of X-ray is in the order of a few thousand of eV. Therefore, electron from outer and inner core shells of atoms/molecules can be excited in XPS, whereas UPS can only knockout electrons those are in valance band. X-ray photoelectron spectroscopy (XPS) is a spectroscopic technique which quantitatively gives the elemental composition, chemical state and charge state of the elements which are there in the material. In XPS, when X-ray photons strike a surface, in vacuum, electrons in core level can get excited and produce photoelectrons. A photoelectron will be emitted only when the photon energy is larger than the binding energy of the electron. These photoelectrons are energy analyzed and provide information on density of state (DOS) of the sample. The binding energy (E_B) of the emitted electrons can be evaluated by following equation

$$E_B = E_{\text{photon}} - (E_{\text{kinetic}} + \Phi) \quad (2.5)$$

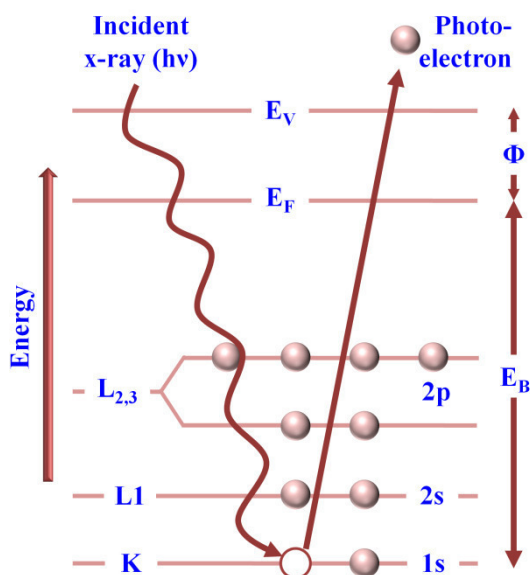


Figure 2.17: Schematic illustration of core energy level during photoelectron emission process.

where, E_{photon} is the energy of the x-ray photon, E_{kinetic} the kinetic energy of the emitted electron and is measured by an electron analyzer; Φ is the work function dependent on material and spectrometer both. Equation 2.5 is essentially coming from the energy conservation. XPS spectrum shows the number of photo electrons as a function of binding energy. As the energy of the photons and work function of the spectrometer are known

quantities, the electron binding energies can be obtained by measuring the kinetic energies of the photoelectrons. XPS system consists of a ultra high vacuum (UHV) chamber that contains an X-ray source, an electron analyzer, and a sample holder. Figure 2.17 shows the schematic representation of core level photoelectron emission process. Generally, samples are mostly investigated with two monoenergetic X-rays such as Mg-K α (1253.6 eV) or Al-K α (1486.6 eV) because of their relative high energy and narrow width.

In this thesis work, X-ray photoelectron spectroscopy (XPS) studies for all the samples have been performed by using PHI 5000 VersaProbe-II (ULVAC-PHI, INC, Japan) system with a micro-focused monochromatic Al-K α source ($h\nu = 1486.6$ eV), a hemispherical analyzer, and a multichannel detector. XPS system base pressure of 6×10^{-10} mbar was maintained during all data acquisition [10, 28].

2.3.5 Raman spectroscopy

Raman scattering is a spectroscopic technique that is used to study vibrational modes of molecules. In 1928, Prof. C V Raman observed that the wavelength of a small fraction of the photons inelastically scattered by certain molecules/atoms differs from the wavelength of incident photon and this shift depends on the chemical configurations of those particular molecules/atoms [31]. This scattering phenomenon gets its name from Sir C V Raman, who won the Nobel Prize in Physics for his discovery in 1930. The Raman effect is based on molecular deformations caused by oscillating electric field E associated with incident electromagnetic radiation (usually laser) determined by molecular polarizability α . When this molecule is placed within the electric field of the laser, an electric dipole moment (P) is induced, given by the equation $P = \alpha E$, where α is the polarizability of the molecule, or the measure of the response of the electronic charge distribution to the electric field (E).

In Raman scattering, energy difference between the incident and scattered light corresponds to the vibrational excitation. When a molecule is irradiated with intense light from a laser, it can be excited from its ground electronic state to a virtual state that is lower in energy than the first excited state. The majority of the time, this light is elastically scattered and the molecule returns to its initial state. This effect is known as Rayleigh scattering. Some light can be inelastically scattered, however, and the molecule can end up in a vibrational state that is different from where it originated. For the spontaneous Raman effect, the molecule will be excited from the ground state to a virtual energy state, and relax into a

vibrational excited state, which gives Stokes Raman scattering line; if the molecule is already in vibrational excited state then it generates anti-Stokes Raman scattering line (Figure 2.18). Intensity of Stokes line will be higher than that of anti-Stokes line, as the vibrational ground state is more populated than the excited states [32].

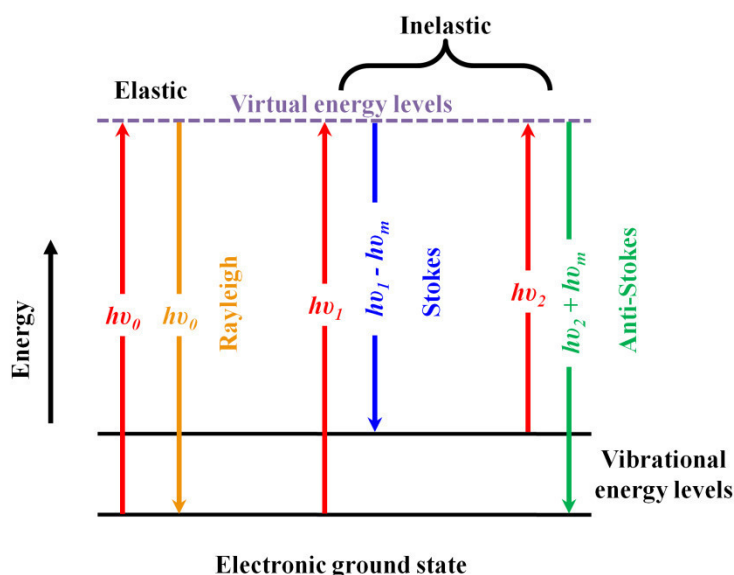


Figure 2.18: Energy level diagram, showing three types of possible scatterings, i.e., Rayleigh, Stokes and Anti-Stokes scattering states involved in Raman signal.

In this thesis, Raman studies of the as-grown samples have been carried out using a Renishaw in Via Raman microscope with a 514 nm laser and a 50× objective with 10 sec exposure time at room temperature.

2.3.6 UV-Vis-NIR

Optical reflectance measurements of as-grown samples (with substrate) have been performed using a Shimadzu UV 3101PC UV-Vis-NIR spectrophotometer equipped with a specular reflectance measurement accessory. The spectral range that can be studied with this instrument is 200 to 3200 nm. In the present thesis, most of the spectra (reflectance mode) were collected over a wavelength range of 250–1000 nm at room temperature. The reflectance mode works in a specular reflection geometry arrangement with 45° incidence angle of light [10]. In addition, UV-Vis absorption measurements of few samples (in liquid mode) have been executed using a deuterium and halogen combined excitation source with the spectra being recorded using an Avaspec-3648 spectrometer at room temperature [28].

2.3.7 Kelvin probe force microscopy (KPFM)

Kelvin probe force microscopy (KPFM) is a technique which enables nanometer-scale imaging of surface potential on a broad range of materials. This technique, which is considered to be a suitable non-contact technique, is an atomic force microscope (AFM) based technique. KPFM has been extensively used as a unique method to characterize the nano-scale electronic or electrical properties semiconductor surfaces and metal-semiconductor devices. When an AFM tip is brought close to the sample surface, an electrical force will be acted between the tip and sample surface, because of their Fermi energy levels differences. An AC voltage is applied to the tip to generate an oscillating electrostatic force between the tip and the sample surface and an apparent contact potential difference (V_{CPD}) will form. Then an external DC potential (V_{DC}) with the same value as V_{CPD} in opposite direction is required to nullify the electrostatic force. So, the mapping of this nullifying V_{DC} versus the lateral position coordinate composes the work function mapping image (called KPFM image) of the sample surface. Therefore, the work function of the sample surface can be evaluated by using the following expression [33]

$$V_{DC} = V_{CPD} = -(\Phi_{tip} - \Phi_{sample})/e \quad (2.6)$$

where, Φ_{sample} and Φ_{tip} are the work functions of the sample and tip, respectively. The work function of the tip has been calibrated with respect to standard HOPG sample and hence Φ_{sample} will be

$$\Phi_{sample} = \Phi_{tip} + eV_{CPD} \quad (2.7)$$

So, lower value of V_{CPD} eventually signifies the lower work function.

In this thesis, KPFM technique have been employed to determine the local work function of the samples by ex-situ atomic force microscopy (AFM, Asylum Research, MFP-3D) in lift mode (lift height ≈ 50 nm) using conductive Ir/Pt-coated tips with a resonant frequency of ≈ 75 kHz and force constant of ≈ 2.8 N-nm⁻¹ [10, 28].

2.4 Applications

We have employed as-grown MoO₃, Ag-MoO₃ and MoO₂ samples towards potential applications, such as, electron field emitters, UV visible light photodetector applications, and robust SERS template for the detection of low concentration dye-molecules, which have been covered in this thesis work. In this section, the working principles and instrumentations about

the major measurement/applications techniques/machineries utilized for the above purposes will be discussed.

2.4.1 Field emission (FE)

Electron emission is the emission of electrons from the surface of a material induced by external energy/field to the electrons in the material. Emission of electrons from a material can be accomplished by various ways. Depending upon the type of external energy source, the process can be categorized as photoemission, thermionic emission, secondary electron emission and field emission (FE) etc. where light, heat (therm), energetic electrons and electric field are applying as external energy sources respectively. This phenomenon is most frequently observed in metals as there are more free electrons and in some semiconductors also. It is much known to all that the minimum energy, required to remove an electron from the Fermi level in a metal to a point an infinite distance away from the surface is known as the work function of that surface [34]. In this thesis, we have focused only on the electron field emission (EFE) of MoO_3 and Ag-MoO_3 materials. A relevant electron emission mechanism theory will be discussed in brief, where emission is taking place solely under the influence of an electric field.

Fowler-Nordheim Model:

The electron field emission (EFE) mechanism is based on quantum mechanical tunneling mechanism. It was first observed in 1897 by Wood [35] but was first explained correctly by R. Fowler and L. Nordheim in 1928 [36]. Fowler-Nordheim (F-N) explained that electrons are emitted as they tunnel through a potential barrier that is lowered and narrowed because of the presence of intense electric fields and they derived the emission current density. The Fowler-Nordheim (FN) Model [37] described the electron emission from metals in vacuum under high electric field is based on these following assumptions:

- (1) The metal is at 0 K.
- (2) The free electron approximation applies inside the metal.
- (3) The surface is treated to be smooth (compared to width of the potential barrier small roughness was neglected) and
- (4) The effective potential barrier close to the surface in the vacuum region is a combination of image charge potential and potential due to external electric field.

Especially for metal, the electrons are assumed to have a constant effective potential energy - W_a . Then, in presence of an electric field (E), the potential barrier is described by [38]

$$V(x) = -W_a \quad \text{where } x < 0 \quad (2.8)$$

$$= -e^2/4x - eFx \quad \text{where } x > 0 \quad (2.9)$$

Figure 2.19(a) shows the one-dimensional potential energy barrier faced by an electron inside the metal, near the surface. To investigate the emission properties of the samples, FE behavior (J vs. E) can be enumerated theoretically by simplified FN equation [36]

$$J = (A\beta^2 E^2 / \Phi) \exp(-B\Phi^{3/2} / \beta E) \quad (2.10)$$

$$\text{Or, } \ln(J/E^2) = \ln(A\beta^2 / \Phi) - (B\Phi^{3/2} / \beta) \times (1/E) \quad (2.11)$$

where, J is the FE current density ($\mu\text{A}/\text{cm}^2$), E is the applied electric field (V/μ), A and B are constants with $A = 1.54 \times 10^{-6} \text{ A-eV}/\text{V}^2$ and $B = 6.83 \times 10^3 \text{ eV}^{-3/2} - \text{V}/\mu\text{m}$, β is the field enhancement factor (FEF) and Φ is the work function (eV) of the emitter [10]. B depends on several parameters like, geometry of the emitter (such as dimension and shape, aspect ratio etc.), emitter's surroundings and also shape and distance of the counter electrode. β can be calculated by plotting the $\ln(J/E^2)$ vs. $(1/E)$ (called as F-N plot) and finding the slope and using the mathematical expression below

$$\beta = -6830 \times (\Phi)^{3/2} / \text{slope} \quad (2.12)$$

So, smaller slope value correspond higher FEF (β) value [10]. Schematic representation of FE phenomena from a sample is shown in Figure 2.19(b).

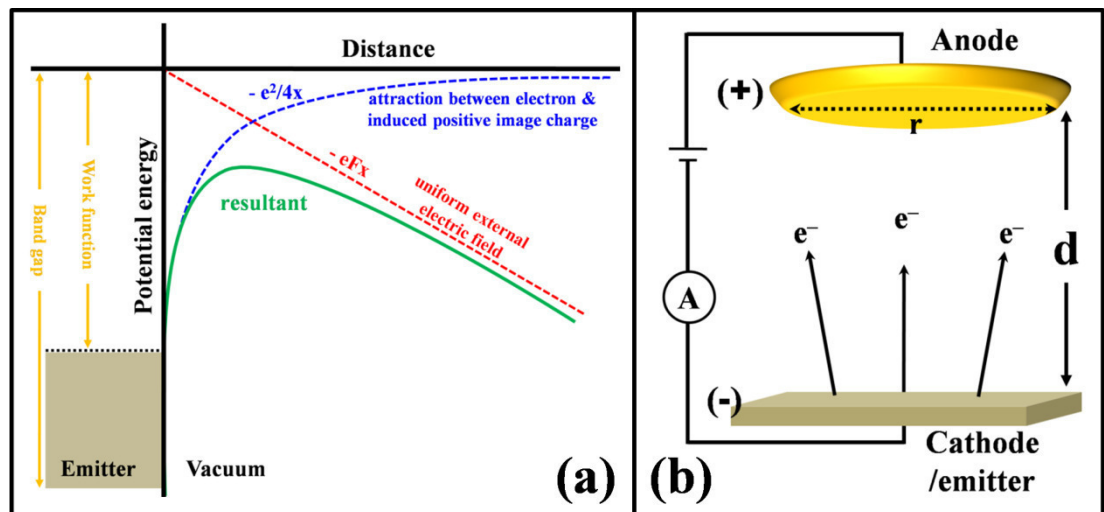


Figure 2.19: (a) 1D Potential energy barrier for an electron near a metal surface, (b) schematic representation of electron field emission (EFE) process, showing the emission of electron from an emitter.

In this thesis, field emission (FE) performances of the as-grown samples (called as emitters) were inspected in a diode configuration in a custom made high vacuum ($\approx 3.6 \times 10^{-7}$ mbar) chamber (Excel Instruments, FE System-150) and current vs. voltage (I-V) data were recorded using Keithley, 2410 as voltage source meter. The as-grown samples, fixed to the bottom plate with a copper tape were used as the cathodes and a copper plate having ≈ 2.5 mm tip diameter was served as the anode. For all FE measurements, electrodes separation was kept same ($\approx 70 \mu\text{m}$) [10].

2.4.2 Photodetector (I-V) characteristics

The current–voltage (I–V) and photoresponse characteristics of the heterojunction device (*p*-type MoO_2 nanostructured film/*n*-type Si) was recorded at room temperature using a Keithley semiconductor parameter analyzer (4200 SCS), along with a He–Cd laser (325 nm, 240 mW/cm^2) as UV light source and a broad band solar simulator (AM 1.5, 100 mW/cm^2) as white light illumination. The external quantum efficiency (EQE) of the device was measured using a Newport quantum efficiency/IPCE measurement system (QEPVSI-b) equipped with a built in lock-in amplifier, a monochromator and a broad band source [28].

2.4.3 Surface enhanced Raman spectroscopy/scattering (SERS)

Surface enhanced Raman scattering (SERS) is a well known effect, discovered in 1974 by M Fleishmann, P J Hendra and A J McMillan [39]. This technique has led to series of investigations on the optical characteristics of uneven surfaces of metal and adsorbates. If molecules are adsorbed on a plasmonic metal nanoparticle (NP) surface, the Raman scattering intensity can be extraordinarily enhanced and this effect is known as SERS. By this technique, even a single molecule can also be detected. The technique is becoming epidemic and is finding new and exciting arenas in diversified fields [40]. There are many approaches to enhance the Raman scattering intensity as Raman scattering has weak intensity; one approach that has been developed and applied successfully beside other approaches is the SERS technique. Even though the mechanism behind SERS phenomena has not been completely understood, it is generally believed that there are two fundamental mechanisms behind the enhancement: electromagnetic enhancement (EME) and chemical enhancement (CE). Van Duyne and Jeanmaire explained this enhancement in Raman signal in terms of

change of the electric field experienced by the molecules, and this phenomenon is known as electromagnetic enhancement (EME). At the same time, Albrecht and Creighton also reported that Raman scattering was enhanced by charge (electron) transfer or chemical bonding developed between the molecules and the metal substrate, which cause change in polarizability α . This enhancement mechanism named as chemical enhancement (CE). The EME results from the amplification of light by the excitation of localized surface plasmon resonances, in which the light concentration occurs preferentially in the gaps, crevices or sharp/nanoscale features (the metal surface's roughness feature) of plasmonic materials, while the CE modifies the electronic states of adsorbate because of chemisorption of analyte molecules. The electromagnetic effect takes the lead in enhancement (a factor of 10^6 – 10^{10}) whereas the chemical effect adds to the enhancement only one order or two orders of magnitude [41–44].

Electromagnetic enhancement (EME) mechanism:

The particle resulting from the quantization of the oscillation of the free electrons is known as plasmon. When the excitation is confined to the near surface region then it is called surface plasmon which can be localized on the surface of a spherical metal nanoparticle. Surface plasmon in conduction materials (noble metal) is formed due to rapid oscillation of their free electron density induced by incident light. In order to produce surface plasmon, the dielectric constant should be negative. When plasmon is restricted to surfaces and interacts strongly with electric field of incident light, a polariton is formed. If metal NPs are exposed to the incident light of proper wavelength, the oscillating electric field localized on the surface can cause the free electrons in the metal NPs to oscillate coherently. When the charged cloud of conduction electrons is oscillated away from the nuclear frame work of the NP, strong columbic attraction arises and forces the oscillation of the conduction electrons cloud back to the nuclear framework (Figure 2.20). This back and forth oscillation results in a large enhancement of electromagnetic field of the light at the surface of metal NP. This enhancement is possible, when the wavelength of the incident light and the Raman signal wavelength nearly match with the plasmon wavelength of metal NP. Then the resonance will occur and the enhancement will be maximized. The particle enhances the incident laser field as well as the Raman scattered field. For a spherical particle (radius \ll incident light wavelength), the field (induced at the sphere's surface) is related to the applied light (laser) by the equation

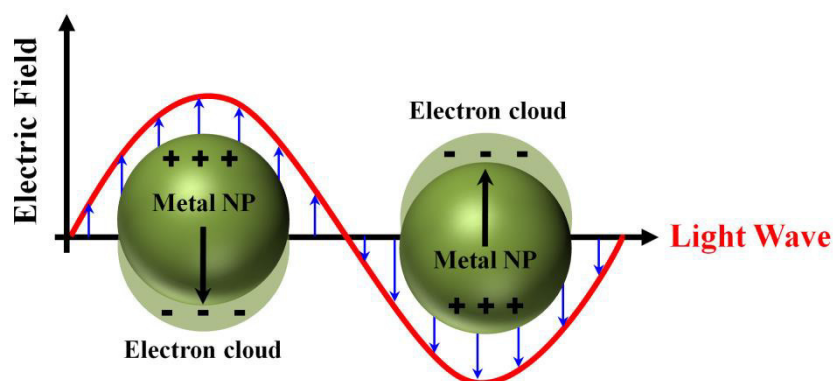


Figure 2.20: (b) Model of LSPR at the spherical nanoparticle surface.

$$E_{\text{induced}} = (\epsilon_1 - 2\epsilon_2) / (\epsilon_1 + 2\epsilon_2) E_{\text{light}} \quad (2.13)$$

where, E_{induced} and E_{light} represent for the electric or electromagnetic (EM) field induced on the surface and electric field of the excitation light. There, ϵ_1 and ϵ_2 are the complex dielectric function and relative permittivity of the surrounding media respectively. From the equation 2.13, resonance will occur when ϵ_1 equals $2\epsilon_2$. Excitation of the surface plasmon greatly enhances the local field experienced by a molecule which is adsorbed on the metal surface; the overall enhancement will be $\approx E^4$ [41–44].

In this thesis, surface enhanced Raman scattering (SERS) measurements were carried out using micro-Raman spectrometer having 2 cm^{-1} spectral resolution using 514 nm (green laser) excitation (power $\approx 40 \text{ mW}$). All SERS measurements were carried out in a backscattering geometry, using a $100\times$ microscope objective lens for focusing with a numerical aperture of 0.7 with a spot size of $\approx 2 \text{ }\mu\text{m}$. The molar concentrations of crystal violet (CV) having different concentrations ($1 \text{ }\mu\text{M}$, $2 \text{ }\mu\text{M}$ etc.) were prepared by dissolving the required amount of CV in ethanol. For each test, $\approx 10 \text{ }\mu\text{l}$ of the CV solution was dropped onto each of the SERS substrates and dried at room temperature.

2.5 References

- [1] G S May and C J Spanos, Fundamentals of Semiconductor Manufacturing and Process Control (John Wiley & Sons, Inc., 2006, ISBN: 10.1002/0471790281).
- [2] K L Chopra, Thin Film Device Applications (Springer, 1983, ISBN: 978-1-4613-3682-2).
- [3] C N R Rao, P J Thomas and G U Kulkarni, Nanocrystals: Synthesis, Properties and Applications (Springer, 2007, ISBN: 978-3-540-68751-1).

- [4] P Alvisato, *Science* **1996**, 271, 933.
- [5] C N R Rao, G U Kulkarni, P J Thomas and P P Edwards, *Chem. – Eur. J.* **2002**, 8, 28.
- [6] I L Maissel and R Glang, *Handbook of Thin Film Technology* (McGraw-Hill Book Co., 1970, ISBN: 007-0-39742-2).
- [7] D M Mattox, *Hand book of Physical Vapor Deposition (PVD) Processing* (Noyes Publications, 1998, ISBN: 978-0-8155-2037-5).
- [8] M Ohring, *Materials Science of Thin Films. Deposition and Structure* (Elsevier, Academic Press, 2002, ISBN: 978-0-12-524975-1).
- [9] P Guha, R R Juluri and P V Satyam, *Nucl. Instr. Meth. Phys. Res. B* **2017**, 409, 209.
- [10] P Guha, A Ghosh, R Thapa, E M Kumar, S Kirishwaran, R Singh and P V Satyam, *Nanotechnology* **2017**, 28, 415602.
- [11] P Guha, R R Juluri, A Bhukta, A Ghosh, S Maiti, S Bhattacharyya, V Srihari and P V Satyam, *CrystEngComm* **2017**, 19, 6811.
- [12] H O Pierson, *Handbook of Chemical Vapor Deposition Principles, Technology and Applications* (Elsevier, William Andrew, 1999, ISBN: 978-0-8155-1300-1)
- [13] J H Park and T S Sudarshan, *Chemical Vapor Deposition (Technology & Engineering*, 2000, ISBN: 978-1-61-503224-2).
- [14] W K Burton, N Cabrera and F C Frank, *Nature* **163**, 398, 1949.
- [15] P L Edwards and S Huang, *J. Am. Ceram. Soc.* **49**, 122, 1966.
- [16] D S Kim, R Scholz, U Gösele and M Zacharias, *Small* **4**, 1615, 2008.
- [17] P R Gardner, *Mater. Des.* 1987, 8, 210.
- [18] M A Nastasi and J W Mayer, *Ion Implantation and Synthesis of Materials* (Springer, 2003, ISBN: 978-3-540-45298-0).
- [19] J Mayer and E Rimini, *Ion Beam Handbook for Material Analysis* (Elsevier, Academic Press, 1977, ISBN: 978-0-323-13986-1).
- [20] D B Williams and C B Carter, *Transmission Electron Microscopy: A Textbook for Materials Science* (Springer, 2009, ISBN: 978-0-387-76500-6).
- [21] J C H Spence, *High-resolution Electron Microscopy* (Oxford Science Publications, 2013, ISBN: 978-0-199-66863-2).
- [22] B Fultz and J Howe, *Transmission Electron Microscopy and Diffractometry of Materials* (Springer, 2005, ISBN: 978-3-642-29761-8).
- [23] M. Knoll and E Ruska, *Z. Physik.* **78**, 318, 1932.
- [24] R F Egerton, *Physical Principles of Electron Microscopy, An Introduction to TEM, SEM, and AEM* (Springer, 2005, ISBN-13: 978-0387-25800-0).

- [25] L A Giannuzzi and F A Stevens, *Introduction to Focused Ion Beams: Instrumentation, Theory, Techniques and Practice* (Springer Press, 2004, ISBN: 978-0-387-23116-7).
- [26] C Suryanarayana and M G Norton, *X-Ray Diffraction: A Practical Approach* (Springer, 1998, ISBN: 978-1-4899-0148-4).
- [27] <https://pf18b.neocities.org> (User Manual 1 for BL-18 B (Indian Beam line) at Photon Factory).
- [28] P Guha, A Ghosh, A Sarkar, S Mondal, S K Ray, D K Goswami and P V Satyam, **2017** (to be submitted).
- [29] J F Watts and J Wolstenholme, *An Introduction to Surface Analysis by XPS and AES* (Wiley & Sons, 2005, ISBN: 978-0-470-86793-8).
- [30] A Einstein, *Ann. Physik* **1905**, 322, 132.
- [31] C V Raman and K S Krishna, *Nature* **121**, 501, 1928.
- [32] R L McCreery, *Raman Spectroscopy for Chemical Analysis* (John Wiley & Sons, New York, 2000, ISBN: 978-0-471-72164-2).
- [33] W Melitz, J Shen, A C Kummel and S Lee, *Surf. Sci. Rep.* **2011**, 66, 1.
- [34] J I Gersten and F W Smith, *The Physics and Chemistry of Materials* (Wiley, 2001, ISBN: 978-0-471-05794-9).
- [35] R W Wood, *Phys. Rev. (Series I)* **1897**, 5, 1.
- [36] R H Fowler and L Nordheim, *Proc. R. Soc. London, Ser A* **1928**, 119, 173.
- [37] A G J V Oostrom, *Validity of the Fowler-Nordheim Model for Field Electron Emission* (Netherland Philips Research Laboratories, 1966).
- [38] E L Murphy and R H Good, *Phys. Rev.* **1956**, 102, 1464.
- [39] M Fleischmann, P J Hendra and A J McQuillan, *Chem. Phys. Lett.* **26**, 163, 1974.
- [40] P L Stiles, J Dieringer and R P Van Duyne, *Annu. Rev. Anal. Chem.* **1**, 601, 2008.
- [41] D L Jeanmaire and R P Van Duyne, *J. Electroanal. Chem.* **84**, 1, 1977.
- [42] M G Albrecht and J A Creighton, *J. Am. Chem. Soc.* **99**, 5215, 1977.
- [43] A Campion and P Kambhampati, *Chem. Soc. Rev.* **27**, 241, 1998.
- [44] B J Marquis, A D McFarland and C L Haynes, *Anal. Chem.* **80**, 3431, 2008.

Chapter 3

In-situ Synchrotron X-ray Diffraction Study of Coherently Embedded Silver Nanostructures Growth in Silicon

3.1 Introduction

This chapter is devoted on silver nanoparticles embedded inside oxide layer (GeO_x) on a silicon substrate. Though the earlier work on the endotaxial Ag nanostructure growth was reported, the formidable task of carrying out real time and in-situ measurements were necessary to shed a light on endotaxial growth. Here, we report on real time in-situ growth of coherently embedded silver nanostructures by performing the growth through chemical vapor obtained from evaporation of Ag of a silver wire under ambient condition during synchrotron based high-temperature X-ray diffraction (XRD) measurements. Besides reporting on the direct evidence for crystalline growth of endotaxial Ag nanostructures, this work also presents the determination of thermal expansion coefficient of Ag nanostructures in a matrix. A ≈ 17 nm thick GeO_x film was grown on native oxide covered silicon substrates ($\text{GeO}_x/\text{SiO}_x/\text{Si}$) using a physical vapor deposition (PVD) method, that were used as substrates for Ag nanostructures growth. For growing Ag nanostructures, silver wires were kept on the specimen hot stage (chemical vapor deposition) along with the above substrates. All the in-situ growth and real time XRD were done under atmosphere conditions. The lattice constant of Ag nanostructures obtained from ex-situ growth specimens were used to compare with the real time - high temperature XRD measurements. As the temperature is increased from room

The work presented in this chapter has been published as P Guha et al., *CrystEngComm* **2017**, 19, 6811.

temperature to 850 °C while performing in-situ growth, the evolutions of various diffraction peaks such as (200), reflecting from growth facets of Ag nanostructures were monitored. By measuring the deviation of Ag lattice parameter due to shift in diffraction peak positions as a function of temperature, thermal expansion coefficients for Ag nanostructures in a matrix has been determined. Thermal expansion coefficient found to decrease from $1.9 \times 10^{-5} / ^\circ\text{C}$ to $1.82 \times 10^{-5} / ^\circ\text{C}$ with the increase of annealing temperature from 750 °C to 850 °C [1].

Nanoscience and nanotechnology are the most extensively exploited terms in the modern science [2, 3]. In nano regime, surface to volume ratio is very high, so the properties of nanostructures (NSs) differ significantly compared with the bulk; the surface (rather the size) plays a crucial role into the properties of the nanomaterial [4, 5] such as melting temperature [6], structural stability [7], thermal expansion coefficient [8–10] electronic structures [4], elasticity [9], activation energy [11] etc. A systematic *real-time* and *in-situ* study on the growth of coherently embedded Ag nanostructures in single crystalline silicon matrix and determining the thermal expansion coefficients of silver are the main emphasis on this report. Novelty in this report is the in-situ growth in ambience using a simple heating stage and real time X-ray diffraction characterizations at a synchrotron beam line experiment. Ex-situ growth was carried out separately and after several days, XRD and electron microscopy measurements were done at room temperature to determine the lattice constant of embedded Ag structures.

Metal nanoparticle on semiconductor matrix is widely studied system in the literature [12–15]. Metals on semiconductors play a vital role in semiconductor industry due to their wide applications [13, 16–19]. Metallic layers buried in single-crystal semiconducting substrates have potential in a variety of applications, such as, metal based transistors [20], microstrip line [21], substrates for surface enhanced Raman spectroscopy (SERS) [13], infrared sensors [22] etc. The most important requirement in silicon technology is high density integration of down-scaled devices into a full wafer; the primary goal of nanofabrication should be compatibility of atomically controlled fabrication with wafer scale processing. For this reason, a *self-assembly* process is promising for future nanostructure systems [23]. Energetics at the surface and interfaces play an important role in nucleation and growth process of *self-assembly*. Epitaxial process refers to the growth of a crystalline over layer on a crystalline substrate. It is known that the self-assembly process of epitaxial growth is governed by the surface and interfacial energies of over layer and the substrate along with the lattice mismatch [24, 25]. Usually, in-situ reflection high energy electron diffraction and scanning tunneling microscopy measurements carried out during epitaxial growth carried

under ultra-high vacuum conditions in a molecular beam epitaxy systems, showed that three types of growth are possible: layer by layer, layer plus island and island growth [26, 27]. The coherent growth of nanostructures inside a crystalline matrix is generally known as endotaxy. In our earlier reports, we have presented detailed work on the ex-situ growth of such Ag endotaxial structures in silicon matrix along with plausible growth mechanism [28–31]. Unlike epitaxial systems, endotaxial systems can be grown under ambient conditions. Hence, this allowed us to report a real time growth of these Ag endotaxial structures by using a simple hot stage for both the generation of Ag vapors and providing temperature for silicon substrates.

3.2 Experimental

Commercially available n-type silicon substrates with orientation (100) were cleaned by using acetone and methanol in an ultrasonic bath. On such silicon surfaces, $\approx 2\text{--}3$ nm thick native oxide (SiO_x) is present. Following the cleaning, a thin layer of GeO_x (≈ 17 nm) was deposited at room temperature on these cleaned Si substrates using physical vapor deposition system (chamber base pressure $\approx 2.9 \times 10^{-6}$ mbar). The GeO_x layer plays an important layer by providing disassociation reaction with SiO_x and helping the Ag diffusion to form endotaxial nanostructures; this mechanism was reported in our ex-situ results [28–31]. In-situ XRD experiments were carried using a heating stage (M/S Anton Paar GmbH) under ambient condition at Indian Beam line 18B, Photon Factory, KEK, Japan.

In-situ XRD experiments were accomplished by keeping the GeO_x deposited specimen (i.e., ≈ 17 nm $\text{GeO}_x/\text{SiO}_x/\text{Si}(100)$) and by placing two silver wires of ≈ 5 mm length besides the substrate on the heating stage; this is schematically shown in Figure 3.1(a). This particular system, where silver wires were used as source for Ag vapors, is termed as *in-situ CVD case*. The procedural steps followed in the ramping the temperature and equilibrium temperatures are shown in Figure 3.1(b). The XRD patterns were collected once a stable temperature was arrived. A ramping rate of ≈ 7 °C/minute was used to arrive high temperatures. The XRD measurements were performed using an X-ray wavelength of 0.8587\AA . It is to be noted that, for this *in-situ case*, the source of Ag for endotaxial structures in silicon is the vapors produced by the hot Ag wires kept on the heating stage. In-situ experiment has been carried out in atmospheric condition. It should be noted that disassociation reaction does not occur at high vacuum conditions as reported earlier [28–31].

Ex-situ measurements were done to determine the lattice parameters of endotaxial silver structures that were annealed at high temperatures (750 °C, 800 °C, and 850 °C) separately. Here, *ex-situ* means, for example, first the substrates were heated at 750 °C, then cooled to room temperature and then XRD measurements were carried out. While in the *in-situ* measurements, the temperature raised to specific temperature (say 750 °C) and then kept at this temperature for 30 minutes; after this equilibrium process of time, XRD measurements were carried when the substrate is at 750 °C, (samples kept on hot stages during XRD measurements).

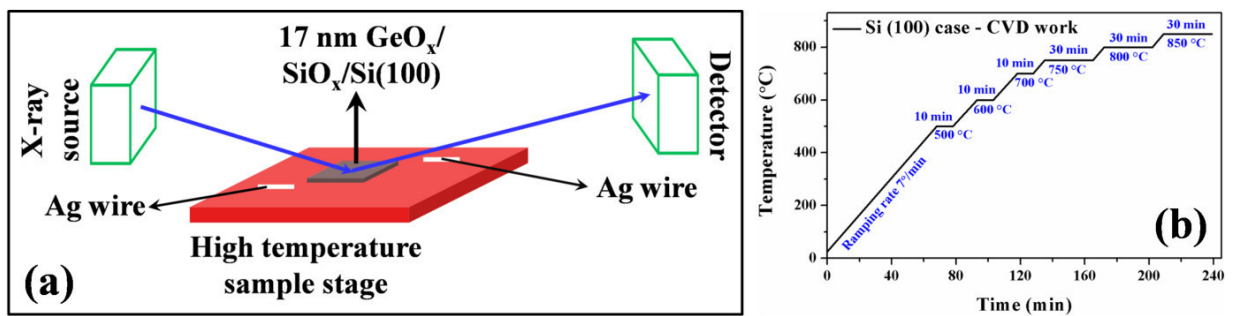


Figure 3.1: (a) Schematic representation for in-situ annealing and cooling of 17 nm GeO_x/SiO_x/Si(100) sample with two silver wires kept close to the sample. (b) Schematic diagram of the experimental procedure followed during annealing.

The high resolution transmission electron microscopy (HRTEM) with 200 keV electrons (JEOL JEM-2010) and field emission gun based scanning electron microscopy (FEG-SEM) with 20 keV electrons (Neon 40 cross-beam system, M/S Carl Zeiss GmbH) have been used to characterize the sample before and after the in-situ experiments. For TEM characterizations, both planar and cross-sectional TEM specimens have been prepared mechanically, followed by ion milling process with low energy Ar ions (Ar⁺) (conventional method).

3.3 Results and discussion

Figure 3.2 shows the cross-sectional TEM micrographs of the 17 nm GeO_x/SiO_x/Si(100) as-deposited sample, depicting \approx 17 nm amorphous GeO_x layer on crystalline silicon (having \approx 2-3 nm amorphous native oxide SiO_x of Si). The graphic of experimental procedure followed during in-situ experiment for CVD case is demonstrated in

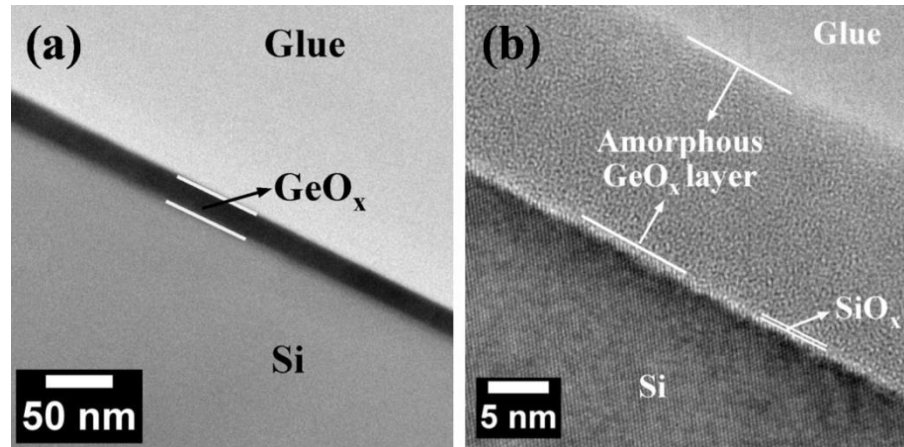


Figure 3.2: (a) Low magnification and (b) high resolution cross-sectional TEM images of 17 nm $\text{GeO}_x/\text{SiO}_x/\text{Si}(100)$.

Figure 3.1(a). The specimen (i.e., 17 nm $\text{GeO}_x/\text{SiO}_x/\text{Si}(100)$) was kept on the heating stage of XRD goniometer and two silver wires were put besides the substrate on the same heating stage as shown in Figure 3.1(a). Figure 3.1(b) shows the experimental procedure followed during the annealing of the sample. No silver peak was observed before 700 °C; a very less intensity peak at $\theta \approx 11.97^\circ$ corresponding to Ag(200) was appeared around $\approx 700^\circ\text{C}$ (Figure 3.3(a)). It is well known to all that, bulk face centered cubic (FCC) crystal systems have minimum energy for (111) orientation [32]. Even though, the lowest energy is for the formation of planes (111) (as silver has FCC crystal structure), no Ag(111) peak was found; only (200) peak was observed. As the temperature increases, intensity of Ag(200) peak is also

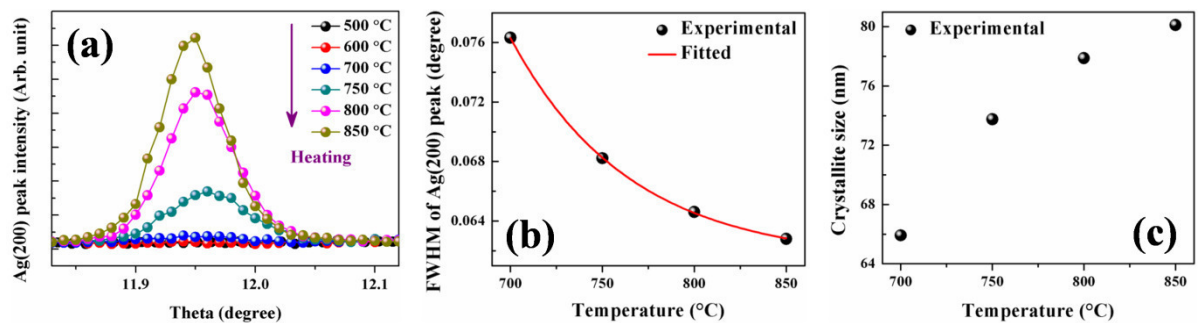


Figure 3.3: (a) Temperature evolution of Ag(200) peak during heating; (b) plot of full width half maxima (FWHM) of Ag(200) peak versus temperature; (c) variation in crystallite size of Ag with temperature.

increasing. Interestingly, we found that the Bragg peaks shifted toward the lower θ values. At higher temperatures, more Ag vapors are generated from the wires and hence more Ag could

be seen along (200) direction. It is also observed that the full width half maxima (FWHM) of Ag(200) is found to decrease with the increase in temperature (see Figure 3.3(b)). Using the FWHM values, the variation of crystallite size for silver structures was determined by Scherrer formula [33] as given below:

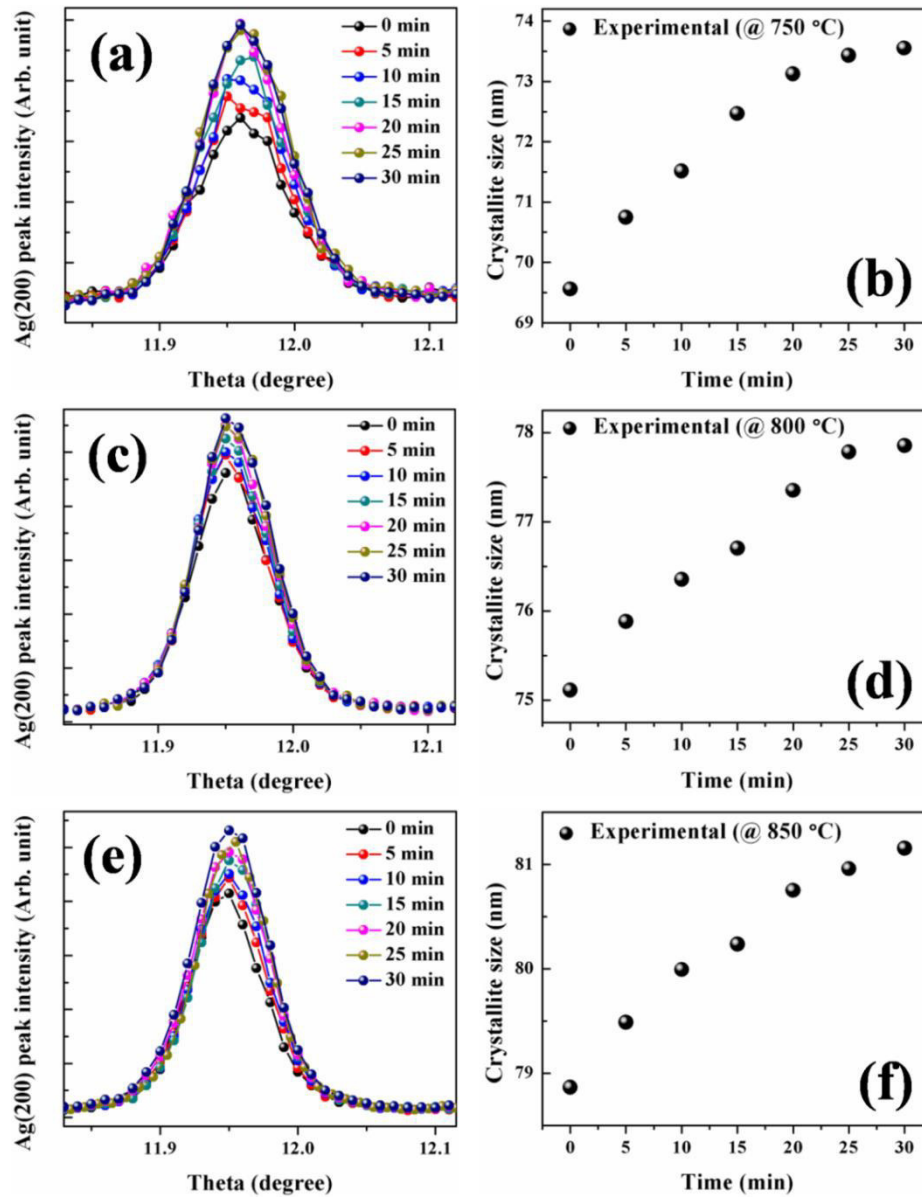


Figure 3.4: Time evolution of the Ag(200) peak at (a) 750 °C, (c) 800 °C and (e) 850 °C; corresponding crystallite size of Ag with respect to stabilization time at (b) 750 °C, (d) 800 °C and (f) 850 °C.

$$\text{Crystallite size} = K\lambda / \{(\cos\theta) \times (\text{FWHM})\} \quad (3.1)$$

where, K is a dimensionless shape factor (close to unity), λ is the X-ray source wavelength, FWHM: full width half maxima (in radian) and θ : Bragg angle (degree). Figure 3.3(c) depicts

the variation of crystallite size as a function of temperature. As temperature increases, more number of silver atoms are available for the diffusion through active reaction front in the GeO_x and SiO_x combination. Figures 3.4(a), 3.4(c) and 3.4(e) show the time evolution of the

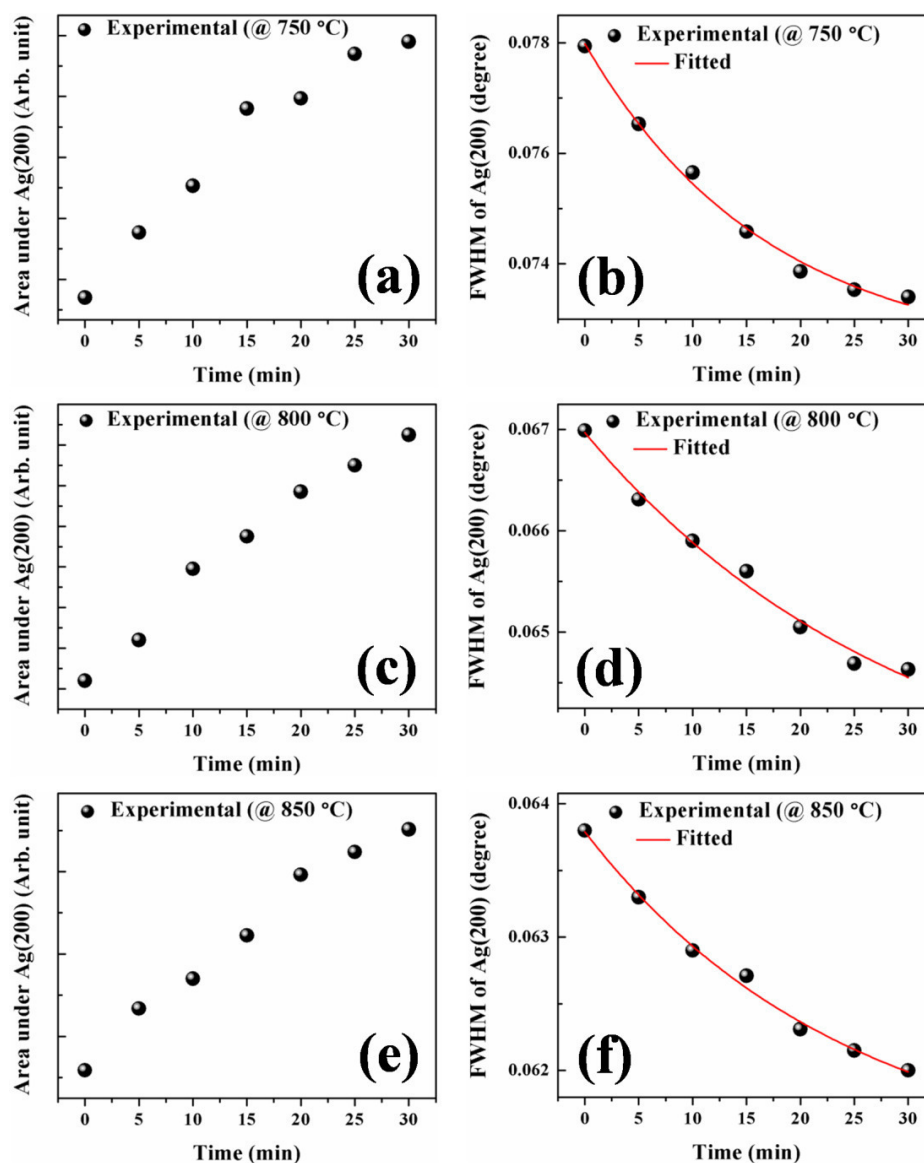


Figure 3.5: Area under Ag(200) peak with respect to stabilization time at (a) 750 °C, (c) 800 °C and (e) 850 °C; corresponding FWHM of Ag(200) peak with respect to stabilization time at (b) 750 °C, (d) 800 °C and (f) 850 °C.

Ag(200) peak for 30 min (with 5 min interval) at 750 °C, 800 °C and 850 °C, respectively; intensity of the peak is increasing with time as more Ag NPs appeared to follow the more ordered structures. At higher temperatures, two factors play a key role in increasing the crystallite size: (a) reactivity of GeO_x and SiO_x layers and (b) increased amount of Ag

content. The variation in crystallite size with time at different temperatures, 750 °C, 800 °C and 850 °C has also been evaluated by using Scherrer formula³² and is shown in Figures 3.4(b), 3.4(d) and 3.4(f) respectively. As the equilibrium temperature is reached at 750 °C, the endotaxial structures formation was observed with a crystallite size of ≈ 69.5 nm and this increases to a value of ≈ 73.5 nm after 30 min. Similar incremental changes towards higher crystallite sizes are found for 800 °C (≈ 75.1 nm to ≈ 77.9 nm) and at 850 °C (≈ 78.8 nm to ≈ 81.3 nm). The rate of increases is not very significant but a positive slope of increase of crystallite is evident. Figures 3.5(a), 3.5(c) and 3.5(e) show the area under Ag(200) peak with respect to stabilization time at 750 °C, 800 °C and 850 °C respectively. Corresponding FWHM of Ag(200) peak with respect to stabilization time at 750 °C, 800 °C and 850 °C are represented in Figures 3.5(b), 3.5(d) and 3.5(f) respectively. Initially FWHM values for every cases were decreasing rapidly and later FWHM values were not decreasing significantly. A plausible mechanism for the formation of substrate-orientation dependent endotaxial silver structures (ex-situ studies) was reported earlier by our group [28–31]. Since we are considering (100) oriented Si substrate in this particular case, we could observe only the Ag(200) peak. After completing the in-situ experiment, the sample has been checked from electron microscopy observations. Figures 3.6(a) and 3.6(b) represent the high magnification SEM and low magnification cross-sectional TEM images of the sample after in-situ annealing respectively; mostly square shaped embedded Ag nanoparticles are formed, which supports the formation of substrate symmetric endotaxial silver nanostructures on silicon substrate. Formation of endotaxial silver nanostructures had also been confirmed by X-ray energy-dispersive spectrometry (EDS) elemental mapping in STEM mode, which was already

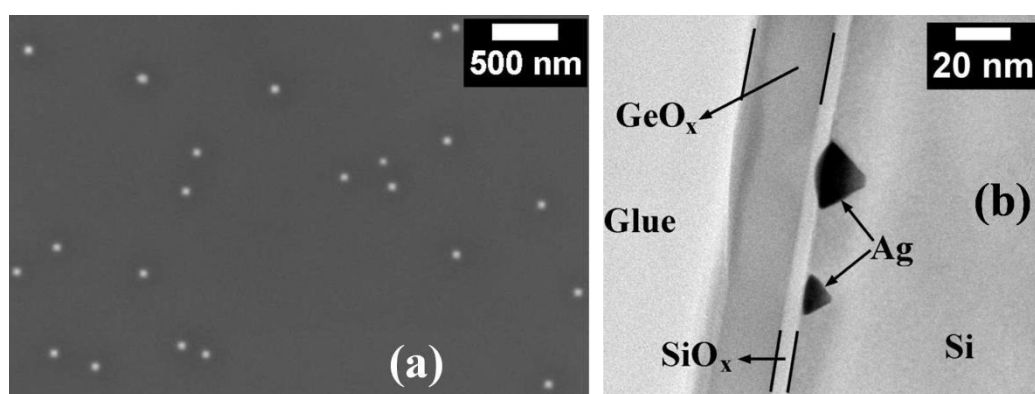


Figure 3.6: (a) and (b) High magnification SEM image and cross-sectional TEM image of the sample after in-situ annealing, confirming the formation of endotaxial silver nanostructures.

reported [29]. To the best of our knowledge, no reports were found on the in-situ and real time characterization of coherently embedded nanostructures. The effect of availability of the atomic Ge plays a crucial role in the formation of these endotaxial nanostructures by studying the effect of the ambient conditions on these structures formation [31]. Removal of native oxide takes place at a temperature of around 750 °C by the following mechanism



But the presence of transition metal particles enhances desorption of SiO₂ via laterally inhomogeneous growth of voids in the oxide layer [34, 35], which will lower the reaction temperature.

3.3.1 Effects of temperature and crystallite size on thermal expansion coefficient (TEC)

Pathak and Shenoy carried out theoretical calculation for the size dependence of the coefficient of thermal expansion of nanostructures and predicted that the fractional change in the CTE from the bulk value scales inversely with the size of the nanostructure [8]. W Li et. al., reported decrease in lattice parameter at higher temperatures (for TiO₂ nanoparticles) for particle size from 12 to 23 nm [11]. For higher particle sizes (> 30 nm), the thermal coefficient expansion remains constant [36, 37]. In the following section, the thermal expansion coefficient (TEC) of embedded silver structure during their growth process will be studied. Substantial shifting of peak position towards lower θ was observed. We had discussed about the variation in crystallite size and shown in Figures 3.3(c). It is interesting to discuss about the variation in the lattice parameters of nanostructures with focus on two parameters: their temperature and crystallite size. To interpret the argument, high resolution XRD measurements at room temperature for Ag(200) peak have been performed on three samples 2 nm Ag/17 nm GeO_x/SiO_x/Si(100) separately annealed at 750 °C, 800 °C, and 850 °C under ambient conditions and presented in Figure 3.7(a). Now onwards, we will refer these measurements as *ex-situ* (by growing endotaxial structures first and then left them for long days). Figure 3.7(b) depicts the $d_{(200)}$ of silver nanostructures vs corresponding crystallite size (calculated from Figure 3.7(a) by using equation 3.1) for these three samples; $d_{(200)}$ is close to bulk value, though the crystallite size of silver is varied. It is interesting to note that, for these Ag nanostructures, no significant deviation from bulk Ag values was found. Due to this reason, we could attribute the variation of lattice parameter to the tempera-

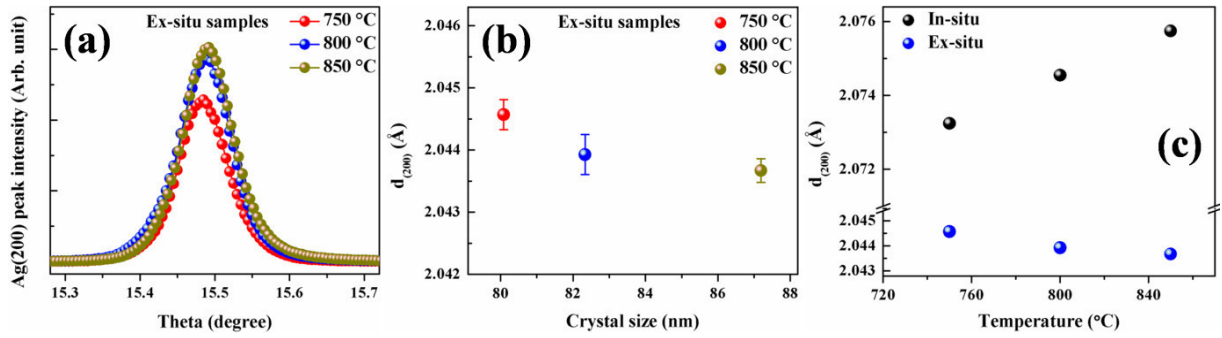


Figure 3.7: (a) Ag(200) peak intensity of 2 nm Ag/GeO_x/SiO_x/Si(100) annealed at three different temperatures 750 °C, 800 °C, 850 °C (ex-situ case). (b) Corresponding crystallite size dependent $d_{(200)}$ of silver. (c) Plot of $d_{(200)}$ vs. T all together (in-situ and ex-situ cases).

-ture effect only and hence we could neglect the size effects. Lattice constant of Ag was calculated at each temperature from the corresponding peak positions of Ag(200) for these two cases *in-situ* and *ex-situ* cases and depicted in Figure 3.7(c) all together. From this figure, it is clear that the ex-situ XRD measurements (error bars are within the data points) show no significant change in lattice parameter (corresponding to the bulk value ($d_{\text{Ag}(200)} \approx 2.045 \text{ Å}$ at 25 °C)). We have also tried to correlate the real silver nanoparticle size (from SEM observations) with the estimated crystallite size from the XRD data (by employing the Scherrer formula). To do so, the ex-situ SEM images of endotaxial Ag nanostructures formed at 750 °C and 800 °C are shown in Figures 3.8(a) and 3.8(c) respectively. Figures 3.8(b) and 3.8(d) depict corresponding size distribution histograms of Ag nanostructures. From Table 3.1, it is quite evident that change in the lattice parameter with the crystallite size for ex-situ samples is negligible. For further discussion on the thermal expansion coefficient, we define two parameters, Δd and ΔT , as given below:

$$\Delta d = [d(T \text{ in } ^\circ\text{C}) - d(25 ^\circ\text{C})] \quad (3.3)$$

Table 3.1: Real particle size (from SEM images), crystallite size (from Scherrer formula) and $d_{(200)}$ of silver structures at different temperatures for all the cases (in-situ and ex-situ cases).

Temperature (°C)	Real particle size (nm)	Crystallite size from Scherrer formula (in-situ) (nm)	Crystallite size from Scherrer formula (ex-situ) (nm)	$d_{(200)}$ (Å)	
	Ex-situ case	In-situ case		In-situ	Ex-situ
750	47±17	73.757	80.086	2.0732	2.0446
800	57±16	77.873	82.331	2.0746	2.0439
850	-	80.117	87.191	2.0758	2.0438

$$\Delta T = T (^{\circ}\text{C}) - 25 ^{\circ}\text{C} \quad (3.4)$$

where, Δd is the change in inter-planar spacing correspond to Ag(200) at T(in $^{\circ}\text{C}$) with respect to inter-planar spacing obtained from the bulk lattice constant of Ag at 25 $^{\circ}\text{C}$ and ΔT = change in temperature with respect to 25 $^{\circ}\text{C}$ (considering the value of d (25 $^{\circ}\text{C}$) = 4.09 \AA).

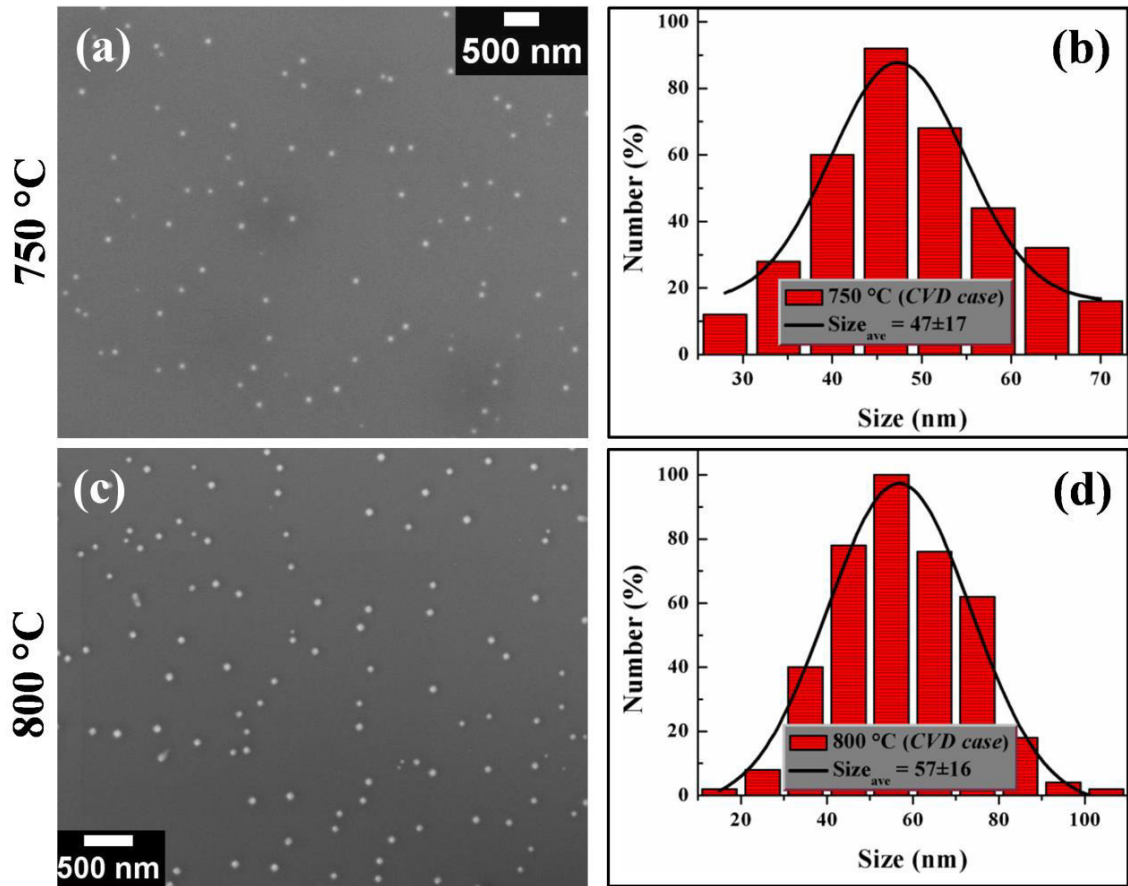


Figure 3.8: Typical SEM images of endotaxial Ag nanostructures formed at (a) 750 $^{\circ}\text{C}$ and (c) 800 $^{\circ}\text{C}$ and corresponding size distribution of endotaxial Ag nanostructures formed at (a) 750 $^{\circ}\text{C}$ and (c) 800 $^{\circ}\text{C}$.

The slope of $\Delta d/d$ versus ΔT would result in obtaining the value of TEC (α) for embedded silver structures. Figure 3.9(a) represents the plot of $\Delta d/d$ versus ΔT for *in-situ* case, revealing the linear dependence with ΔT . From the slope of linear fitting of the plot, the TEC of silver yields $1.2 \times 10^{-5}/^{\circ}\text{C}$ for this case, which differs from its bulk value ($1.9 \times 10^{-5}/^{\circ}\text{C}$). Here, the temperature dependent TEC have also been worked out. The TEC is expressed as:

$$\text{TEC } (\alpha) = \frac{\Delta d/d}{\Delta T} \quad (3.5)$$

where, Δd and ΔT are already defined above. One can calculate α at different ramping temperature and plot α with temperature. Figure 3.9(b) shows temperature dependent TEC

plot; the calculated TEC of silver is decreasing from $1.9 \times 10^{-5}/^{\circ}\text{C}$ to $1.82 \times 10^{-5}/^{\circ}\text{C}$ with the increase of annealing temperature from 750°C to 850°C . Furthermore, we have determined the activation energy (minimum energy required for growing the silver nanostructures). To do this task, we fitted the FWHM of Ag(200) peak vs temperature plot with exponential decay, shown early in Figure 3.3(b) for *in-situ* case. Assuming first order transition and based on the exponential decay fitting, the activation energy (E_0) can be calculated from the slope of the Arrhenius plot $\ln(\text{FWHM})$ vs $1/T$, where T is absolute temperature (in Kelvin) and k_B stands for Boltzmann constant ($k_B = 8.61 \times 10^{-5} \text{ eV/K}$). Figure 3.9(c) depicts the plot of $\ln(\text{FWHM})$ versus $1/T$ and the values of E_0 have come out to be $0.171 \pm 0.004 \text{ eV}$ for our case.

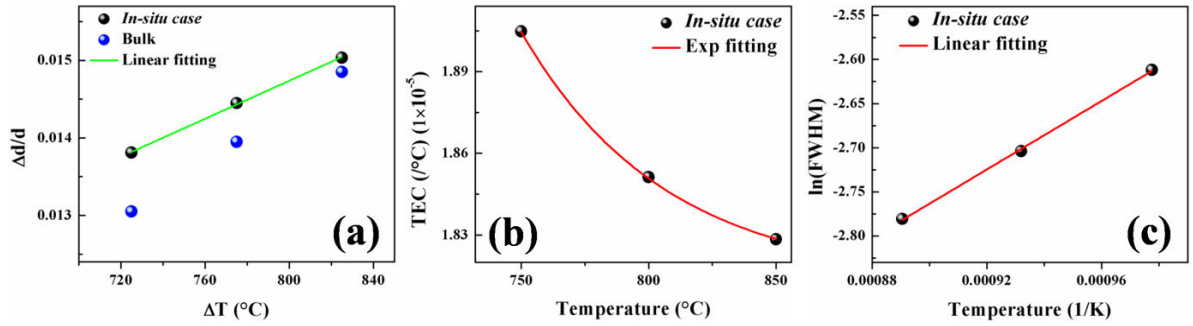


Figure 3.9: (a) Plot of $\Delta d/d$ versus ΔT (in-situ case); (b) corresponding temperature dependent TEC. (c) Plot of $\ln(\text{FWHM})$ versus $1/T$ (in-situ case).

3.4 Conclusion

The real time, in-situ XRD study for the growth of the endotaxial silver nanostructures using CVD method were performed successfully. The XRD reflection corresponding to Ag (200) was monitored as a function of growth temperature for endotaxial Ag nanostructures by determining the peak positions and their full width at half maxima (FWHM) values. With the increase of temperature, the FWHM of Ag(200) was decreasing and the position of the peaks were found to shift towards lower θ , corresponding to the increment in the effective lattice constant values and the reduction in thermal expansion coefficients (TECs) corresponding to Ag nanostructures. Here, the TECs go inversely with the growth temperature for this particular case. Crystallite size didn't contribute significantly. The temperature dependent TEC values were determined and found to vary from $\approx 1.9 \times 10^{-5}/^{\circ}\text{C}$ to $1.82 \times 10^{-5}/^{\circ}\text{C}$ with temperature from 750°C to 850°C . The activation energy (E_0) for the growth of silver nanostructures estimated to be $0.171 \pm 0.004 \text{ eV}$ for this case. Next

chapter, we will discuss the effect of ion irradiation on the growth of endotaxial nanostructures.

3.5 References

- [1] P Guha, R R Juluri, A Bhukta, A Ghosh, S Maiti, S Bhattacharyya, V Srihari and P V Satyam, *CrystEngComm* **2017**, *19*, 6811.
- [2] A P Alivisatos, *Science* **1996**, *271*, 933.
- [3] C Burda, X Chen, R Narayanan and M A El-Sayed, *Chem. Rev.* **2005**, *105*, 1025.
- [4] C N R Rao, G U Kulkarni, P J Thomas and P P Edwards, *Chem. Eur. J* **2002**, *8*, 28.
- [5] W Luo, W Hu and S Xiao, *J. Phys. Chem. C* **2008**, *112*, 2359.
- [6] Q Jiang, S Zhang and M Zhao, *Mater. Chem. Phys.* **2003**, *82*, 225.
- [7] C C Yang and S Li, *J. Phys. Chem. C* **2008**, *112*, 16400.
- [8] S Pathak and V B Shenoy, *Phys. Rev. B* **2005**, *72*, 113404.
- [9] X Y Zhou, B L Huang and T Y Zhang, *Phys. Chem. Chem. Phys.* **2016**, *18*, 21508.
- [10] W Yin Hai, Y Jingjing, Y Changhui, F Xiaosheng and Z Lide, *Nanotechnology* **2004**, *15*, 1437.
- [11] W Li, C Ni, H Lin, C P Huang and S I Shah, *J. Appl. Phys.* **2004**, *96*, 6663.
- [12] M Fujii, S Hayashi and K Yamamoto, *Jpn. J. Appl. Phys.* **1991**, *30*, 687.
- [13] O A Yeshchenko, I M Dmitruk, A A Alexeenko, M Y Losytskyy, A V Kotko and A O Pinchuk, *Phys. Rev. B* **2009**, *79*, 235438.
- [14] A Hilonga, J K Kim, P B Sarawade and H T Kim, *Appl. Surf. Sci.* **2009**, *255*, 8239.
- [15] K Awazu, M Fujimaki, C Rockstuhl, J Tominaga, H Murakami, Y Ohki, N Yoshida and T Watanabe, *J. Am. Chem. Soc.* **2008**, *130*, 1676.
- [16] P Christopher, H Xin and S Linic, *Nat. Chem.* **2001**, *3*, 467.
- [17] C Clavero, *Nat. Photon.* **2014**, *8*, 95.
- [18] R Jiang, B Li, C Fang and J Wang, *Adv. Mater.* **2014**, *26*, 5274.
- [19] A Ghosh, P Guha, S Mukherjee, R Bar, S K Ray and P V Satyam *Appl. Phys. Lett.*, **2016**, *109*, 123105.
- [20] J C Hensel, A F J Levi, T Tung and J M Gibson, *Appl. Phys. Lett.* **1985**, *47*, 151.
- [21] H Roskos, M C Nuss, W Goossen, D W Kisker and A E White, *App. Phys. Lett.* **1991**, *58*, 2604.

- [22] R W Fathauer, J M Ianelli, C W Nieh and S Hashimoto, *Appl. Phys. Lett.* **1990**, *57*, 1419.
- [23] T Ogino, H Hibino and K Prabhakaran, *J. Vac. Sci. Tech. B* **1996**, *14*, 4134.
- [24] A A Baski and H Fuchs, *Surf. Sci.* **1994**, *313*, 275.
- [25] P W Palmberg, T N Rhodin and C J Todd, *Appl. Phys. Lett.* **1967**, *10*, 122.
- [26] I. N. Stranski and L. Krastanow, *Akademie der Wissenschaften Wien* **1938**, *146*, 797.
- [27] I V Markov, *Crystal Growth for Beginners Fundamentals of Nucleation, Crystal Growth and Epitaxy* (World Scientific, 1995, ISBN: 981-238-245-3).
- [28] R R Juluri, A Rath, A Ghosh and P V Satyam, *J. Phys. Chem. C* **2013**, *117*, 13247.
- [29] R R Juluri, A Rath, A Ghosh, A Bhukta, R Sathyavathi, D N Rao, K Müller, M Schowalter, K Frank, T Grieb, F Krause, A Rosenauer and P V Satyam, *Sci. Rep.* **2014**, *4*, 4633.
- [30] P Guha, R R Juluri and P V Satyam, *Nucl. Instr. Meth. Phys. Res. B* **2017**, *409*, 209.
- [31] R R Juluri, A Ghosh, A Bhukta, R Sathyavathi and P V Satyam, *Thin Solid Films* **2015**, *586*, 88.
- [32] Y N Wen and J M Zhang, *Solid State Comm.* **2007**, *144*, 163.
- [33] P Scherrer, *Gött. Nachr.* **1918**, *2*, 98.
- [34] M Leih, H Dallopatra and J E Lewis, *Appl. Phys. Lett.* **1988**, *53*, 589.
- [35] H Dallopatra, M Leih and J E Lewis, *Phys. Rev. B* **1990**, *41*, 5075.
- [36] M Zhao and Q Jiang, *Key Eng. Mater.* **2010**, *444*, 189.
- [37] Y H Zhao and K Lu, *Phys. Rev. B* **1997**, *56*, 14330.

Chapter 4

Ion Beam Induced Endotaxial Silver Nanostructures in Silicon

4.1 Introduction

In previous chapter, we have discussed on real time and in-situ growth of endotaxial Ag nanostructures in silicon by performing growth through chemical vapor obtained from evaporation of Ag from a silver wire. In this current chapter, we are focusing on the ion irradiated effects of silver (Ag) ions on $\text{GeO}_x/\text{SiO}_x/\text{Si}$ system to exploit the nature of defects formed during irradiation for enhancing the Ag diffusion to form endotaxial nanostructures and the obtained results have been compared with un-irradiated systems to understand the role of defects in the formation of Ag endotaxial nanostructures. Here, the growth of silver (Ag) endotaxial structures in silicon using the aspects of both ion implantation and irradiation has been performed. In one case, endotaxial nanostructures of Ag at the Si interface are formed with 30 keV negatively charged silver ions (Ag^-) on $\text{GeO}_x/\text{SiO}_x/\text{Si}$ system. In another case, 30 keV Ag^- ions are used to create defects in GeO_x , SiO_x and in silicon substrate. Further deposition of a thin layer of Ag on irradiated $\text{GeO}_x/\text{SiO}_x/\text{Si}$ system yielded endotaxial Ag nanostructures relatively at lower temperature (700 °C) compared to the system without any irradiation effects. We will also reveal that the irradiation effects with 1.8 MeV Ag^+ ions do not influence the early onset temperature of endotaxial nanostructure formation (unlike low energy ions). Finally, we will show that it is essential to have crystalline silicon substrate to grow silver endotaxial nanostructures [1].

Nobel metal (Au, Ag, Pt) nanoparticles (NPs) are of great scientific significance in diverse technological applications, such as, optical, electrical and biological applications due to their plasmonic properties and large surface to volume ratio [2–5]. Among metal NPs, silver (Ag) shows highest electrical conductivity and is the best applicant for electrical characterization [6, 7]; Ag is also the leading candidate for detecting organic dye-molecules, bio-molecules via surface enhanced Raman spectroscopy (SERS) technique [8, 9]. Embedded Ag nanostructures are known to be efficient for detecting the dye-molecules via SERS technique [10, 11]. In general, nanomaterial synthesis and ion beam induced modification and their optical, electrical, magnetic properties have been studied [12–14]. Ion irradiation is used to generate variety of defects, which may induce structural deformation, phase change, strain etc., in the systems [15, 16]. Earlier, we studied on the growth of coherently embedded endotaxial Ag nanostructures (NSs) in ambient conditions using chemical vapor deposition (CVD) [17] and physical vapor deposition (PVD) [10] techniques *without any use of ion beams*. Earlier reports suggest that the energetic ion beams have been useful to grow embedded metal nanostructures [18–20]. In these studies, volatile nature of GeO_x and SiO_x and Ag diffusion through these layers has been exploited to fabricate various size and shapes of coherently embedded (i.e., endotaxial) Ag nanostructures in crystalline silicon substrate with various orientations. The Ag NSs grown using above methods were used as SERS substrates to detect sub-micro molar dye-molecule, such as, crystal violet (CV) [10, 11].

4.2 Experimental

Commercially available silicon substrates with (100) orientation were first ultrasonically cleaned with acetone and then with alcohol for 5 minutes, each. Three systems with variable thickness of GeO_x layers, viz., ≈ 15 nm, ≈ 50 nm and ≈ 70 nm were deposited on silicon substrates by using physical vapor deposition (PVD) technique (chamber pressure $\approx 1.2 \times 10^{-6}$ mbar during the growth) at room temperature. A thin native oxide (SiO_x) (≈ 2 – 3 nm) is found to be present on Si(100) substrates, which usually acts as a diffusion barrier for overgrown layers on silicon substrates. The 15 nm $\text{GeO}_x/\text{SiO}_x/\text{Si}(100)$ substrates were first irradiated with 1.8 MeV Ag ions at room temperature at a particular fluence, 1×10^{15} ions/cm² using the 3.0 MV pelletron accelerator facility at Institute of Physics, Bhubaneswar (IOPB), India. This system with 1.8 MeV Ag ions is termed as “*high energy irradiation system*”. In another set of experiments, irradiations on 15 nm, 50 nm and 70 nm $\text{GeO}_x/\text{SiO}_x/\text{Si}(100)$ (at

room temperature) under high vacuum conditions ($\approx 5 \times 10^{-7}$ mbar) were carried out with 30 keV Ag ions at two fluences: 5×10^{15} ions/cm² and 2×10^{16} ions/cm² using low energy ion implanter facility at IOPB. Hereafter, we will refer these systems as “*low energy irradiation systems*”. After both *high and low energy irradiations*, a Ag film of ≈ 2 nm thickness was deposited on the irradiated specimen using PVD system. In one set of irradiated specimen, no Ag film was deposited as this specimen is used to grow endotaxial nanostructures using 30 keV Ag implanted ions. To understand the onset temperature of the endotaxial formation, annealing was carried out at different temperatures (500 °C – 800 °C) for 30 min in ambient conditions.

Structural characterizations of all the samples have been carried out using field emission gun based scanning electron microscopy (FEGSEM) with 20 kV electrons (Neon 40 cross-beam system, M/S Carl Zeiss GmbH, Germany) and high resolution transmission electron microscopy (HRTEM) with 200 keV electrons (JEM-2010, JEOL, Japan). For TEM observations, both planar and cross-sectional TEM specimens were prepared using conventional methods where preliminary thinning was carried out using abrasive materials (mechanical process) followed by ion milling process with low energy Ar ions (Ar⁺).

4.3 Results and discussion

4.3.1 Un-irradiated system

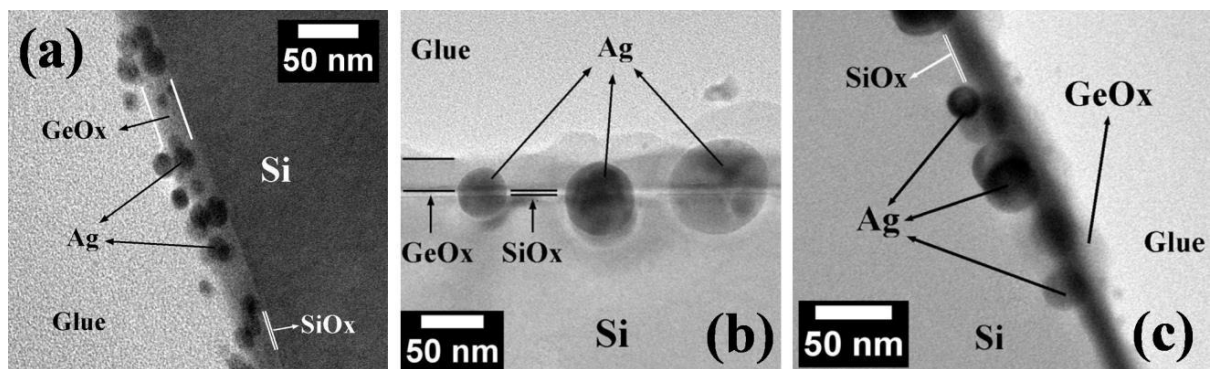


Figure 4.1: Cross-sectional TEM micrographs of 2 nm Ag/15 nm GeO_x/SiO_x/Si(100) (no irradiation) annealed at (a) 600 °C, (b) 650 °C and (c) 700 °C.

Un-irradiated specimen (2 nm Ag/15 nm GeO_x/SiO_x/Si(100)) were annealed at 600 °C, 650 °C and 700 °C at ambient conditions and corresponding cross-sectional TEM

micrographs are shown in Figures 4.1(a), 4.1(b) and 4.1(c). It is important to note that the substrate is crystalline in nature. No coherently embedded structures are seen on these systems even around 700 °C; however, only embedding of Ag nanostructures (and not endotaxy) could be seen at this temperature. However, annealing them at 800 °C would enable to form endotaxial structures as shown in earlier reports [10, 11]. Below, we will show that similar results obtained for high energy irradiation systems as well (i.e., no endotaxy even at 700 °C: see Figure 4.2) but with low energy irradiation systems, one can observe formation of endotaxial structures \approx 700 °C (Figure 4.6 and Figure 4.10). One of the possible reasons for this could be due to large number defects (including displacements) with low energy ions resulting in enhancement of diffusion of Ag atoms from the deposited layer and these aspects are presented at later sections in this chapter.

4.3.2 High energy (MeV) irradiated system

A \approx 2 nm Ag thin film, deposited on the *high energy irradiated* samples at fluence 1×10^{15} ions/cm², were annealed at 600 °C, 650 °C and 700 °C for 30 min in air. Figures 4.2(a), 4.2(c) and 4.2(e) present low magnification planar TEM images for 600 °C, 650 °C and 700 °C cases respectively; corresponding low magnification cross-sectional TEM micrographs have been displayed in Figures 4.2(b), 4.2(d) and 4.2(f) respectively. Planar images show the formation of almost spherical Ag nanoparticles (NPs) with different sizes for 600 °C, 650 °C and 700 °C, respectively. We have observed the formation of Ag NPs just reaching the SiO_x/Si(100) interface at 600 °C (Figure 4.2(b)); at other higher temperatures, Ag diffusion towards the substrate is more (Figures 4.2(d) and 4.2(f)). All the images in Figure 4.2 clearly show no formation of endotaxial Ag NPs, while only embedded Ag NPs at 650 °C and 700 °C [10, 17]. We haven't found any significant difference between irradiated (high energy) samples and normal samples (i.e., without irradiation), which is evident from the comparison of Figure 4.1 and Figure 4.2. It is to be noted that the projected range (R_p) of 1.8 MeV Ag ions in GeO_x/Si system is \approx 780 nm (obtained using SRIM software [21]). Therefore, the defects formation is more around R_p (that is \approx 780 nm for 1.8 MeV Ag ions) and hence there is no appreciable changes occurred and results are similar to un-irradiated systems. To understand the role of enhanced diffusion due to irradiation induced defects, we used 30 keV Ag ions and are discussed in the following section.

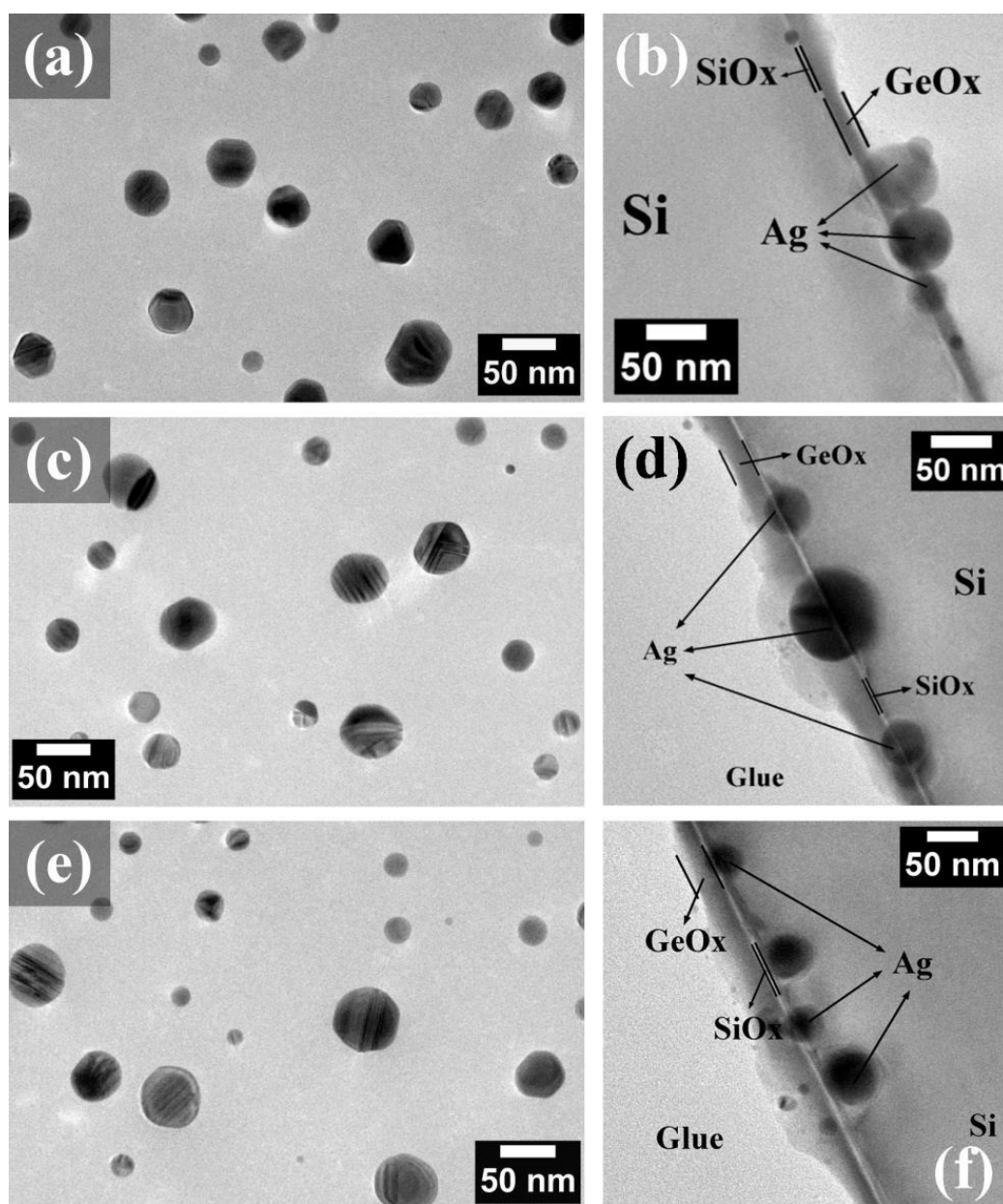


Figure 4.2: Planar TEM and corresponding cross-sectional TEM micrographs of 2 nm Ag on 15 nm GeO_x/SiO_x/Si(100) - 1×10^{15} ions/cm² annealed at (a) and (b) 600 °C, (c) and (d) 650 °C and (e) and (f) 700 °C. The results are similar as shown in Figure 4.1 (un-irradiated systems).

4.3.3 Low energy (keV) irradiated system

Figure 4.3(a) depicts the low magnification cross-sectional TEM image of 15 nm GeO_x/SiO_x/Si(100) sample. After 30 keV Ag irradiation at 5×10^{15} ions/cm² fluence, cross-sectional TEM study of the sample and Figure 4.3(b) displays the high magnification micrograph of the corresponding sample; Figures 4.3(c) and 4.3(d) show the high resolution

TEM images from the yellow and red marked regions in Figure 4.3(b) respectively. It is to be noted that the sputtering yield at lower energies is very appreciable due to large value of nuclear stopping cross-section and this results in reduction of thickness of GeO_x layer from ≈ 15 nm to ≈ 6 nm. The amorphous nature of the silicon substrate found to be present up to a depth of ≈ 34 nm (Figure 4.3(b)). From SRIM calculations, it is found that the projected range (R_p) of 30 keV Ag ions in GeO_x system ≈ 20.1 nm to ≈ 23.4 nm for “x” varying from 1.0 to 2.0, respectively. After the irradiations, a ≈ 2 nm thick Ag thin film was deposited on the 15 nm $\text{GeO}_x/\text{SiO}_x/\text{Si}(100)$ -Ir (5×10^{15} ions/cm²) and then annealed the specimens at different temperatures: 500 °C, 600 °C, 700 °C, and 800 °C for 30 min in ambient conditions. Figures 4.4(a) and 4.4(b) present low magnification planar SEM and low magnification cross-sectional TEM images respectively for the specimen annealed at 500 °C. Mostly, spherical

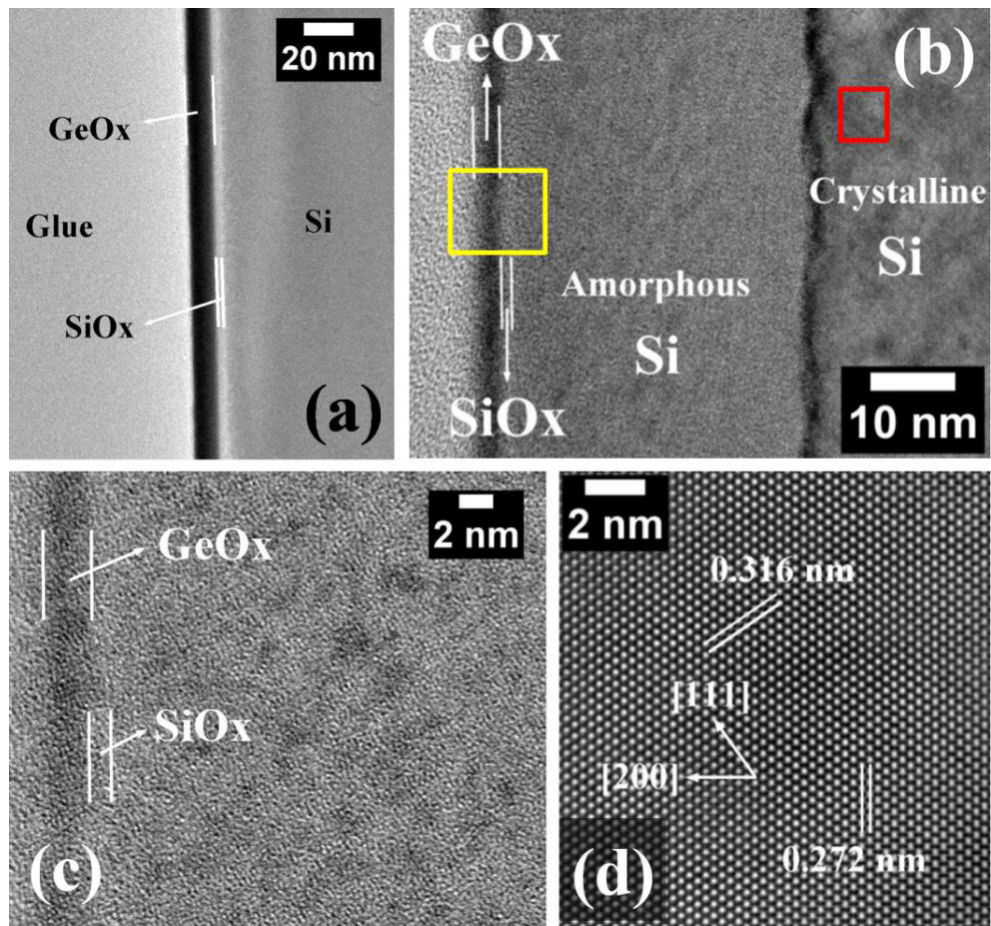


Figure 4.3: (a) Cross-sectional TEM image of 15 nm $\text{GeO}_x/\text{SiO}_x/\text{Si}(100)$ sample. (b) Cross-sectional TEM image of 15 nm $\text{GeO}_x/\text{SiO}_x/\text{Si}(100)$ - 5×10^{15} ions/cm² (as-implanted) sample; (c) high resolution TEM image from the yellow region in (b), showing the amorphous silicon due to ion implantation and (d) corresponding high resolution TEM image from red region in (b).

Ag NPs have been formed and found to be present in the GeO_x layer (see Figure 4.4(b)). Figures 4.4(c) and 4.4(d) depict high resolution TEM images taken from the yellow and red regions in Figure 4.4(b) respectively. In the similar fashion, we have framed the microscopy observations for 600 °C case in Figure 4.5. Figures 4.5(a) and 4.5(b) represent the low magnification planar SEM and low magnification cross-sectional TEM micrographs, respectively. Ag NPs could be seen at the substrate interface diffusing through the GeO_x layer. Corresponding high resolution TEM image of silver-silicon interface and GeO_x layer are shown in Figures 4.5(c) and 4.5(d) respectively. Figure 4.6 illustrates the microscopy

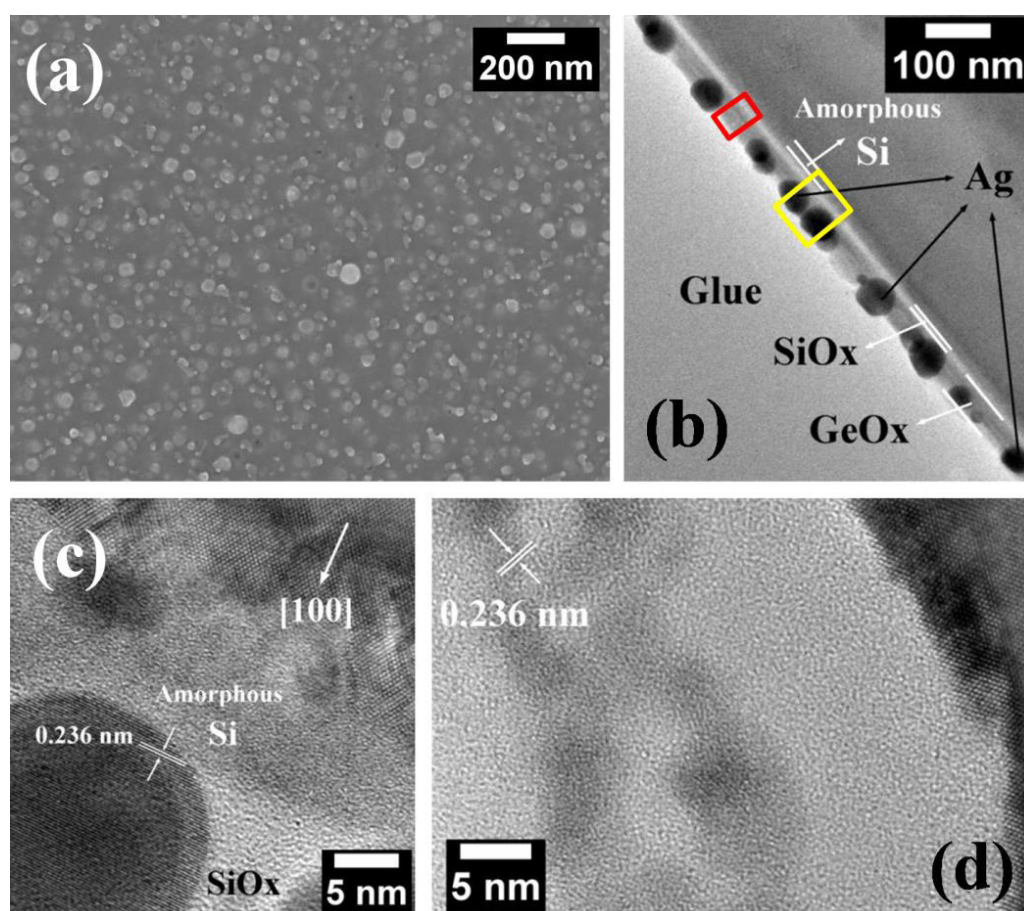


Figure 4.4: (a) and (b) SEM and cross-sectional TEM images of 2 nm Ag on 15 nm $\text{GeO}_x/\text{SiO}_x/\text{Si}(100)$ - 5×10^{15} ions/cm² annealed at 500 °C; (c) and (d) high resolution TEM images taken from the yellow and red regions in (b), respectively.

studies for 700 °C where Figures 4.6(a) and 4.6(b) display the low magnification planar SEM and low magnification cross-sectional TEM images respectively. Here, the initial formation of endotaxial nanostructures is seen, representing the onset temperature. As the interfacial region of substrate is amorphous, we find that the coverage of endotaxial structures is partial.

Interestingly, we haven't observed any endotaxial NSs formation in case of *un-irradiated* or *high energy irradiation* systems, as shown in the main Figure 4.1(c) and Figure 4.2(f). The possible reason behind this observation is as follows: for the *high energetic irradiation*, the majority of the defects are created in the silicon substrate well below from the interfacial region. However, in case of *low energy irradiation*, the defects formation in GeO_x layer and

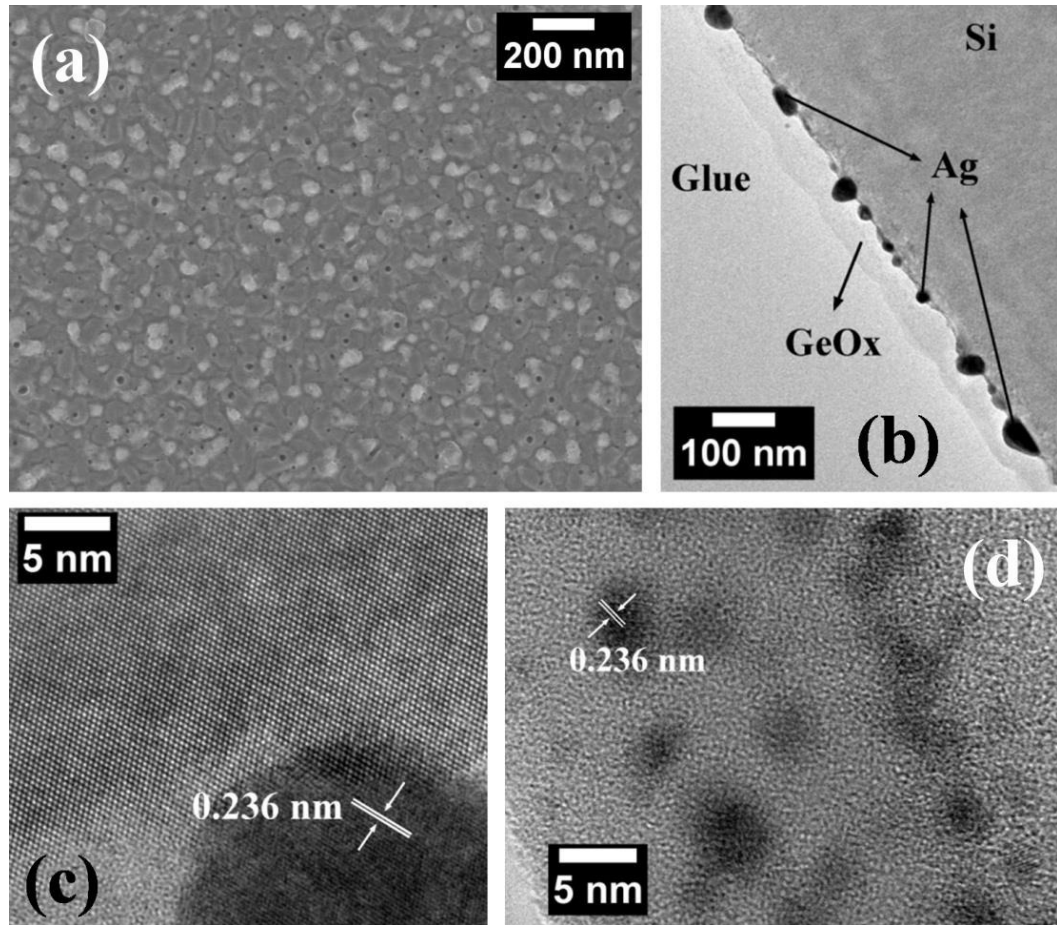


Figure 4.5: (a) and (b) SEM and cross-sectional images of 2 nm Ag on 15 nm $\text{GeO}_x/\text{SiO}_x/\text{Si}(100)$ - 5×10^{15} ions/cm² annealed at 600 °C; (c) and (d) corresponding high resolution cross-sectional TEM images of silver-silicon interface and GeO_x layer with silver nanoclusters, respectively.

at the same time in the silicon substrates (≈ 34 nm) as R_p is much smaller. Therefore, defects in GeO_x layer could be enhancing Ag diffusion towards substrate. Partial endotaxial nanostructures were formed because of some amorphous region in substrate. High resolution cross-sectional TEM image of silver-silicon interface and GeO_x layer are shown in Figures 4.6(c) and 4.6(d). Figures 4.7(a) and 4.7(b) exhibit the low magnification planar SEM and low magnification cross-sectional TEM micrographs for 800 °C. From these micrographs, it

is evident that all the Ag NSs found to be endotaxial in nature. Figure 4.7(c) shows the corresponding high magnification TEM image; Ag NPs are embedded into silicon. High resolution TEM image of the GeO_x layer is framed into Figure 4.7(d), showing crystalline Ag

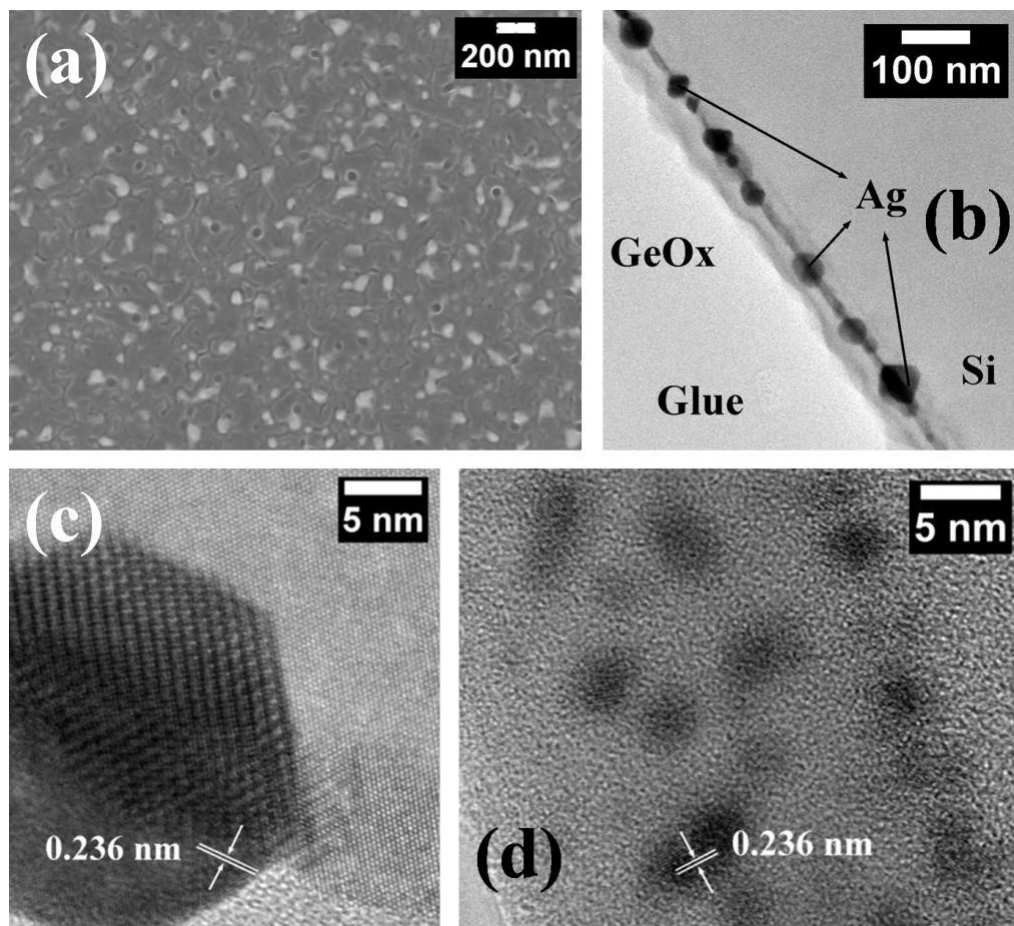


Figure 4.6: (a) and (b) SEM and cross-sectional images of 2 nm Ag on 15 nm $\text{GeO}_x/\text{SiO}_x/\text{Si}(100)$ - 5×10^{15} ions/cm² annealed at 700 °C; (c) and (d) corresponding high resolution cross-sectional TEM images of silver-silicon interface and GeO_x layer with silver nanoclusters, respectively.

nanoclusters and amorphous GeO_x . It is found that amorphous nature of the silicon substrate interface is playing role in the formation of endotaxial structures at comparative lower temperature. In a simple procedure, either use of low energy ion beam such that only GeO_x thin film would be affected by irradiation or GeO_x thickness can be increased such that all the incident beams would be stopped inside the over-layer film of $\text{GeO}_x/\text{SiO}_x$. Hence, the silicon substrate interface would be crystalline in nature even after irradiation. Now to achieve this, we have chosen the second option (as there were technical problems in reducing the beam

energies), i.e., GeO_x layer of different thicknesses ≈ 50 nm and ≈ 70 nm were deposited on native oxide covered silicon substrate. For 50 nm case, ≈ 7 nm amorphous silicon layer has

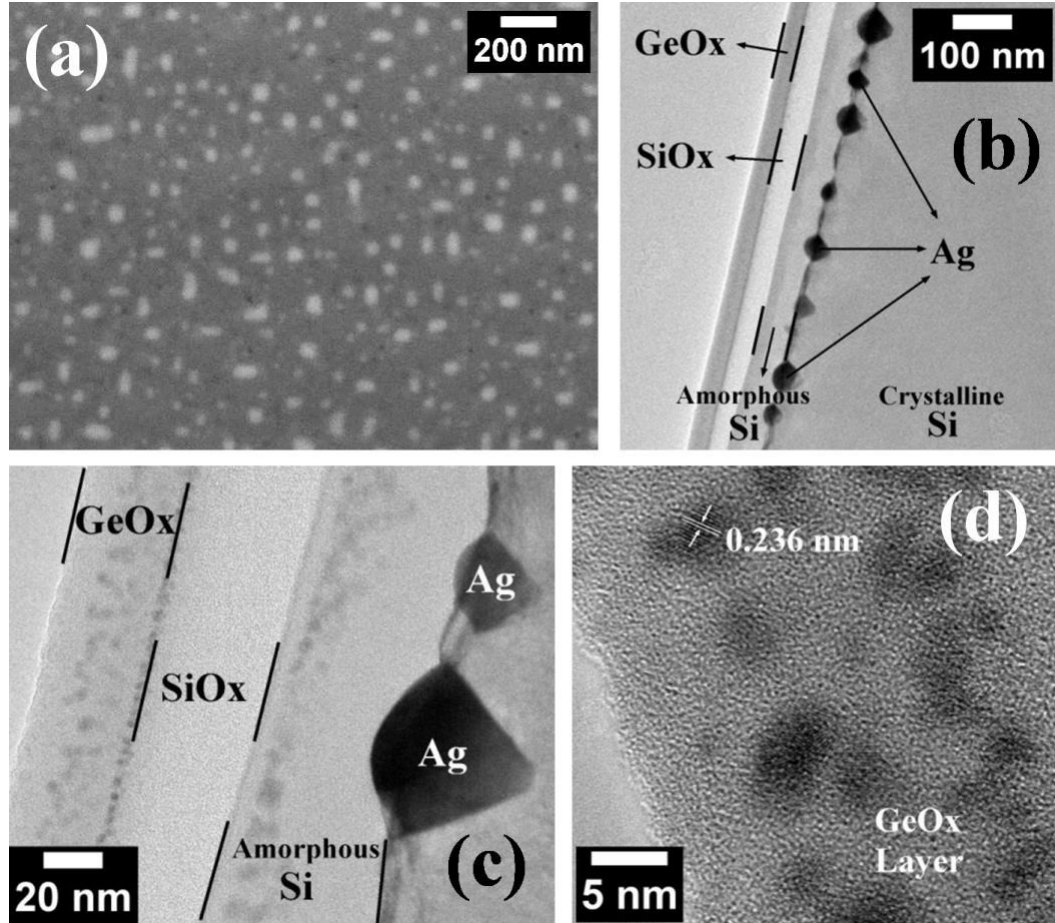


Figure 4.7: (a) and (b) SEM and cross-sectional TEM images of 2 nm Ag on 15 nm $\text{GeO}_x/\text{SiO}_x/\text{Si}(100)$ - 5×10^{15} ions/cm² annealed at 800 °C; (c) corresponding high magnification TEM image; (d) high resolution TEM image of the GeO_x layer along with silver nanoclusters, showing crystalline Ag nanoclusters and amorphous GeO_x .

been observed after irradiation with 5×10^{15} ions/cm² fluence and GeO_x layer thickness has got down to ≈ 25 nm (Figures 4.8(a-b)). But, in the case of ≈ 70 nm GeO_x layer, GeO_x has been reduced to ≈ 34 nm and no amorphous silicon has been introduced (see Figure 4.9(a)). One needs to keep in mind that, GeO_x film is reduced due to sputtering phenomena. Selected area electron diffraction (SAED) pattern and high resolution TEM image taken from solid yellow area and solid red area in Figure 4.9(a) are shown in Figure 4.9(b) and Figure 4.9(c), revealing single crystalline nature of substrate without any amorphous signature. As no amorphization of silicon substrate for the case of ≈ 70 nm GeO_x layer at irradiation condition

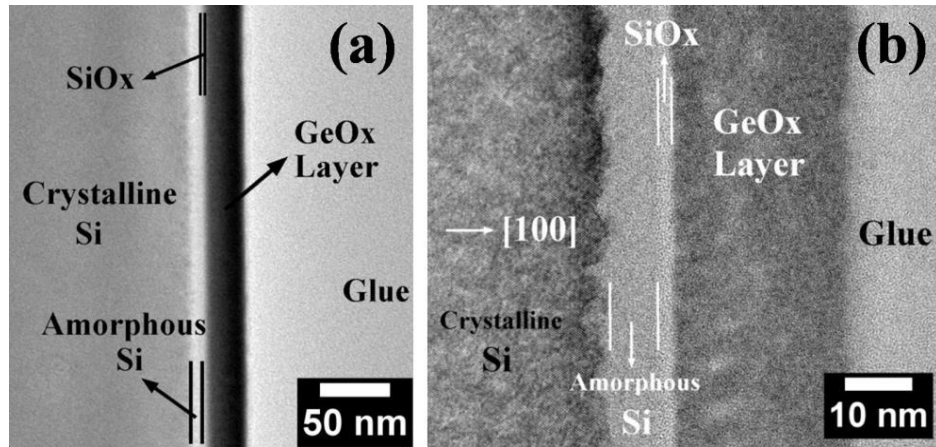


Figure 4.8: Cross-sectional TEM images of 50 nm $\text{GeO}_x/\text{SiO}_x/\text{Si}(100)$ - 5×10^{15} ions/ cm^2 (as-implanted) sample.

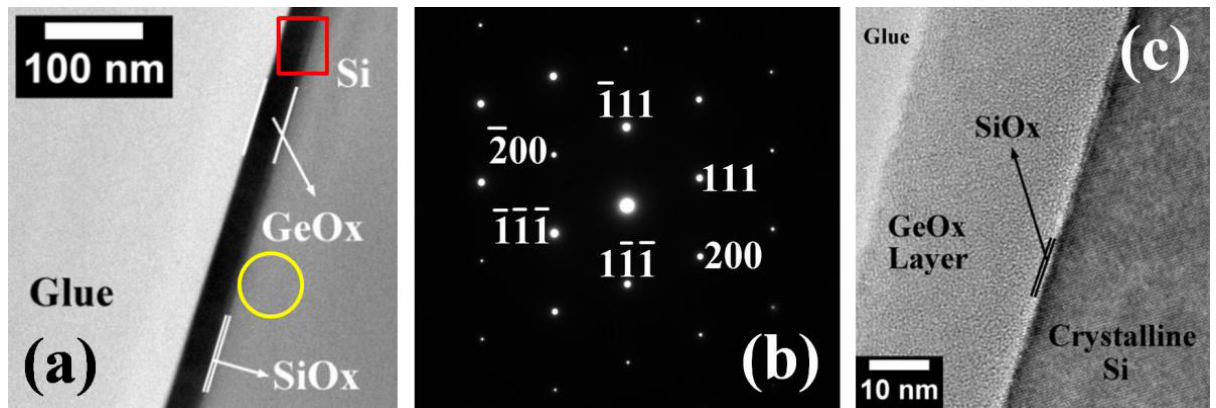


Figure 4.9: (a) Cross-sectional TEM image of 70 nm $\text{GeO}_x/\text{SiO}_x/\text{Si}(100)$ - 5×10^{15} ions/ cm^2 (as-implanted) sample; (b) corresponding SAED pattern taken from yellow dotted marked region in (a); (c) corresponding high resolution TEM image from red dotted rectangular area in (a).

at fluence of 5×10^{15} ions/ cm^2 , a Ag thin film of ≈ 2 nm thick was deposited after the irradiation. This system was annealed at 700 °C and 750 °C for 30 min in ambient conditions. Low magnification planar TEM images for 700 °C and 750 °C cases are shown in Figures 4.10(a) and 4.10(c), respectively; Figures 4.10(b) and 4.10(d) exhibit corresponding low magnification cross-sectional TEM micrographs. Figures 4.10(a-b) manifest Ag NSs with $\approx 55\%$ endotaxial in nature. From Figures 4.10(c-d), all the Ag NSs are unambiguously in the form of endotaxy. After protecting the silicon from amorphization, formation of endotaxial nanostructures has been increased to 55% from 15% at 700 °C. Hence, creating the defects in the GeO_x layer and preserving crystalline silicon from amorphization together enhances Ag

diffusion and aid to form endotaxial nanostructures completely at 750 °C, 50 °C lower than previous cases.

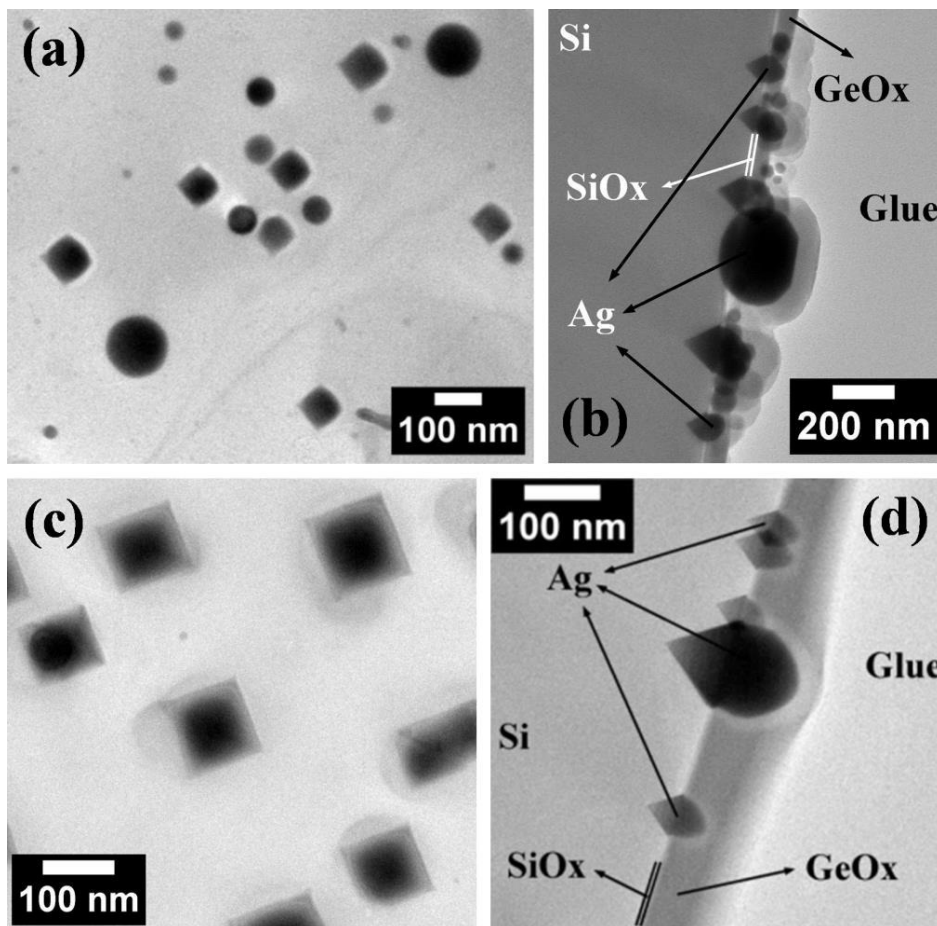


Figure 4.10: Planar TEM images of 2 nm Ag on 70 nm GeO_x/SiO_x/Si(100)-Ir 5×10^{15} ions/cm² annealed at (a) 700 °C and (c) 750 °C; corresponding cross-sectional TEM images are presented in (b) and (d) respectively.

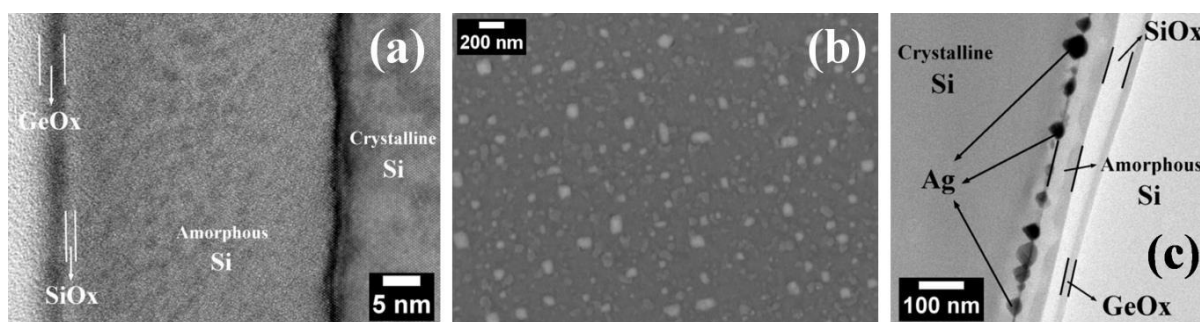


Figure 4.11: (a) Cross-sectional TEM image of 15 nm GeO_x/SiO_x/Si(100) - 2×10^{16} ions/cm² (as-implanted) sample. (b) and (c) SEM and cross-sectional TEM images of 15 nm GeO_x/SiO_x/Si(100) - 2×10^{16} ions/cm² annealed at 800 °C.

Interestingly, Ag endotaxial nanostructures could also be obtained even without any additional Ag film deposition. In such cases, implanted Ag ions (that are present due to irradiation experiment) would diffuse to substrate interface and form endotaxial structures. Figure 4.11(a) depicts a low magnification cross-sectional TEM image of 15 nm $\text{GeO}_x/\text{SiO}_x/\text{Si}(100)\text{-Ir}$ (2×10^{16} ions/ cm^2). After annealing at 800 °C in air, low magnification SEM planar micrograph of the corresponding sample is shown in Figure 4.11(b); Figure 4.11(c) represents the corresponding low magnification cross-sectional TEM image. Figures 4.11(b-c) confirm the formation of the endotaxial Ag NSs convincingly; presence of GeO_x and any form of Ag will produce coherently embedded Ag nanostructures, which validate our proposed plausible growth mechanism in earlier reports [10, 17]. We have tabulated all the results obtained from *low energy irradiation* specimens in Table 4.1 below.

Table 4.1: Microscopy observations from the low energy irradiated samples.

Sample details	Observations
2 nm Ag on 15 nm $\text{GeO}_x/\text{SiO}_x/\text{Si}(100)\text{-Ir}$ 5×10^{15} @ 500 °C	Spherical Ag nanoparticles formation in GeO_x layer
2 nm Ag on 15 nm $\text{GeO}_x/\text{SiO}_x/\text{Si}(100)\text{-Ir}$ 5×10^{15} @ 600 °C	Ag nanoparticles at the SiO_x/Si interface
2 nm Ag on 15 nm $\text{GeO}_x/\text{SiO}_x/\text{Si}(100)\text{-Ir}$ 5×10^{15} @ 700 °C	15 % Ag endotaxial nanostructures formation
2 nm Ag on 15 nm $\text{GeO}_x/\text{SiO}_x/\text{Si}(100)\text{-Ir}$ 5×10^{15} @ 800 °C	Completion of Ag endotaxial nanostructures formation (100%)
2 nm Ag on 70 nm $\text{GeO}_x/\text{SiO}_x/\text{Si}(100)\text{-Ir}$ 5×10^{15} @ 700 °C	55 % Ag endotaxial nanostructures formation
2 nm Ag on 70 nm $\text{GeO}_x/\text{SiO}_x/\text{Si}(100)\text{-Ir}$ 5×10^{15} @ 750 °C	Completion of Ag endotaxial nanostructures formation (100%)
15 nm $\text{GeO}_x/\text{SiO}_x/\text{Si}(100)\text{-Ir}$ 2×10^{16} @ 800 °C (no Ag over layer)	Completion of Ag endotaxial nanostructures formation (100%)

4.4 Conclusion

In conclusion, endotaxial Ag nanostructures were found to have a lower onset temperature (at 700 °C) for a system irradiated with lower energy Ag⁻ ions compared to either un-irradiated or high energy irradiated systems. This is the result with introduction of additional defects in over-layer using 30 keV Ag⁻ ions irradiation on GeO_x/SiO_x/Si system. Under *low energy irradiation*, GeO_x layer would be sputtered out and amorphization was observed in silicon substrate. It is also noticed that Ag diffusion is more when the defects are directly created in GeO_x layer; simultaneously clean crystalline silicon is required for coherently embedded Ag NSs formation at comparative lower temperature 700 °C. To avoid amorphization in silicon substrate from 30 keV Ag⁻ ions, a \approx 70 nm thick GeO_x layer has been utilized. However, high energy (1.8 MeV) Ag ions do not have any impact for endotaxial Ag NSs formation at less than 800 °C. In the next chapter, we will move to silver nanoparticles above oxide surfaces.

4.5 References

- [1] P Guha, R R Juluri and P V Satyam, *Nucl. Instr. Meth. Phys. Res. B* **2017**, 409, 209.
- [2] Y C Yeh, B Creran and V M Rotello, *Nanoscale* **2012**, 4, 1871.
- [3] C J Murphy, T K Sau, A M Gole, C J Orendorff, J Gao, L Gou, S E Hunyadi and T Li, *J. Phys. Chem. B* **2005**, 109, 13857.
- [4] N V Long, N D Chien, T Hayakawa, H Hirata, G Lakshminarayana and M Nogami, *Nanotechnology* **2010**, 21, 035605.
- [5] D L Fedlheim and C A Foss, *Metal Nanoparticles: Synthesis, Characterization, and Applications* (Marcel Dekker, Inc, 2002, ISBN: 0-8247-0604-8).
- [6] A H Alshehri, M Jakubowska, A Młozniak, M Horaczek, D Rudka, C Free and J. D. Carey, *ACS Appl. Mater. Interfaces* **2012**, 4, 7007.
- [7] D Chen, X Qiao, X Qiu and J. Chen, *J. Mater. Sci.* **2009**, 44, 1076.
- [8] K G Stampelcoskie, J C Scaiano, V S Tiwari and H Anis, *J. Phys. Chem. C* **2011**, 115, 1403.
- [9] B Sharma, R R Frontiera, A I Henry, E Ringe and R P V Duyne, *Mater. Today* **2012**, 15, 16.
- [10] R R Juluri, A Rath, A Ghosh, A Bhukta, R Sathyavathi, D Narayana Rao, K Muller, M

- Schowalter, K Frank, T Grieb, F Krause, A Rosenauer and P V Satyam, *Sci. Rep.* **2014**, *4*, 4633.
- [11] R R Juluri, A Ghosh, A Bhukta, R Sathyavathi and P V Satyam, *Thin Solid Films* **2015**, *586*, 88.
- [12] S O Kucheyev, J S Williams, C Jagadish, J Zou, C Evans, A J Nelson and A V Hamza, *Phys. Rev. B* **2003**, *67*, 094115.
- [13] G A Müller, E Carpene, R Gupta, P Schaaf, K Zhang and K P Lieb, *Eur. Phys. J. B* **2005**, *48*, 449.
- [14] F P Luce, E Oliviero, G de M Azevedo, D L Baptista, F C Zawislak and P F P Fichtner, *J. Appl. Phys.* **2016**, *119*, 035901.
- [15] D K Avasthi and G K Mehta, *Swift Heavy Ions for Materials Engineering and Nanostructuring* (Springer, Netherlands, 2011, ISBN: 978-94-007-1229-4).
- [16] L Pelaz, L A Marques and J Barbolla, *J. Appl. Phys.* **2004**, *96*, 5947.
- [17] R R Juluri, A Rath, A Ghosh, and P V Satyam, *J. Phys. Chem. C* **2013**, *117*, 13247.
- [18] R Carles, C Farcau, C Bonafos, G Benassayag, B Pecassou and A Zwick, *Nanotechnology* **2009**, *20*, 355305.
- [19] S Mohapatra, Y K Mishra, J Ghatak, D Kabiraj and D K Avasthi, *J. Nanosci. Nanotechnol.* **2008**, *8*, 4285.
- [20] J Leveneur, J Kennedy, G V M Williams, J Metson and A Markwitz, *Appl. Phys. Lett.* **2011**, *98*, 053111.
- [21] <http://www.srim.org>.

Chapter 5

Ag Nanoparticles Decorated Molybdenum Oxide Structures: Growth, Characterization, DFT Studies and Their Application to Enhanced Field Emission

5.1 Introduction

In last two chapters, we discussed about silver nanostructures inside oxide material. Now, in this chapter onwards, we will discuss about very interesting and successful incorporation of silver nanoparticles on another oxide material. Here, we are reporting a simple single step growth of α -MoO₃ structures and energetically suitable site specific Ag nanoparticles (NPs) decorated α -MoO₃ structures on varied substrates, having almost similar morphologies and oxygen vacancies. We have elucidated possible growth mechanism in the light of experimental findings and density functional theoretical (DFT) calculations. We have experimentally established and verified by DFT calculations that MoO₃(010) surface as weakly interacting and stable surface compared to other orientations. From DFT study, the binding energy is found to be higher for (100) and (001) surfaces (≈ -0.98 eV), compared to (010) surface (≈ -0.15 eV) and thus it is likely that Ag NPs formation is not favorable on MoO₃(010) surface. Ag decorated MoO₃ (Ag-MoO₃) nanostructured sample shows enhanced field emission (FE) properties with ≈ 2.1 times lower turn-on voltage of 1.67 V/ μ m and one

order higher field enhancement factor (β) of 8.6×10^4 compared to MoO_3 sample without Ag incorporation. From Kelvin probe force microscopy (KPFM) measurements, the average local work function (Φ) is found to be ≈ 0.47 eV smaller for Ag- MoO_3 sample ($\approx 5.70 \pm 0.05$ eV) compared to MoO_3 sample ($\approx 6.17 \pm 0.05$ eV) and the reduction in Φ can be attributed to the shifting Fermi level of MoO_3 toward vacuum via electrons injection from Ag NPs to MoO_3 . Presence of oxygen vacancies together with Ag NPs lead to the highest β and lowest turn-on field among the reported values under MoO_3 emitters' category [1].

Molybdenum oxides, wide band gap (2.6–3.2 eV) [2, 3] n-type (intrinsically) semiconductors are found to be one the most fascinating transition metal oxide (TMO), as for their unique structural, electrical, optical, mechanical properties and multi-directional applications [2, 4, 5]. Depending on oxygen concentrations and oxidation states (+6, +5, +4, +3, +2) of Mo, molybdenum oxide shows several phase structures like MoO_3 , Mo_9O_{26} , Mo_8O_{23} , Mo_5O_{14} , Mo_4O_{11} , MoO_2 etc. and exhibits different electrical, optical properties [2, 6, 7]. Molybdenum oxide has been extensively utilized in diverge advanced applications and showed promising performances in photochromic devices [8, 9], electrochromic devices [10], gas sensing [11–13], photocatalysis [14, 15], resistive switching [16], lithium ion batteries [17, 18], field emission [19–21], photovoltaic [10], transistors [22], inorganic light emitting diode [23], capacitors [4, 24], panel displays [8] and smart windows [9] etc. Even though MoO_3 is being employed as potential applicant in several fields, its poor electrical and ionic conductivity have become roadblocks for its manifold uses [25, 26]. By incorporating oxygen vacancies into lattice [20, 25], conjugating with metal nanoparticles (NPs) with MoO_3 structures [27–29], metal doping [30] etc., it is possible to enhance the conductivity properties.

Normally, molybdenum trioxide (MoO_3) appears as three different forms: thermodynamically most stable orthorhombic MoO_3 (α - MoO_3), meta-stable monoclinic MoO_3 (β - MoO_3), and meta-stable hexagonal MoO_3 (h- MoO_3) [3, 17, 31]. α - MoO_3 , carrying a unique two-dimensional layered structure, falls under the $P_{\{bnm\}}$ space group with unit cell parameters $a = 3.96$ Å, $b = 13.85$ Å and $c = 3.71$ Å (JCPDS: 35-0906) [32]. Crystal structures of α - MoO_3 projected from [100], [010] and [001] directions have already shown in Figure 1.x in chapter 1. α - MoO_3 is composed of bi-layers of distorted MoO_6 octahedra along [010], connected via the weak van der Waals forces [32–34]. Within the double layers, MoO_6 are bounded by covalent and ionic bonds [34]. In XZ plane, the MoO_6 octahedra forms corner sharing along [100] and edge-sharing zig-zag along [001] directions [33, 34]. Oxygen atoms

in MoO₃ crystal are categorized into three; (1) terminal oxygen atom bonded to only one Mo atom (≈ 1.67 Å), (2) symmetric bridging oxygen bonded to two Mo atoms (≈ 1.95 Å, equidistant) and weakly bonded to another Mo atom (≈ 2.33 Å), (3) asymmetric bridging oxygen atoms bonded to two Mo atoms (≈ 1.74 Å and ≈ 2.25 Å) [4, 32, 33]. Among the three principle surfaces (100), (010) and (001) of α -MoO₃, the most stable surface is MoO₃(010) [35, 36]. MoO₃ nanostructures (NSs) with different morphologies such as nanowires [19, 24], nanotubes [37], nanorods [11], nanobelts [14, 18, 38, 39], nanoflakes [20], nanoribbons [15], whiskers [40], nanosheets [41], and nanostructures [42] etc. have been prepared via various physical and chemical methods. Up to the present-day, diversified routes for synthesizing MoO₃ NSs successfully have been addressed, such as, thermal evaporation [12, 41, 43], chemical vapor deposition [10, 11], pulsed laser deposition [7], hydrothermal [39], flame synthesis [38], sputtering [44], electrochemical technique [45], infrared irradiation [46], sol-gel [47], sonochemical approach [40] etc.

Unlike the other heterostructures (HSs), such as, Ag-WO₃ [48], Au-ZnO [49], Ag-TiO₂ [50], Au-GeO₂ [51] etc., coupling of MoO₃ with metal NPs is not very easy in a single step process. However, the combination of plasmonic metal and semiconductor nanomaterials have been comprehensively explored in the past decades because these heterostructure materials can offer even better performances in diverse territories compared to individuals [27, 48–51]. When metal NPs are proximal to semiconductor, the electrons from metal can be directly transferred into conduction band (CB) of the semiconductor [48–50, 52]. This electron transfer process provides improved results in many application contests like sensing, catalysts, Li-ion batteries and field emission etc [27, 30, 48–50, 53]. Field emission process is the emission of electrons from material through tunneling under high applied electric field. According to the Fowler–Nordheim theory [54], FE characteristic of any material is ascertained by field enhancement factor (β) where, β is the ratio of the local field to the applied field. This β value completely depends on the morphology and the work function (Φ) of that material. Till now, very few, FE properties of MoO₃ NSs have been addressed, offering as attractive candidates in cold cathode electron emission device [19–21, 55]. However, the synthesis of intrinsically self assembled Ag-MoO₃ HSs in a single step process and their improved field emission characteristics have not yet been studied methodically. Silver (Ag) is selected as it is considered to be the best metal for electrical characterization because of its highest electrical conductivity ($\sigma_{\text{Ag}} = 6.30 \times 10^7$ S/m at 20 °C).

5.2 Experimental

5.2.1 Growth

α -MoO₃ structures were grown in a horizontal quartz tube (length \approx 100 cm and inner diameter \approx 4.5 cm) furnace with single zone side entry on diverse single crystalline substrates (commercially available silicon (Si), gallium arsenide (GaAs), indium tin oxide (ITO) coated glass and germanium (Ge) substrates). Prior to the deposition in the tube furnace chamber, bare wafers were ultrasonically cleaned in acetone for 5 min and then in methanol for 5 min. For silver decorated MoO₃ (Ag-MoO₃ heterostructures (HSs)) growth, first \approx 4 nm thick silver (Ag) film was deposited on pre-cleaned substrates by physical vapor deposition (PVD) technique in high vacuum condition ($\approx 1.2 \times 10^{-6}$ mbar) using Mo boat. 10 mg MoO₃ powder was put at the center of a ceramic boat and loaded into the furnace at its central position (Figure 5.1). Substrates (either bare wafers or Ag thin film deposited substrates) on another ceramic boat were kept \approx 19.5 cm away from source such that substrate temperature will be \approx 550 °C when furnace reaches at 750 °C (Figure 5.1). The furnace was ramped up to 750 °C from room temperature with ramping rate of 7 °C/min and stayed for 20 min at 750 °C. From the very beginning of the ramping, constant 45 sccm argon gas was introduced as carrier. Finally, samples were collected from the system after cooling down to room temperature.

Temperature dependent growth has also been carried out for Ag decoration case to understand the growth mechanism. We have kept 4 nm Ag/SiO_x/Si substrates separately at

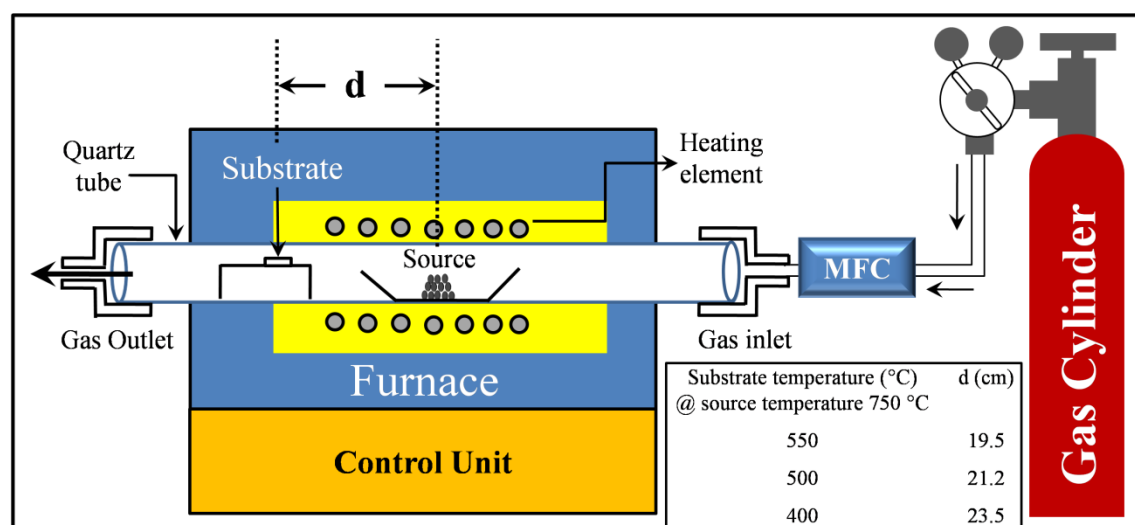


Figure 5.1: Schematic illustration of the single zone side entry horizontal quartz tube furnace for MoO₃ and Ag-MoO₃ growth.

two different temperatures 500 °C and 400 °C (≈ 21.2 cm and ≈ 23.5 cm away from the source position respectively), while keeping all other conditions including source temperature (750 °C) remain same.

5.2.2 Characterization

Surface morphology, shape and size, structural characterizations of as-grown samples were examined using field emission gun based scanning electron microscopy (FEG-SEM) with 20 kV electrons (Neon 40 cross-beam system, M/S Carl Zeiss GmbH) and high resolution transmission electron microscopy (HRTEM) with 200 keV electrons (JEOL JEM-2010). For TEM characterizations, the as-prepared samples were scraped off from the substrates and dispersed into methanol and then drop casted on carbon coated copper grids. To obtain large scale crystalline information of the samples, X-ray diffraction (XRD) measurements were done by using Bruker DAVINCI D8 ADVANCE diffractometer equipped with Cu K α radiation ($\lambda = 0.15406$ nm). For chemical composition analysis of the samples, X-ray photoelectron spectroscopy (XPS) studies were performed using PHI 5000 VersaProbe-II (ULVAC-PHI, INC, Japan) system with a micro-focused monochromatic Al-K α source ($h\nu = 1486.6$ eV), a hemispherical analyzer, and a multichannel detector. Raman studies of the samples were carried out by using Renishaw in Via Raman microscope with 514 nm Laser and a 50 \times objective with 10 second exposure time at room temperature. The optical properties of the samples were measured at room temperature using an ultraviolet-visible-near infrared (UV-Vis-NIR) spectrophotometer (Shimadzu Corporation, UV-3101PC). Field emission (FE) performances of the samples (called as emitters) were inspected in a diode configuration in a custom made high vacuum ($\approx 3.6 \times 10^{-7}$ mbar) chamber (Excel Instruments, FE System-150) and current vs. voltage (I-V) data were recorded using Keithley, 2410 as voltage source meter. The as-grown samples, fixed to the bottom plate with a copper tape were used as the cathodes and a copper plate having ≈ 2.5 mm tip diameter was served as the anode. For all FE measurements, electrodes separation was kept same (≈ 70 μ m). Kelvin probe force microscopy (KPFM) technique was employed to determine the local work function of the as-grown samples by ex-situ atomic force microscopy (AFM, Asylum Research, MFP-3D) in lift mode (lift height ≈ 50 nm) using conductive Ir/Pt-coated tips with a resonant frequency of ≈ 75 kHz and force constant of ≈ 2.8 N-nm $^{-1}$.

5.2.3 Computational details

We have performed the calculations using spin polarized density functional theory as implemented in the Vienna ab-initio simulation package (VASP) [56]. The generalized gradient approximation (GGA) – PBE functional [57] was employed for the exchange and correlation effects of the electrons. The potentials of the atoms were described by the projected augmented wave (PAW) [58] method. The cut-off energy is taken equal to 450 eV and the Brillouin zone integration within the Monkhorst Pack scheme with $3 \times 3 \times 1$ k-point mesh in reciprocal space. All the structures were optimized until the total energy converged to less than 10^{-5} eV per atom. We have considered vacuum of 15 Å along c-axis in the model geometry to avoid the spurious interactions. We have defined the binding energy (E_b) between the silver and the particular surface of MoO_3 as

$$E_b = E_{\text{Ag/MoO}_3} - E_{\text{MoO}_3} - E_{\text{Ag}} \quad (5.1)$$

where, $E_{\text{Ag/MoO}_3}$ is the total energy of Ag- MoO_3 heterostructure, E_{MoO_3} and E_{Ag} are the total energy of the MoO_3 and silver respectively.

5.3 Results and discussion

5.3.1 Structural characterization

Growth of MoO_3 nanometre-thick sheets, nanobelts, microrods from commercially available MoO_3 powder via thermal evaporation has been reported in the past [12, 41, 43]. Here, vapor-solid mechanism technique has been employed to grow densely packed orthorhombic MoO_3 ($\alpha\text{-MoO}_3$) structures on varied substrates over a large scale. Figures 5.2(a) and its inset display low and high magnification SEM micrographs of as-grown products on Si substrate respectively. To get the large scale crystalline information of this as-prepared sample, the X-ray powder diffraction analysis is framed into Figure 5.2(b). All the peaks can be indexed to orthorhombic phase of MoO_3 ($\alpha\text{-MoO}_3$) (JCPDS card, #35-0906) and they are oriented mostly along $\langle 0\ 2k\ 0 \rangle$. From XRD spectra, stronger intensities are observed for the reflection peaks of (020), (040), (060) and so on (i.e., $(0\ 2k\ 0)$) indicating the anisotropic growth of the $\alpha\text{-MoO}_3$ structures as the growth rates along the three principle axes are different: $[001] > [100] \gg [010]$ [14, 15]. Figure 5.2(c) presents low magnification TEM image of MoO_3 structures. Selected area electron diffraction (SAED) from the yellow circular dotted area in Figure 5.2(c), taken along $[010]$ direction of $\alpha\text{-MoO}_3$ is shown in the inset of

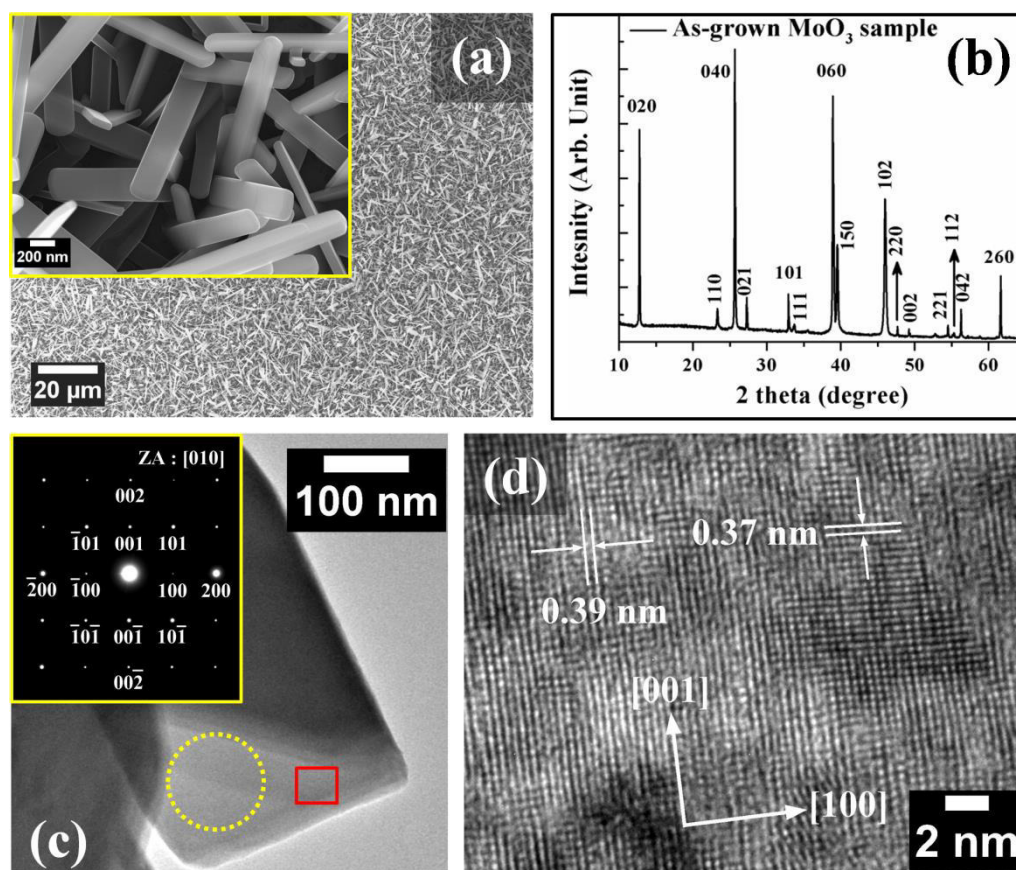


Figure 5.2: (a) Low magnification SEM micrograph of as-grown products grown on silicon substrate; inset shows corresponding high magnification SEM image. (b) XRD spectrum of the corresponding sample. (c) TEM micrograph of MoO₃ structure; inset shows selected area electron diffraction (SAED) pattern from dotted yellow region, taken along [010] zone axis, suggests single crystalline nature of as-synthesized product. (d) High resolution TEM (HRTEM) image obtained from marked region (red) of (c), representing preferential growth along [001], which is consistent with SAED pattern.

Table 5.1: Dimensions and areal densities of the as-grown samples.

Samples	Average Length (μm)	Average Width (nm)	Average Thickness (nm)	Areal density (per cm ²)
MoO ₃	1.3 ± 0.6	250 ± 33	150 ± 42	2.19 × 10 ⁸
Ag-MoO ₃ HSs	1.2 ± 0.9	235 ± 40	160 ± 36	2.60 × 10 ⁸

Figure 5.2(c), which confirms the single crystalline nature of as-grown structure. The high-resolution TEM (HRTEM) image as Figure 5.2(d) exhibits that the MoO₃ structure has lattice

planes with spacings of 0.37 nm and 0.39 nm, corresponding to the d spacings (d_{001} and d_{100}) of the (001) and (100) planes of the α - MoO_3 respectively. HRTEM micrograph is representing the preferential growth of MoO_3 structures along [001], which is consistent with SAED pattern (inset of Figure 5.2(c)). Dimensionality of the as-grown MoO_3 structures analyzed from electron microscopy observations have been tabulated in Table 5.1.

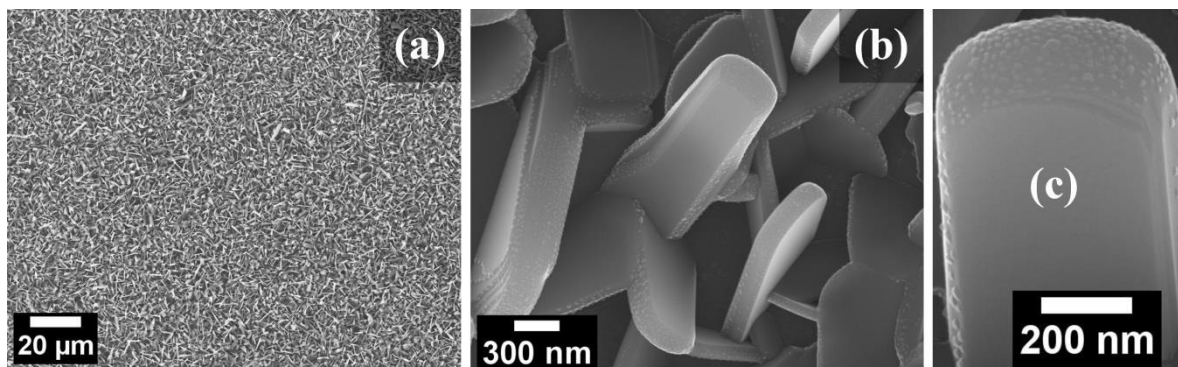


Figure 5.3: (a) Low and (b) high magnification SEM micrographs of the as-grown structures grown on 4 nm $\text{Ag/SiO}_x/\text{Si}$ substrate. (c) SEM image of a single structure.

We have successfully grown highly dense Ag- MoO_3 heterostructures (HSs) for the first time in a single step process. Figures 5.3(a) and 5.3(b) represent low and high magnification SEM images of the as-grown Ag- MoO_3 HSs products on 4 nm $\text{Ag/SiO}_x/\text{Si}$ substrate. From Figure 5.3(b) we have noticed that all the Ag NPs, which are formed during the growth (@ 550 °C), are decorated on the MoO_3 structures. Average size of the decorated Ag NPs is figured out to be 22 ± 3 nm (Figure 5.4(a)). Interestingly, Ag NPs are not present on all the surface of MoO_3 structures. To earn better visualization, a single Ag- MoO_3 HS is shown in Figure 5.3(c); here it is cleared that Ag NPs are not present at all on some particular

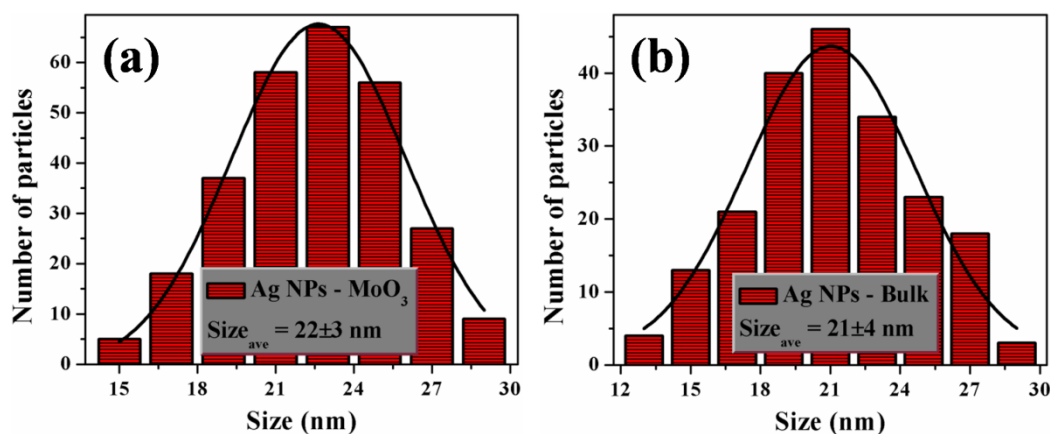


Figure 5.4: Size distributions of (a) Ag NPs on MoO_3 structures and (b) bulk Ag NPs on Si.

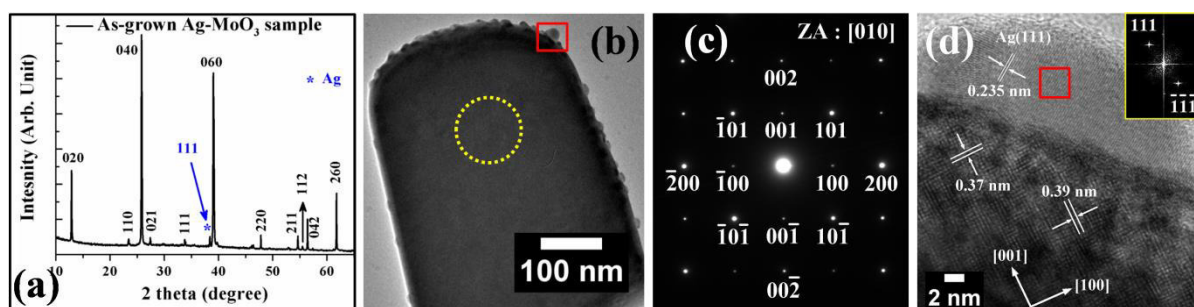


Figure 5.5: (a) XRD spectrum obtained from as-synthesized Ag-MoO₃ heterostructures (HSs). (b) TEM micrograph of Ag-MoO₃ HS. (c) SAED pattern taken from the dotted marked (yellow) region in (b) along [010] zone axis, suggests single crystalline nature of as-synthesized product. (d) High resolution TEM (HRTEM) image of Ag-MoO₃ structure from the solid marked (red) region in (b), represents preferential growth of MoO₃ along [001], which is consistent with SAED pattern; inset shows the FFT pattern with the plane (111) of silver obtained from the red region in (d).

surfaces. Figure 5.5(a) presents X-ray powder diffraction spectrum of the as-grown heterostructures sample. All the peaks can be assigned to orthorhombic structured MoO₃ (α -MoO₃) (JCPDS card, #35-0906) except the only one peak around $2\theta \approx 38.2^\circ$ that can be indexed to FCC silver (111) (marked in blue color). As like the earlier case, XRD spectrum exhibits the stronger intensities for (0 2k 0) reflection, indicating the anisotropic growth of the structures [14, 15]. Low magnification TEM image of single Ag-MoO₃ HS is shown in Figure 5.5(b). Except on the top surface and bottom surface (confirmed through SEM also; bottom one is unable to see) of the MoO₃ structure, Ag NPs are present on the other surfaces. Figure 5.5(c) displays SAED pattern taken from the dotted marked (yellow) region of Figure 5.5(b) along [010] zone axis, suggesting single crystalline nature of as-synthesized products as the previous one. High resolution TEM (HRTEM) image of Ag-MoO₃ structure (see Figure 5.5(d)) from the red solid marked sector in Figure 5.5(b), showing preferential growth of MoO₃ along [001], which is also consistent with SAED pattern. In the inset of Figure 5.5(d), the fast furrier transform (FFT) pattern, taken from squared region in Figure 5.5(d) can readily be indexed with Ag(111) which is in agreement with the XRD result. So, here we observed that the decorated NPs are pure metal silver and Ag NPs decoration density is more on MoO₃(001) than MoO₃(100) surface; *interestingly, the presence of Ag NPs on MoO₃(010) surface is not observed at all.* The structural details of the as-grown Ag-MoO₃ HSs are given in Table 5.1. From Table 5.1, it's quite obvious that the molybdenum oxide structures for both the samples are having almost similar morphologies except the Ag NPs decoration on

specific sites of MoO_3 surfaces for the Ag- MoO_3 sample. However, we have performed the Ag- MoO_3 heterostructures growth using ≈ 1.5 nm pre-deposited silver thin film on SiO_x/Si . Figures 5.6(a) and 5.6(b) show high magnification and corresponding high resolution SEM micrographs of the corresponding sample. Since the amount of silver is less compared to previous case (4 nm Ag), silver decoration density on MoO_3 surfaces is also less.

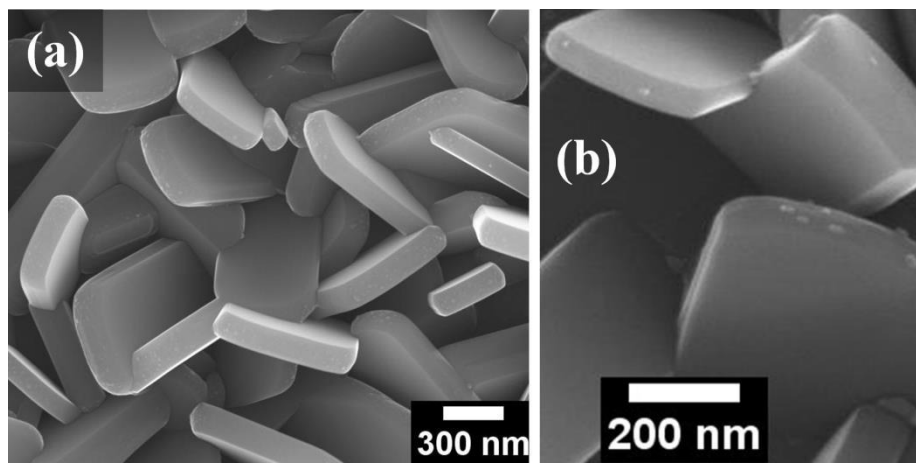


Figure 5.6: (a) High magnification and (b) corresponding high resolution SEM micrographs of the as-grown sample grown on 1.5 nm Ag/ SiO_x/Si substrate.

5.3.2 Growth mechanism: theoretical model

To understand the selective Ag growth on MoO_3 surfaces viz., (100) and (001) surface, computational studies have been performed. We have considered the cubic crystal structure of silver and the orthorhombic phase of MoO_3 for constituting the Ag- MoO_3 heterostructure. To realize the experimental findings, the supercell approach is essential to fix the lattice mismatch for all type of heterostructures. The Ag(111)/ MoO_3 (001) heterostructure has been constructed by considering the $(4\sqrt{3} \times 5 \times 1)$ supercell of Ag(111) layer and $(5 \times 1 \times 1)$ supercell of MoO_3 (001) surface. For the Ag(111)/ MoO_3 (001) heterostructure, two layers of Ag and four layers of MoO_3 unit are accounted, having total 40, 120 and 80 atoms of Mo, O and Ag respectively (see Figure 5.7(a)). The estimated lattice mismatch has come out to be only 3.12%, indicating the formation of Ag particle on MoO_3 (001) is highly possible. Similarly to design Ag(111)/ MoO_3 (100) heterostructure, we have taken $(3\sqrt{3} \times 5 \times 1)$ supercell of Ag(111) layer and $(1 \times 4 \times 1)$ supercell of MoO_3 (001) surface with 32 Mo atoms, 96 O atoms and 60 Ag atoms. The respective atomic structure with two layers of Ag and two layers of MoO_3 unit is shown in Figure 5.7(b). In this case, the lattice mismatch has been found to be

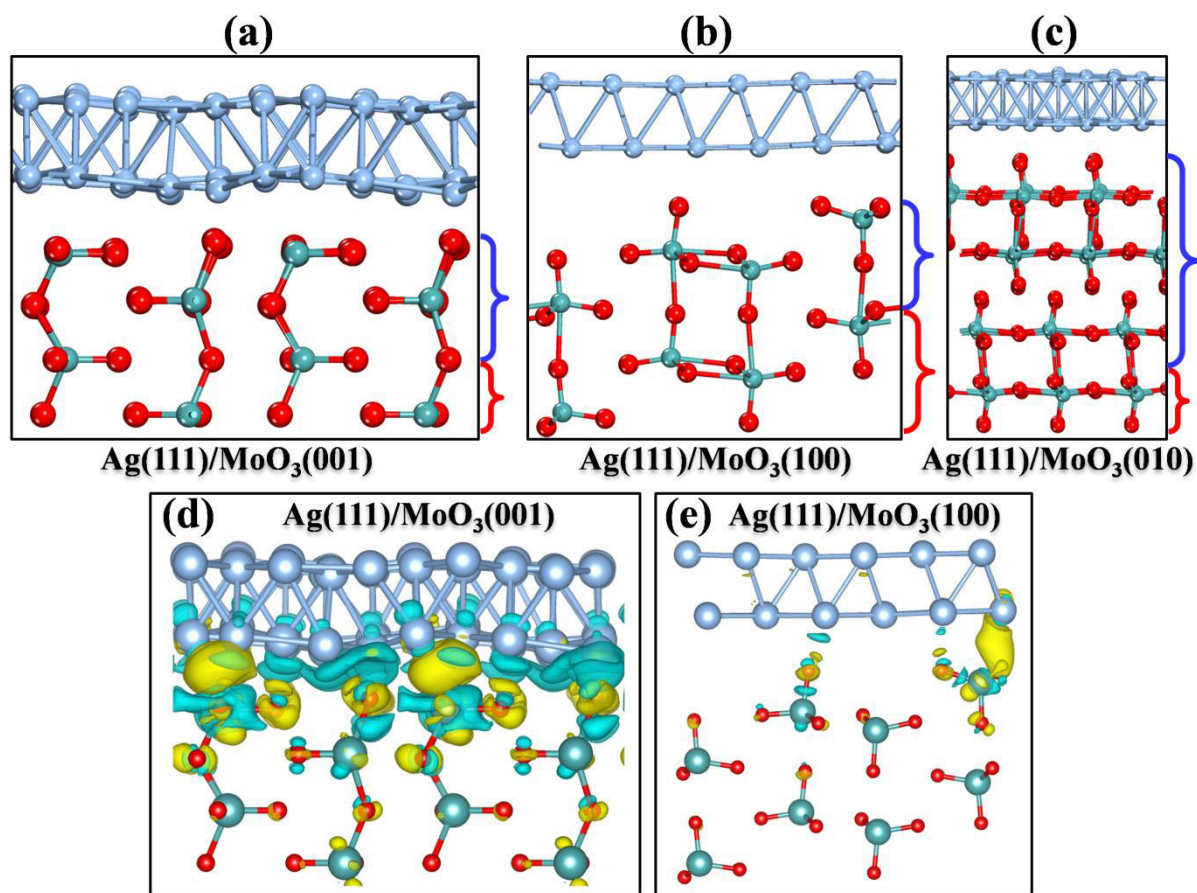


Figure 5.7: The optimized heterostructures for (a) Ag(111)/MoO₃(001), (b) Ag(111)/MoO₃(100) and (c) Ag(111)/MoO₃(010). Blue and red brace represents the free and fixed layers in the heterostructures respectively. ●, ●, ● represent the silver, molybdenum and oxygen atoms respectively. The 3D charge density difference plot of (d) Ag(111)/MoO₃(001) and (e) Ag(111)/MoO₃(100). Blue (negative isosurface) and yellow (positive isosurface) show charge depletion and accumulation zones respectively.

5.72% and the formation of Ag particle on MoO₃ (100) is also possible. Lastly to compose Ag(111)/MoO₃(010) heterostructure, (3√3×5×1) supercell of Ag(111) layer (2 layers) and (4×3×1) supercell of MoO₃(010) surface (4 layers) have been considered, shown in Figure 5.7(c). Here, the total number of Mo, O and Ag atoms are 48, 144 and 48 respectively. For this particular heterostructure, the lattice mismatch is about 9.13% even after considering very large supercell and hence the formation of Ag particle of MoO₃(001) is largely unfavorable. For further confirmation, we have estimated the binding energy between the Ag(111) layers and different MoO₃ surfaces. The optimized interlayer distance between the Ag(111) layers and MoO₃(100), (010), (001) surfaces are about 2.62 Å, 2.47 Å and 2.17 Å respectively. From our calculations among the three principle surfaces, it has been observed

that the binding energy (E_b) of Ag(111) layers is higher with $\text{MoO}_3(001)$ and (100) surfaces compared $\text{MoO}_3(010)$. The E_b is found in the range of ≈ -0.98 eV for these two surfaces (001) and (100), indicates there is a chance of charge distribution on this heterostructures. Whereas, in case of MoO_3 (010) surface the binding energy with Ag(111) layers is found to be in the range of -0.15 eV. The charge density difference calculation is also performed for Ag(111)/ $\text{MoO}_3(001)$ and Ag(111)/ $\text{MoO}_3(100)$ surfaces to confirm the charge distribution between layers, shown in Figures 5.7(d) and 5.7(e) respectively. The yellow lobes correspond to the accumulation of charges, and the blue lobes correspond to the depletion of charges. The value we chose for plotting the isosurface was $3 \times 10^{-3} e \text{ Bohr}^{-3}$ for both the surfaces (Figure 5.7(d)-(e)). Accumulation zones (yellow) are created by electron transfer from Ag(111) surface to MoO_3 surface, which lead to the depletion zones (blue) at Ag(111) surface. This clearly mimics that the growth of Ag NPs on this surface is extremely probable. In case of Ag(111)/ $\text{MoO}_3(100)$ heterostructure, the charge density distribution is less showing moderate interaction between these two layers. This clearly implies that the decoration of Ag nanoparticles on these two surfaces (001) and (100) is highly credible than the (010) surface of MoO_3 .

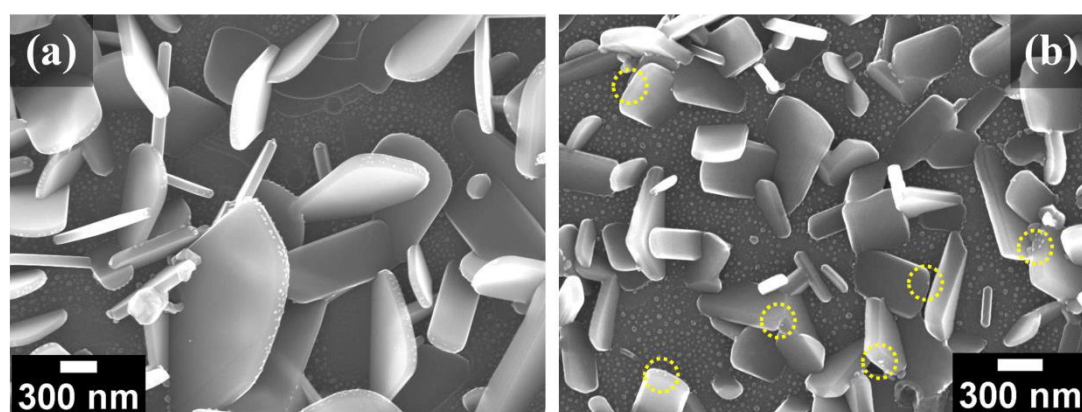


Figure 5.8: Temperature dependent growth study: substrate temperature (a) 500 °C and (b) 400 °C.

To understand the growth mechanism behind the Ag- MoO_3 HSs, we have performed the temperature dependent growth study. Figure 5.8(a) and 5.8(b) illustrate SEM images of as-grown samples with substrate temperatures 500 °C and 400 °C respectively. Structural density of MoO_3 is getting lesser with decreasing substrate temperature, because MoO_x vapor concentration is getting lower on the substrates kept at longer distance from the source. At the same time, Ag NPs decoration density over MoO_3 surface is getting deteriorated in the

following order of substrate temperature $550\text{ }^{\circ}\text{C} > 500\text{ }^{\circ}\text{C} > 400\text{ }^{\circ}\text{C}$. So, at lower temperatures more number of Ag NPs are getting unreacted and situated on the substrate surface itself instead of decorated on MoO_3 surface. Further we have characterized the as-grown sample (only $400\text{ }^{\circ}\text{C}$ case) by XRD, Raman and XPS techniques and will be demonstrated below as Figure 5.12 from where we haven't noticed any change in phase of as-grown MoO_3 . Growth model for the site specific decoration of Ag NPs on MoO_3 surfaces is schematically presented in Figure 5.9. At the beginning as the temperature increases, Ag thin film first gets transformed into Ag NPs via dewetting process ($\approx 350\text{ }^{\circ}\text{C}$). In the next stage, at moderate temperature ($\approx 400\text{ }^{\circ}\text{C}$), constant supply of MoO_3 crystals supplied from MoO_3 source powder by evaporation lead to the initiation of MoO_3 structures growth via vapor-solid (VS) mechanism on the Si substrate comprises of Ag NPs [49, 59]. As temperature increases and time progresses dimension of the MoO_3 structures increases in presence of Ag NPs on the Si substrate. Then finally at the growth temperature (optimized $\approx 550\text{ }^{\circ}\text{C}$) Ag NPs are found to be decorated on some particular surfaces of MoO_3 structures like (100), (001). But not a single Ag NP is present on $\text{MoO}_3(010)$. So, most plausible reason behind the formation of Ag NPs on MoO_3 surfaces could be due to the suitable surface energetic between Ag and MoO_3 surfaces compared to Ag on Si substrate at that growth temperature. We have already theoretically discussed the reason behind the site specific Ag NPs decoration on MoO_3 surfaces.

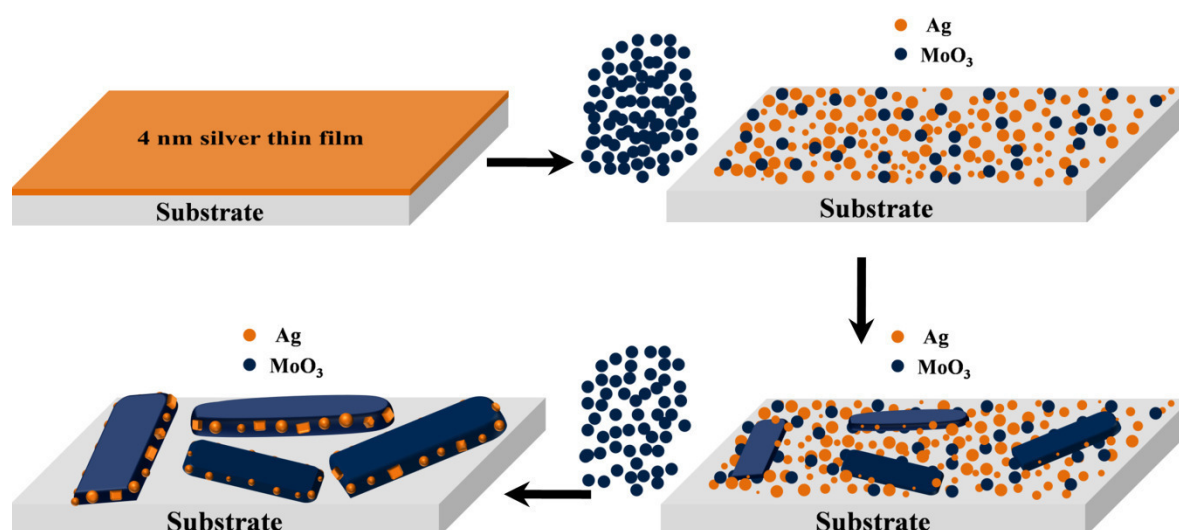


Figure 5.9: Schematic presentations on the possible growth model for site specific silver nanoparticles decorated MoO_3 structure (focusing on very few Ag- MoO_3 heterostructure (HS)).

5.3.3 XPS

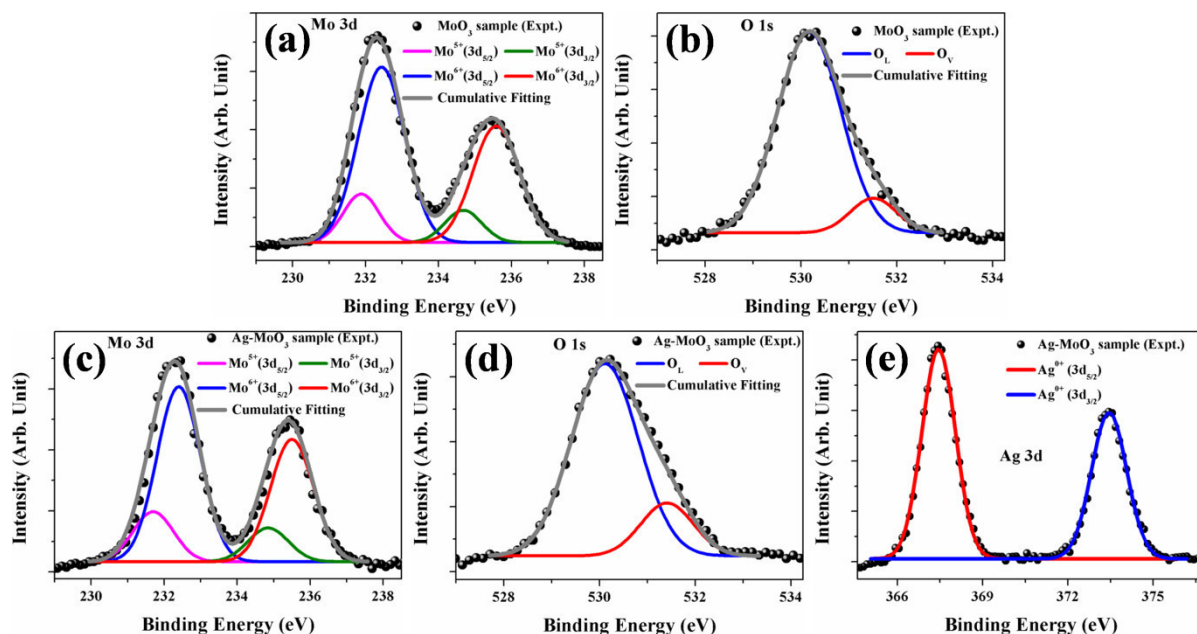


Figure 5.10: (a) Mo 3d and (b) O 1s XPS spectra from MoO₃ sample; (c) Mo 3d, (d) O 1s and (e) Ag 3d XPS spectra from Ag-MoO₃ sample.

The chemical compositions of the as-grown MoO₃ and Ag-MoO₃ samples were surveyed by X-ray photoelectron spectroscopy (XPS) technique. Results illustrate the admixture of Mo⁶⁺ and Mo⁵⁺ in both the samples and the leading contribution is coming from Mo⁶⁺ for both the cases. The origin of Mo⁵⁺ can be associated with oxygen vacancies, present in the MoO₆ octahedra in MoO₃ lattice [13, 25]. Figure 5.10(a) represents the XPS spectrum of Mo 3d levels for the as-prepared MoO₃ sample which can be deconvoluted into four Gaussian distributions at four different peaks located at 232.44 eV, 235.58 eV, 231.80 eV and 234.72 eV corresponding to the Mo⁶⁺ 3d_{5/2}, Mo⁶⁺ 3d_{3/2}, Mo⁵⁺ 3d_{5/2} and Mo⁵⁺ 3d_{3/2} respectively [5, 13, 25]. Similarly, Mo 3d spectrum from as-grown Ag-MoO₃ sample can also be decomposed with four Gaussian distributions, showing peaks at 232.39 eV, 235.50 eV, 231.71 eV and 234.85 eV corresponding to the Mo⁶⁺ 3d_{5/2}, Mo⁶⁺ 3d_{3/2}, Mo⁵⁺ 3d_{5/2} and Mo⁵⁺ 3d_{3/2} respectively (see Figure 5.10(c)) [5, 13, 25]. It is reported that oxygen deficiencies result in the reduction of Mo atoms neighboring to the oxygen vacancies from the Mo⁶⁺ state to the Mo⁵⁺ state, contracting the inter-atomic distance between the pair of Mo atoms [60]. To correlate Mo⁵⁺ state with oxygen vacancies, O 1s XPS spectra taken from the corresponding samples were inspected. The O 1s core level spectrum of as-grown MoO₃ sample can be fitted with two Gaussian distributions centered at 530.17 eV and 531.51 eV as shown in

Figure 5.10(b). The peak at 530.17 eV is related with the lattice oxygen in the orthorhombic MoO_3 (O_L) whereas the peak at 531.51 eV is originated from the oxygen deficiency within

Table 5.2: XPS analyses of the as-grown samples in detail.

Samples	XPS spectra details	Peak (eV)	FWHM (eV)	Area (Arb. Unit)	Area ratio
MoO_3	$\text{Mo}^{6+} 3d_{5/2}$	232.44±0.005	1.51	24090	1.498
	$\text{Mo}^{6+} 3d_{3/2}$	235.58±0.009	1.51	16080	
	$\text{Mo}^{5+} 3d_{5/2}$	231.80±0.009	1.18	5210	1.488
	$\text{Mo}^{5+} 3d_{3/2}$	234.72±0.011	1.19	3500	
	O_L	530.17±0.014	1.56	21930	5.992
	O_V	531.51±0.017	1.14	3660	
Ag- MoO_3	$\text{Mo}^{6+} 3d_{5/2}$	232.39±0.007	1.40	18550	1.495
	$\text{Mo}^{6+} 3d_{3/2}$	235.50±0.011	1.389	12400	
	$\text{Mo}^{5+} 3d_{5/2}$	231.71±0.008	1.306	4000	1.481
	$\text{Mo}^{5+} 3d_{3/2}$	234.85±0.011	1.306	2700	
	O_L	530.11±0.015	1.64	16800	5.805
	O_V	531.41±0.019	1.29	2895	
	$\text{Ag}^{0+} 3d_{5/2}$	367.45±0.005	1.48	4120	1.485
	$\text{Ag}^{0+} 3d_{3/2}$	373.45±0.005	1.48	2774	

the MoO_3 matrix (O_V) [14, 53]. Similarly, Figure 5.10(d) displays the O 1s spectrum of as-grown Ag- MoO_3 sample, which can be fitted with two Gaussian distributions centered at 530.11 eV and 531.41 eV, assigned to O_L and O_V respectively [14, 53]. The detail analysis of XPS spectra from the both samples is tabulated in the Table 5.2. In Figure 5.10(e), the Ag 3d spectrum is presented, confiding the metallic nature of silver in Ag- MoO_3 sample from the corresponding $\text{Ag}^{0+} 3d_{5/2}$ and $\text{Ag}^{0+} 3d_{3/2}$ binding energy peaks at 367.45 eV and 373.45 eV,

respectively [61]. It is cleared from the Table 5.2 that both the samples contain approximately equal amount of oxygen vacancies. In conclusion, the molybdenum oxide structures for both the samples are non-stoichiometric in nature, having almost equivalent deficiencies of oxygen atoms (O_V) in the MoO_3 lattice.

5.3.4 Raman

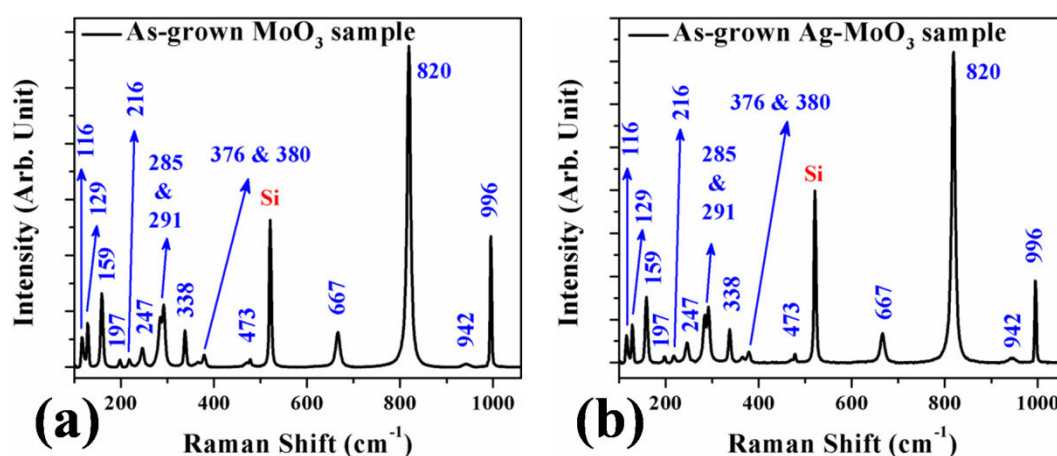


Figure 5.11: Raman spectra of (a) as-grown MoO_3 sample and (b) as-grown Ag decorated MoO_3 heterostructures.

As-grown samples are further characterized by Raman spectroscopy to determine the molecular structures of the samples. Typical Raman spectra of as-grown MoO_3 and Ag- MoO_3 HSs samples are framed into Figures 5.11(a) and 5.11(b) respectively. In general, the bands at 1000-600, 600-300, and below 200 cm^{-1} are originated from the stretching, deformation and lattice modes of α - MoO_3 respectively [14]. First we will discuss about Raman spectrum of MoO_3 sample (see Figure 5.11(a)). Spectrum shows several peaks around 116 cm^{-1} , 129 cm^{-1} , 159 cm^{-1} , 197 cm^{-1} , 216 cm^{-1} , 247 cm^{-1} , 285 cm^{-1} , 291 cm^{-1} , 338 cm^{-1} , 376 cm^{-1} , 380 cm^{-1} , 520 cm^{-1} , 667 cm^{-1} , 820 cm^{-1} , 842 cm^{-1} , 996 cm^{-1} . However, the peak at 520 cm^{-1} is appearing from the silicon substrate. Strongest intensity peak has been obtained \approx 820 cm^{-1} , attributed to the stretching vibration of Mo–O bonds (A_g mode) along b axis of MoO_3 orthorhombic crystal structure [62, 63]. Second intense peak is positioned at \approx 996 cm^{-1} , which can be recognized as stretching vibration of Mo–O bonds (A_g) along a axis of MoO_3 orthorhombic crystal structure [62, 63]. As the 820 cm^{-1} peak is the strongest one, we can conclude that MoO_3 structures are parallel to (010) surface, which is in agreement with our XRD result (Figure 2(b)) [63]. The peak \approx 942 cm^{-1} indicates to the oxygen vacancies present on the

MoO₃ surface, which has already been noticed in the O 1s spectra (Figure 5.10(b)) [62, 63]. The Raman peak ≈ 667 cm⁻¹ (B_{2g}, B_{3g}) and 473 cm⁻¹ (A_g) correspond to O–M–O stretching and O–M–O stretching and bending respectively. Further, the Raman bands around 380 cm⁻¹ (B_{1g}) and 366 cm⁻¹ (A_{1g}) are coming from O–M–O scissoring, 334 cm⁻¹ (A_g, B_{1g}) from O–M–O bending, 293 cm⁻¹ (B_{3g}) and 285 cm⁻¹ (B_{2g}) from O=M=O wagging, 247 cm⁻¹ (B_{3g}) and 197 cm⁻¹ (B_{2g}) from O=Mo=O twisting modes. In addition, the peaks around 116 cm⁻¹, 129 cm⁻¹, 159 cm⁻¹ and 216 cm⁻¹ are originated from the translational (T_c) rigid MoO₄ chain mode (B_{2g}), translational (T_c) rigid MoO₄ chain mode (B_{3g}), translational (T_b) rigid MoO₄ chain mode (A_g/B_{1g}) and rotational (R_c) rigid MoO₄ chain mode (A_g) respectively [62–64]. Figure 5.11(b) shows the Raman spectrum of Ag-MoO₃ HSs sample. Likewise, we have noted the similar nature in the Raman spectrum of Ag-MoO₃ sample as the previous one; the strongest peak 820 cm⁻¹ validates our XRD result (Figure 5.5(a)); the 942 cm⁻¹ peak is certifying our XPS results (Figure 5.10(d)) [62, 63]. We couldn't able to find any noticeable difference between the Raman spectra of Ag-MoO₃ sample and MoO₃ sample, indicating that decoration of Ag NPs does not significantly modify the MoO₃ structure.

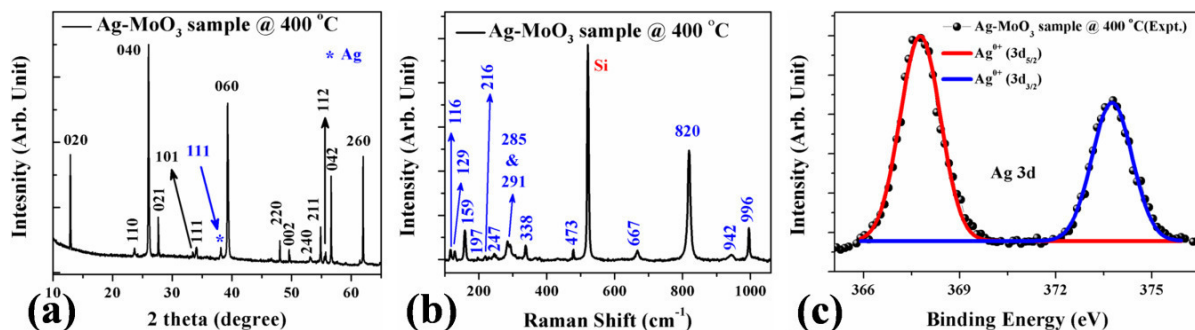


Figure 5.12: (a) XRD and (b) Raman spectra of Ag-MoO₃ sample grown at 400 °C; (c) Ag 3d XPS spectrum of the corresponding sample.

XRD data of the Ag-MoO₃ sample grown at 400 °C is shown in Figure 5.12(a), indicating the orthorhombic phase of MoO₃ (α -MoO₃) (JCPDS card, #35-0906) with intense peaks from (0 2k 0) reflections like earlier cases mentioned in the main article [14, 15]. One extra peak $2\theta \approx 38.1^\circ$ can be assigned to FCC Ag(111). Raman spectrum of the corresponding sample (see Figure 5.12(b)) shows the similar nature as of other two samples (MoO₃ and Ag-MoO₃ samples); the strongest peak ≈ 820 cm⁻¹ is also endorsing the XRD result (Figure 5.12(a)); the peak ≈ 942 cm⁻¹ can be referred to oxygen vacancies present in MoO₃ lattice [62, 63]. Figure 5.12(c) shows the Ag 3d XPS spectrum of the corresponding

sample. The $\text{Ag}^{0+} 3d_{5/2}$ and $\text{Ag}^{0+} 3d_{3/2}$ binding energy peaks are positioned at 367.77 eV and 373.77 eV, respectively which are very closed to bulk values (367.9 eV and 373.9 eV) [61]. Furthermore, there is a ≈ 0.32 eV shift towards higher binding energy of the Ag 3d states compared to Ag 3d spectrum of Ag-MoO₃ HSs sample (see Figure 5.10(e)), which is attributed to the partial oxidation of Ag because the combination of Ag and MoO₃ adjusts their Fermi level for HSs sample grown at 550 °C [65].

5.3.5 Field emission and KPFM results

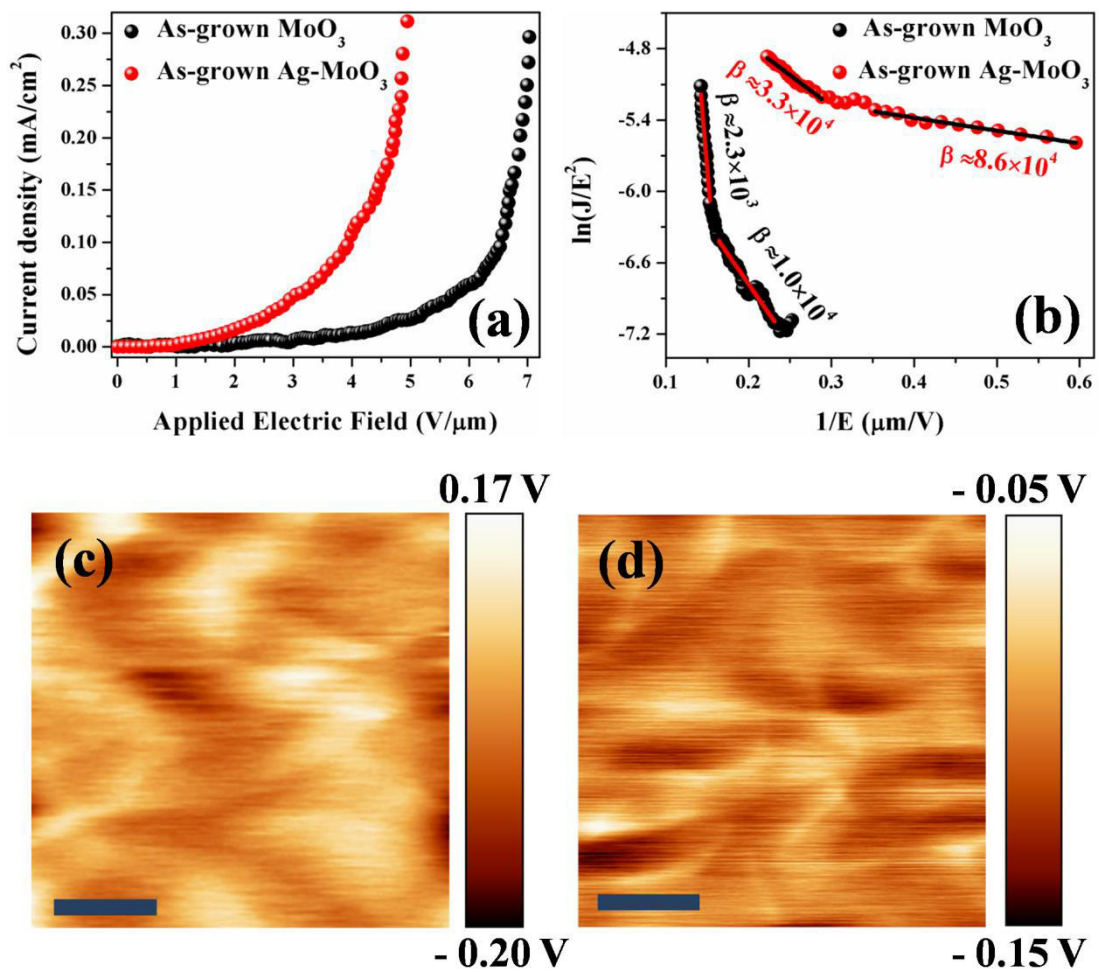


Figure 5.13: (a) Field electron emission current density as a function of applied field (J – E) for the as-grown MoO₃ sample (black) and Ag-MoO₃ heterostructures sample (red); (b) Corresponding Fowler–Nordheim (F – N) plots. Work function mapping images of the as-grown (c) MoO₃ and (d) Ag-MoO₃ heterostructures samples using Kelvin probe force microscopy (KPFM). Scale bars in the images correspond to 2 μm for both cases.

We have investigated the field emission properties of these two as-grown samples MoO₃ and Ag-MoO₃ heterostructures. Figure 5.13(a) displays the field emission current density (J) versus applied electric field (E) plot with $\approx 70 \mu\text{m}$ anode-sample separation for both the samples. Here, we have defined turn-on field (E_{to}) as the electric field required to draw $10 \mu\text{A}/\text{cm}^2$ current density. So, the turn-on voltages (E_{to}) were obtained about $\approx 3.50 \text{ V}/\mu\text{m}$ and $\approx 1.67 \text{ V}/\mu\text{m}$ for MoO₃ and Ag-MoO₃ samples respectively (see Figure 5.13(a)). To investigate the emission properties of the samples, FE behavior (J vs. E) can be enumerated theoretically by simplified Fowler–Nordheim equation [54]

$$J = (A\beta^2 E^2 / \Phi) \exp(-B\Phi^{3/2} / \beta E) \quad (5.2)$$

$$\text{Or, } \ln(J/E^2) = \ln(A\beta^2 / \Phi) - (B\Phi^{3/2} / \beta) \times (1/E) \quad (5.3)$$

where, J is the FE current density ($\mu\text{A}/\text{cm}^2$), E is the applied electric field (V/μ), A and B are constants with $A = 1.54 \times 10^{-6} \text{ A-eV}/\text{V}^2$ and $B = 6.83 \times 10^3 \text{ eV}^{-3/2} - \text{V}/\mu\text{m}$, β is the field enhancement factor (FEF) and Φ is the work function (eV) of the emitter [53]. β can be calculated by plotting the $\ln(J/E^2)$ vs. $(1/E)$ (called as F-N plot) and finding the slope and using the mathematical expression below

$$\beta = -6830 \times (\Phi)^{3/2} / \text{slope} \quad (5.4)$$

So, smaller slope value correspond higher FEF (β) value [53]. Figure 5.13(b) depicts the F-N plots for both the samples, showing two slopes behavior in two different regions (high field and low field regions). Slope values are found out to be -81.86 and -10.11 for MoO₃ sample and -5.22 and -1.08 for Ag-MoO₃ sample at higher and lower field regions respectively. As the slope values in both field regions are less for Ag-MoO₃ HSs sample compared to MoO₃ sample, so β values will be more for HSs sample than the other one (Equation 5.4). Undoubtedly Ag-MoO₃ sample is presenting better field emission characteristics than MoO₃ sample considering lower E_{to} and higher β . Electrons emission from different energy levels at different applied electric field can interpret this two-slope nature in the F–N plots [53, 66]. So, in the low field regime, electrons, coming only from the conduction band (CB) are participating into emission current density. But at higher applied electric field, not only the electrons coming from CB but also the electrons coming from the valance band (VB) are taking part into the current density. Hence, one can presume that the effective work function (Φ_{eff}) at higher field region will be the work function of the emitter (Φ) with an addition of band gap (E_g). It is well known that β depends on the geometry of the emitter as well as the work function of the emitter. However, we haven't found much geometrical difference in our

two category samples (see Table 5.1); effectively the EFE (β) is expected to be dependent only on the work function of the emitter.

We have experimentally evaluated the work function of these two samples using Kelvin probe force microscopy (KPFM) technique, which is considered to be a suitable non-contact technique. When an AFM tip is brought close to the sample surface, an electrical force will be acted between the tip and sample surface, because of their Fermi energy levels differences. An AC voltage is applied to the tip to generate an oscillating electrostatic force between the tip and the sample surface and an apparent contact potential difference (V_{CPD}) will form. Then an external DC potential (V_{DC}) with the same value as V_{CPD} in opposite direction is required to nullify the electrostatic force [53, 67]. So, the mapping of this nullifying V_{DC} versus the lateral position coordinate composes the work function mapping image (called KPFM image) of the sample surface. Therefore, the work function of the sample surface can be evaluated by using the following expression [53, 67]

$$V_{DC} = V_{CPD} = -(\Phi_{tip} - \Phi_{sample})/e \quad (5.5)$$

where, Φ_{sample} and Φ_{tip} are the work functions of the sample and tip, respectively. The work function of the tip has been calibrated with respect to standard HOPG sample and comes out to be $\Phi_{tip} = 5.8$ eV. So, Φ_{sample} will be

$$\Phi_{sample} = \Phi_{tip} + eV_{CPD} \quad (5.6)$$

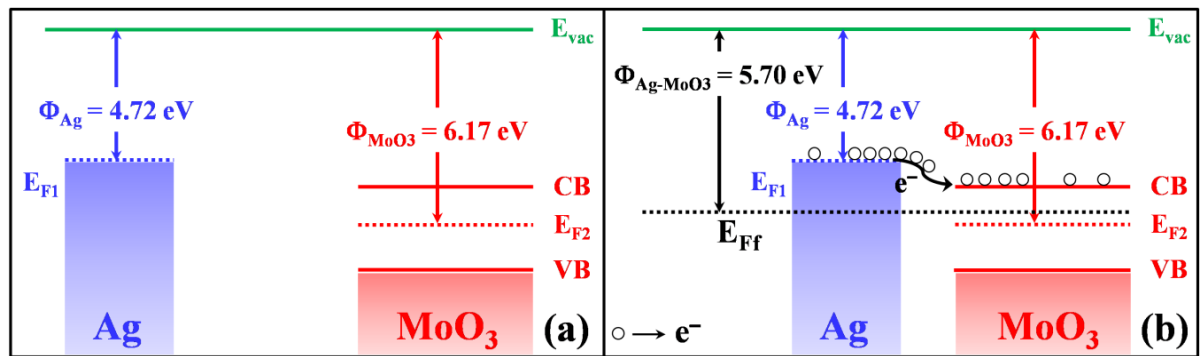


Figure 5.14: (a) Schematic illustration of energy levels of silver and MoO₃ separately. (b) Schematic representation of energy levels when Ag NP is on the surface of MoO₃, showing the uniform Fermi energy level due to the transfer of electron from Ag NP to MoO₃. (The mentioned work function values $\Phi_{MoO3} = 6.17$ eV and $\Phi_{Ag-MoO3} = 5.70$ eV are obtained from our samples using KPFM technique).

So, lower value of V_{CPD} eventually signifies the lower work function. Figures 5.13(c) and 5.13(d) represent the work function mapping images (KPFM images) of the as-grown MoO₃

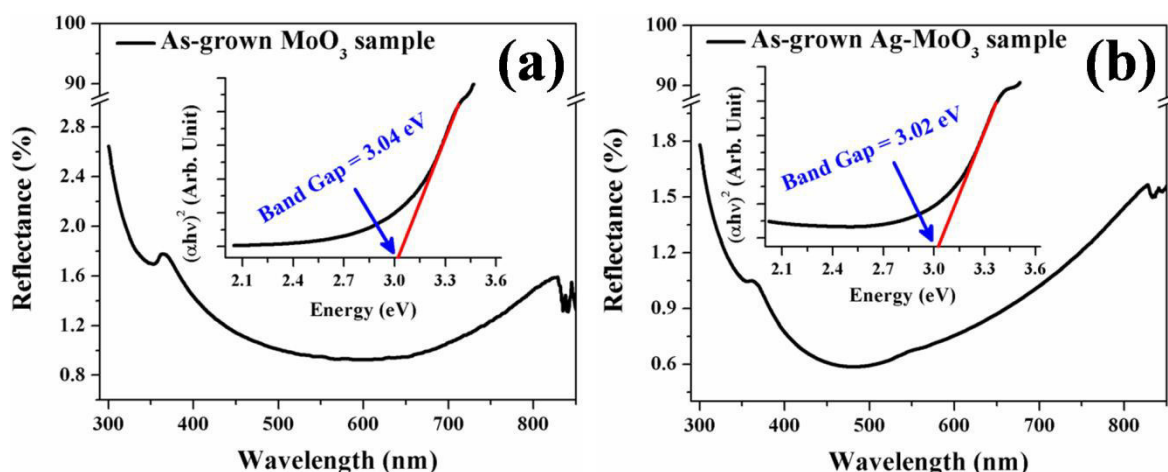


Figure 5.15: UV-Vis reflectance data from (a) MoO₃ and (b) Ag-MoO₃ samples; insets of (a) and (b) are the corresponding $(\alpha h\nu)^2$ vs. $h\nu$ plots.

sample and Ag-MoO₃ heterostructures sample, respectively and the work function values are found to be $\approx 6.17 \pm 0.05$ eV and $\approx 5.70 \pm 0.05$ eV for respective samples. So far, it is utterly clear from both the experimental results that Ag-MoO₃ HS shows lower work function than MoO₃. The work function of Ag ($\Phi_{\text{Ag}} = 4.74$ eV) [68] is smaller than MoO₃ ($\Phi_{\text{MoO}_3} = 6.17$ eV; experimentally measured value), as a consequence Fermi energy level position of Ag (E_{F1}) is higher than that of MoO₃ (E_{F2}) (Figure 5.14(a)). When Ag NP is on MoO₃ surface, electrons can be easily transferred from Ag NP to the surface of MoO₃, resulting in a uniform Fermi energy level (E_{Ff}) in the Ag-MoO₃ HS shown in Figure 5.14(b). The transferred electrons subsequently are assembled at the interface of Ag and MoO₃. Subsequently, work function of HS will be reduced by lifting the Fermi energy level of MoO₃ (E_{F2}) towards vacuum (E_{v}), (see Figure 5.14(b)). This is the main origin for obtaining lower work function value of Ag-MoO₃ HSs sample than MoO₃ sample from KPFM measurements, which in turn improve the field emission performance of Ag-MoO₃ HSs sample over MoO₃ sample. Since work function values of the emitters are known, easily one can calculate the effective work function values (Φ_{eff}) for the two field regimes as discussed earlier and henceforth FEF (β) can be calculated using the relation (5.4). For as-grown MoO₃ sample effective work function (Φ_{eff}) values will be ≈ 6.17 eV and ≈ 9.21 eV in low field and high field zones respectively, taking the experimentally measured band gap value ≈ 3.04 eV from UV-Vis measurements (presented in Figure 5.15(a)). Whereas effective work function (Φ_{eff}) values are determined to be ≈ 5.70 eV and ≈ 8.72 eV at low field and high field regimes respectively for Ag-MoO₃ HSs sample, taking ≈ 3.02 eV as band gap (see Figure 5.15(b)). We have theoretically calculated the work functions for bare MoO₃ and Ag/MoO₃ heterostructures in absence as

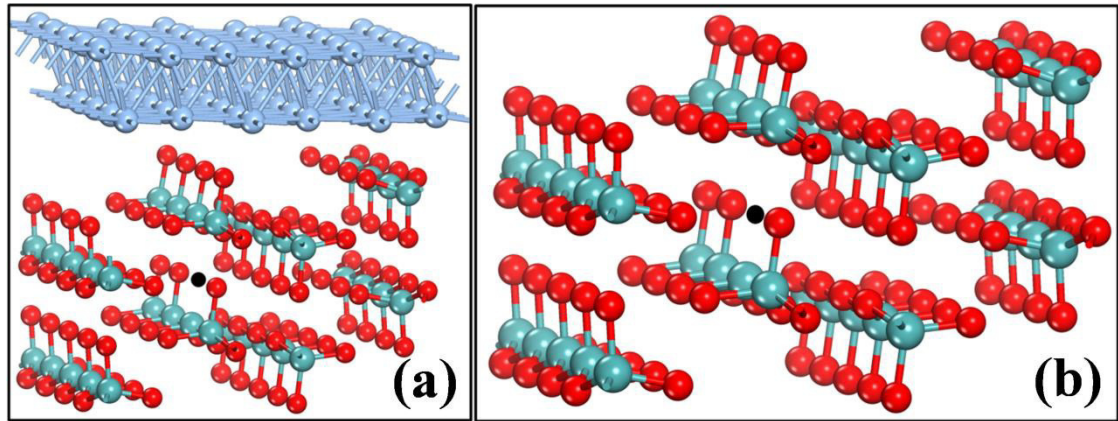


Figure 5.16: The optimized structures of (a) Ag(111)/MoO₃(100), (b) MoO₃(100) in presence of oxygen vacancy. The black sphere represents oxygen vacancy site in the structures.

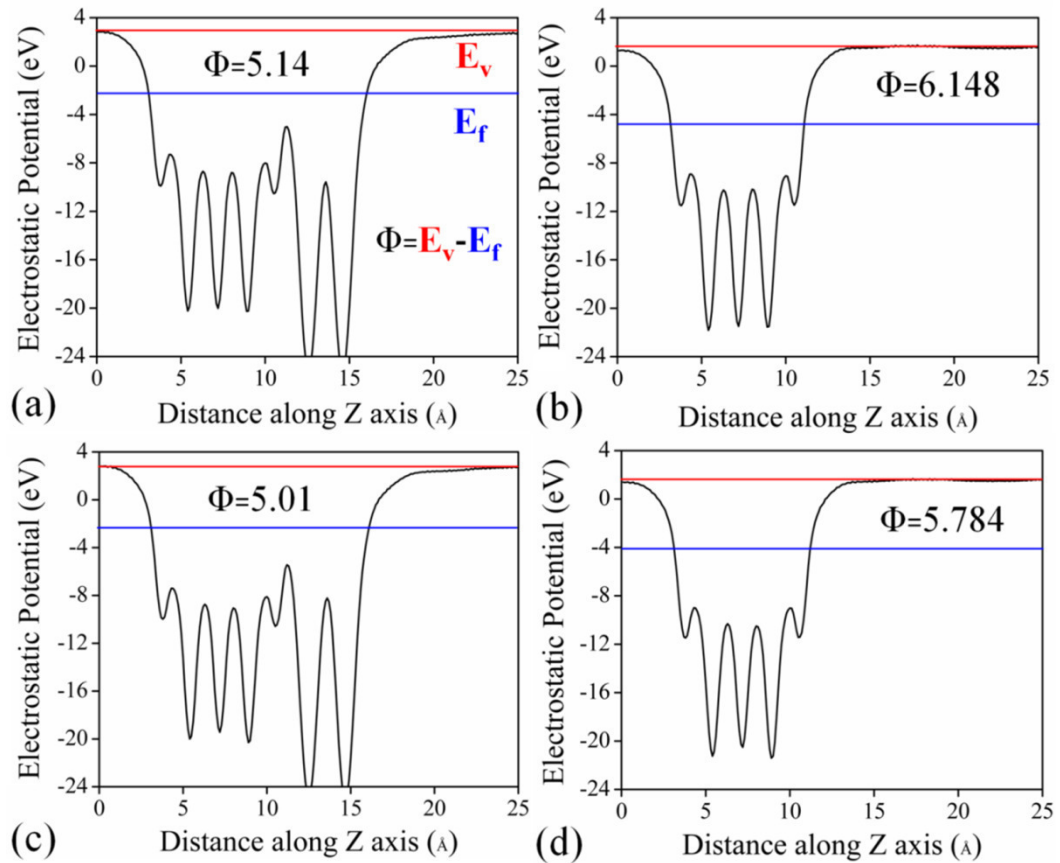


Figure 5.17: Electrostatic potential along the z -axis considering vacuum as the reference energy for (a) Ag(111)/MoO₃(100) (b) MoO₃(100) (c) O vacancy in Ag(111)/MoO₃(100) and (d) O vacancy in MoO₃(100). Energy of the Fermi and vacuum level is represented by E_f and E_v , respectively. Φ defines the work function of the defined surface.

well as presence of oxygen vacancy in MoO₃ as shown in Figure 5.17. For example, the relaxed structures of Ag(111)/MoO₃(100) and MoO₃(100) considered for the DFT

calculations with the oxygen vacancy (black sphere) are shown in Figures 5.16(a) and 5.16(b) respectively. Figures 5.17(a) and 5.17(b) represent work functions for Ag(111)/MoO₃(100) and MoO₃(100) structures respectively without considering oxygen vacancy in them. Interestingly, we have found that indeed the presence of Ag on MoO₃ structure reduces work function by ≈ 1.0 eV. We have further computed work function values for Ag(111)/MoO₃(100) and MoO₃(100) structures (see Figures 5.17(c) and 5.17(d)) in presence of oxygen vacancy in them (optimized structures are already shown in Figure 5.16). It is noticed that oxygen deficiency in MoO₃(100) and Ag(111)/MoO₃(100) further reduces their effective work function compared to the without oxygen vacancy cases (i.e., with pure MoO₃(100)). It is now crucial to be emphasized that presence of Ag on the oxygen deficient MoO₃ structure provide lowest work function by ≈ 0.77 eV reduction, which is qualitatively in agreement with experimentally observed value (≈ 0.47 eV) and also consistent with previously published result on other material [53]. All the DFT results on work function have been tabulated in Table 5.3. Finally, calculated FEF (β) values are $\approx 2.3 \times 10^3$ and $\approx 1.0 \times 10^4$ for MoO₃ sample and $\approx 3.3 \times 10^4$ and $\approx 8.6 \times 10^4$ for Ag-MoO₃ sample at high field and low

Table 5.3: Work function analysis of pure and oxygen vacant structures MoO₃(001), MoO₃(100), MoO₃(010), Ag(111)/MoO₃(001), Ag(111)/MoO₃(100) and Ag(111)/MoO₃(010) along with the energy values of E_f , E_v and Φ .

Surfaces	E_f (eV)	E_v (eV)	Work function (Φ) ($E_v - E_f$) (eV)
MoO ₃ (100)-pure	-4.74	1.408	6.148
MoO ₃ (001)-pure	-3.775	1.729	5.504
MoO ₃ (010)-pure	-4.359	3.093	7.452
Ag(111)/MoO ₃ (100)-pure	-2.244	2.932	5.176
Ag(111)/MoO ₃ (001)-pure	-1.709	3.136	4.845
Ag(111)/MoO ₃ (010)-pure	-1.748	4.494	6.242
MoO ₃ (100)-O _{vac}	-4.103	1.681	5.784
MoO ₃ (001)-O _{vac}	-3.539	1.801	5.34
MoO ₃ (010)-O _{vac}	-3.757	3.012	6.769
Ag(111)/MoO ₃ (100)-O _{vac}	-2.24	2.765	5.005
Ag(111)/MoO ₃ (001)-O _{vac}	-1.661	3.161	4.822
Ag(111)/MoO ₃ (010)-O _{vac}	-1.647	4.402	6.049

field regimes respectively. So far, our Ag-MoO₃ sample exhibits the lowest turn-on field and the highest field enhancement factor among all the reported values especially in MoO₃ class [19–21, 55, 69]. To the best of our knowledge, there are no such reports on field emission from oxygen deficient MoO₃ in conjunction with metal NPs. Ag NPs on oxygen deficient MoO₃ surfaces makes Ag-MoO₃ sample as efficient field emitter following its lower tunneling barrier due to the reduction in Φ by charge transfer induced shifting of Fermi level towards vacuum [48–50, 52].

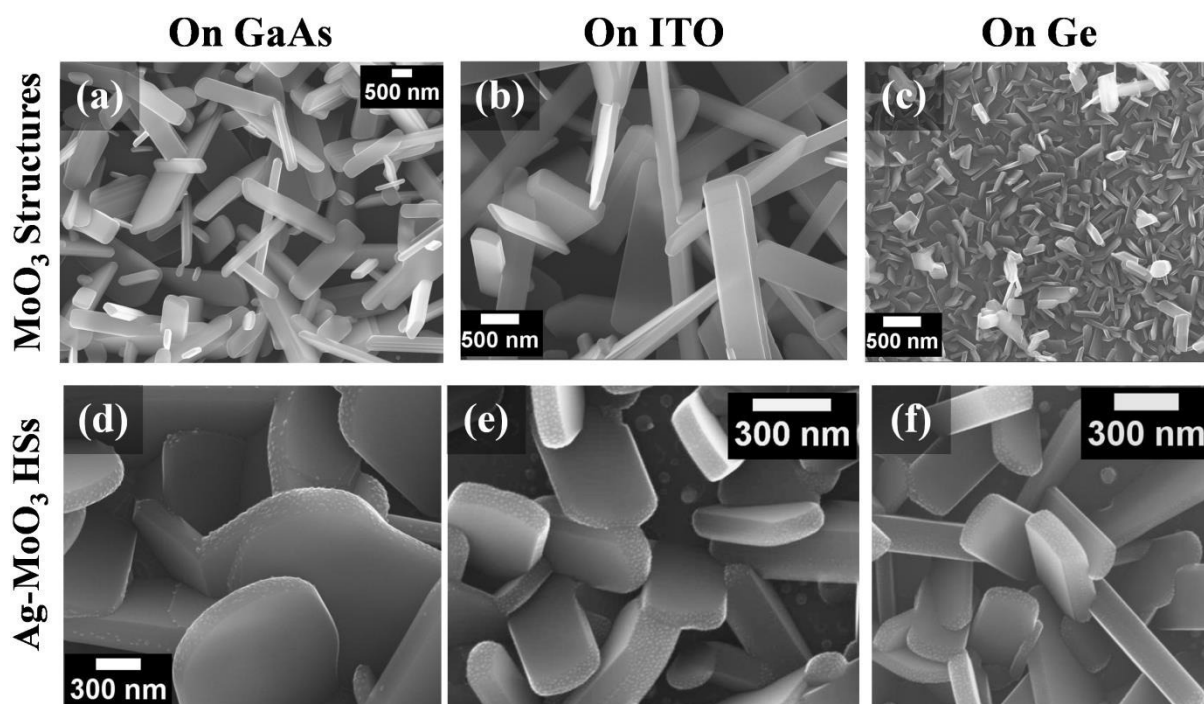


Figure 5.18: SEM micrographs of as-grown MoO₃ structures grown on (a) GaAs, (b) ITO and (c) Ge substrates and Ag-MoO₃ HSs on (d) GaAs, (e) ITO and (f) Ge substrates.

Finally, MoO₃ structures and Ag-MoO₃ HSs were also synthesized with high density on commercially available different substrates as GaAs, ITO and Ge; their corresponding morphologies have been presented in Figure 5.18. We have retained the same growth parameters as earlier except for the Ge substrate, the substrate temperature was 530 °C and rests were unchanged. We have chosen different temperature for Ge substrate as germanium oxide formation will be started above 550 °C [51]. We haven't recognized any significant change in their morphology affected by the substrate for both as-grown MoO₃ and Ag-MoO₃ structures. Here also, all the Ag NPs are decorated on MoO₃ surfaces except MoO₃(010) surface as happened like Si substrate. The growth of MoO₃ structures and especially the Ag-

MoO₃ HSs are almost independent of substrates; furthermore site specific Ag NPs decoration on MoO₃ surfaces is substrate independent phenomena.

5.4 Conclusion

In summary, we have reported a simple technique to grow packed MoO₃ structures and Ag-MoO₃ HSs on varied substrates in a single step process. XRD and TEM data reveal the orthorhombic phase of MoO₃ (α -MoO₃) with [001] > [100] >> [010] growth rate order, oriented along [0 2k 0] direction. All the Ag NPs are decorated on specific MoO₃ surfaces ((100) and (001)) following the surface energetics. We have demonstrated the probable growth mechanism for site specific Ag decoration on MoO₃ surfaces by calculating surface energies of Ag(111)/MoO₃(100), Ag(111)/MoO₃(010) and Ag(111)/MoO₃(001) structures employing density functional theory (DFT). Computed higher surface energies of MoO₃(100) and (001) surfaces compared to (010), made them available for site specific decoration of Ag NPs during growth. Site specific Ag decoration is almost a substrate independent phenomenon. To best of our knowledge, we did not find any reports where MoO₃(010) has been experimentally found to be weakly interacting and stable surface compared to its other surfaces. We have explored enhanced field emission properties of Ag-MoO₃ sample compared to MoO₃ sample in terms of ≈ 2.1 times lower turn-on voltage and ≈ 10 times higher field enhancement factor. The reason behind this better FE performance has been assigned to the ≈ 0.47 eV reduction in work function of Ag-MoO₃ sample, as experimentally probed by KPFM technique. The reduction in Φ value of Ag-MoO₃ sample can be understood by the electrons transfer induced lifting Fermi energy of MoO₃ towards vacuum, which we have discussed in details. In the next chapter, the role of ambiances on the growth of site specific silver nanoparticles decorated MoO₃ structures and their applications to robust SERS substrates for detecting sub-micro molar crystal violet (CV) molecules have been discussed.

5.5 References

- [1] P Guha, A Ghosh, R Thapa, E M Kumar, S Kirishwaran, R Singh and P V Satyam, *Nanotechnology* **2017**, 28, 415602.
- [2] B Hu, L Mai, W Chen and F Yang, *ACS Nano* **2009**, 3, 478.
- [3] P F Carcia and E M McCarron, *Thin Solid Films* **1987**, 155, 53.

- [4] T Brezesinski, J Wang, S H Tolbert and B Dunn, *Nat. Mater.* **2010**, 9, 146.
- [5] D O Scanlon, G W Watson, D J Payne, G R Atkinson, R G Egddell and D S L Law, *J. Phys. Chem. C* **2010**, 114, 4636.
- [6] T Ressler, R E Jentoft, J Wienold, M M Gunter and O Timpe, *J. Phys. Chem. B* **2000**, 104, 6360.
- [7] V Bhosle, A Tiwaria and J Narayan, *J. Appl. Phys.* **2005**, 97, 083539.
- [8] J N Yao, K Hashimoto and A Fujishima, *Nature* **1992**, 355, 624.
- [9] C Bechinger, S Ferrere, A Zaban, J Sprague and B A Gregg, *Nature* **1996**, 383, 608.
- [10] K Gesheva, A Szekeres and T Ivanova, *Solar. Energy Mater. Solar. Cells* **2003**, 76, 563.
- [11] E Comini, L Yubao, Y Brando and G Sberveglieri, *Chem. Phys. Lett.* **2005**, 407, 368.
- [12] M B Rahmani, S H Keshmiri, J Yu, A Z Sadek, L Al-Mashat, A Moafi, K Latham, Y X Li, W Wlodarski and K Kalantar-zadeh, *Sens. Actuators, B* **2010**, 145, 13.
- [13] S S Sanu, E Prabhu, V Jayaraman, K I Gnanasekar, T K Seshagiri and T Gnanasekaran, *Sens. Actuators, B* **2004**, 101, 161.
- [14] Y Chen, C Lu, L Xu, Y Ma, W Hou and J J Zhu, *CrystEngComm* **2010**, 12, 3740.
- [15] L Cheng, M Shao, X Wang and H Hu, *Chem. Eur. J.* **2009**, 15, 2310.
- [16] D Lee, D J Seong, I Jo, F Xiang, R Dong, S Oh and H Hwang, *Appl. Phys. Lett.* **2007**, 90, 122104.
- [17] D Mariotti, H Lindstrom, A C Bose and K Ostrikov, *Nanotechnology* **2008**, 19, 495302.
- [18] L Q Mai, B Hu, W Chen, Y Y Qi, C S Lao, R S Yang, Y Dai and Z L Wang, *Adv. Mater.* **2007**, 19, 3712.
- [19] J Zhou, S Z Deng, N S Xu, J Chen and J C She, *Appl. Phys. Lett.* **2003**, 83, 2653.
- [20] B Yan, Z Zheng, J Zhang, H Gong, Z Shen, W Huang and T Yu, *J. Phys. Chem. C* **2009**, 113, 20259.
- [21] Y B Li, Y Bando, D Golberg and K Kurashima, *Appl. Phys. Lett.* **2002**, 81, 5048.
- [22] S Balendhran, J Deng, J Z Ou, S Walia, J Scott, J Tang, K L Wang, M R Field, S Russo, S Zhuiykov, M S Strano, N Medhekar, S Sriram, M Bhaskaran and K Kalantar-zadeh, *Adv. Mater.* **2013**, 25, 109.
- [23] P S Wang, I W Wu, W H Tseng, M H Chen and C I Wu, *Appl. Phys. Lett.* **2011**, 98, 173302.
- [24] R Linag, H Cao and Q Qian, *Chem. Commun.* **2011**, 47, 10305.
- [25] D Xiang, C Han, J Zhang and W Chen, *Sci. Rep.* **2014**, 4, 4891.

- [26] X Hu, W Zhang, X Liu, Y Mei and Y Huang *Chem. Soc. Rev.* **2015**, *44*, 2376.
- [27] W Dong, H Huang, Y Zhu, X Li, X Wang, C Li, B Chen, G Wang and Z Shi, *Nanotechnology* **2012**, *23*, 425602.
- [28] H Sinaim, A Phuruangrat, S Thongtem and T Thongtem, *Mater. Chem. Phys.* **2012**, *132*, 358.
- [29] Y Wang, X Zhang, Z Luo, X Huang, C Tan, H Li, B Zheng, B Li, Y Huang, J Yang, Y Zong, Y Ying and H Zhang, *Nanoscale* **2014**, *6*, 12340.
- [30] Y Xu, X Cao and Y Zhang, *Can. J. Chem.* **2014**, *92*, 16.
- [31] L Zheng, Y Xu, D Jin and Y Xie, *Chem. Mater.* **2009**, *21*, 5681.
- [32] L Kihlberg, *Arkiv. Kemi.* **1964**, *21*, 357.
- [33] M Chen, U V Waghmare, C M Frienda and E A Kaxiras, *J. Chem. Phys.* **1998**, *109*, 6854.
- [34] A Michalak, K Hermann and M Witko, *Surf. Sci.* **1996**, *366*, 323.
- [35] F Li and Z Chen, *Nanoscale* **2013**, *5*, 5321.
- [36] M Wang, X X Song, X L Cheng, X Zhou, X F Zhang, Z Cai, Y M Xu, S Gao, H Zhao and L H Huo, *RSC Adv.* **2015**, *5*, 85248.
- [37] S Hu and X Wang, *J. Am. Chem. Soc.* **2008**, *130*, 8126.
- [38] L Cai, P M Rao and X Zheng, *Nano Lett.* **2011**, *11*, 872.
- [39] S Wang, Y Zhang, X Ma, W Wang, X Li, Z Zhang and Y Qian, *Solid State Commun.* **2005**, *136*, 283.
- [40] C V Krishnan, J Chen, C Burger and B Chu, *J. Phys. Chem. B* **2006**, *110*, 20182.
- [41] K Kalantar-zadeh, J Tang, M Wang, K L Wang, A Shailos, K Galatsis, R Kojima, V Strong, A Lech, W Wlodarski and R B Kaner, *Nanoscale* **2010**, *3*, 429.
- [42] X W Lou and H C Zeng, *J. Am. Chem. Soc.* **2003**, *125*, 2697.
- [43] W Li, F Cheng, Z Tao and J Chen, *J. Phys. Chem. B* **2006**, *110*, 119.
- [44] I Navas, R Vinodkumar, K J Lethy, A P Detty, V Ganesan, V Sathe and V P M Pillai, *J. Phys. D: Appl. Phys.* **2009**, *42*, 175305.
- [45] D D Yao, J Z Ou, K Latham, S Zhuikyov, A P O'Mullane, K Kalantar-zadeh, *Cryst. Growth Des.* **2012**, *12*, 1865.
- [46] Y Li and Y Bando, *Chem. Phys. Lett.* **2002**, *364*, 484.
- [47] K Galatsis, Y X Li, W Wlodarski, E Comini, G Sberveglieri, C Cantalini, S Santucci and M Passacantando, *Sens. Actuators, B* **2002**, *83*, 276.
- [48] J Ding, Y Chai, Q Liu, X Liu, J Ren and W L Dai, *J. Phys. Chem. C* **2016**, *120*, 4345.

- [49] A Ghosh, P Guha, A K Samantara, B K Jena, R Bar, S K Ray and P V Satyam, *ACS Appl. Mater. Interfaces* **2015**, 7, 9486.
- [50] L Zhang, J C Yu, H Y Yip, Q Li, K W Kwong, A W Xu and P K Wong, *Langmuir* **2003**, 19, 10372.
- [51] A Ghosh, P Guha, S Mukherjee, R Bar, S K Ray and P V Satyam, *Appl. Phys. Lett.* **2016**, 109, 123105.
- [52] P V Kamat and B Shanghavi, *J. Phys. Chem. B* **1997**, 101, 7675.
- [53] A Ghosh, P Guha, R Thapa, S Selvaraj, M Kumar, B Rakshit, T Dash, R Bar, S K Ray and P V Satyam, *Nanotechnology* **2016**, 27, 125701.
- [54] R H Fowler and L Nordheim, *Proc. R. Soc. London Ser. A* **1928**, 119, 173.
- [55] G Wei, W Qin, D Zhang, G Wang, R Kim, K Zheng and L Wang, *J. Alloys Compd.* **2009**, 481, 417.
- [56] G Kresse and J Furthmüller, *Comput. Mat. Sci.* **1996**, 6, 15.
- [57] J P Perdew, K Burke and M Ernzerhof, *Phys. Rev. Lett.* **1996**, 77, 3865.
- [58] P E Blöchl, *Phys. Rev. B* **1994**, 50, 17953.
- [59] A Ghosh, R R Juluri, P Guha, R Sathyavathi, A Dash, B K Jena and P V Satyam, *J. Phys. D: Appl. Phys.* **2015**, 48, 055303.
- [60] B Dasgupta, Y Ren, L M Wong, L Kong, E S Tok, W K Chim and S Y Chiam, *J. Phys. Chem. C* **2015**, 119, 10592.
- [61] G Schon, *Acta Chem. Scand.* **1973**, 27, 2623.
- [62] M A Py, P E Schmid and J T Vallin, *Nuov Cim B* **1977**, 38, 271.
- [63] D Wang, J N Li, Y Zhou, D H Xu, X Xiong, R W Peng and M Wang, *Appl. Phys. Lett.* **2016**, 108, 053107.
- [64] M Dieterle, G Weinberg and G Mestl, *Phys. Chem. Chem. Phys.* **2002**, 4, 812.
- [65] W Song, X Han, L Chen, Y Yang, B Tang, W Ji, W Ruan, W Xu, B Zhao and Y Ozaki, *J. Raman Spectrosc.* **2010**, 41, 907.
- [66] N S Ramgir, D J Late, A B Bhise, I S Mulla, M A More, D S Joag and V K Pillai, *Nanotechnology* **2006**, 17, 2730.
- [67] W Melitz, J Shen, A C Kummel and S Lee, *Surf. Sci. Rep.* **2011**, 66, 1.
- [68] M Chelvayohan and C H B Mee, *J. Phys. C: Solid State Phys.* **1982**, 15, 2305.
- [69] Q W Yang, Z R Wei, M Gao, Y Chen, J Xu, C L Chen and Y Lin, *J. Alloys Compd.* **2013**, 576, 332.

Chapter 6

Role of Ambience on the Growth of Site Specific Ag Nanoparticles Decorated MoO₃ Structures: Applications to Surface Enhancement Raman Scattering

6.1 Introduction

In the previous chapter, incorporation of silver (Ag) nanoparticles (NPs) on MoO₃ surfaces in a *single step* growth process has been discussed. Here, present work deals with the experimental observations on the role of ambience during the growth process as well as the detection of sub-micro molar crystal violet (CV) molecules by surface enhancement Raman scattering (SERS) technique using Ag-MoO₃ heterostructures (HSs)/Si substrates. A ≈ 4 nm Ag thin film was deposited on as-grown MoO₃ structures (Ss)/Si and subsequently annealed at 450 °C in different ambiances in order to produce site specific Ag NPs decorated MoO₃ structures; the growth of site specific Ag NPs decoration on MoO₃ surfaces has been observed only in argon atmosphere. These Ag-MoO₃ HSs/Si samples have been used as *free standing* SERS substrates to detect sub-micro molar CV molecules (lowest 1 μ M CV) with an analytical enhancement factor (AEF) of $\approx 10^4$ and with high repeatability for 5 μ M CV [1].

In previous chapter, we have described the growth of site specific Ag nanoparticle (NP) decorated α -MoO₃ structures in *single step* process on varied substrates. Interestingly, Ag NPs are not present on all the surface of the MoO₃ structures. We have demonstrated the

This chapter contains unpublished work by P Guha et al.

probable growth mechanism for site specific Ag decoration on MoO₃ surfaces from binding energy calculations employing density functional theory (DFT). From the DFT studies, the binding energy of Ag(111) is found to be higher for MoO₃(100) and MoO₃(001) surfaces (≈ -0.98 eV), compared to the MoO₃(010) surface (≈ -0.15 eV) and thus it is likely that Ag NP formation is not favorable on the MoO₃(010) surface [2]. In this work, we report on the effect of ambience to obtain the Ag-MoO₃ HSs growth by annealing under various conditions, such as argon flow, air, low vacuum (LV) and high vacuum (HV) and the results would be compared to our previously as-grown site specific Ag NPs decorated MoO₃ Ss.

Molybdenum oxides, wide band gap (2.6–3.2 eV) [3, 4] n-type (intrinsically) semiconductors are found to be one the most fascinating transition metal oxide (TMO), as for their unique structural, electrical, optical, mechanical properties and multi-directional applications [3, 5–8]. Very recently different metals such as Ag, Au, Li, Ce or Zr have been conjugated with molybdenum oxides structures to improve the electrical, optical, photocatalytic, sensing properties particularly by surface enhanced Raman scattering (SERS) technique [9–12]. SERS technique (discovered in the late 1970s) is a unique technique to detect low concentrated molecules adsorbed on rough or nanostructured plasmonic (i.e., noble metals) substrates [13–15]. The success and the usefulness of the SERS technique depends on several important factors, including structure and surface properties of the substrate, interaction between target analyte molecules and substrate, orientation of analyte molecules, and wavelength of light that should ideally match the surface plasmon resonance (SPR) absorption of the metal substrate [13, 16, 17]. SERS substrates are generally made of pure metallic nanostructures (in particular Au, Ag and Cu as their SPR falls in the visible regime) of various size, shape and architectures [9–12, 18–21].

6.2 Experimental

The α -MoO₃ structures (Ss) were grown in a horizontal quartz tube (length ≈ 100 cm and inner diameter ≈ 4.5 cm) furnace with single zone side entry on diverse single crystalline silicon substrates by vapor-solid (VS) mechanism [2], mentioned in the previous chapter (chapter 5) in detail. Following this, a ≈ 4 nm thick silver (Ag) film was deposited on the MoO₃ structures/Si specimens by physical vapor deposition (PVD) technique in high vacuum condition ($\approx 1.2 \times 10^{-6}$ mbar), using Mo boat. These ≈ 4 nm Ag/MoO₃/Si samples have been

annealed at 450 °C for 20 min in various ambient conditions: a) under 45 sccm Ar flow, b) in air, c) in low vacuum (LV) ($\approx 10^{-3}$ mbar) and d) in high vacuum (HV) ($\approx 10^{-6}$ mbar).

Surface morphology, shape and size, structural characterizations of as-grown samples were examined using field emission gun based scanning electron microscopy (FEG-SEM) with 20 kV electrons (Neon 40 cross-beam system, M/S Carl Zeiss GmbH).

Surface enhanced Raman scattering (SERS) measurements were carried out using micro-Raman spectrometer having 2 cm^{-1} spectral resolution using 514.5 nm (green laser) excitation (power $\approx 40\text{ mW}$). All SERS measurements were carried out in a backscattering geometry, using a 100 \times microscope objective lens for focusing with a numerical aperture of 0.7 with a spot size of $\approx 2\text{ }\mu\text{m}$. The molar concentrations of crystal violet (CV) having different concentrations (1 μM , 5 μM etc.) were prepared by dissolving the required amount of CV in ethanol. For each test, $\approx 10\text{ }\mu\text{l}$ of the CV solution was dropped onto each of the SERS substrates and dried at room temperature.

6.3 Results and discussion

6.3.1 Ambient dependency: structural characterization

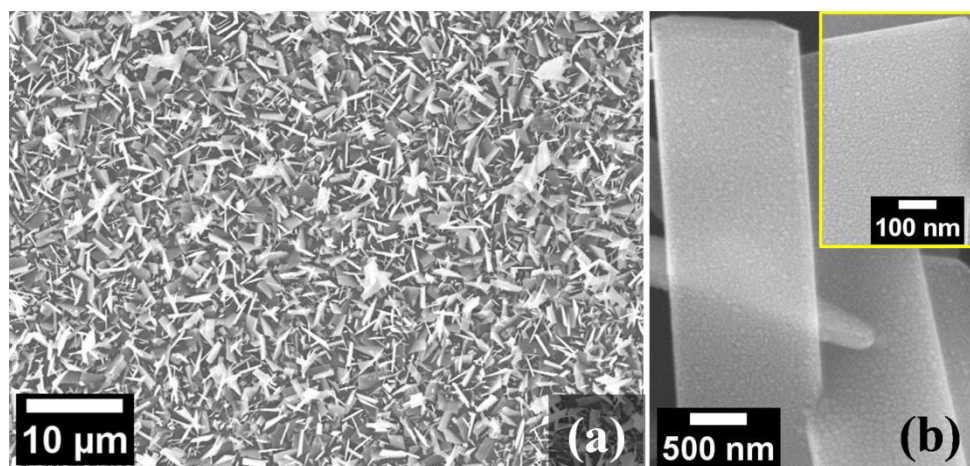


Figure 6.1: (a) Low magnification and (b) high magnification SEM images of $\approx 4\text{ nm}$ Ag deposited on $\alpha\text{-MoO}_3$ structures/Si, showing the MoO_3 structures fully covered with silver nanoparticles.

Figure 6.1 shows the SEM observations of $\approx 4\text{ nm}$ thick silver film deposited on as-grown $\alpha\text{-MoO}_3$ structures (Ss)/Si (i.e., first $\alpha\text{-MoO}_3$ Ss have been grown on Si and then 4 nm silver has been deposited); MoO_3 Ss have been fully covered with silver nanoparticles. Now

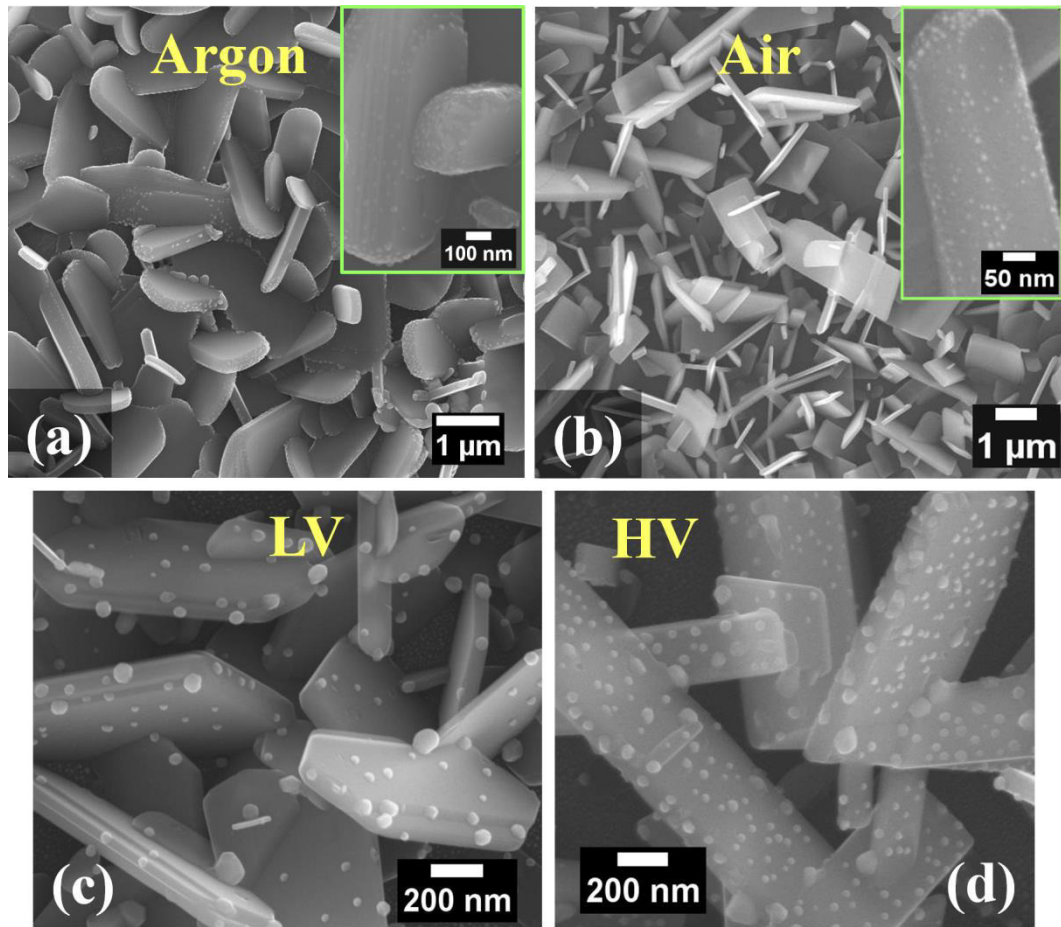


Figure 6.2: ≈ 4 nm Ag/MoO₃ Ss/Si annealed at 450 °C for 20 min in different ambient conditions: (a) 45 sccm argon flow, (b) air, (c) low vacuum (LV; $\approx 10^{-3}$ mbar) and (d) high vacuum (HV; $\approx 10^{-6}$ mbar).

this specimen has been annealed in different ambiances and SEM micrographs of corresponding samples are presented in Figure 6.2. Figures 6.2(a), 6.2(b), 6.2(c) and 6.2(d) and the insets of Figures 6.2(a) and 6.2(b) present the low magnification and high magnification SEM images of the 4 nm Ag/MoO₃/Si @ 450 °C for 20 min under 45 sccm Ar flow, in atmospheric condition, under LV ($\approx 10^{-3}$ mbar) and HV ($\approx 10^{-6}$ mbar), respectively. It has been observed from the SEM images that, only under argon ambience site specific silver nanoparticles decorated MoO₃ structures have been grown, which mimics our previous Ag-MoO₃ heterostructures (HSs). For air annealed sample, few silver nanoparticles are still present on MoO₃(010) surface (see the inset of Figure 6.2(b)). The plausible reason behind the formation of Ag NPs on MoO₃ surfaces could be due to the suitable surface energetic between Ag and MoO₃ surfaces (for example, MoO₃(100), MoO₃(010), MoO₃(001) etc.) at that growth conditions (ambience, temperature, vapor pressure etc.) Here only the experimental observations have been presented.

6.3.2 SERS substrates: detection of crystal violet (CV) molecules

Now, we will discuss about the SERS results for CV molecules detection. 1 μM and 5 μM concentrated CV molecules have been dropcasted (10 μL) on 4 nm Ag/MoO₃/Si @ 450 °C for 20 min under 45 sccm Ar flow and also on our as-grown Ag-MoO₃ HSs (previously grown in a *single step* process mentioned in chapter 5. We have also dropcasted 1 mM CV (10 μL) on bare silicon and Ag nanoparticles grown on silicon to enable comparison with Ag-MoO₃ samples. Analytical enhancement factors (AEF) have calculated for the characteristic peak (taking 1176 cm^{-1}) of crystal violet using the following equation [16, 20, 21]

$$\text{AEF} = (I_{\text{SERS}}/C_{\text{SERS}})/(I_{\text{RS}}/C_{\text{RS}}) \quad (6.1)$$

where, I_{SERS} and I_{RS} are the Raman signals under SERS and normal conditions, respectively; C_{SERS} and C_{RS} are the concentrations of the CV molecules in the SERS and normal samples. Figure 6.3(a) shows the SERS spectrum of 5 μM concentrated CV molecules dropcasted on 4 nm Ag/MoO₃ structures/Si annealed at 450 °C under argon atmosphere with 514.5 nm excitation. For this sample, the AEF are found to be 6.9×10^3 . This enhanced SERS activity produced by Ag-MoO₃/Si sample compared Ag/Si sample can be interpreted in the following manner. UV-vis specular reflectance spectra obtained from 4 nm Ag/MoO₃/Si @ 450 °C (argon atmosphere) and Ag NPs/Si samples have been depicted in Figure 6.3(b) and Figure 6.3(c) respectively. Reflectance minima are observed to be $\approx 30\%$ for Ag NPs/Si system whereas, the reflectance minima has been scaled down to 2% for Ag-MoO₃/Si sample. So, Ag-MoO₃/Si specimen shows very good antireflection property compared to Ag/Si system and the antireflection nature of Ag-MoO₃/Si can be achieved as MoO₃ produces optical

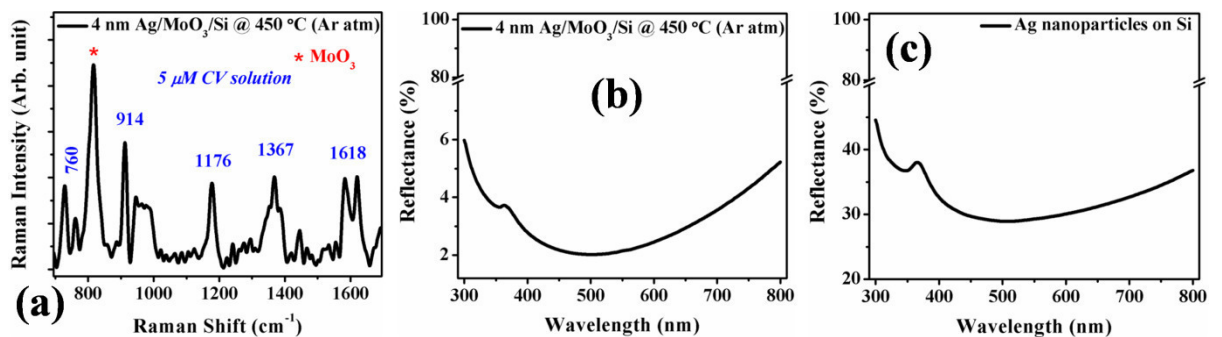


Figure 6.3: (a) SERS spectrum of 5 μM concentration CV on 4 nm Ag/MoO₃ structures/Si annealed at 450 °C under argon atmosphere with 514.5 nm excitation. UV-vis specular reflectance spectra obtained from (b) 4 nm Ag/MoO₃ structures/Si @ 450 °C (argon atmosphere) and (c) Ag nanoparticles/Si samples.

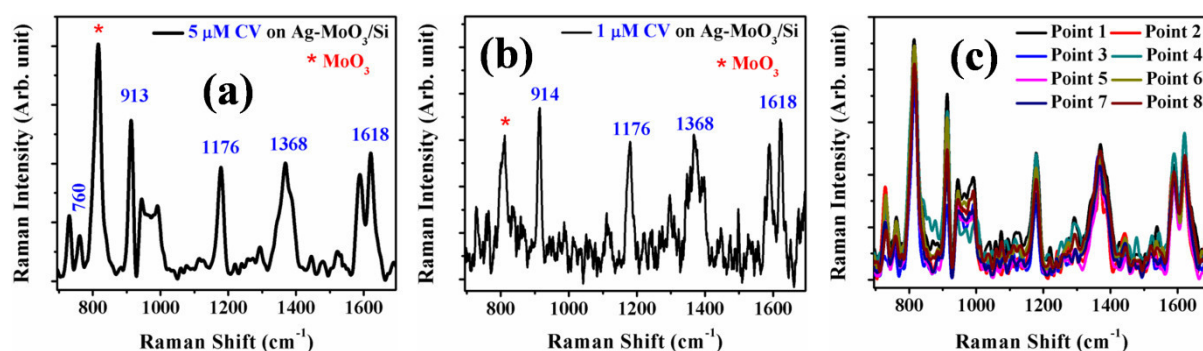


Figure 6.4: (a) SERS spectrum of 5 μM concentration of CV on as-grown Ag-MoO₃ HSs/Si (in a single step process) with 514.5 nm excitation. (b) SERS spectrum of lowest concentrated CV (1 μM) on the Ag-MoO₃ HSs/Si sample with 514.5 nm. (c) Reproducible SERS spectra of CV for 5 μM concentration dropcasted on the as-grown Ag-MoO₃ HSs/Si.

impedance match between air and Si substrate, leading to an exceptional light trapping [16, 22]. We have also performed the SERS measurements for CV dropcasted on as-grown Ag-MoO₃ HSs/Si (grown in a single step) and displayed the results in Figure 6.4. SERS spectrum of CV molecules having 5 μM concentration on 4 nm Ag-MoO₃ HSs/Si with 514.5 nm excitation is presented in Figure 6.4(a); the AEF are calculated to be 8.5×10^3 for this sample. It is also paramount to emphasize that the samples with lower reflectance, exhibit higher SERS signal enhancement, which is in agreement with previous reports [16, 23, 24]. However, CV molecules as low as 1 μM concentration have been found to be detected by our Ag-MoO₃ HSs sample (see Figure 6.4(b)). Figure 6.4(c) represents reproducible SERS spectra of 1 μM CV on Ag-MoO₃ HSs/Si recorded with 514.5 nm, from which we can conclude that Ag-MoO₃/Si samples are reproducible and robust in nature, which is a prerequisite for SERS applications.

6.4 Conclusion

In conclusion, we have observed the experimental findings on the role of different ambiances viz argon (Ar), air, low vacuum (LV) and high vacuum (HV) on energetically favorable site specific silver nanoparticles decorated MoO₃ structures. Site specific growth was found only in Ar ambience; in air ambience, few silver nanoparticles still exist on MoO₃(010) surfaces, implying that vapor pressure and also oxygen partial pressure are very crucial for this growth. These Ag-MoO₃ HSs have been used as free standing SERS substrates to detect sub-micro molar Crystal Violet (as low as 1 μM CV solution) molecule

with an analytical enhancement factor (AEF) of $\approx 10^4$ using 514.5 nm green laser as excitation.

6.5 References

- [1] P Guha, A Ghosh and P V Satyam (On-going work, 2018).
- [2] P Guha, A Ghosh, R Thapa, E M Kumar, S Kirishwaran, R Singh and P V Satyam, *Nanotechnology* **2017**, 28, 415602.
- [3] B Hu, L Mai, W Chen and F Yang, *ACS Nano* **2009**, 3, 478.
- [4] P F Carcia and E M McCarron, *Thin Solid Films* **1987**, 155, 53.
- [5] T Brezesinski, J Wang, S H Tolbert and B Dunn, *Nat. Mater.* **2010**, 9, 146.
- [6] D O Scanlon, G W Watson, D J Payne, G R Atkinson, R G Egdell and D S L Law, *J. Phys. Chem. C* **2010**, 114, 4636.
- [7] E K Fodjo, D W Li, N P Marius, T Albertb and Y T Long, *J. Mater. Chem. A* **2013**, 1, 2558.
- [8] L Mai, F Yang, Y Zhao, X Xu, L Xu, B Hu, Y Luo and H Liu, *Mater. Today* **2011**, 14, 346.
- [9] I A de Castro, R S Datta, J Z Ou, A Castellanos-Gomez, S Sriram, T Daeneke and K Kalantar-zadeh, *Adv. Mater.* **2017**, 29, 1701619.
- [10] H Sinaim, A Phuruangrat, S Thongtem and T Thongtem, *Mater. Chem. Phys.* **2012**, 132, 358.
- [11] G Nagaraju, G T Chandrappa and J Livage, *Bull. Mater. Sci.* **2008**, 31, 367.
- [12] M Feng, M Zhang, J M Song, X G Li and S H Yu, *ACS Nano* **2011**, 5, 6726.
- [13] B Sharma, R R Frontiera, A I Henry, E Ringe and R P Van Duyne, *Mat. Today* **2012**, 15, 16.
- [14] J Kneipp, H Kneipp, . Wittig and K Kneipp, *Nanomed. Nanotech. Bio. Med.* **2010**, 6, 214.
- [15] S E J Bell and N M S Sirimuthu, *Chem. Soc. Rev.* **2008**, 37, 1012.
- [16] A Ghosh, R R Juluri, P Guha, R Sathyavathi, A Dash, B K Jena and P V Satyam, *J. Phys. D: Appl. Phys.* **2015**, 48, 055303.
- [17] A Campion and P Kambhampati, *Chem. Soc. Rev.* **1998**, 27, 241.
- [18] M J Banholzer, J E Millstone, L Qin and C A Mirkin, *Chem. Soc. Rev.* 2008, 37, 885.

- [19] K L Wustholz, A I Henry, J M McMahon, R G Freeman, N Valley M E Piotti, M J Natan, G C Schatz and R P V Duyne, *J. Am. Chem. Soc.* **2010**, *132*, 10903.
- [20] R R Juluri, A Rath, A Ghosh, A Bhukta, R Sathyavathi, D Narayana Rao, K Muller, M Schowalter, K Frank, T Grieb, F Krause, A Rosenauer and P V Satyam, *Sci. Rep.* **2014**, *4*, 4633.
- [21] R R Juluri, A Ghosh, A Bhukta, R Sathyavathi and P V Satyam, *Thin Solid Films* **2015**, *586*, 88.
- [22] S H Lee, G E Jellison, C E Duty and J Xu, *Appl. Phys. Lett.* **2011**, *99*, 153113.
- [23] H Huang, L Liu, P Peng, A Hu and Y Zhou, *J. Appl. Phys.* **2012**, *112*, 123519.
- [24] Y J Oh, J J Kim and K H Jeong, *Adv. Mater.* **2012**, *24*, 2234.

Chapter 7

***P-type* β -MoO₂ Nanostructures on *n*-Si by Hydrogenation Process: Synthesis and Application towards Self-Biased UV-Visible Photodetection**

7.1 Introduction

In the last two chapters, we have discussed about the growth and applications of MoO₃ conjugated with silver nanoparticles. However, MoO₃ has low intrinsic thermal and optical conductivity and weak photoresponse [1], which makes very less number of reports on MoO₃ based photodetectors or any optoelectronic nano-devices. It is reported that electrical conductivity of MoO_x ($2 \leq x \leq 3$) increases with decreasing value of x; MoO₂ discloses metallic behavior [2]. Ng et. al., demonstrated that black colored molybdenum oxide (i.e., MoO_{3-x}), prepared by vacuum annealing of MoO₃, exhibits wide spectral photoresponse across UV–visible–IR range [3]. Furthermore D Xiang et. al., showed no photoresponse of MoO₃ for the visible spectrum. But after H₂ annealing, the photodetector possessed wide visible spectrum response [1]. In this context, we believe that MoO₂ nanostructures can offer superior photoresponse characteristics; so far no report has been made related to this material. Hydrogenation process is not a new process [2, 4–6], rather the application will be new in the scientific community. So, our main motive is to explore MoO₂ material towards photodetection device application. Here, we report a simple growth of

The work presented in this chapter will be published as P Guha et al. [*Nanotechnology* **2018** (under review)].

monoclinic *p*-type MoO₂ nanostructures (NSs) on *n*-type silicon substrate and further explore their potential in UV-visible photodetection application using the as-grown *p*-type MoO₂/*n*-type Si heterojunction itself. Monoclinic MoO₂ NSs (β -MoO₂) have been grown from previously grown α -MoO₃ structures/*n*-type Si via hydrogenation process at 450 °C. We have confirmed using XRD, XPS, and HRTEM that after hydrogenation α -MoO₃ NSs were completely mostly into β -MoO₂ NSs without presence of any sub-oxidized phase of molybdenum oxide. As-grown nanostructured film exhibits very good *p*-type electrical conductivity of $\approx 2.02 \times 10^3 \text{ S-cm}^{-1}$ with hole mobility of $\approx 7.8 \pm 1.3 \text{ cm}^2 \text{ V}^{-1} \text{ Sec}^{-1}$ as evident from Hall measurements. To explore the optoelectronic properties of *p*-type β -MoO₂ NSs, we have fabricated *p*-type MoO₂/*n*-type Si heterojunction (as-grown) photodetector device with Au as top and Al as bottom contacts. The device exhibits peak photoresponsivity of 0.155 A/W with maximum detectivity $1.28 \times 10^{11} \text{ cm-Hz}^{1/2}\text{-W}^{-1}$ and 44% external quantum efficiency around $\approx 436 \text{ nm}$, following its highest photoresponse ($I_{\text{ph}}/I_{\text{d}} \approx 6.4 \times 10^2$) and fast response speed (raising time $\sim 29 \text{ ms}$ and decay time $\sim 38 \text{ ms}$) at -1.5 V . Importantly, this device also shows good self powered high speed (raising time $\sim 47 \text{ ms}$ and decay time $\sim 70 \text{ ms}$) photodetection performance with peak responsivity and detectivity of $\approx 45 \text{ mA/W}$ and $\approx 4.05 \times 10^{10} \text{ cm-Hz}^{1/2}\text{-W}^{-1}$, respectively. This broad-band UV-visible light detection feature can be attributed to the coordinated effects of MoO₂ band-edge absorption, interfacial defects and self absorption in Si. The photodetection behavior of the fabricated device has been understood by proposed energy band diagrams with the help of experimentally derived work function, band gap and valence band maximum position of the as-grown MoO₂ nanostructured thin film [7].

Last few years, expeditious growth in semiconductor optoelectronic devices has transmuted our globe [8, 9]. Photodetector is one of indispensable optoelectronic devices, where optical energy is absorbed and then it is converted to electrical energy (manifested as photocurrent) [10, 11]. Among diverse optoelectronic devices, photodetectors are widely used in optical communication system, medical diagnostics, security monitoring, remote sensing etc [12–14]. In recent times, the field of optoelectronics based on semiconductors at nanoscale has got immense attentions because almost all materials exhibit uniquely tunable physical, chemical, electrical and optical properties in nanoscale dimension, which are significantly different from their bulk [15]. A large research is enduring on integrating various devices using low-dimensional semiconductors with high sensitivity, low noise, wide bandwidth, high reliability and also having low cost [11]. Different materials with various morphologies at nano-dimensions have been exploited for photodetection applications in

different operational range like ultra-violet (UV), visible, and infra-red (IR) [9–11, 14, 16–19]. Very recently, people have started working on molybdenum oxide material grown by different methodologies for the photoelectric device fabrication in UV and visible regime [1, 19, 20].

Among all the molybdenum oxide phases, monoclinic molybdenum dioxide has attracted much attention because of its metallic conductivity, high melting point, high chemical and thermal stabilities [21]. Monoclinic MoO₂ crystal structure falls under P2₁/c space group with lattice parameters $a = 5.620 \text{ \AA}$, $b = 4.860 \text{ \AA}$, $c = 5.630 \text{ \AA}$ and $\beta = 120.94^\circ$ (JCPDS card, #78-1070). Till now, many methods such as hydrothermal reaction, thermal evaporation, solution based synthesis [22–24] etc. have been employed to synthesize MoO₂ material with different morphologies, such as, nano-sized MoO₂ particles [25], hollow MoO₂ sphere [26], MoO₂ sheets [27], large-scale MoO₂ nanowire [28], MoO₂ nanostar [23], MoO₂ hollow fiber [29] and MoO₂ spherical flowerlike nanostructures on carbon nanotubes [30] etc. MoO₂ is very useful material for gas sensing, dye-degradation performance, catalyst for alkane isomerization or oxidation reactions, electron field emissions, Li ion batteries, supercapacitors etc [21, 23–26, 28, 30, 31].

7.2 Experimental

First, we grew densely packed orthorhombic MoO₃ (α -MoO₃) structures (SS) on commercially available ultrasonically cleaned n-type silicon (Si(100)) substrate (resistivity $\approx 6\text{--}14 \text{ }\Omega\text{-cm}$) over a large scale via vapor-solid (VS) mechanism technique (commercially available MoO₃ powder was used as source material), which have been reported earlier by our group [32]. This as-synthesis α -MoO₃ structures/n-type Si(100) was subsequently heated in the same horizontal tubular furnace [32] at 450 °C with a ramping rate 7 °C/min in H₂ atmosphere for 8 hours (ad-mixture of 100 sccm H₂ and 10 sccm Ar) to obtain MoO₂ nanostructures (NSs) on n-type Si (black-colored product) for this work (see Figure 7.1). Room temperature Hall effect measurements were done to probe the type (n-type or p-type) of conductivity of the as-grown sample after growing similar MoO₂ NSs on $\approx 300 \text{ nm}$ SiO₂/Si(100) substrate by following exactly similar growth conditions. It is noteworthy that as-grown MoO₂ sample was found to be *p-type* highly conducting semiconductor (similar to metallic) having hole concentration of $\approx 10^{19} \text{ cm}^{-3}$, conductivity of $\approx 2.02 \times 10^3 \text{ S/cm}$ with hole mobility of $\approx 7.8 \pm 1.23 \text{ cm}^2 \text{ V}^{-1} \text{ Sec}^{-1}$, which is in agreement with earlier results [33, 34].

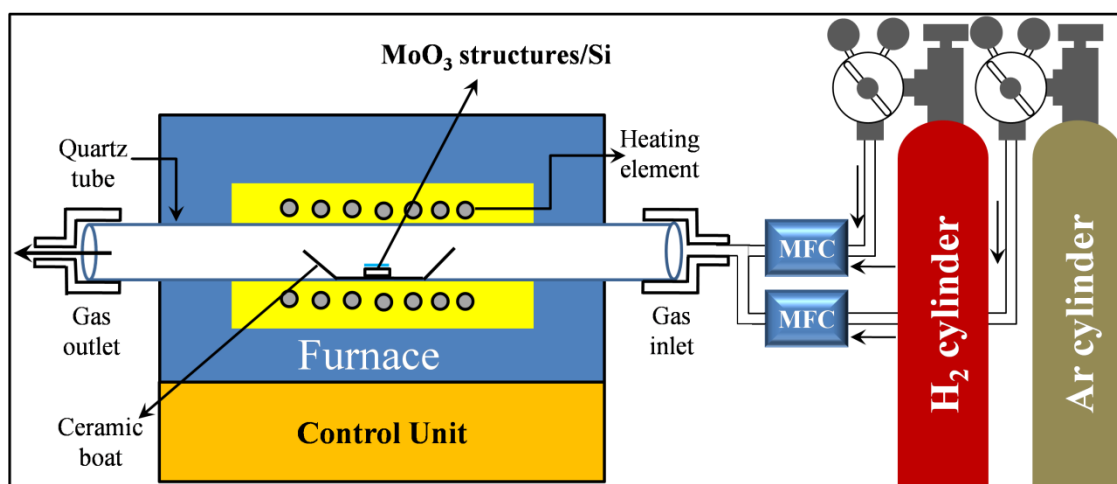


Figure 7.1: Schematic illustration of the single zone horizontal quartz tube furnace that is used for hydrogenation process to grow MoO_2 from MoO_3 .

Structural and morphological characterizations of the as-grown sample was examined by using field emission gun based scanning electron microscope (FEG-SEM, Neon-40, Carl Zeiss) with 20 keV electrons and high resolution transmission electron microscope ((HRTEM JEOL JEM-2010) with 200 keV electrons. For TEM analyses, the as-synthesized sample was scrapped from the substrate, dispersed in methanol followed by ultrasonication for 10 min, and then the solution was drop-casted on carbon coated copper grid. X-ray diffraction (XRD) measurement (Bruker D8 Advance diffractometer with Cu $K\alpha$ radiation ($\lambda = 0.15406$ nm)) was performed to obtain the large scale crystalline property of the as-grown sample. For chemical composition examination of as-grown sample, X-ray photoelectron spectroscopy (XPS) studies were carried out by using PHI 5000 Versa Probe-II (ULVAC-PHI, INC, Japan) system with a micro-focused monochromatic Al- $K\alpha$ source ($h\nu = 1486.6$ eV), a hemispherical analyzer, and a multichannel detector. Raman study of the sample was performed using Renishaw in Via Raman microscope with 514 nm Laser and a 50 \times objective with 10 second exposure time at room temperature. UV-visible absorption measurement was executed with a deuterium and halogen combined excitation source with the spectra being recorded using an Avaspec-3648 spectrometer. For determining the local work function value of the as-grown sample nanostructured film, Kelvin probe force microscopy (KPFM) technique was used in ex-situ atomic force microscopy (AFM, Asylum Research, MFP-3D) with lift mode (lift height ≈ 50 nm) using conductive Ir/Pt-coated tips having resonant frequency of ≈ 75 kHz and force constant of ≈ 2.8 N-nm $^{-1}$ [7].

UV-visible photodetection characteristic of MoO_2 material was inspected by making a ≈ 10 nm MoO_3/p -type MoO_2 NSs/n-type Si(100) device with top gold (Au) and bottom

aluminum (Al) contacts. Since, the as-produced MoO₂ NSs behaves as a *p-type* material [34], which was grown on an *n-type* Si substrate; naturally there is a formation of a p-n heterojunction in the as-grown sample itself. Because of significant roughness in the as-grown nanostructured film, we have completed device fabrication by depositing a very thin film of MoO₃ (≈ 10 nm) followed by top (Au) and bottom (Al) contacts using a thermal evaporator (at the base pressure of $\approx 5 \times 10^{-6}$ mbar). The current–voltage (I–V) and photoresponse characteristics of the heterojunction devices were recorded at room temperature using a Keithley semiconductor parameter analyzer (4200 SCS), along with a He–Cd laser (325 nm, 240 mW/cm²) as UV light source and a broad band solar simulator (AM 1.5, 100 mW/cm²) as white light illumination. The external quantum efficiency (EQE) of the device was measured using a Newport quantum efficiency/IPCE measurement system (QEPVSI-b) equipped with a built in lock-in amplifier, a monochromator and a broad band source [7].

7.3 Results and discussion

7.3.1. Structural characterization

Figure 7.2(a) depicts low magnification SEM micrograph of as-grown MoO₂ nanostructures (NSs) on n-type Si substrate, confirming large scale uniform growth; parent material (i.e., α -MoO₃ structures) is shown in the inset of Figure 7.2(a). Figure 7.2(b) represents high magnification SEM micrograph of as-grown black colored products on Si; its inset shows SEM image of single structure from corresponding sample. From high magnification SEM micrographs it is quite evident that average dimensions (length $\approx 0.86 \pm 0.25$ μ m, width $\approx 218 \pm 40$ nm and thickness $\approx 121 \pm 28$ nm) of the as-grown β -MoO₂ NSs have been reduced compared to that of parent α -MoO₃ structures (length $\approx 1.3 \pm 0.6$ μ m, width $\approx 250 \pm 33$ nm and thickness $\approx 150 \pm 42$ nm [32]). X-ray diffraction (XRD) data has been presented in Figure 7.2(c), which reveals that all the obtained peaks can assigned to the monoclinic phase of MoO₂ (β -MoO₂) [35]. We haven't observed any peak related to α -MoO₃ or any sub-oxidized phase of molybdenum oxide and thus parent structure (i.e., α -MoO₃) has been converted into MoO₂ phase perfectly. From SEM studies, dimensions (thickness and specially length) of MoO₂ NSs have been found to decrease compared to α -MoO₃ structures. But there is no specific morphology of as-grown MoO₂ structures, which might be due to

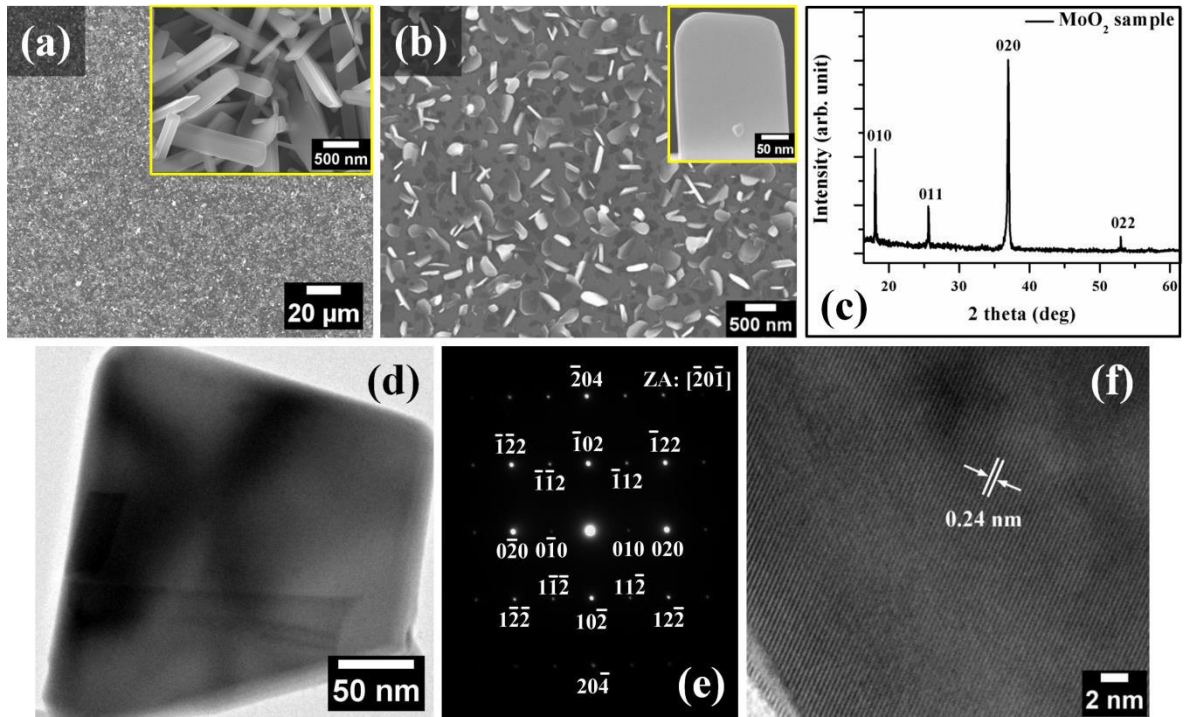


Figure 7.2: (a) Low and (b) high magnification SEM micrographs of as-grown MoO₂ nanostructures grown on Si substrate; inset of (a) shows high magnification SEM image of the parent α -MoO₃ structures on Si substrate; inset of (b) presents single MoO₂ structure. (c) XRD spectrum of the corresponding sample, showing β -MoO₂ phase. (d) Low magnification TEM micrograph of as-prepared MoO₂ structure. (e) SAED pattern and (f) high resolution TEM image from the corresponding structure.

longer time annealing under hydrogen atmosphere. Figure 7.2(d) represents low magnification TEM image of single MoO₂ nanostructure. Selected area electron diffraction (SAED) pattern from the corresponding structure, taken along the $[-2\ 0\ -1]$ zone axis of β -MoO₂ has been framed into Figure 7.2(e), which supports XRD findings (see Figure 7.2(c)). Figure 7.2(f) shows high-resolution TEM (HRTEM) image taken from red rectangular marked area in Figure 7.2(d), revealing β -MoO₂ phase with lattice spacing of ≈ 0.24 nm, corresponding to $d_{(020)}$ [7].

7.3.2 Growth mechanism

Reduction of MoO₃ to MoO₂ has been reported by many researchers in past [2, 4–6, 36–42]. It has been proposed that MoO₃ can be reduced in two ways: 1) one step process or 2) via a new phase α -Mo₄O₁₁. In one step process (< 425 °C), MoO₂ can be produced directly

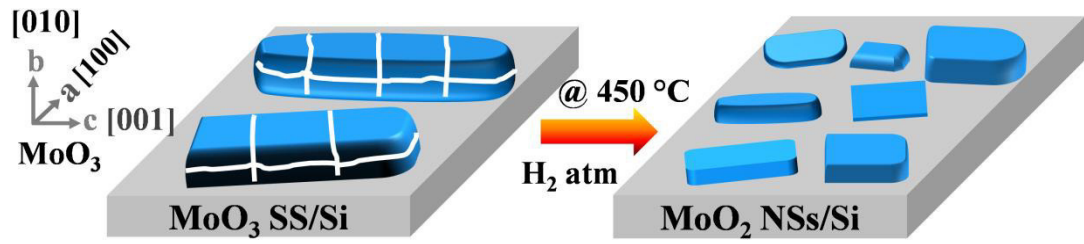
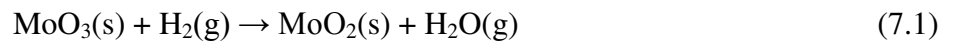
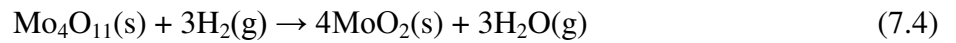
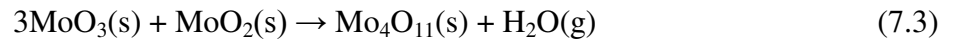
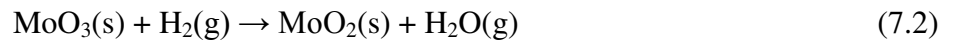


Figure 7.3: A schematic diagram of hydrogenation process to demonstrate the conversion of MoO₃ structures (SS) to MoO₂ nanostructures.

from MoO₃ by the following reaction:



If temperature is $> 425^\circ\text{C}$, second mechanism would be followed:



The later one is the most accepted path for the conversion, in which a new product α -Mo₄O₁₁ would be formed by the reaction between MoO₃ and MoO₂ and finally converted into MoO₂. Since we have performed the hydrogenation process at 450°C , transformation of α -MoO₃ to β -MoO₂ most probably follow the solid state reaction mentioned in the equations (7.2–7.4). So far, chemical reaction mechanism behind the hydrogenation process has been conferred. Following Hu *et. al.*, growth mechanism, we are going to address the plausible mechanism for MoO₂ growth from morphological viewpoint, which has been depicted in Figure 7.3 [2]. The SEM observations of the parent structures and final products have driven us to propose two probable ways by which the conversion could be attained. It is quite evident from SEM images that the thickness and specially length of MoO₂ structures have been reduced with respect to the dimensions of parent α -MoO₃ NSs (source material). Generally, α -MoO₃, is associated with bi-layers of distorted MoO₆ octahedra along [010], connected via the weak van der Waals forces. In the XZ plane, the MoO₆ octahedra forms corner sharing along [100] and edge-sharing zig-zag along [001] [2, 20]. There are three types oxygen atoms in the MoO₃ crystal: (1) terminal oxygen atom bonded to only one Mo atom, (2) symmetric bridging oxygen bonded to two Mo atoms and weakly bonded to another Mo atom and (3) asymmetric bridging oxygen atoms bonded to two Mo atoms [32]. During the conversion process, it is assumed that H₂ would rupture MoO₃, while reacting with it and defects (vacancies or interstitial) in MoO₃ structures are speculated to be active sites for the cracking [2, 4, 5]. In our case, MoO₃ structures contain oxygen vacancies confirmed using XPS, which

is reported in chapter 5 [32]. These vacancy sites could also facilitate H₂ reduction following relatively lower activation energy [5]. In addition, requirement of lesser energy to break the chemical bonds along the [001] direction over [100] direction of MoO₃ NSs, lead to the reduced length of the final β -MoO₂ NSs compared to α -MoO₃ SS [2, 4]. Moreover, reduction in the thicknesses of the MoO₂ NSs compared to the MoO₃ SS can be attributed to the preferential breaking of planes (connected via weak van der Waals force) along [010] direction of MoO₃ structures [5].

7.3.3 Spectroscopic studies

The chemical state and purity of the as-grown β -MoO₂ nanostructured thin film have been analyzed by X-ray photoelectron spectroscopy (XPS) and the results are presented in Figure 7.4. Figure 7.4(a) and 7.4(b) show Mo 3d and O 1s XPS spectra of the corresponding sample, revealing a commixture of Mo⁴⁺ and Mo ^{δ +} states. Here, the main oxidation state is Mo⁴⁺. XPS core level spectrum of Mo 3d level (see Figure 7.4(a)) can be deconvoluted into four Gaussian distributions at four different peaks located at 232.44 eV, 235.58 eV, 231.80 eV and 234.72 eV corresponding to Mo⁴⁺ 3d_{5/2}, Mo⁴⁺ 3d_{3/2}, Mo ^{δ +} 3d_{5/2} and Mo ^{δ +} 3d_{3/2}, respectively [23]. In this case, δ has been defined as $4 > \delta > 0$, because Mo ^{δ +} 3d_{5/2} or Mo ^{δ +} 3d_{3/2} peak is situated between Mo⁴⁺ 3d_{5/2} (eV) and Mo⁰⁺ 3d_{5/2} (eV) or Mo⁴⁺ 3d_{3/2} (eV) and Mo⁰⁺ 3d_{3/2} (eV). The origin of Mo ^{δ +} can be correlated with oxygen vacancies, present in the MoO₂ lattice [32]. The O 1s XPS spectrum of MoO₂ sample is displayed in Figure 7.4(b), which can be fitted with three Gaussian peaks centered at 530.17 eV, 531.51 eV and 532.8 eV. The first peak (530.17 eV) is associated with lattice oxygen (O_L) in MoO₂ lattice [32]. The second peak at 531.51 eV can be assigned to oxygen vacancies (O_V) within the MoO₂ matrix [16, 32]. The remaining peak (532.8 eV) in the O 1s XPS spectrum corresponds to the OH⁻ bond, which may be arises due to the effect of hydrogenation process [43, 44]. Diffused H atoms make bonding with oxygen atoms, resulting oxygen vacancies in MoO₂ matrix [45].

Raman spectrum of the as-grown sample is depicted in Figure 7.4(c), where the spectrum shows several peaks around 207 cm⁻¹, 230 cm⁻¹, 349 cm⁻¹, 367 cm⁻¹, 460 cm⁻¹, 467 cm⁻¹, 497 cm⁻¹, 570 cm⁻¹, 746 cm⁻¹, 942 cm⁻¹. These Raman bands (except 942 cm⁻¹) are the characteristics of β -MoO₂, reported by other groups [35, 46]. The Raman peaks at \approx 207 cm⁻¹, 349 cm⁻¹, 367 cm⁻¹ and 746 cm⁻¹ correspond to Ag- δ (OMo₂), Ag- δ (OMo₃), Ag- δ (O=Mo) and the stretching vibration of the Mo-O (II) group in the MoO₂ lattice; attributions

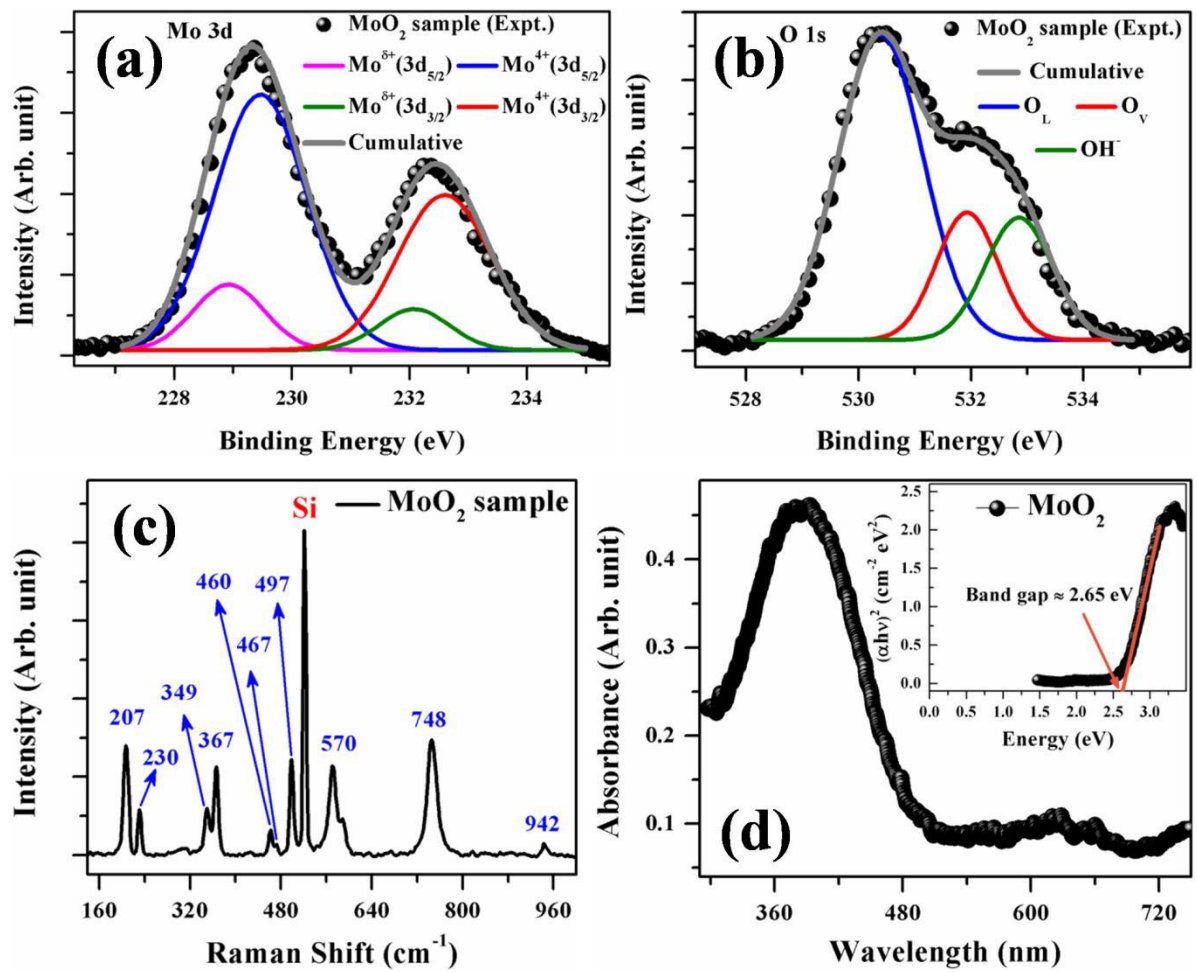


Figure 7.4: (a) Mo 3d and (b) O 1s XPS spectra from as-grown MoO₂ sample. (c) Raman spectrum of as-grown MoO₂ sample. (d) UV-vis absorption spectrum from MoO₂ nanostructures in methanol; inset shows corresponding plot of $(\alpha h\nu)^2$ as a function of photon energy ($h\nu$).

to the remaining peaks are not available in the literature till now [35, 46]. The peak at ≈ 942 cm⁻¹ can be assigned to the oxygen vacancies present on the surface of as-grown MoO₂ NSs, which is also reflected in the O 1s XPS spectrum (see Figure 7.4(b)) [32]. However, the peak at 520 cm⁻¹ is coming due to the silicon substrate.

7.3.4 UV-Vis absorbance

Figure 7.4(d) depicts UV-Vis absorbance spectrum of as-grown MoO₂ NSs dispersed in methanol, showing a sharp absorption in UV range around $\lambda \approx 386$ nm and extended up to ≈ 505 nm i.e., as-grown MoO₂ structures absorb strongly in the UV region and some part of

visible light. For correct determination of band gap, the spectral dependence of the absorption coefficient (α) for direct transitions between the allowed bands is often described as follows:

$$\alpha = A \frac{(h\nu - E_g)^{1/2}}{h\nu} \quad (7.5)$$

where, A is a constant (independent of wavelength) and $h\nu$ is incident photon energy. It follows from the above relation that the spectral dependence of absorption coefficient must linearize in Tauc coordinates $(\alpha h\nu)^2$ vs. $h\nu$; obviously the point of intersection in x-axis for $\alpha = 0$, determines the band gap (E_g) of the material. The measured band gap of p-type β -MoO₂ is found to be ≈ 2.65 eV from the Tauc plot shown in the inset of Figure 7.4(d).

7.3.5 Photodetector device characterization

We have explored the UV-visible photodetection property of *p-type* MoO₂/*n-type* Si heterojunction device by fabricating a device structure, schematically presented in Figure 7.5(a). Figure 7.5(b) presents room temperature typical I-V characteristics under dark recorded in ambient condition. Asymmetry nature of the I-V curve confirms that there is a formation of p-n junction between *n-type* Si and *p-type* MoO₂. The rectification ratio is found to be $\approx 6 \times 10^2$ at a bias voltage of ± 5 V, which is smaller compared to other metal-oxide semiconductor based devices which is possibly due to the interfacial defects driven high leakage current (i.e., reverse bias dark current) [16, 47–50]. The characteristics of an ideal diode can be described using Richardson-Schottky equation considering thermionic emission and diffusion of carriers over barriers, given by [51],

$$I = I_0 \left[\exp \left\{ \frac{q(V - IR_S)}{\eta K_B T} \right\} - 1 \right] \quad (7.6)$$

where I is current across the vertical heterojunction, I_0 the dark current or reverse saturation current, R_S is series resistance, and η is the ideality factor of the diode, q is the elementary charge, K_B is the Boltzmann constant and T is the temperature. The diode parameters have been determined by fitting the dark forward bias I vs. V region using equation (7.6) (inset of Figure 7.5(b)) and the values of η and R_S are found to be 5.75 and 8.2 k Ω . A relatively higher ideality factor presumably originates from the interfacial defects in the heterojunction and high series resistance R_S may be attributed to the crude way of device fabrication as well as un-optimized metal contacts. We also have determined the barrier potential (ϕ_0) of the heterojunction using the reverse saturation current equation given by [51],

$$I_0 = AA^* T^2 \exp \left(-\frac{\phi_0}{K_B T} \right) \quad (7.7)$$

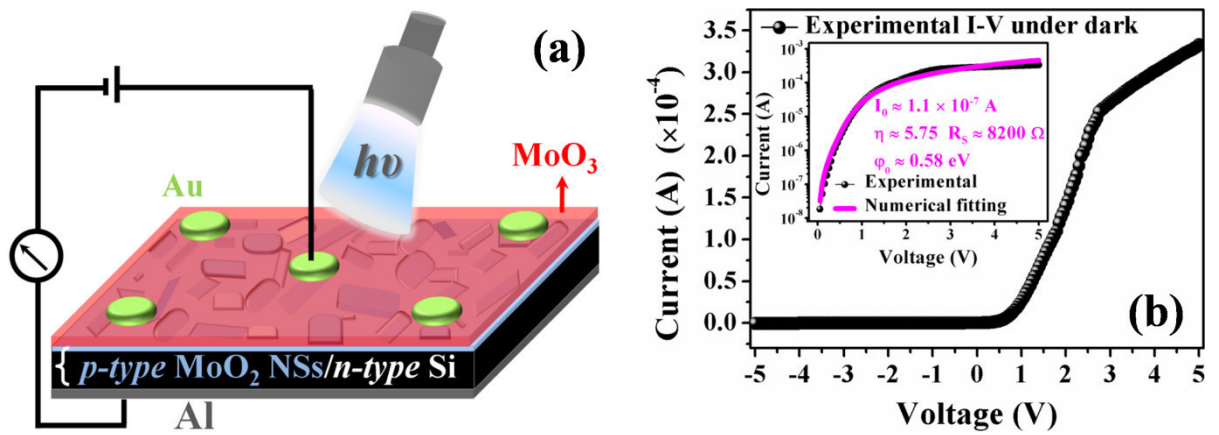


Figure 7.5: (a) Schematic illustration of p-type MoO_2 /n-type Si heterojunction photodetector device structure under illumination. (b) I–V characteristics of the as-prepared device under dark condition; inset shows numerical fitting of forward bias I–V characteristics of the device under dark condition using diode equations.

where, A is the device area ($\approx 3.14 \times 10^{-2} \text{ cm}^2$), A^* is the effective Richardson's constant (considering value of $A^* = 120 \text{ A-cm}^{-2}\text{-K}^{-2}$), ϕ_0 is the barrier potential at zero-bias, K_B is the Boltzmann constant and T is the temperature. The barrier potential at zero-bias for this p-type MoO_2 /n-type Si heterojunction device is estimated to be $\approx 0.58 \text{ eV}$. It is observed that there is a significant increment in the reverse current under both, 325 nm UV illumination ($\approx 240 \text{ mW/cm}^2$) and white light (100 mW/cm^2) illumination, due to the photogenerated minority carriers in the depletion region of the p-n junction device, rendering the UV-visible light sensitivity of our as-grown heterojunction device. It is also interesting to note that photoresponse (photocurrent (I_{Ph})/dark current (I_{D})) of the device is ≈ 5 times more under white light illumination (6.4×10^2) compared to the illumination of 325 nm UV illumination (1.2×10^2). This finding will be understood in the latter discussions. Moreover, there is no significant change in photoresponse ($I_{\text{Ph}}/I_{\text{D}}$) after -1.5 V , which is reflected in Figure 7.6(a) under both UV and white light illuminations. To extract the contribution from MoO_2 nanostructured film in the photoresponse characteristics, we have fabricated control device (Au/n-type Si/Al) and found that control device has very less photoresponse ($I_{\text{Ph}}/I_{\text{D}} \leq 10$) compared to our heterojunction device as evident from Figure 7.6(b). The fabricated heterojunction device is light sensitive even at zero bias, which endows applicability of this device for self-powered, unattended photodetector for security monitoring. As the as-fabricated heterojunction device was enough sensitive at zero bias (0 V) and photoresponse ($I_{\text{Ph}}/I_{\text{D}}$) was maximum at -1.5 V , we have carried out further device characterizations at 0 V and -1.5 V only. The transient photoresponse characteristics of the heterojunction device

have been tested by turning “ON” and “OFF” the white light source (100 mW/cm²) under two different biasing conditions (0 V and –1.5 V) over five consecutive cycles (shown in Figure 7.6(c)). It is evident from Figure 7.6(c) that device is revealing pretty reversible switching performance between high resistivity (OFF state) and low resistivity (ON state) with great stability.

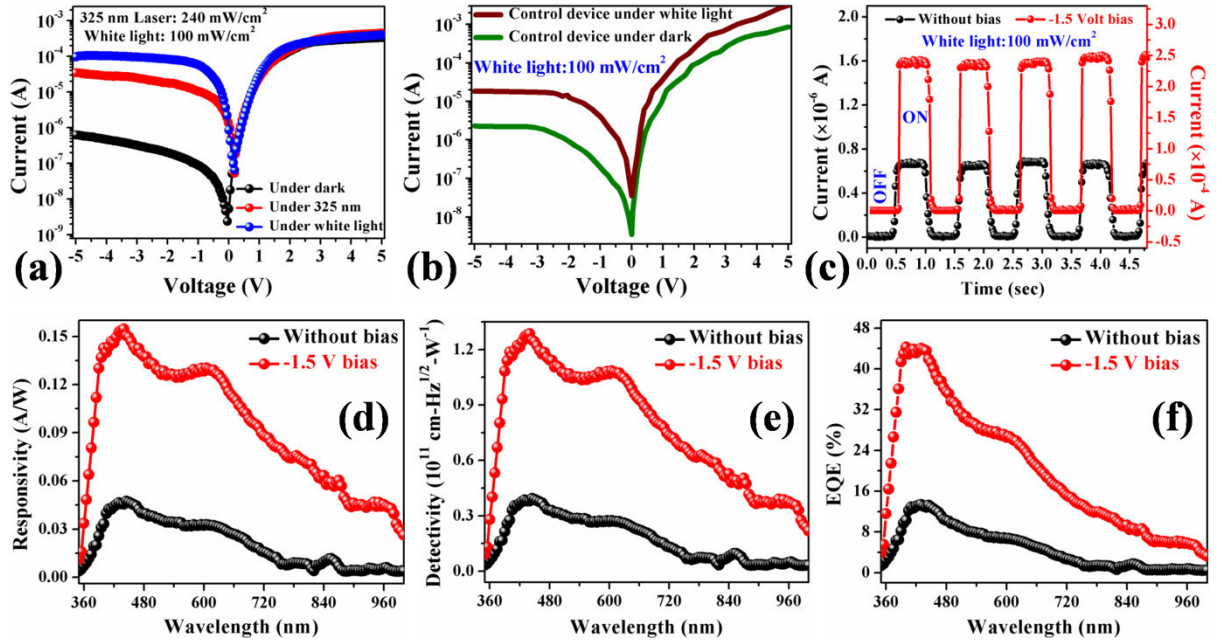


Figure 7.6: (a) *I–V characteristics of as-fabricated device measured in the dark, under 325 nm UV-illumination (240 mW/cm²) and white light (100 mW/cm²).* (b) *I–V characteristics of controlled device (i.e., Au/n-type Si/Al)* (c) *Time responses of the device at two different applied biases under white light.* (d-f) *Figure of merits, i.e., spectral responsivity, detectivity and EQE spectra of the corresponding device respectively.*

Responsivity and detectivity are the main figure of merits, by which the performance of a photodetector is assessed. The responsivity (R) of a photodetector is defined as the ratio of photocurrent (I_{Ph}) to the incident optical power (P_{Opt}) for a particular wavelength λ [16, 50].

$$R(\lambda) = I_{Ph}(\lambda)/P_{Opt} \quad (7.8)$$

Responsivity in wide spectral range from 350 nm to 1000 nm (using a broadband source) with a fixed applied bias of –1.5 V (red color) is displayed in Figure 7.6(d) and compared with zero applied bias (black color). Without bias, the peak responsivity value from our device is found to be 45 mA/W at the wavelength \approx 436 nm. With the increment of applied bias (at –1.5 V bias), the responsivity peak value (0.155 A/W) has been increased by almost \approx

3.2 times in comparison with zero bias case. However, the peak positions remain same for both biases. This peak can be attributed to the UV-visible absorption characteristic of as-grown MoO₂ structures owing to the band gap of the material (see Figure 7.4(d)). Moreover one small peak ≈ 614 nm in the spectral responsivity has been observed for both the biases. Origin of this peak is not very clear to us at this stage but could be assigned partially to the presence of oxygen vacancy and other defect states present in the MoO₂ and at the interface of the device. Detectivity (D) is another important parameter for characteristic of a photodetector, from which signal-to-noise performance of that device will be manifested. Considering the contribution of shot noise to the dark current as the major one, the detectivity of device at a particular wavelength can be evaluated using the following equation [50],

$$D(\lambda) = A^{\frac{1}{2}}R(\lambda)/\sqrt{(2qI_D)} \quad (7.9)$$

where, A is the device area, q is the charge of an electron and I_D is the dark current. Figure 7.6(e) shows the detectivity spectrum of the device at 0 V and -1.5 V, calculated from equation (7.9). Detectivity of the device shows similar kind of nature as observed in spectral responsivity. The peak detectivity of the device is 1.28×10^{11} cm-Hz^{1/2}-W⁻¹ at -1.5 V bias, which is also ≈ 3.1 times higher than that of without bias (4.05×10^{10} cm-Hz^{1/2}-W⁻¹) case. EQE of a detector can be figured out from the spectral responsivity (R) data by employing the relation provided below [16]

$$E(\lambda) = \frac{100 \times 1240 \times I_{ph}}{\lambda \times P_{opt}} = \frac{100 \times 1240 \times R(\lambda)}{\lambda} \quad (7.10)$$

Spectral EQE, evaluated from the above relation, is presented in Figure 7.6(f), from where we have found that the spectral EQE peak (≈ 436 nm) value is 13.5% for zero bias and has been increased to 44% at -1.5 V applied bias. The behavior of *p*-type MoO₂/n-type Si heterojunction device under illumination indicates that the device has potential towards UV-visible broadband photodetection application.

7.3.6 Energy band diagram

The observed UV-visible photodetection characteristics of *p*-type MoO₂/n-type Si heterojunction device can be understood further by proposed model of energy level diagram. To sketch a complete schematic representation of our proposition, it is imperative to know the work function and valence band maximum (VBM) position of the as-grown MoO₂ nanostructured film, which imposes us to perform Kelvin probe force microscopy (KPFM) and XPS valence band measurements. The work function of the sample surface has been

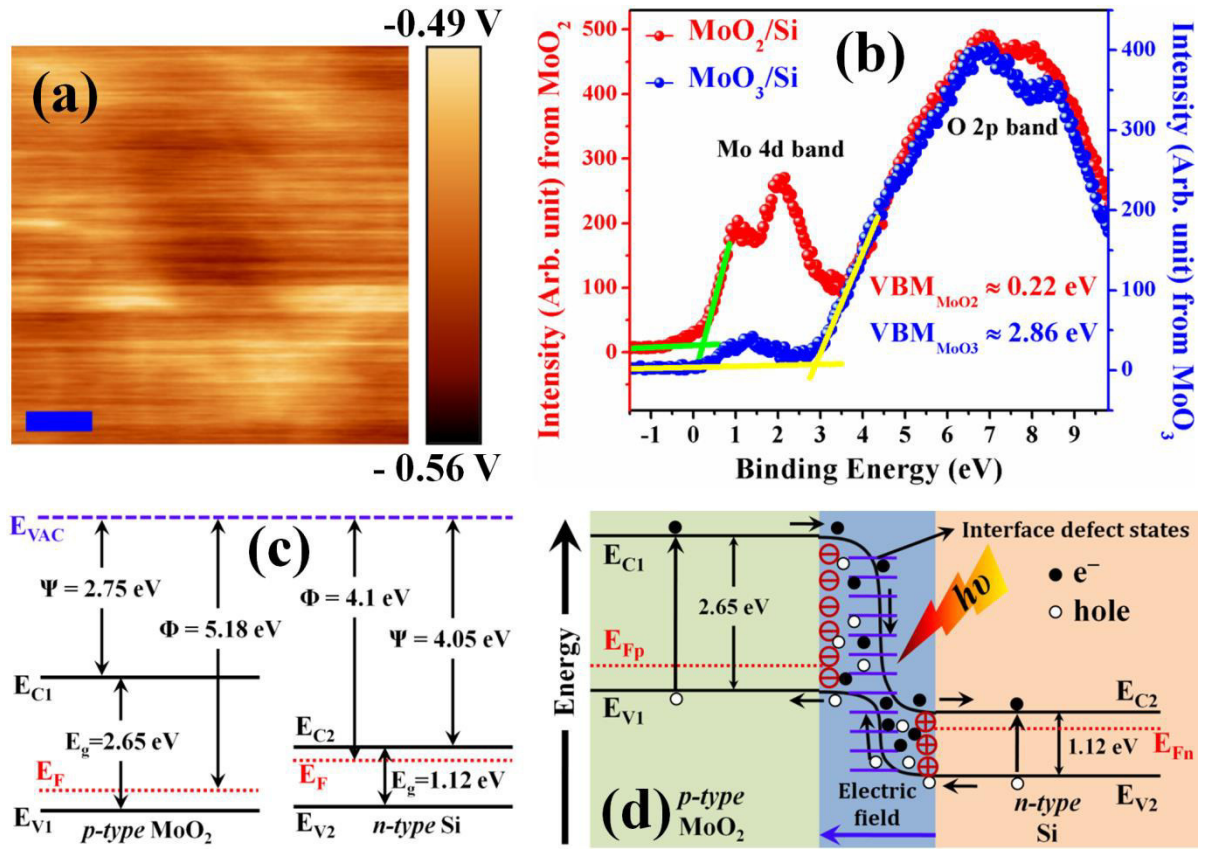


Figure 7.7: (a) Work function mapping image of the as-grown MoO₂ sample using Kelvin probe force microscopy (KPFM) technique; scale bars in the image corresponds to 500 nm. (b) Valence band XPS spectra of the parent α -MoO₃ and as-grown β -MoO₂ on Si substrates acquired at the pass energy of 50 eV. (c) Energy band diagram of isolated MoO₂ nanostructured film and Si substrate. Where, Φ is work function, ψ is electron affinity, E_g is band gap, E_F is Fermi level, E_C is the bottom of conduction band and E_V is the top of valence band for corresponding materials. (d) Energy band diagram of p-type MoO₂/n-type Si heterojunction device at reverse bias condition under illumination.

evaluated by using the following expression [32, 52]

$$V_{DC} = V_{CPD} = -(\Phi_{tip} - \Phi_{sample})/e \quad (7.11)$$

$$\Phi_{sample} = \Phi_{tip} + eV_{CPD} \quad (7.12)$$

where, Φ_{tip} and Φ_{sample} are the corresponding work functions of the tip and sample, respectively; V_{CPD} is the contact potential difference and V_{DC} is an external DC potential applied in the opposite direction (having same magnitude of V_{CPD}) to nullify V_{CPD} . Figure 7.7(a) exhibits the local work function mapping (called as KPFM image) of as-grown MoO₂ nanostructured film on Si. The work function of the tip has been calibrated with respect to the standard HOPG sample and appeared to be $\Phi_{tip} \approx 5.7$ eV. Hence, Φ_{sample} is found out to be \approx

5.18±0.05 eV. Figure 7.7(b) represents XPS valence band spectra taken from the parent α -MoO₃ and as-grown β -MoO₂ NSs grown on Si substrate. Spectrum from α -MoO₃ sample composed of two main regions: the O 2p band, at higher binding energies, from around -10.0 eV to -3.0 eV and a weak band associated with occupied Mo 4d states appears close to the Fermi level (E_F) are kind of non-local states in the band gap possibly arises due to the oxygen related defects [53, 54]. On the other hand, spectrum corresponding to as-grown β -MoO₂ sample also contains two major bands: strong O 2p band at higher binding energies and a distinct Mo 4d band closer to the E_F , which is in close agreement with previous reports [53, 54]. Valence band maximum (VBM) position is defined by the intersection of linear extrapolations of the valence band edge and almost zero intensity base line in the XPS valence band spectrum [55]. VBM position for α -MoO₃ and β -MoO₂ samples have been found out to be ≈ 2.86 eV and ≈ 0.22 eV with respect to the E_F position (shown in Figure 7.7(b)). We have used these experimentally evaluated VBM position, band gap and work function of as-grown β -MoO₂ sample to propose probable energy band diagram of the heterojunction device. Figure 7.7(c) represents schematic energy level diagram of isolated MoO₂ nanostructured film and n-type Si substrate, constructed using our experimentally measured along with earlier reported values of band gap, valence band maximum position and work function/electron affinity of the respective samples [53–55]. After forming p-n junction, with increasing applied reverse bias, corresponding electric field across the depletion region will increase gradually. Now, upon irradiation of proper wavelength, lot of electron–hole pairs are generated at the p-n junction and drift towards the opposite electrodes after dissociation at the interfaces in the presence of electric field, resulting in photocurrent. In this condition Fermi level gets splitted into quasi-Fermi levels for electrons E_{Fn} and for holes E_{Fp} in the respective region [16]. Figure 7.7(d) shows the Fermi level splitting as well as the carrier transportation across the junction of our heterojunction device under reversed bias condition upon illumination.

Table 7.1 summarizes the photoresponsivity, EQE and the response time (raising and decay time) values observed of our fabricated device and compares those values to molybdenum oxide and other oxide materials (TiO₂, Cu₂O etc.) based photodetectors reported in recent days [56, 57]. Table 7.1 clearly corroborates that our device is superior in different regards especially compared to other oxide semiconductor and MoO_x based several photodetectors. The novelty of this work is the highly reproducible synthesis of *p-type* conducting β -MoO₂ nanostructured film on *n-type* silicon substrate and probably the first attempt towards demonstration of self-biased photodetection application of this potential

Table 7.1: Comparison of molybdenum oxide and related oxide materials based various photodetectors

Material	Spectral	Responsivity	EQE	Response time	Ref
Black molybdenum oxide (BMO)	a) NIR b) 320 - 700 nm	a) 12 mA/W (at -3 V) b) 70 mA/W (at -1.5 V)	a) 1.5% (at -3 V) b) 0.1% (at -1.5 V)	- -	3
MoO ₃ nanosheets	UV (250 - 460 nm)	183 mA/W & 524 mA/W (at 10 V & 30 V resp.)	171% (at 30 V)	~ 1.0 sec (at 10 V)	20 (b)
Single MoO ₃ Nanobelt (intrinsic MoO ₃ → no photo-response)	Visible (400 – 700 nm)	56 A/W (at 0.1 V) with very high laser power ~112 mW/cm ²	16300 % (at 0.1 V) with very high laser power ~112 mW/cm ²	> 1 sec	1
MoO ₃ nanobridged	UV	3.3 mA/W (at 10 V) with UV laser power 10 mW/cm ²	-	2 nd raising time and decay time are very high; $t_r = 8.47$ sec $t_d = 16.0$ sec (at 10 V)	20 (a)
In-doped TiO ₂ /n-Si	UV-visible (source power ~ 0.5 mW/cm ²)	16.9 mA/W & 1990 mA/W (at -2 V & -4 V resp.)	5–7% & 250–400% (at -2 V & -4 V resp.)	< 0.05 sec	56 (a)
N-doped TiO ₂ /n-Si		53.3 mA/W & 1090 mA/W (at -2 V & -4 V)	15–17% & 200–250% (at -2 V & -4 V resp.)	< 0.05 sec	
TiO ₂ nanorods/n-Si	UV-visible (source power ~ 0.1 mW/cm ²)	10 ⁻⁶ A/W, 10 ⁻³ A/W & 0.3 A/W (at 0 V, -2 V & -4 V resp.) with 415 nm light	10 ⁻⁴ %, ~0.3% & >90% (at 0 V, -2 V & -4 V resp.) (415 nm light)	-	56 (b)

Cu ₂ O/Si radial nanowire array hetero-junctions	Broadband	0.52 mA/W, 13.05 mA/W and 6.96 mA/W (at -0.5 V) for 405 nm, 532 nm and 1064 nm lasers respectively		-	57
Single phase MoO ₂ (self biased broad-band photo-detection)	Broadband 350 nm - 1000 nm (broadband light source power < 10 mW/cm ²)	45 mA/W (at zero bias) and 155 mA/W (at -1.5 V) with a incident light power < 10 mW/cm ²	13.5% (at zero bias) and average 30 % over broad-band spectra (at -1.5 V)	t _r = ~47 ms t _d = ~70 ms (at 0 V) t _r = ~29 ms t _d = ~38 ms (at -1.5 V)	Our work [7]

material. We have thoroughly studied structural, optical, electronic and optoelectronic properties of as-grown β -MoO₂. It is noteworthy that by probing band gap, valence band maxima position and local work function of β -MoO₂ we have tried to elucidate photodetection mechanism in the light of possible energy band diagrams. It is expected that our work will motivate large community of researchers for further investigation of this interesting material.

7.4. Conclusion

In summary, we have successfully grown β -MoO₂ nanostructures from earlier grown α -MoO₃ structures on n-type Si substrate via annealing under hydrogenation atmosphere (100 sccm H₂ + 10 sccm Ar flow) at 450 °C for 8 hours. TEM, XRD, XPS and Raman measurements confirmed the monoclinic phase of MoO₂; therefore parent α -MoO₃ structure has been fully converted into monoclinic MoO₂ phase without presence of any sub-oxidized phases of molybdenum oxide. A possible growth model behind the growth of β -MoO₂ from α -MoO₃ through hydrogenation process has been proposed. Hall measurement results suggest that as-grown β -MoO₂ can be a good candidate as hole transporting layer (HTL) in optoelectronic devices following its high p-type conductivity of $\approx 2.02 \times 10^3$ S-cm⁻¹ along with moderate hole mobility of $\approx 7.85 \pm 1.28$ cm² V⁻¹ Sec⁻¹. Possibly for the first time potential of β -MoO₂ as possible candidate for UV-Visible photodetection has been realized using as-grown *p-type* MoO₂/*n-type* Si(100) sample itself with Au/~10 nm MoO₃/*p-MoO₂*/*n-Si*/Al device configuration. The device manifested a peak photoresponsivity of 0.155 A/W

with 44% EQE and detectivity $1.28 \times 10^{11} \text{ cm-Hz}^{1/2}\text{-W}^{-1}$ around 436 nm at reverse bias of 1.5 V. Moreover, the this device can be operated in self biasing condition with peak responsivity and detectivity of 45 mA/W and $4.05 \times 10^{10} \text{ cm-Hz}^{1/2}\text{-W}^{-1}$ respectively. Device response speed is significantly faster ($\leq 38 \text{ ms}$ at -1.5 V) compared to recently reported oxide semiconductors based photodetectors even in self biased condition ($\leq 70 \text{ ms}$ at 0 V). The photodetection characteristic of device is modeled by schematic energy band diagram. This broad-band photodetection feature can be attributed to the synergistic effects of MoO₂ band-edge absorption, interfacial defects states induced absorption and self absorption of Si.

7.5 References

- [1] D Xiang, C Han, J Zhang and W Chen, *Sci. Rep.* 2014, **4**, 4891.
- [2] B Hu, L Mai, Chen W and F Yang, *ACS Nano*. **2009**, 3, 478.
- [3] T W Ng, Q D Yang, H W Mo, M F Lo, W J Zhang and C S Lee, *Adv. Opt. Mater.* 2013, *1*, 699.
- [4] L Wu, X Wang, Y Sun, Y Liu and J Li, *Nanoscale* **2015**, 7, 7040.
- [5] Y Sun, X Hu, J C Yu, Q Li, W Luo, L Yuan, W Zhang and Y Huang, *Energy Environ. Sci.* **2011**, 4, 2870.
- [6] J Dang, G H Zhang, K C Chou, R G Reddy, Y He and Y Sun, *Int. J. Refract. Met. Hard Mater.* **2013**, 41, 216.
- [7] P Guha, A Ghosh, A Sarkar, S Mandal, S K Ray, D K Goswami and P V Satyam, *Nanotechnology*, **2018** (under review).
- [8] Y Li, F Qian, J Xiang and C M Lieber, *Mater. Today* **2006**, 9, 18.
- [9] T Zhai, X Fang, M Liao, X Xu, H Zeng, B Yoshio and D Golberg, *Sensors* 2009, 9, 6504.
- [10] E Monroy, F Omnes` and F Calle, *Semicond. Sci. Technol.* **2003**, 18, R33.
- [11] L Sang, M Liao and M Sumiya, *Sensors* **2013**, 13, 10482.
- [12] T Mueller, F Xia and P Avouris, *Nat. Photonics* **2010**, 4, 297.
- [13] A K Bansal, S Hou, O Kulyk, E M Bowman and D W Samue, *Adv. Mater.* **2015**, 27, 7638.
- [14] C J Chen, K K Choi, W H Chang and D C Tsui, *Appl. Phys. Lett.* **1998**, 72, 7.
- [15] G Cao, *Nanostructures & Nanomaterials: Synthesis, Properties & Applications* (Imperial College Press, 2004, ISBN: 978-981-4322-50-8).

- [16] A Ghosh, P Guha, S Mukherjee, R Bar, S K Ray and P V Satyam, *Appl. Phys. Lett.* **2016**, *109*, 123105.
- [17] F H L Koppens, T Mueller, P Avouris, A C Ferrari, M S Vitiello and M Polin, *Nat. Nanotechnol.* **2014**, *9*, 780.
- [18] A V Barve, S J Lee, S K Noh and S Krishna, *Laser Photon. Rev.* **2010**, *4*, 738.
- [19] Zhao C, Z Liang, M Su, P Liu, W Mai and W Xie, *ACS Appl. Mater. Interfaces* **2015**, *7*, 25981.
- [20] (a) Q Zheng, J Huang, H Yang and Y Chen, *Nanotechnology* **2017**, *28*, 045202.
(b) Q Zheng, J Huang, S Cao and H Gao, *J. Mater. Chem. C* **2015**, *3*, 7469.
- [21] L Mai, F Yang, Y Zhao, X Xu, L Xu, B Hu, Y Luo and H Liu, *Mater. Today* **2011**, *14*, 346.
- [22] H Hu, J Xu, C Deng and X Ge, *J. Nanosci. Nanotechnol.* **2014**, *14*, 4462.
- [23] A Khademi, R Azimirad, A A Zavarian and A Z Moshfegh, *J. Phys. Chem. C* **2009**, *113*, 19298.
- [24] L Zheng, Y Xu, D Jin and Y Xie, *J. Mater. Chem.* **2010**, *20*, 7135.
- [25] X Zhang, Z Hou, X Li, J Liang, Y Zhu and Y Qian *Electrochim. Acta* **2016**, *213*, 416.
- [26] L Zeng, X Huang, X Chen, C Zheng, R Liu, G Chen, Q Qian, Q Chen and M Wei, *RSC Adv.* **2016**, *6*, 105558.
- [27] X Liu, Y He, S Wang and Q Zhang, *J. Alloys Compd.* **2011**, *509S*, S408.
- [28] J Zhou, N S Xu, S Z Deng, J Chen, J C She and Z L Wang, *Adv. Mater.* **2003**, *15*, 1835.
- [29] M Suemitsu, T Abel, H J Na and H Yamane, *Jpn. J. Appl. Phys.* **2005**, *44*, 12.
- [30] A Bhaskar, M Deepa and T N Rao, *ACS Appl. Mater. Interfaces* **2013**, *5*, 2555.
- [31] C A Ellefson, O M Flores, S Ha and M G Norton, *J. Mater. Sci.* **2012**, *47*, 2057.
- [32] P Guha, A Ghosh, R Thapa, E M Kumar, S Kirishwaran, R Singh and P V Satyam, *Nanotechnology* **2017**, *28*, 415602.
- [33] Q Xie, X Zheng, D Wu, X Chen, J Shi, X Han, X Zhang, G Peng, Y Gao and H Huan, *Appl. Phys. Lett.* **2017**, *111*, 093505.
- [34] T Matsushima and C Adachi, *J. Appl. Phys.* **2008**, *103*, 034501.
- [35] L Kumari, Y R Ma, C C Tsai, Y W Lin, S Y Wu, K W Cheng and Y Liou *Nanotechnology* **2007**, *18*, 115717.
- [36] J Orehotzky, L Jamiolkowski and J Gerboc, *Mater. Sci. Eng.* **1979**, *41*, 237.
- [37] F Delanna, *Phys. Stat. Sol. (a)* **1982**, *73*, 529.
- [38] J Słoczyn'ski and W Bobin'ski, *J. Solid State Chem.* **1991**, *92*, 436.

- [39] P A Spevack and N S McIntyre, *J. Phys. Chem.* **1992**, 96, 9029.
- [40] J Słoczyn'ski, *J. Solid State Chem.* **1995**, 118, 95.
- [41] T Ressler, R Jentoft E, J Wienold, M M Gulnter and O Timpe, *J. Phys. Chem. B* **2000**, 104, 6360.
- [42] E Lalik, *Catal. Today* **2011**, 169, 85.
- [43] A Roustila, J Chene and C Severac, *J. Alloys Compd.* **2003**, 356, 330.
- [44] A Borgschulte, O Sambalova, R Delmelle, S Jenatsch, R Hany and F Nüesch, *Sci. Rep.* **2017**, 7, 40761.
- [45] J Z Ou, J L Campbell, D Yao, W Wlodarski and K Kalantar-zadeh, *J. Phys. Chem. C* **2011**, 115, 10757.
- [46] M A Camacho-López, L Escobar-Alarcón, M Picquart, R Arroyo, G Córdoba and E Haro-Poniatowski, *Opt. Mater.* **2011**, 33, 480.
- [47] Q Hong, Y Cao, J Xu, H Lu, J He and J L Sun, *ACS Appl. Mater. Interfaces* **2014**, 6, 20887.
- [48] Y Xie, L Wei, Q Li, Y Chen, H Liu, S Yan, J Jiao, G Liu and L Mei, *Nanoscale* **2014**, 6, 9116.
- [49] H Zhou, G Fang, L Yuan, C Wang, X Yang, H Huang, C Zhou and X Zhao, *Appl. Phys. Lett.* **2010**, 96, 053102.
- [50] A Sarkar, A K Katiyar, S Mukherjee and S K Ray, *J. Phys. D: Appl. Phys.* **2017**, 50, 145104.
- [51] S Mukherjee, S Biswas, S Das and S K Ray, *Nanotechnology* **2017**, 28, 135203.
- [52] A Ghosh, P Guha, R Thapa, S Selvaraj, M Kumar, B Rakshit, T Dash, R Bar, S K Ray and P V Satyam, *Nanotechnology* **2016**, 27, 125701.
- [53] F Werfel and E Minni, *J. Phys. C: Solid State Phys.* **1983**, 16, 6091.
- [54] D O Scanlon, G W Watson, D J Payne, G R Atkinson, R G Egdell and D S L Law, *J. Phys. Chem. C* **2010**, 114, 4636–4645.
- [55] X Li, L Liang, H Cao, R Qin, H Zhang, J Gao and F Zhuge, *Appl. Phys. Lett.* **2015**, 106, 132102.
- [56] (a) T Ji, Q Liu, R Zou, Y Zhang, L Wang, L Sang, M Liao and J Hu, *J. Mater. Chem. C* **2017**, 5, 12848.
(b) T Ji, Q Liu, R Zou; Y Sun, K Xu, L Sang, M Liao, Y Koide, L Yu and J Hu, *Adv. Funct. Mater.* **2016**, 26, 1400.
- [57] J Xu, Y Cao, J Wei, J L Sun, J Xu and J He, *Mater. Res. Express* **2014**, 1, 015002.

Chapter 8

Summary and Conclusions

The thesis work dealt with novel approaches for incorporating metal nanostructures on the surfaces and at the interfaces of oxide materials. Here, *coherent* growth of silver nanostructures that can be either *on (epi)* the oxide layers or *in (endo)* the oxide/substrate nanoscale systems have been studied carefully. The focus is on the silver nanostructures growth with two oxide materials: inside germanium oxide (GeO_x) and above molybdenum trioxide (MoO_3); incorporation of Ag nanostructures enhanced the properties. In the result section in this thesis (i.e., chapters 3 and 4), emphasis was given on two aspects: (i) real time *in-situ* XRD study of the growth kinetics of Ag nanostructures along with determination of thermal expansion coefficient and (ii) use of energetic ion beams to reduce the process temperature for the growth of endotaxial Ag nanostructures in silicon. This was followed with a *single step novel* technique to grow silver nanoparticles above MoO_3 structures. Ag nanoparticles have been decorated on MoO_3 structures; surprisingly $\text{MoO}_3(010)$ surface didn't incorporate any silver nanoparticles. Experimental findings have been complemented with density functional theory (DFT) calculations. Ambient dependent studies were accomplished to examine on the growth of site specific Ag nanoparticle decoration on MoO_3 structures. This intrinsically self assembled Ag-decorated MoO_3 structures have been used for electron field emission device, detecting sub-micro molar dye molecules. However, the intrinsic MoO_3 exhibits low electrical and thermal conductivity and weak photoresponse. In order to improve the conductance, H_2 annealing has been employed to enhance the conductivity. We have prepared MoO_2 structures from MoO_3 structures via H_2 process and UV-Vis photodetection device application of as-grown MoO_2 , which are presented in the 7th chapter of this thesis.

In chapter 1, a brief introduction to the need of growing silver (Ag) nanoparticles (NPs) either inside or on the oxide materials (GeO_x or MoO_3) and their intrinsic properties with possible applications were outlined. Introduction chapter also includes the motivation of the work being carried out for this thesis. The working principles and instrumentations of all the major experimental techniques that were employed for the materials growth, characterizations and their applications related to this thesis work were briefly narrated in second chapter.

The chapters three and four result about the silver nanoparticles embedded inside oxide layer (GeO_x) on a silicon substrate. In the 3rd chapter, *real time in-situ* growth of coherently embedded silver nanostructures were reported (by performing the growth through chemical vapor obtained from evaporation of Ag of a silver wire under ambient condition during synchrotron based high-temperature X-ray diffraction (XRD) measurements under atmospheric conditions). A ≈ 17 nm thick GeO_x film was grown on native oxide covered silicon substrates ($\text{GeO}_x/\text{SiO}_x/\text{Si}$) using a physical vapor deposition (PVD) method, that were used as substrates for Ag nanostructures growth. As the temperature is raised from room temperature to 850 °C during in-situ growth, the evolutions of various diffraction peaks such as (200), reflecting from growth facets of Ag nanostructures were monitored as a function of growth temperature and time. The lattice constant of Ag nanostructures obtained from ex-situ growth specimens were used to compare with the real time – *in-situ* high temperature XRD measurements. With the increase of temperature, the FWHM of Ag(200) was decreased and the position of the peaks were found to shift towards lower θ , corresponding to the increment in the effective lattice constant values and the reduction in thermal expansion coefficients (TECs) corresponding to Ag nanostructures. TEC values found to decrease from 1.9×10^{-5} /°C to 1.82×10^{-5} /°C with temperature increment from 750 °C to 850 °C. Most importantly, crystallite size didn't contribute significantly in TEC, for our case. The activation energy (E_0) for the growth of silver nanostructures calculated to be 0.171 ± 0.004 eV.

In chapter 4, ion irradiated effects of silver (Ag) ions on $\text{GeO}_x/\text{SiO}_x/\text{Si}$ system found to reduce the formation temperature of the endotaxial nanostructures (NSs). This was attributed to the defects formed at the interfaces due to ion irradiation. Endotaxial nanostructures of Ag at the Si interface were formed with 30 keV negatively charged silver ions (Ag^-) on $\text{GeO}_x/\text{SiO}_x/\text{Si}$ system. Furthermore, 30 keV Ag^- ions were used to create defects in GeO_x , SiO_x and in silicon substrate followed by ≈ 2 nm thin layer of silver deposition, yielded endotaxial Ag nanostructures relatively at lower temperature (700 °C). However, high energy (1.8 MeV) Ag ions didn't have any impact on the growth temperature

for endotaxial Ag NSs as the structures were formed at 800 °C. It should be noted that, ion irradiation would result in sputtering the top GeO_x layer results in the amorphization of the silicon substrate. It is also noticed that Ag diffusion is more when the defects are directly created in GeO_x layer; it was essential to have crystalline silicon substrate to grow coherently embedded Ag NSs at comparative lower temperature 700 °C. To avoid amorphization in silicon substrate from 30 keV Ag ions, a ≈ 70 nm thick GeO_x layer has been utilized.

In next two chapters i.e., chapters 5 and 6, a very interesting and successful inclusion of silver (Ag) nanoparticles on another oxide material (MoO_3) were conferred. We reported a simple technique to grow packed MoO_3 structures and Ag- MoO_3 heterostructures (HSs) on varied substrates in a single step process (in chapter 5). XRD and TEM data revealed the orthorhombic phase of MoO_3 ($\alpha\text{-MoO}_3$) with $[001] > [100] \gg [010]$ growth rate order, oriented along $[0\ 2k\ 0]$ direction. All the Ag NPs were decorated on specific MoO_3 surfaces ((100) and (001)) following the surface energetics. The probable growth mechanism for site specific Ag decoration on MoO_3 surfaces has been discussed by calculating surface energies of Ag(111)/ MoO_3 (100), Ag(111)/ MoO_3 (010) and Ag(111)/ MoO_3 (001) structures employing density functional theory (DFT). The DFT calculations showed that the MoO_3 (010) surface is weakly interacting and stable surface compared to other orientations. From DFT studies, the binding energy was found to be higher for (100) and (001) surfaces (≈ -0.98 eV), compared to (010) surface (≈ -0.15 eV) and thus it is likely that Ag NPs formation is not favorable on MoO_3 (010) surface. Site specific Ag decoration was found to be a substrate independent phenomenon. We explored enhanced field emission properties of Ag- MoO_3 sample compared to MoO_3 sample in terms of ≈ 2.1 times lower turn-on voltage and ≈ 10 times higher field enhancement factor. From Kelvin probe force microscopy (KPFM) measurements, the average local work function (Φ) was found to be ≈ 0.47 eV smaller for Ag- MoO_3 sample ($\approx 5.70 \pm 0.05$ eV) compared to MoO_3 sample ($\approx 6.17 \pm 0.05$ eV) and the reduction in Φ could be attributed to the shifting Fermi level of MoO_3 toward vacuum via electrons injection from Ag NPs to MoO_3 . Presence of oxygen vacancies together with Ag NPs led to the highest β and lowest turn-on field among the reported values under MoO_3 emitters' category.

The role of different ambience viz argon (Ar), air, low vacuum (LV) and high vacuum (HV) on energetically favorable site specific silver nanoparticles decorated MoO_3 structures was observed from experimental viewpoint. Site specific growth has been noticed only in Ar ambience. In the case of air ambient condition, few silver nanoparticles are observed on MoO_3 (010) surface. Hence, vapor pressure and also oxygen partial pressure are found to be crucial for this type of growth. These Ag- MoO_3 heterostructures have been used as free

standing SERS substrates to detect sub-micro molar Crystal Violet (as low as 1 μM CV solution) molecule with an analytical enhancement factor (AEF) of $\approx 10^4$ using 514.5 nm green laser as excitation.

However, the intrinsic MoO_3 exhibits low electrical and thermal conductivity and weak photoresponse. In order to improve the conductance, H_2 annealing is appeared to be the best process for enhancing the conductivity. In the last chapter of this thesis, rational synthesis and UV-visible photodetection application of *p-type* MoO_2 nanostructures (NSs) on Si platform were reported. We grew monoclinic MoO_2 NSs ($\beta\text{-MoO}_2$) from previously grown $\alpha\text{-MoO}_3$ structures/*n-type* Si via hydrogenation process at 450 $^\circ\text{C}$ for 8 hours (100 sccm H_2 +10 sccm Ar flow). We have confirmed using XRD, XPS, and HRTEM that after hydrogenation $\alpha\text{-MoO}_3$ NSs were completely converted into $\beta\text{-MoO}_2$ NSs without presence of any sub-oxidized phase of molybdenum oxide. A possible growth model behind the growth of $\beta\text{-MoO}_2$ from $\alpha\text{-MoO}_3$ through hydrogenation process was proposed from morphological aspect. To explore the optoelectronic properties of *p-type* MoO_2 NSs, we have fabricated *p-type* MoO_2 /*n-type* Si heterojunction (as-grown) photodetector device with Au as top and Al as bottom contacts. The device manifested a peak photoresponsivity of 0.155 A/W with 44% external quantum efficiency (EQE) and detectivity $1.28 \times 10^{11} \text{ cm}\cdot\text{Hz}^{1/2}\cdot\text{W}^{-1}$ around 436 nm at reverse bias of 1.5 V. Moreover, the this device can be operated in self biasing condition with peak responsivity and detectivity of 45 mA/W and $4 \times 10^{10} \text{ cm}\cdot\text{Hz}^{1/2}\cdot\text{W}^{-1}$ respectively. The photodetection characteristic of device was modeled by schematic energy band diagram. This broad-band photodetection feature can be attributed to the synergistic effects of MoO_2 band-edge absorption, interfacial defects states induced absorption and self absorption of Si.

Looking at more generalized view for future, it would be both fascinating and beneficial to generalize the endotaxial growth for other materials (like Au, Co, Pt etc.). Replacing GeO_x with other oxide materials on endotaxial growth can be studied systematically. One can attempt to grow MoO_3 heterostructures with other metals in a *single step* process. Moreover, *single step* growth technique for growing other wide direct band gap oxide semiconductors specially layered materials which will be coupled with silver nanoparticles, can be investigated. At current scenario, molybdenum oxide is very useful material for oxygen evolution reaction (OER) and hydrogen evolution reaction (HER). The MoO_3 and MoO_2 structures possess oxygen deficiencies (O_V) and specially MoO_2 has OH^- ions (due to hydrogenation process), it would be interesting to study their OER and HER

performances as a function of O_V and OH^- both from experimental and theoretical perspectives on which we have already started working.